Nonspherical deformed atomic fragments and nonselfconsistent density functionals from *ab initio*

Dissertation
zur Erlangung des Grades eines Doktors
der Naturwissenschaften

vorgelegt von
Alexander Poddey
aus Karlsruhe

genehmigt von der Fakultät für Material- und Natur-
wissenschaften der Technischen Universität Clausthal

Tag der mündlichen Prüfung:
28. November 2008

Hiermit erkläre ich an Eides Statt, dass ich die bei der Fakultät für Material- und Naturwissenschaften der Technischen Universität Clausthal eingereichte Dissertation selbständig und ohne unerlaubte Hilfe verfasst und die benutzten Hilfsmittel vollständig angegeben habe.

Clausthal, 22. September 2008   Alexander Poddey

Hiermit erkläre ich an Eides Statt, dass die eingereichte Dissertation weder in Teilen noch in ihrer Gesamtheit einer anderen Hochschule zu Begutachtung vorliegt oder vorgelegen hat, und dass ich noch kein Promotionsversuch unternommen habe.

Clausthal, 22. September 2008   Alexander Poddey

Die Arbeit wurde angefertigt am
Institut für Theoretische Physik der Technischen Universität Clausthal.

Vorsitzender der Promotionskommission: Prof. Winfried Daum

Hauptberichterstatter: Prof. Dr. Peter E. Blöchl

Berichterstatter: Prof. Dr. Tom Kirchner

Vita brevis, ars longa, occasio praeceps, experientia fallax.

Das Leben ist kurz, die Kunst lang, die Gelegenheit flüchtig, die Erfahrung trügerisch.
Hippokrates

Contents

Abstract

The main numerical effort in common electronic structure methods is spent in the setup and diagonalization of the Hamiltonian. Without further approximations, this effort scales cubicly with the number of particles involved. The complexity of quantum mechanics usually requires an iterative approach. This is unfavorable, because the badly scaling system of equations needs to be solved several times in order to reach sufficiently accurate results. Over the years, there have been several more or less sophisticated approaches to circumvent these problems. The effort in reducing the numerical demands usually either results in less intelligible approaches, theoretically not well funded approximations or representations which make it hard to extract the physical meaning.

The approach presented in this work is focused on a formulation which is consistent with the physico-chemical intuition and makes use of straight forward and well controllable approximations to reduce the numerical effort. In order to achieve this goal, the transformation from *isolated* to *clustered* atoms is splitt in two steps: deformation from the atomic to a reference state, and clustering. An ab initio based construction of embedding potentials allows to deform the individual atoms such that the non-spherically deformed fragment densities reflect the crystal structure. The numerical effort in this step corresponds to isolated atom calculations and scales virtually linear with system size. The superposition of fragment densities however comes close to the clusters density. It can therefore be used as input-density for non-selfconsistent calculations. Furthermore, a new non-selfconsistent functional, based on energies relative to the isolated atom, is introduced. It allows to reduce the numerical errors due to enhanced error cancellation and improves the interpretability of results. Because of the localized nature of the deformed densities, the cluster's Hamiltonian becomes sparse. This additionally reduces the numerical effort.

Due to the non-spherical character of the deformed fragments, the crystal structure is reflected in the input-density. The new construction therefore overcomes the limitations of usually applied frozen atomic fragments. This is confirmed by systematic analysis of a H_2 model system.

Pros and cons of several possible numerical implementations are discussed in detail.

1 Introduction

Although the common citizen does not realize, a good portion of the modern technical world's advances involves the application of quantum theory. This reaches from amenities such as portable mp3 players, which are able to store several Gigabyte of coded music and decode it on the fly with an energy consumption so low, that a micro-battery lasts for ten's of hours. The underlying semiconductor devices are nowadays present in almost every area of life. Quantum mechanically driven materials engineering on the other hand allows to develop new alloys which are e.g. used in astronautics, automobiles or medical devices such as hip joint endoprosthesis. Besides these quite technical applications, quantum theoretical methods even contribute to the progress in understanding biological systems and the basic principles of life. All these outstanding applications however correspond to fruits matured on a tree fostered and nourished by generations of scientists. The nutriments thereby come from basic research. Development of new methods usually starts with an idea, which first of all needs to be formulated on a theoretical basis. The complexity of quantum mechanics usually does not allow to solve the corresponding mathematical equations analytically. In order to apply new approaches to all day work problems, theoretically well funded approximations need to be applied. In the framework of computational approaches, appropriate numerical implementations need to be found. The effort in reducing the numerical demands however usually either results in less intelligible approaches, theoretically not well funded approximations or representations which make it hard to extract the physical meaning.

The approach presented in this work[1] is focused on a formulation which is consistent with the physico-chemical intuition. We thereby apply theoretically well funded and straight forward approximations. In our view, intuition, well controllable approximations and numerical efficiency do not have to be mutually exclusive, but can lead to synergetic effects[2].

The thesis consists of four main parts. The first part addresses the basic concepts. It prepares the ground in which the seeds of the novel theory, discussed in part two will be sowed. As in any fruit-growing, the first grafts need to be thoroughly examined. This is done in part three. The last part of this thesis finally provides detailed background information concerning the specific prospects and sensitivities of the new approach.

---

[1]In the presented thesis, I keep the internal working title *SESM* - which is derived from Simple (to interpret) Electronic Structure Method. The final denomination of the approach however may be different.

[2]I use the plural *we* in this statement, because the development of the new approach rests on contributions from several current and former members of our institute.

It should allow the interested gardener to grow the plantlet to strong trees, full of sweet fruits.

Part I

State of the art

2 Basic concepts and tool kit preparation

2.1 The Hamiltonian for a multi-particle system

The solution of the time independent Schrödinger equation

$$\hat{H}|\Psi\rangle = E|\Psi\rangle \tag{2.1}$$

gives access to the total energy E of a given system. Considering a system of N nuclei and n electrons the wave function[1] $\Psi\left(\mathbf{x}_1, ..., \mathbf{x}_n, \mathbf{R}_1, ..., \mathbf{R}_N\right)$ is depending on the coordinates of every nuclei $\mathbf{R}_i$ and electron $\mathbf{x}_i$. The coordinates $\mathbf{x}_i$ comprise space coordinates $\mathbf{r}_i$ and spin coordinates s_i. The contributions to the Hamiltonian operator $\hat{H}$ can be divided as follows (the terms on the right of the equals signs correspond to the expressions in configurational space):

- Kinetic energy of the nuclei
  $\hat{T}_n = -\sum_i \frac{\hbar^2}{2m_i}\nabla^2_{\mathbf{R}_i}$

- Nuclei-nuclei interaction
  $\hat{V}_{nn} = \frac{1}{2}\sum_{i \neq j} \frac{Z_{\mathbf{R_i}} \cdot Z_{\mathbf{R_j}} \cdot e^2}{4\pi\varepsilon|\mathbf{R}_i - \mathbf{R}_j|}$

- Kinetic energy oft the electrons
  $\hat{T} = -\sum_i \frac{\hbar^2}{2m_e}\nabla^2_{\mathbf{r}_i}$

- Electron-electron interaction
  $\hat{V}_{ee} = \frac{1}{2}\sum_{i \neq j} \frac{e^2}{4\pi\varepsilon|\mathbf{r}_i - \mathbf{r}_j|}$

- Electron-nuclei interaction
  $\hat{V}_{en} = -\sum_{i,j} \frac{Z_{\mathbf{R}_j} \cdot e^2}{4\pi\varepsilon|\mathbf{r}_i - \mathbf{R}_j|}$

- External potential
  $\hat{V}_{ext'} = \sum_i \left(V_{ext'e}(\mathbf{x}_i) + V_{i,ext'n}(\mathbf{R}_i)\right)$.

---

[1] $\Psi(\mathbf{r})$ is a projection of $|\Psi\rangle$ on the configurational space according to $|\Psi\rangle = \int |\mathbf{r}\rangle \underbrace{\langle \mathbf{r}|\Psi\rangle}_{\Psi(\mathbf{r})} \, d\mathbf{r}$. $|\mathbf{r}\rangle$ thereby is an abbreviation of the form $|\mathbf{r}\rangle = \lim_{\Delta\tilde{\mathbf{r}} \to 0} \frac{|\tilde{\mathbf{r}}\rangle}{\sqrt{\Delta\tilde{\mathbf{r}}}}$, with discrete $|\tilde{\mathbf{r}}\rangle$ [1].

Following the Born-Oppenheimer[2] approximation one can decouple the electronic from the atomic motion [2]. The electrons then experience an external potential with contributions from the static atomic geometry and the Hamiltonian can be written as:

$$
\begin{aligned}
\hat{H} &= \hat{T} + \hat{V}_{ee} + \hat{T}_n + \hat{V}_{nn} + \hat{V}_{en} + \hat{V}_{ext'} \\
&= \hat{T} + \hat{V}_{ee} + \hat{V}_{ext}
\end{aligned}
\tag{2.2}
$$

Using Hartree atomic units[3] ($\hbar = e = m_e = 4\pi\varepsilon_0 = 1$) [3] this can be written as:

$$
\hat{H} = -\sum_i \frac{1}{2}\nabla^2_{\mathbf{r}_i} + \frac{1}{2}\sum_{i\neq j}\frac{1}{|\mathbf{r}_i - \mathbf{r}_j|} + \hat{V}_{ext}
\tag{2.3}
$$

The above setup with division of physical systems in classical nuclei and quantum mechanically treated electrons will in the following simply be referred to as *system.*

2.2 Empirical tight-binding

Empirical tight-binding was introduced in 1954 by Slater and Koster [4] as an interpolation method to be used in connection with more accurate calculations. It is based on the method of linear combination of atomic orbitals (LCAO), which Bloch extended to periodic potentials [5]. Bloch showed that the wave function in a periodic potential can be written as the product of a periodic function times a phase factor. This suggests that superposition of the atomic orbitals of a certain species, residing on all periodic images of a crystal, may be an appropriate basis set for the solution of the corresponding Schrödinger equation. These so called Bloch sums can be written as

$$
\Phi^n(\mathbf{k},\mathbf{r}) = \frac{1}{\sqrt{N}}\sum_j e^{i\mathbf{k}\mathbf{R}_j}\phi^n(\mathbf{r} - \mathbf{R}_j)
\tag{2.4}
$$

with ϕ^n denoting the n'th atomic orbital for a given species residing at the various crystal sites $\mathbf{R}_j$ and $\mathbf{k}$ being the wave vector. The sum in principle is to be extended over all (N) periodic images.

The resulting expressions for the Hamiltonian matrix elements at a given $\mathbf{k}$ are

---

[2] The Born-Oppenheimer approximation rests on the fact that the nuclei are much more massive than the electrons and therefore move much slower. This allows the electrons to relax almost immediately while the nuclei are moving. The movement of the electrons is therefore adiabatic and decoupled from the nuclei motion. The Born-Oppenheimer approximation is also called "adiabatic approximation".

[3] These will be used in the following (unless otherwise specified). The length unit is the Bohr radius $a_0 = 0.5392$Å, the charge unit is the charge of an electron e, the mass unit is the mass of an electron m_e and the energy unit H corresponds to twice the ground-state energy of an electron in an hydrogen atom ($2 \times 13.6 eV$).

linear combinations of integrals of the form

$$\int \phi^n \left(\mathbf{r} - \mathbf{R}_i \right) H \phi^m \left(\mathbf{r} - \mathbf{R}_j \right) \mathrm{d}^3 \mathbf{r}. \tag{2.5}$$

For ϕ^n and ϕ^m residing on two different sites $(\mathbf{R}_i - \mathbf{R}_j \neq \mathbf{0})$, the part of the Hamiltonian describing the interaction with the potential of a third site, leads to three center integrals. As Koster and Slater stated, it becomes almost impossibly difficult to carry out all these calculations with full rigor[4].

A first step towards simplification is to set up new atomic orbitals such, that the resulting linear combinations obey the same symmetry properties as the original ones, but are orthogonal across different atomic sites. Therefore the overlap matrix becomes diagonal and the secular equation simplifies. This can be achieved by Löwdin functions [6].

Koster and Slater proposed to account only for the potential contributions originating from the sites of the atomic orbitals ϕ^n and ϕ^m. This approximation allows parametrization of the Hamiltonian matrix - and hence the band-structure energy derived thereof - according to the symmetry properties of the involved orbitals and the separation of the corresponding sites. The free parameters can then be fitted against a number of reference data for certain $\mathbf{k}$. The references can be exact calculations e.g. for high symmetry $\mathbf{k}$ points or even experimental data. The band structure energy can then be extrapolated into regions where exact determination is unfavorable.

The following crucial point should be mentioned: atomic orbitals have been used in the derivation of the parametrization scheme. In implementations of the method, basis functions however were never explicitly determined. In fact, the fitting procedure introduces corrections into the Hamiltonian which can not be described by atomic orbitals. We will illustrate this by a simple example. It is common practice to reduce the dimension of the empirical Hamiltonian to valence states. This actually requires the introduction of a constraint, which forces the resulting valence states to be orthogonal to the excluded core states. In the empirical tb-approach approach however, this constraint is not explicitly accounted for. Fitting the free parameters against reference data, which takes core orthogonalisation into account, indirectly introduces the orthogonalisation into the valence only Hamiltonian.

Andersen and Jepsen 1984 published a first principles tight-binding based construction [7], which was derived from linear muffin tin orbitals [8]. The results emphasize the fact that atomic orbitals are far from ab initio tb-orbitals (see section 2.5 for more details).

A common approximation in empirical tb is the restriction to nearest neighbor interactions. This is problematic in case of orthogonalized atomic basis functions as

---

[4]Although the computer power has multiplied since then, Koster and Slater's statement still holds. This is because - applying no further approximations - the numerical costs to set up and diagonalize the Hamiltonian and overlap matrix scale cubic with the number of involved particles. This limits the number of particles per unit cell that can be calculated in full rigor even on modern supercomputers to a few hundred.

originally proposed by Koster and Slater. The orthogonalization leads to extended basis functions. The Hamiltonian matrix therefore exhibits nonzero contributions, even for well separated particles. These problems can either be circumvented by non-orthogonal tight-binding approaches e.g. applied by Hoffmann [9] or by enforcing the localization of the basis set [10, 11, 12].

A more detailed discussion of these and other (tight-binding specific) topics like extension to atomistic calculations, transferability of parametrization, charge transfer and self consistency is out of the scope of this thesis. A review can be found in [10, 13].

2.3 Density functional theory

2.3.1 Predecessors of DFT

Density functional theory (DFT) is a successful approach for the efficient quantum mechanical description of ground state properties of many-body systems. It is widely used in solid state physics and quantum chemistry. The basic principles rest on considerations taken earlier by Hartree [3], Fock [14], Slater [15], Thomas [16], Fermi [17] et al. DFT was no isolated development but incorporated many ideas from earlier quantum-chemical approaches. Basic knowledge of these approaches facilitates the comprehension of DFT. Appendix A will illustrate these concepts as well as some standard implementations of DFT in more detail.

2.3.2 The Hohenberg-Kohn theorems

The properties of a system are entirely determined by the corresponding many-body wave function $|\Psi\rangle$, which itself is a solution of Schrödinger's equation, and therefore only depends on the number of electrons n and the external potential $V_{ext}(\mathbf{r})$.

In their first theorem, Hohenberg and Kohn (1964) [18] proved, that one can use the electron density $n(\mathbf{r})$ instead of the wave function $|\Psi\rangle$ as basic variable for (non degenerate) ground states. This means that for each electron density (which is determined by an external potential) the external potential is uniquely assigned. The basic idea of Hohenberg and Kohn's proof is rather simple: the assumption of the existence of two different external potentials (differing by more than a constant) which should be assigned to the same ground-state electron density leads to a contradiction while applying the minimum-energy principle for the ground state upon the appropriate Hamiltonians.

The second Hohenberg-Kohn theorem shows that the variational principle holds for density functionals [18]:

for a trial density $\tilde{n}(\mathbf{r})$, such that $\tilde{n}(\mathbf{r}) \geq 0$ and $\int \tilde{n}(\mathbf{r})\,\mathrm{d}\mathbf{r} = n$,

$$E_0 \quad \leq \quad E[\tilde{n}]$$

$$\text{where } E[\tilde{n}] = \underbrace{T[\tilde{n}] + V_{ee}[\tilde{n}]}_{F_{HK}} + V_{ne}[\tilde{n}] = \int \tilde{n}(\mathbf{r}) \, V_{ext}(\mathbf{r}) \, d\mathbf{r} + F_{HK}[\tilde{n}].$$

As already mentioned above the Hohenberg-Kohn theorems imply that (even the trial) electron density can be determined by an external potential (*is V-representable*[5]). There exist physical systems (for example systems with ground state degeneracy > 2) for which this condition can not be fulfilled. This problem can be circumvented by following Levy's constrained-search formulation of the density functional theory [19, 20, 21]. In this formulation a weaker condition, namely the "n-representability" of electron densities is required. In mathematical terms this means:

$$n(\mathbf{r}) \geq 0, \quad \int n(\mathbf{r}) \, d\mathbf{r} = n, \quad and \quad \int \left| \nabla n^{\frac{1}{2}}(\mathbf{r}) \right|^2 d\mathbf{r} < \infty.$$

For canonical and grand-canonical ensembles at finite temperature, the equilibrium state is similar to the ground state at zero temperature. By applying statistical mechanics, the density functional theory can even be expanded to these systems [22].

2.3.3 Exchange and Correlation

The Hohenberg-Kohn theorems legitimize the usage of the electron density to describe the ground-state properties of a system. There are two densities which are of main interest in density functional theory: the one electron ($n(\mathbf{r})$) and the two electron density ($n(\mathbf{r}, \mathbf{r}')$). The one electron density for a multi-electron system can be written as

$$n(\mathbf{r}) \quad = \quad \langle \Psi | \hat{n} | \Psi \rangle = \langle \Psi | \sum_{i=1}^{n} \delta(\mathbf{r}_i - \mathbf{r}) | \Psi \rangle \tag{2.6}$$

and corresponds to the probability to find one of the n electrons at the position $\mathbf{r}$, whereas the two electron density is associated with the probability to find one electron at position $\mathbf{r}$ and, at the same time, a second one at $\mathbf{r}'$. In classical electrodynamics this would just be

$$n_{class}(\mathbf{r}, \mathbf{r}') \quad = \quad n(\mathbf{r}) n(\mathbf{r}')$$

because the second electron is independent from first one. In quantum mechanics, the determination of one electron's position affects the possible residence of the other

---

[5]An electron density $n(\mathbf{r})$ is referred to as V-representable if it is the density associated with the antisymmetric ground-state wave function of a Hamiltonian of the form (2.2) with some external potential $V(\mathbf{r})$.

electrons. Taking this into account, the two electron density has to be written as[6]:

$$n(\mathbf{r}, \mathbf{r}') \quad = \quad \langle \Psi | \frac{1}{2} \sum_{i \neq j} \delta(\mathbf{r}_i - \mathbf{r}) \delta(\mathbf{r}_j - \mathbf{r}') | \Psi \rangle. \tag{2.7}$$

An electron at $\mathbf{r}$ feels the density of the remaining $n - 1$ electrons which is given as[7]:

$$\bar{n}(\mathbf{r}, \mathbf{r}') \quad := \quad \frac{2n(\mathbf{r}, \mathbf{r}')}{n(\mathbf{r})} \tag{2.8}$$

The difference between the one electron density $n(\mathbf{r}')$ and the two electron density $\bar{n}(\mathbf{r}, \mathbf{r}')$, which accounts for the exchange interaction is called "exchange hole":

$$\bar{n}(\mathbf{r}, \mathbf{r}') - n(\mathbf{r}') \quad = \quad h(\mathbf{r}, \mathbf{r}'). \tag{2.9}$$

Combining (2.8) and (2.9) the two electron density can be written in terms of one electron densities

$$n(\mathbf{r}, \mathbf{r}') \quad = \quad \frac{1}{2} \left[n(\mathbf{r})n(\mathbf{r}') + n(\mathbf{r})h(\mathbf{r}, \mathbf{r}') \right]$$

and the electron-electron interaction energy splits in:

$$\langle \Psi | \hat{V}_{ee} | \Psi \rangle \quad = \quad \iint \frac{n(\mathbf{r}, \mathbf{r}')}{|\mathbf{r} - \mathbf{r}'|} \, \mathrm{d}\mathbf{r} \, \mathrm{d}\mathbf{r}' \tag{2.10}$$

$$= \quad \underbrace{\frac{1}{2} \iint \frac{n(\mathbf{r})n(\mathbf{r}')}{|\mathbf{r} - \mathbf{r}'|} \, \mathrm{d}\mathbf{r} \, \mathrm{d}\mathbf{r}'}_{V_H} + V_{xc} \tag{2.11}$$

with

$$V_{xc} \quad = \quad \frac{1}{2} \int n(\mathbf{r}) \int \frac{h(\mathbf{r}, \mathbf{r}')}{|\mathbf{r} - \mathbf{r}'|} \, \mathrm{d}\mathbf{r}' \, \mathrm{d}\mathbf{r}$$

and V_H being equal to the (classical) electrostatic energy of the electrons. V_{xc} corresponds to the Coulomb interaction of the electrons with their exchange-hole.

2.3.4 The Kohn-Sham Method

Using the results from section (2.3.3) the total energy can be written as follows:

$$E \quad = \quad \langle \Psi | \hat{T}_e | \Psi \rangle + \int n(\mathbf{r}) V_{ext}(\mathbf{r}) \, \mathrm{d}\mathbf{r} + \frac{1}{2} \iint \frac{n(\mathbf{r})n(\mathbf{r}')}{|\mathbf{r} - \mathbf{r}'|} \, \mathrm{d}\mathbf{r} \, \mathrm{d}\mathbf{r}' + V_{xc} \tag{2.12}$$

---

[6]Note that we define the two particle density including the factor $\frac{1}{2}$, which is then not explicitly present in (2.10).

[7]Note that $\bar{n}(\mathbf{r}, \mathbf{r}') \xrightarrow{\mathbf{r} \to \mathbf{r}'} 0$.

where the kinetic energy term for the electrons still contains the many-body wave function.

The kinetic energy of non-interacting electrons can be obtained by minimization of the kinetic energy with respect to the many-body wave function $|\Psi\rangle$ for a constant electron density $n(\mathbf{r})$:

$$T_s[n] := \min_{\substack{\Psi \\ n[\Psi] \overset{!}{=} n}} \langle\Psi|\hat{T}_e|\Psi\rangle. \tag{2.13}$$

It can be shown that the many-body wave function $|\Psi\rangle$ for the ground state of non-interacting electrons can be written as Slater determinant of one-electron wave functions $|\psi_i\rangle$. These were usually referred to as *Kohn-Sham orbitals*.

One can then separate the kinetic energy of non interacting electrons in the following way:

$$E = T_s + \left[\int n(\mathbf{r})V_{ext}(\mathbf{r})\,\mathrm{d}\mathbf{r} + \frac{1}{2}\iint \frac{n(\mathbf{r})n(\mathbf{r}')}{|\mathbf{r}-\mathbf{r}'|}\,\mathrm{d}\mathbf{r}\,\mathrm{d}\mathbf{r}' + E_{xc} \right]$$

with

$$E_{xc} = \langle\Psi|\hat{T}_e|\Psi\rangle - T_s + V_{xc}$$

called the *energy of exchange and correlation*. It usually cannot be determined explicitly, but it is expressed as functional of the density. See section 2.3.5 for details.

Choosing an arbitrary effective potential V_{eff} the n one-electron Schrödinger equations look like:

$$\left[\hat{T}_e + V_{eff} \right] |\psi_i\rangle = \varepsilon_i|\psi_i\rangle \tag{2.14}$$

and the energy for the non interacting system is

$$E^{non} := \sum_i \langle\psi_i|\hat{T}_e + V_{eff}|\psi_i\rangle. \tag{2.15}$$

Minimization of (2.15) grants access to the ground state one electron wave functions

$\psi_{0,i}$, the ground state energy and the electron density [8]:

$$
\begin{aligned}
E_0^{non} &= \min_{\psi_i} \sum_i \langle \psi_i | \hat{T}_e + V_{eff} | \psi_i \rangle = T_s + \sum_i \langle \psi_{0,i} | V_{eff} | \psi_{0,i} \rangle \\
n_0(\mathbf{r}) &= \sum_i \sum_s \psi_{0,i}^*(\mathbf{r}, s) \psi_{0,i}(\mathbf{r}, s).
\end{aligned}
\tag{2.16}
$$

Variation of the effective potential is equivalent to a variation of the density $n(\mathbf{r})$. The functional derivative of E_0^{non} is:

$$
\begin{aligned}
\left. \frac{\delta E^{non}}{\delta n} \right|_{n_0} &= \left. \frac{\delta T_s}{\delta n} \right|_{n_0} + V_{eff} = 0 \\
\Rightarrow \left. \frac{\delta T_s}{\delta n} \right|_{n_0} &= -V_{eff}
\end{aligned}
$$

The total energy of an interacting system can be written as functional of the density:

$$
\begin{aligned}
E[n] &= T_s[n] + \left[\int n(\mathbf{r}) V_{ext}(\mathbf{r}) \, \mathrm{d}\mathbf{r} + \frac{1}{2} \iint \frac{n(\mathbf{r})n(\mathbf{r}')}{|\mathbf{r} - \mathbf{r}'|} \, \mathrm{d}\mathbf{r} \, \mathrm{d}\mathbf{r}' + E_{xc}[n] \right] \\
&= T_s[n] + E_{pot}[n]
\end{aligned}
\tag{2.17}
$$

with

$$
E_{pot}[n] = \left[\int n(\mathbf{r}) V_{ext}(\mathbf{r}) \, \mathrm{d}\mathbf{r} + \frac{1}{2} \iint \frac{n(\mathbf{r})n(\mathbf{r}')}{|\mathbf{r} - \mathbf{r}'|} \, \mathrm{d}\mathbf{r} \, \mathrm{d}\mathbf{r}' + E_{xc}[n] \right].
\tag{2.18}
$$

Substituting $\frac{\delta T_s}{\delta n}$ in the functional derivative of the total energy with respect to the density $n(\mathbf{r})$ leads to:

$$
\frac{\delta E}{\delta n} = -V_{eff} + \underbrace{\left[V_{ext}(\mathbf{r}) + \int \frac{n(\mathbf{r}')}{|\mathbf{r} - \mathbf{r}'|} \, \mathrm{d}\mathbf{r}' + \frac{\delta E_{xc}[n]}{\delta n} \right]}_{\frac{\delta E_{pot}}{\delta n}}.
\tag{2.19}
$$

The derivative vanishes if $n(\mathbf{r})$ equals the ground state density $n_0(\mathbf{r})$. The ground state effective potential is then defined as

$$
V_{0,eff} = V_{ext}(\mathbf{r}) + \int \frac{n_0(\mathbf{r}')}{|\mathbf{r} - \mathbf{r}'|} \, \mathrm{d}\mathbf{r}' + \left. \frac{\delta E_{xc}[n(\mathbf{r})]}{\delta n(\mathbf{r})} \right|_{n_0}
\tag{2.20}
$$

---

[8]Note that the ground state of the many particle non interacting Hamiltonian is a Slater-determinant. Therefore, we can switch to a single particle picture (we have to choose the potential which produces the correct density) in order to determine the single particle wave functions which build up the Slater determinant. It can be shown that for one particle operators $\langle \Psi | Op | \Psi \rangle$ folds down to $\sum_i f_i \langle \varphi_i | Op | \varphi_i \rangle$. Therefore we can directly determine T_s from the one particle wave functions φ_i.

and (2.14) becomes:

$$\left[-\frac{1}{2}\nabla_{\mathbf{r}}^2 + V_{ext}(\mathbf{r}) + \int \frac{n_0(\mathbf{r}')}{|\mathbf{r}-\mathbf{r}'|}\,\mathrm{d}\mathbf{r}' + \frac{\delta E_{xc}[n(\mathbf{r})]}{\delta n}\bigg|_{n_0} \right]\psi_i \;=\; \varepsilon_i\psi_i. \quad (2.21)$$

Equations (2.20) and (2.21) are the Kohn-Sham equations [23]. An iterative solution cycles the following steps:

1. Choose an arbitrary effective potential.

2. Solve the Schrödinger equation (2.14) to obtain the one electron wave functions ψ_i.

3. Use them to calculate the electron density of the non interacting system ($n(\mathbf{r})$) according to (2.16).

4. Use it to calculate the derivative of the total energy of the interacting system with respect to the electron density ($\frac{\delta E}{\delta n(\mathbf{r})}$) in (2.19)

5. Build a new effective potential[9] $V_{new,eff} = V_{eff} + \alpha\frac{\delta E}{\delta n(\mathbf{r})}$.

6. Do the next step of the iteration with the new effective potential starting at 2.

The calculation of the corrected effective potential as shown above is just one possibility. Other correction terms can be used in addition. See section 2.4 for a comparison of the Kohn-Sham and the Harris-Foulkes method.

2.3.5 Approximation of the Exchange and Correlation Energy

To be able to determine the derivative of the total energy of the interacting system with respect to the electron density, one needs an explicit form for the exchange and correlation energy $E_{xc}[n(\mathbf{r})]$. I will introduce three of the simplest (nevertheless successful) approximations in the following.

- The local density approximation (LDA) uses the uniform-electron-gas approach

$$E_{xc}^{LDA}[n] \;=\; \int n(\mathbf{r})\varepsilon_{xc}(n)\,\mathrm{d}\mathbf{r}$$

  where $\varepsilon_{xc}(\mathbf{r})$ stands for the exchange and correlation energy per particle of a uniform electron gas of density n. The different spin densities $n_\uparrow$ and $n_\downarrow$ are usually treated as if they had the same weight: $n = n_\uparrow + n_\downarrow$. Unlike LDA, the

---

[9]α is called "mixing parameter" and determines the weight of the correction term in the new effective potential. This corresponds to $V_{new,eff} = V_{eff} + \alpha(V^{out} - V_{eff}^{in})$

local spin density approximation (LSDA) composes the energy functional of two functionals, one for each spin density:

$$E_{xc}^{LSDA}[n_\uparrow, n_\downarrow] \quad = \quad \int n_\uparrow(\mathbf{r}) \varepsilon_{xc}(n_\uparrow, n_\downarrow) \, \mathrm{d}\mathbf{r} + \int n_\downarrow(\mathbf{r}) \varepsilon_{xc}(n_\uparrow, n_\downarrow) \, \mathrm{d}\mathbf{r}$$

- An improvement of the LDA approximation is the generalized gradient approximation (GGA). It additionally includes information about the gradient of the density:

$$E_{xc}^{GGA}[n] \quad = \quad \int n(\mathbf{r}) \varepsilon[n, \nabla n] \, \mathrm{d}\mathbf{r}.$$

- The X_α method approximates the Hartree-Fock exchange potential by a local potential of the form:

$$E_{xc}(\mathbf{r}) \quad = \quad -\frac{3}{2} \alpha \left[\frac{3}{\pi} n(\mathbf{r}) \right]^{\frac{4}{3}}.$$

The parameter α can be extracted from Hartree-Fock calculations.

2.4 Non self-consistent DFT

2.4.1 Historical background

The Hohenberg-Kohn and Kohn-Sham theorems (discussed in section 2.3) allow to access the many-particle total energy as functional of the density. This functional (2.17) has some remarkable inherent properties: it is stationary and variational at the ground state density $n^0(\mathbf{r})$. From the latter follows, that an approximate energy obtained from an approximate ground state density $\bar{n}$ lies above the exact ground state energy ($E[\bar{n}(\mathbf{r})] \geq E[n^0(\mathbf{r})]$). The stationary principle implies, that the relative quality of approximate energies is better than the approximate densities - as long as the deviation from the ground state density ($\delta n = \bar{n} - n^0$) is small. Given an appropriate density $\bar{n}$, the ground state total energy, in principle, can be estimated with satisfactory accuracy without the need for self-consistency. The Kohn Sham equations however do not provide direct access to the total energy of a given density.

Three different groups of authors independently took advantage of the stationary principle to suggest density functionals, which allow a non self-consistent evaluation of the total energy. The first have been Wendel and Martin [24]. They applied the technique on phonon mode calculations in silicon. Harris [25] examined the coupling energy of small molecules, built from weakly interacting fragments. He proposed to estimate the molecular ground state density as superposition of the fragment densities. Foulkes et. al. [26, 27] utilized the stationary principle in order to make connection

between DFT and empirical tight-binding. This provided the tight-binding approach a second fundamental basis[10].

Non self-consistent density functionals derived from equation (2.17) using the stationary principle are usually referred to as *Harris-Foulkes functional* approaches. They have widely been used in the context of semi-empirical tight-binding, as well as in ab initio methods (see the sections 2.4.4 and 2.5 for more details).

2.4.2 Alternative derivation of the Harris-Foulkes functional

The formulation of an appropriate non self-consistent density functional is an essential part of our new method discussed in the main part of this work. The underlying principles (partly) rest on considerations taken earlier in the context of Harris-Foulkes functional approaches. Some basic expressions will therefore already be introduced in this section. The derivation presented here will not follow the original formulation of Harris and Foulkes. The resulting functional (2.40) is usually derived in a more compact way. Our approach however allows a consistent treatment of error contributions to the total energy. The discussion of the frozen core approximation, error cancellations and numerical errors in the main part of this work are mainly based on the equations derived in the following.

Basic definitions

The total energy of noninteracting electrons, given a many-particle wave function Ψ and a potential $\bar{v}$ can be determined as follows[11]:

$$
\begin{aligned}
E^{non}[|\Psi\rangle, \bar{v}] &= \langle \Psi | \hat{T} + \bar{v} | \Psi \rangle \\
&= \iint \Psi^*(\mathbf{r}_1, \ldots, \mathbf{r}_n) \sum_i \left[-\frac{1}{2} \nabla_i^2 + \bar{v}(\mathbf{r}_i) \right] \Psi(\mathbf{r}_1, \ldots, \mathbf{r}_n) d^3 r_1, \ldots, d^3 r_n
\end{aligned}
$$

$$(2.22)$$

The many-particle wave function does not necessarily have to be a solution to the corresponding Schrödinger equation. Following Levys constrained search [19, 20, 21], we could sort all many-particle wave functions according to their particle density $n(\mathbf{r})$ in virtual boxes (see equation 2.6 for further details concerning the one particle density). Note that the particle number $N = \int n(\mathbf{r}) d^3 r$ per box is constant. We

---

[10]The connection between DFT and empirical tight-binding has also been discussed by Sutton et. al. [28], who applied Harris formulation. Another fundamental basis has been laid by O. K. Andersen as discussed in section 2.5.

[11]Here and in the following I partly mix real space integral formulation and Dirac's notation. It is understood, that all expressions operating on bra's and ket's have to be operators. For the sake of readability, I stay as close as possible to the real space notation.

define the minimum total energy per box as follows:

$$E^{'}[n, \bar{v}] \quad := \quad \min_{\substack{|\Psi\rangle \\ \langle\Psi|\hat{n}|\Psi\rangle = n(\mathbf{r})}} \quad \langle\Psi|\hat{T} + \bar{v}|\Psi\rangle \tag{2.23}$$

The potential energy contribution, $\langle\Psi|\bar{v}|\Psi\rangle$, within a certain box is constant (because the density is constant). We can therefore access the kinetic energy as functional of the density[12]:

$$T_s[n] \quad = \quad E^{'}[n, \bar{v}] - \int n(\mathbf{r})\bar{v}(\mathbf{r})d^3r. \tag{2.24}$$

$T_s[n]$ was defined in (2.13).

Sorting all boxes with the same particle number N according the energy $E^{'}[n, \bar{v}]$ defines one special density $n'[\bar{v}]$, which minimizes (2.23) for a given potential $\bar{v}$:

$$n'[\bar{v}] \quad : \quad E^{'}[n'[\bar{v}], \bar{v}] = \min_{\substack{n \\ \int n(\mathbf{r})d^3r = N}} \quad E^{'}[n, \bar{v}] \tag{2.25}$$

$E^{'}[n'[\bar{v}], \bar{v}]$ corresponds to the ground state total energy of a noninteracting system in a given potential $(\bar{v})$. It can easily be determined from one particle Schrödinger equations as follows:

$$\left(\hat{T} + \bar{v}\right)|\varphi_i\rangle \quad = \quad \varepsilon_i|\varphi_i\rangle \tag{2.26}$$

$$E^{'}[n'[\bar{v}], \bar{v}] \quad = \quad \sum_i f_i\varepsilon_i \tag{2.27}$$

$$n'(\mathbf{r}) \quad = \quad \sum_i f_i\varphi_i^*(\mathbf{r})\varphi_i(\mathbf{r}) \tag{2.28}$$

Due to the stationary principle, an approximation of $E^{'}[n, \bar{v}]$ by $E^{'}[n'[\bar{v}], \bar{v}]$ intro-

---

[12]Note that the many-particle wave function is not required to be a solution of the corresponding Schrödinger equation for the potential $\bar{v}$. The kinetic energy therefore is independent from the shape of the potential.

duces only errors to second order in $(n - n')$:

$$E'[n, \bar{v}] \quad = \quad E'[n'[\bar{v}], \bar{v}] + \underbrace{O\left((n - n')^2\right)}_{O_a} \tag{2.29}$$

with

$$\begin{aligned} O_a \quad &= \quad \frac{1}{2} \iint \left.\frac{\delta^2 E'}{\delta n(\mathbf{r})\delta n(\mathbf{r}')}\right|_{n'} (n(\mathbf{r}) - n'(\mathbf{r}))(n(\mathbf{r}') - n'(\mathbf{r}'))d^3r d^3r' \\ &\quad + O\left((n - n')^3\right) \end{aligned} \tag{2.30}$$

Introducing a trial density

The total energy of an interacting system for a given density (2.17) can then be written as:

$$\begin{aligned} E[n] \quad &= \quad T_s[n] + E_{pot}[n] \\ &\overset{(2.24)}{=} \quad E'[n, \bar{v}] - \int n(\mathbf{r})\bar{v}(\mathbf{r})d^3r + E_{pot}[n] \\ &\overset{(2.29)}{=} \quad E'[n'[\bar{v}], \bar{v}] - \int n(\mathbf{r})\bar{v}(\mathbf{r})d^3r + E_{pot}[n] + O\left((n - n')^2\right) \quad (2.31) \\ &\approx \quad E'[n'[\bar{v}], \bar{v}] - \int n(\mathbf{r})\bar{v}(\mathbf{r})d^3r + E_{pot}[n] \tag{2.32} \end{aligned}$$

The potential $\bar{v}$ thereby, in principle, is arbitrary. The density n' and hence the quality of the approximation in the last line is however affected by the choice of $\bar{v}$. For the sake of readability, we write the potential in a local form.

Equation (2.31) allows to access the total energy of an interacting system as functional of the density in a numerical convenient way. In real life applications, one would typically want to determine the ground state total energy $E[n_0]$. The ground state density n_0 is usually not known, but can be estimated by a trial density. In a first step, we expand $E_{pot}[n]$ up to linear order around a trial density $\bar{n}$:

$$E_{pot}[n] \quad = \quad E_{pot}[\bar{n}] + \int v([\bar{n}], \mathbf{r})\left(n(\mathbf{r}) - \bar{n}(\mathbf{r})\right)d^3r + \underbrace{O\left((n - \bar{n})^2\right)}_{O_b} \tag{2.33}$$

with

$$v([\bar{n}], \mathbf{r}) \quad := \quad \left.\frac{\delta E_{pot}}{\delta n}\right|_{\bar{n}} \tag{2.34}$$

and

$$\begin{aligned} O_b \quad &= \quad \frac{1}{2} \iint \left.\frac{\delta^2 E_{pot}}{\delta n(\mathbf{r})\delta n(\mathbf{r}')}\right|_{\bar{n}} (n(\mathbf{r}) - \bar{n}(\mathbf{r}))(n(\mathbf{r}') - \bar{n}(\mathbf{r}'))d^3r d^3r' \\ &\quad + O\left((n - \bar{n})^3\right) \end{aligned} \tag{2.35}$$

The total energy (2.31) can then be written as (we write here several identities, for use in later discussions):

$$
\begin{aligned}
E[n] \;=\;& E^{'}[n'[\bar{v}],\bar{v}] - \int n(\mathbf{r})\bar{v}(\mathbf{r})d^3r + E_{pot}[\bar{n}] + \int v([\bar{n}],\mathbf{r})\left(n(\mathbf{r})-\bar{n}(\mathbf{r})\right)d^3r \\
& +O\left((n-n^{'})^2\right) + O\left((n-\bar{n})^2\right) \hspace{5cm} (2.36)\\
=\;& E^{'}[n'[\bar{v}],\bar{v}] - \int \bar{n}(\mathbf{r})\bar{v}(\mathbf{r})d^3r + E_{pot}[\bar{n}] + \int \left(v([\bar{n}],\mathbf{r})-\bar{v}(\mathbf{r})\right)\left(n(\mathbf{r})-\bar{n}(\mathbf{r})\right)d^3r \\
& +O\left((n-n^{'})^2\right) + O\left((n-\bar{n})^2\right) \hspace{5cm} (2.37)\\
=\;& E^{'}[n'[\bar{v}],\bar{v}] - \int \bar{n}(\mathbf{r})v([\bar{n}],\mathbf{r})d^3r + E_{pot}[\bar{n}] + \int n(\mathbf{r})\left(v([\bar{n}],\mathbf{r})-\bar{v}(\mathbf{r})\right)d^3r \\
& +O\left((n-n^{'})^2\right) + O\left((n-\bar{n})^2\right) \hspace{5cm} (2.38)
\end{aligned}
$$

The Harris-Foulkes functional

The freedom in the arbitrary potential $\bar{v}$ allows to get rid of the explicit dependence on the density n. The following restriction:

$$
\bar{v}(\mathbf{r}) \;\overset{!}{=}\; v([\bar{n}],\mathbf{r}) \hspace{5cm} (2.39)
$$

results in the Harris-Foulkes functional:

$$
\begin{aligned}
E[n] \;=\;& E^{'}\left[n'[v([\bar{n}],\mathbf{r})],v[\bar{n}]\right] - \int \bar{n}(\mathbf{r})v([\bar{n}],\mathbf{r})d^3r + E_{pot}[\bar{n}] \\
& +O\left((n-n^{'})^2\right) + O\left((n-\bar{n})^2\right) \hspace{4cm} (2.40)
\end{aligned}
$$

Note that I use a short hand notation $E^{'}[n'[v([\bar{n}]\mathbf{r})],v[\bar{n}]] = E^{'}[n'[v],v[\bar{n}]]$ in the following. The ground state total energy can then be approximated as follows:

$$
\begin{aligned}
E[n_0] \;\approx\;& E^{'}\left[n'[v],v[\bar{n}]\right] - \int \bar{n}(\mathbf{r})v([\bar{n}],\mathbf{r})d^3r + E_{pot}[\bar{n}] \hspace{1cm} (2.41)\\
=\;& \sum_i f_i\varepsilon_i - \frac{1}{2}\iint \frac{\bar{n}(\mathbf{r})\bar{n}(\mathbf{r}')}{|\mathbf{r}-\mathbf{r}'|}d^3rd^3r' + E_{xc}[\bar{n}] \hspace{1cm} (2.42)\\
& -\int \bar{n}(\mathbf{r})\mu_{xc}([\bar{n}],\mathbf{r})d^3r
\end{aligned}
$$

$$
\text{with}
$$

$$
\mu_{xc}([\bar{n}],\mathbf{r}) \;:=\; \left.\frac{\delta E_{xc}}{\delta n}\right|_{\bar{n}} \hspace{5cm} (2.43)
$$

We used (2.18), (2.27) and (2.34) in the last step.

The advantage of equation (2.38) over (2.40) lies in the presence of the arbitrary potential. Although $\bar{v}$ should be close to $v([\bar{n}], \mathbf{r})$ (see the following error discussion) (2.38) allows an explicit deviation and provides a closed expression for the determination of the introduced error[13], namely $\int n(\mathbf{r}) \left(v([\bar{n}], \mathbf{r}) - \bar{v}(\mathbf{r}) \right) d^3r$.

Error discussion

The energy $E'[n'[\bar{v}], \bar{v}]$ corresponds to the ground state of a noninteracting system and therefore is a lower bound for $E'[n, \bar{v}]$. From this and (2.29) follows:

$$O_a \geq 0.$$

The exact total energy $E[n]$ therefore is an upper bound for (2.32). The same holds for the corresponding contributions to the functionals (2.38) and (2.40), respectively. The higher order errors $O\left((n - \bar{n})^2\right)$ may however be either positive or negative. The Harris-Foulkes functional therefore in fact is stationary, in particular at the ground state density n_0, but does not necessarily correspond to a minimum.

2.4.3 Comparison to Kohn-Sham-DFT

Let us point out again, that the total energy as functional of the density (2.17) is stationary at the ground state density. This implies, that the relative quality of approximate energies is better than the approximate densities - as long as the deviation from the ground state density ($\delta n = \bar{n} - n^0$) is small. Given an appropriate density $\bar{n}$, self-consistency therefore is, in principle, dispensable. The Kohn Sham equations however do not provide direct access to the total energy of a given density. This is, because the kinetic energy for a given density $T_s[n]$ can not easily be determined. Without further approximations, a numerical convenient calculation of the $T_s[n]$ can only be achieved in terms of one particle equations. This however requires an appropriate effective potential (see section 2.3 for further details). For a single, non self-consistent step, the Kohn Sham method provides no closed expression for V_{eff}. In order to illustrate this, we rewrite (2.17) analogue to the Harris-Foulkes expressions:

$$
\begin{aligned}
E[\bar{n}] &= T_s[\bar{n}] + E_{pot}[\bar{n}] \\
&= \sum_i f_i \varepsilon_i - \int \bar{n}(\mathbf{r}) \left. \frac{\delta E_{pot}}{\delta n} \right|_{n^{in}} d^3r + E_{pot}[\bar{n}]
\end{aligned}
\tag{2.44}
$$

The one particle energies need to be determined in the potential $\left. \frac{\delta E_{pot}}{\delta n} \right|_{n^{in}}$. n^{in} thereby is to be choosen such, that the ground state one particle wave functions φ_i

---

[13] Note that for an explicit calculation, the density $n(\mathbf{r})$ needs to be known. The aim of usual numerical implementations of the Harris-Foulkes functional however is to determine the ground state total energy $E[n_0]$ without exactly knowing the ground state density n_0 (see eq. (2.41)).

add up to the density $\bar{n}$. The corresponding Harris-Foulkes functional:

$$E[\bar{n}] \quad \approx \quad \sum_i f_i \varepsilon_i - \int \bar{n}(\mathbf{r}) \left. \frac{\delta E_{pot}}{\delta n} \right|_{\bar{n}} d^3 r + E_{pot}[\bar{n}]$$

allows to determine the one particle energies in a potential which is a functional of the trial density. From a physical point of view, it is much easier to estimate a good trial density $\bar{n}$ than a density n^{in} - or an appropriate potential - which leads to the trial density $\bar{n}$.

Even if we could estimate an appropriate effective potential for a one step Kohn-Sham calculation, the Harris-Foulkes method is numerically advantageous. This is, because the eigenvectors of (2.26) never have to be determined. For self consistent cycles, however, the advantages of the method are lost.

2.4.4 Generating input densities

As discussed in the previous sections, the quality of the predicted ground state total energy of the Harris Foulkes functional significantly depends on the quality of the input density. The most obvious approach is to use superimposed free-atom charge densities, as proposed by Harris [25]. Good agreement with full self consistent calculations can e.g. be achieved for weakly interacting fragments, several metallic crystals, silicone bulk properties and even the ionic NaCl compound [29]. The results however are not satisfactory in general. Read and Needs [30] as well as Finnis [31] e.g. addressed the problem of defect structures such as surfaces and vacancies. They found the predicted Harris energies not to be sufficiently accurate. Finnis was the first to suggest a renormalized atomic density in the context of Harris Foulkes functional calculations[14]. He fitted the atomic charge density by three Gaussians such, that the density significantly drops beyond a certain radius. This spherically contracts the input densities and dramatically improved the results for the aluminum surface systems studied. Chetty et. al. [32] carried out an analysis of self-consistent densities for various bulk and surface structures in reciprocal space. They found that contributions due to surface and bulk character decouple in reciprocal space. The surface character shows up in the long wavelength region, whereas the bulk properties can be described by short wavelengths. This allows to combine both contributions to transferable densities. The spherically averaged real space representation thereof corresponds to Finnis contracted densities. These densities are furthermore similar to those obtained by embedding the atom in a homogeneous electron gas. Hartford et. al. [33] followed the latter approach. The differences in surroundings each fragment experiences may - to a certain extent - be mapped onto a varying embedding homogeneous electron gas density. Adapted input densities for a certain configuration

---

[14]In fact, Finnis was inspired by the renormalisation approach of Weinert and Watson. They constrained the atomic charge density within a spherical symmetric potential in order to correct surface dipole contributions to work functions.

can then be obtained from jellium calculations using estimated embedding densities characterizing the surrounding in this configuration.

Besides so called *one shot* calculations, the Harris Foulkes functional can be solved self consistently (see section 2.4.3 for further details). The simplest step beyond the frozen atomic fragment approaches discussed above has been suggested by Averill and Painter [34]. They use the frozen atomic fragments as basis and decompose the output density such, that the norm is conserved. The atomic fragments thereby may be spherically compressed, which corresponds to a self-consistent basis set optimization. This approach, as well as the approaches discussed above, however, approximate the trial density as superpositions of spherically densities. Due to this approximation, self consistency does - in general - not result in the exact many particle ground state. Nevertheless, the spherical approximation has been successfully applied to small molecules [34]. We will discuss this in more detail in the context of H_2 (chapter 6).

All flavors of approximations and numerical techniques developed in the context of density functional theory can, in principle also be applied to the Harris Foulkes functional. The implementation in an existing DFT code therefore is straightforward and has been accomplished by a countless number of groups. The efficient generation of appropriate input densities, however, is in a class of its own.

2.5 Ab initio tight-binding

The complexity of seemingly simple quantum mechanical many body problems and the limited access to computer power have been the driving force for the development of empirical tight-binding methods. Although applied successfully in many fields, empirical tight-binding generally suffers from typical limitations of empirical techniques. Correct description of a class of problems fitted against is understood. But the transferability of a parameterization to a new class of problems is at least questionable. This is a strong argument for ab initio approaches. Starting form first principles, almost any level of simplification can be achieved by a well defined series of approximations. This allows to judge the applicability of certain techniques and the quality of obtained results more precisely.

In the context of ab initio tight-binding there exist three main roots: localized muffin tin orbitals tracing back to O. K. Andersen, atomic like orbitals related to Sankey and Niklewski's scheme and Car-Parrinello dynamic localized orbitals schemes introduced by Galli and Parrinello.

Localized muffin tin orbitals

Andersen and Jepsen 1984 published a first principles tight-binding based construction [7], derived from linear muffin tin orbitals [8]. The basic approach to muffin tin orbitals is to separate the crystal potential in spherical regions around the nuclei and flat interstitial regions outside the spheres. Inside the spheres, a basic finding is applied: the difference between the atomic and the crystal solution can - to linear

order - be mapped onto a contribution of the energy derivative of the atomic solution. Due to the assumption of a flat potential, the solutions in the interstitial region correspond to spherical waves originating from the atomic sites. The total solution is then constructed by matching the linear combination of the atomic solution and its energy derivative (angular momentum dependent) to spherical waves at the sphere boundary. The original interstitial muffin tin orbitals die out proportional to $r^{-(l+1)}$, with r being the distance from the corresponding atomic site. They are therefore not sufficiently localized for tight-binding calculations.

In 1984, Andersen et. al. [7] introduced a localization transformation of the LMTO's. The basic idea corresponds to screening of charges: a certain spherical wave is superimposed by several waves[15] originating from nearest neighbor sites such that the result dies out exponentially beyond second nearest neighbor distances. A review can be found in [35].

A more recent development are the so called *third generation muffin tin orbitals*. In this approach, an even stronger shielding is achieved by forcing parts of the linear combinations of interstitial waves exactly to zero within neighboring spheres. See [36] for a detailed discussion.

Sankey-Niklewski and related schemes

Sankey and Niklewski [12] derived a tabulation scheme in the spirit of Koster and Slater. There are, however, three main differences to corresponding empirical tight-binding methods. First of all, the approach is based on the first principles Harris Foulkes functional, which, in case of self-consistency, provides access to the exact many-particle ground state energy. Secondly, three center integrals were not neglected but explicitly included. Last but not least, a localized atomic orbital basis is used. It is obtained by enclosing the isolated atom in a spherical hard box[16] . Interpolation tables for two and three center integrals are then calculated. Some contributions, such as the energy of exchange and correlation, explicitly depend on the electronic density, which can not be known beforehand. In order to speed up the method, Sankey and Niklewski therefore introduced an approximative method, which allows to estimate these contributions in terms of overlap and density matrix elements in a numerically efficient way.

The Sankey-Niklewski method has been extended to allow for double numeric basis sets and iterative charge transfer. This extension is usually related to as *FIREBALL* [37].

Confined atomic orbital basis sets are meanwhile applied by several groups[17]. The localization potential thereby varies from the original hard sphere over exponential,

---

[15]corresponding to interstitial solutions

[16]$\varphi = 0|_{r>r_c}$

[17]I classify the following methods as Sankey-Niklewski related in the sense, that they start from first principles, take three center contributions into account, use localized atomic orbitals as basis and make use of certain approximations to speed up numerics.

and r^6 to harmonic shape [38, 39, 40]. Delley on the other hand supplements free atomic orbitals by orbitals of positively charged ions [41]. The actual choice depends on the desired localization and the tolerance for kinks in the potential and its derivatives.

Most of the state of the art simulation packages in this field make use of flexible implementations. The user can choose from different confinement potentials as well as from several levels of approximations. The latter usually is achieved by applying Harris Foulkes functional approaches. They can be used in *single shot* mode or self-consistently. The basis can thereby be fixed or even be adapted iteratively [42, 43, 40].

The full potential localized orbital method (FPLO) [44] is exceptional in the sense that it uses locally finite lattice sums for the treatment of the multi-center integrals. It is based on a multi-cycle scheme with a flexible, localized orbital base. The basis is obtained as follows. The crystal potential is spherically averaged around each atomic site and, in case of valence states, supplemented by a confinement potential defined as $v^{conf} = \left(\frac{r}{r_0}\right)^4$ with $r_0 = \left(\frac{x_0 r_{NN}}{2}\right)^{\frac{3}{2}}$. r_{NN} corresponds to the nearest neighbor distance. x_0 is a dimensionless scaling parameter. It allows to minimize the total energy with respect to the strength of localization of the basis functions in each iterative cycle. The numerical implementation is done in 3D real space in terms of finite lattice sums. This approach allows to incorporate the coherent potential approximation for the efficient handling of substitutionally disordered solid systems. For a review see [45].

Car-Parrinello dynamic localized orbital scheme

Car and Parrinello 1985 introduced a fictitious Lagrangian formulation including the electrons [46]. It allows to propagate the wave functions according to quasi classical equations of motion. This enables molecular dynamic simulations at finite temperature (simulated annealing) and, by application of friction, lets the system iteratively converge to (local) minima[18]. Instead of direct diagonalisation of the Hamilton matrix in each step, the ground state hence is approached in small corrections to the preceding time step. The procedure however not necessarily leads to localized one particle states. Galli and Parrinello therefore introduced an additional localization potential per atom in the Hamiltonian. A consistent extension of the fictitious dynamics then allows to converge the system in localized states such, that the result corresponds to a unitary transformation of the result obtained from the original system [47]. Nevertheless, an exact unitary transformation between localized orbitals and exact ground state density is not possible in general. The localization potential then leads to a variational approximation of the ground state energy. The above approach is well justified for periodic insulators, for which exponentially localized Wannier functions can be constructed. The Wannier functions will be discussed in the following section.

---

[18]We extended the nucleonic part of the fictitious Lagrangian formulation to allow for so called *dimer* calculations for finding transition states within Car-Parrinello dynamics. See section 12 for details.

For details on implementations see [48, 49, 50].

Self-consistent atomic deformation (SCAD) method

Recently, a self-consistent method for the deformation of atomic orbitals has been published by Boyer et. al. [51]. This approach, just as the Car-Parrinello dynamic localized orbital scheme, applies an additional localization potential on the electrons. These localization potentials are derived from the overlap contribution to the kinetic energy and therefore depend on the self-consistent density of the system. This however introduces the need for self-consistent iterations. In addition, this approach brakes the natural error cancellation of DFT. A detailed discussion of the differences to our approach is most simply done in the terms introduced in the main part of this thesis. I therefore decided to shift the discussion to section 7.6.

A word about the chemists *absolutely localized molecular orbitals*

In the context of energy decomposition analysis (EDA) [52, 53], the notation *absolutely localized molecular orbitals* appears. In this approach, large systems of (e.g. molecular clusters) are logically divided into non overlapping subsets. Each subset represents a part, which interacts weakly with the rest of the system. The boundaries between subsets must not cross covalent bonds in molecules. In a second step, occupied molecular orbitals on a fragment are expanded in terms of atomic orbitals of the same fragment. These constraints produce molecular orbitals that are localized on fragments in the same sense as atomic orbitals are localized on atoms. The authors therefore call these molecular orbitals *absolutely localized.*

This denomination however is exaggerated. Atomic orbitals, in which the molecular orbitals of the fragments are expanded, usually are quite long-ranged. Therefore, the separation between two subsets of the system which can be divided into individual fragments following this approach needs to be large. This obviously is totally different from the fragment localization presented in this work. We introduce a method which allows to localize quasi-atomic orbitals such, that molecules and crystals can be divided in strongly interacting fragments. Our fragment boundaries therefore explicitly cross covalent bonds.

2.6 Wannier functions

The electronic groundstate of periodic potentials can be described by Bloch states (2.4). These states are extended across the crystal and therefore are contradictory to the chemical picture of bonding. Electron transport, bulk polarisation and many body correlations are, for example, more naturally discussed in terms of local orbitals.

Bloch states - as every solution to Schrödingers equation - carry an arbitrary phase. Gregory Wannier in 1937 used this fact to introduce a unitray transformation of Bloch states into local orbitals (nowadays refered to as *Wannier functions*) [54]. Due to a

remaining arbitrariness in the phase, the Wannier representaion however is not unique. In order to obtain *maximally localized* Wannier functions, an additional localisation condition needs to be applied. Mazari and Vanderbilt 1997 introduced an algorithm to iteratively determine a set of unitary transformations of Bloch states while minimizing the spread of the resulting Wannier functions in real space [55]. The result is refered to as *maximally localized generalized* Wannier functions.

The notation *maximally localized* is however misleading in two ways: at first, the localisation is maximal only with respect to the localization criterion used. In fact, there exist different plausible choices. They were partly discussed in the context of localized molecular orbitals since the 1960's. Among others these are measures for the chemically invariance [56, 57], the Coulomb self-repulsion [58] and the projection on Mulliken populations [59]. The resulting Wannier function e.g. differ in the quality of reproduction of $\sigma-$ and $\pi-$charater of double bonds. The localisation is furthermore affected by the choice of intermixing unoccupied Bloch states. For a detailed discussion and possible implementations see [60] and [61, 62, 63, 64].

A more recent approach is the formulation of quasiatomic minimal basis orbitals (QUAMBO's) [65]. The localisation condition corresponds to maximum overlap with free atomic orbitals.

The achievable localization of Wannier functions, in general, depends on the underlaying physical system. The decay was found to be algebraic for metals and exponential for insulators[66, 67, 68].

The notation *maximally localized* is misleading in a second way. The Wannier functions dicussed above correspond to a unitary transformation of Bloch states. The Bloch states and hence the resulting Wannier functions are orthonormal. It can formally be shown, that the orthonormality condition prevents further localisation [69]. This lead to the developement of *nonorthogonal generalized* Wannier functions [70, 71, 43, 42]. The basic concept is to construct the density matrix from nonorthogonal, so called *support functions*. The support functions are expanded in realspace localized basis functions. This can, for example, be periodic, bandwidth limited delta functions [43], b-splines [70] or polynomials [71]. The localisation is achieved as follows. Contributions to a certain support function is allowed only from those basis functions, which fully reside inside a given sphere around that support function. The total energy is then minimized in a nested loop approach. In a first step, the total energy is minimized with respect to the expansion coefficients of the allowed basis functions (the shape of the support functions is optimized). In a second step, the expansion coefficients of the now fixed support functions are optimized. During optimization, two constraints need to be fulfilled. The total number of electrons has to be constant and the resulting groundstate densitymatrix needs to be idempotent[19].

A recent approach by Qian et. al. corresponds to a reformulation of the QAMBO method. Instead of projecting the Bloch states onto atomic orbitals, the atomic

---

[19]Idempotency of the groundstate density matrix corresponds to the eigenfunctions of the Kohn-Sham Hamiltonian beeing orthonormal.

orbitals are projected into the subspace spanned by the Bloch states. This results in a nonorthogonal but complete basis of quasiatomic orbitals (QO). There however seem to be open issues for cases in which the QO's become approximately linear dependent. For a detailed discussion see [72].

2.7 Frozen core approximation

The chemical picture of bonding suggests that the sensitivity of core electrons to the chemical environment should be small. From this follows, that the core wavefunctions in an altered chemical environment may not have to be recalculated, but could be replaced by the atomic core. In fact, electronic structure methods which neglect the redistribution of core electrons lead to results, which are close to the fully self consistent ones. This approximation, usually refered to as *frozen core approximation* [73], is numerically convenient and therefore widely used.

Full core calculations, however demonstrate, that the core wavefunctions are all but insensitive to the chemical environment. The good agreement between frozen- and fullcore total energies instead arises from the stationarity of the density functional[20]. This has been pointed out by Barth and Gelatt [73]. They have been the first to propose a closed expression for the second order correction in the selfconsistent case.

We derive the frozen core equations from the density functional $E[n]$, discussed in section 2.3. For the groundstate density n_0, the total energy $E[n_0]$ can be written in terms of oneparticle solutions ψ_i^0:

$$
\begin{aligned}
E[n_0] \quad = \quad & \sum_i f_i \langle \psi_{0,i} | \hat{T} | \psi_{0,i} \rangle + E_{pot}[n_0] \\
& - \sum_{j,k} \lambda_{j,k} \left[\langle \psi_{0,j} | \psi_{0,k} \rangle - \delta_{j,k} \right]
\end{aligned}
\tag{2.45}
$$

The one particle solutions need to be obtained from the Kohn-Sham equations (2.21). The density n_0 is related to the one particle solutions according to (2.16). The potential $v[n_0]$ corresponds to the groundstate effective potential defined in (2.20). The last term is the orthonormality constraint due to Fermis exclusion principle, with $\lambda_{j,k}$ and $\delta_{j,k}$ beeing Lagrange multipliers and the Kronecker-Delta, respectively. Note that the constraints are equal to zero in the above situation.

We can then define a functional of one particle wavefunctions[21]:

$$
\begin{aligned}
\tilde{E}[\psi_i] \quad := \quad & \sum_i f_i \langle \psi_i | \hat{T} | \psi_i \rangle + E_{pot}[n] \\
& - \sum_{j,k} \lambda_{j,k} \left[\langle \psi_j | \psi_k \rangle - \delta_{j,k} \right] .
\end{aligned}
\tag{2.46}
$$

---

[20]See section 2.4 for a detailed discussion.
[21]We use the shorthand notation $E[\psi_i] = E[\{\psi_i^*\}, \{\psi_i\}]$

Obviously, $\tilde{E}[\psi_{0,i}] = E[n_0]$. Furthermore, the following relation holds:

$$\left.\frac{\partial \tilde{E}}{\partial \psi_i}\right|_{\psi_{0,i}} = \left.\frac{\partial E}{\partial n}\right|_{n_0} = 0. \qquad (2.47)$$

The functional $\tilde{E}[\psi_i]$ is stationary and variational at $\psi_{0,i}$:

$$
\begin{aligned}
\tilde{E}[\psi_i] &= \tilde{E}[\psi_{0,i}] + \sum_i (\psi_i - \psi_{0,i}) \left.\frac{\partial \tilde{E}}{\partial \psi_i}\right|_{\psi_{0,i}} + O((\psi_i - \psi_{0,i})^2) \\
&= \tilde{E}[\psi_{0,i}] + \underbrace{O((\psi_i - \psi_{0,i})^2)}_{\tilde{O}} \\
\text{with} \\
\tilde{O} &\geq 0.
\end{aligned}
$$

Within the frozen core approximation, the one-particle core wavefunctions are kept fixed while the valence is allowed to adapt to the chemical environment. For a given set of core wavefunctions, minimization of (2.46) with respect to the valence wavefunctions results in an approximation of the total energy with the smallest possible error. The minimum condition translates in a set of coupled differential equations for the valence wavefunctions[22]:

$$\left[-\frac{1}{2}\nabla^2 + v[n]\right]\psi_i - \sum_{k \neq i} \lambda_{i,k}\psi_k = \varepsilon_i \psi_i \qquad (2.48)$$

with $i \in$ valence and k running over all states. This equation can be solved selfconsistenly, by introduction of a basis which, per definition, is orthogonal to the frozen core states.

In many implementations of the frozen core approximation, the orthogonality condition is not fullfilled in a stringent way [73]. The valence wavefunctions are kept orthogonal to the core wavefunctions ψ_i', which correspond to the potential $v[n]$. For spherical potentials, this is numericaly convenient, as the condition can be fulfilled without explicit determination of ψ_i'. Barth and Gelatt [73] found, that the errors of this approximation vanish to first order in the charge density differences.

Connection to Harris-Foulkes

Given a set of selfconsistent frozen core wavefunctions ψ_i^{sfc}, and the corresponding density as superposition of core and valence contributions $\bar{n} = n_c^{fc} + n_v^{fc}$. We could

---

[22]We use $\sum_{j,k} \lambda_{j,k} \left[\langle\psi_j|\psi_k\rangle - \delta_{j,k}\right] = \sum_{j \neq k} \lambda_{j,k} \left[\langle\psi_j|\psi_k\rangle - \delta_{j,k}\right] + \sum_j \varepsilon_j \left[\langle\psi_j|\psi_j\rangle - 1\right]$

use $\bar{n}$ as trial density for the Harris-Foulkes functional discussed in section 2.4:

$$
\begin{aligned}
E^{HFo}[\bar{n}] & = E'[n'[v], v[\bar{n}]] - \int \bar{n}(\mathbf{r}) v([\bar{n}], \mathbf{r}) d^3 r + E_{pot}[\bar{n}] \\
& = \underbrace{\sum_{i\epsilon c} f_i \varepsilon_i + \sum_{j\epsilon v} f_j \varepsilon_j - \int \bar{n}(\mathbf{r}) v([\bar{n}], \mathbf{r}) d^3 r}_{t_{HFo}} + E_{pot}[\bar{n}]
\end{aligned}
$$

The energy in frozen core approximation $\tilde{E}[\psi_i^{sfc}]$ deviates from $E^{HFo}[\bar{n}]$ in the kinetic energy. The Harris-Foulkes oneparticle energies ε_i correspond to the output wavefunctions ψ_i' of the potential $v[\bar{n}]$. Due to the variationality of $E'[n'[v], v[\bar{n}]]$, the following relation holds:

$$
\begin{aligned}
t_{HFo} & = \sum_i \int \psi_i' \left(-\frac{1}{2}\nabla^2 + v([\bar{n}], \mathbf{r}) \right) \psi_i' d^3 r - \int \bar{n}(\mathbf{r}) v([\bar{n}], \mathbf{r}) d^3 r \\
& = \underbrace{\sum_i \int \psi_i^{sfc} \left(-\frac{1}{2}\nabla^2 + v([\bar{n}], \mathbf{r}) \right) \psi_i^{sfc} d^3 r}_{E^{sfc}} + \underbrace{O((\psi_i^{sfc} - \psi_i')^2)}_{O_{sfc}} \\
& \quad - \int \bar{n}(\mathbf{r}) v([\bar{n}], \mathbf{r}) d^3 r \\
& = \underbrace{\sum_i \int \psi_i^{sfc} \left(-\frac{1}{2}\nabla^2 \right) \psi_i^{sfc} d^3 r}_{t_{sfc}} + O((\psi_i^{sfc} - \psi_i')^2) \\
& = t_{sfc} + O((\psi_i^{sfc} - \psi_i')^2) \qquad\qquad (2.49)
\end{aligned}
$$

The output wavefunctions ψ_i' correspond to the ground state of a noninteracting Hamiltonian and minimize $E'[n'[v], v[\bar{n}]]$. For any other wavefunction, the noninteracting total energy lies above the groundstate energy. In the present case: $E^{sfc} \geq E'[n'[v], v[\bar{n}]]$. The introduced error O_{sfc} in line two of (2.49) therefore is smaller than or equal to zero. From all this follows:

$$
\begin{aligned}
E^{HFo}[\bar{n}] & = \tilde{E}[\psi_i^{sfc}] + \underbrace{O((\psi_i^{sfc} - \psi_i')^2)}_{O_{sfc}} \\
& \text{with} \\
O_{sfc} & \leq 0. \qquad\qquad (2.50)
\end{aligned}
$$

The Harris-Foulkes energy of a frozen core density therefore is a lower bound to the frozen core energy[23].

2.8 Madelung energy and Born repulsion

Empirical approaches sometimes divide the potential energy of a system into two parts in order to derive parametrized potentials:

$$E \;\; = \;\; E_{mad} + E_{born}.$$

The Madelung term E_{mad} is the electrostatic interaction between all nuclei and electrons treated as point charges[24]:

$$E_{mad} \;\; = \;\; \frac{1}{2} \sum_{i,j} \frac{Q_i Q_j}{|\mathbf{r}_i - \mathbf{r}_j|}. \tag{2.51}$$

The second term, E_{born}, accounts for the fact that electrons correspond to overlapping electron clouds which obey Fermi's exclusion principle. This leads to a purely repulsive character of exponential form and reflects the exponential decay of the electronic density for large distances. It was originally discussed by Max Born who, for numerical convenience, proposed an approximation according to $E_{born} = B/r^n$ [74]. It should be stressed that the *Born repulsion* includes two contributions: the effects of Fermi's exclusion principle - which usually are denoted as *Pauli repulsion* - and the compensation for the point charge terms, already accounted for in E_{mad}. In section 4.3, we will derive so called *Pauli potentials*, which are mainly based on Pauli repulsion.

---

[23]Note however, that the Harris-Foulkes energy may be below the exact groundstate total energy. The deviation of the Harris-Foulkes energy from the exact groundstate for a frozen core density therefore may be larger than the one of the frozen core functional (2.46).

[24]Note that this is not the Madelung constant. It can however be derived from E_{mad} for binary compounds.

Part II

Novel theory: the SESM approach

3 Outline

3.1 Introduction

The new approach consists of a combination of several, partly new, theoretical concepts. The approach is not only characterized by the sum of concepts used, but significantly depends on the fine-tuning thereof. A certain part might hence not always become immediately clear to the reader not being aware of the complete approach. In this section, we will therefore focus on the full picture without going too much into detail. The theoretical subtleties will be dealt with in section 4.

First of all, we will motivate our fundamental energy functional. The physical meaning of the individual contributions and how they might be accessed will then be discussed in section 3.3.

3.2 Derivation of the fundamental energy functional

3.2.1 Basic ideas

The underlying question usually addressed by electronic structure methods can be boiled down to: 'What happens when we bring isolated atoms together (so that they can form molecules or crystals)?' The approach of splitting the total energy of electronic systems into individual, physically meaningful contributions, nowadays referred to as *energy decomposition analysisis* [52, 75], in principle is as old as quantum mechanics [76].

One can identify some specific transformations: The atomic charge density will be deformed. The Pauli principle disallows two electrons to have the same quantum numbers. This leads to the so called Pauli repulsion which is maximal in the vicinity of the neighboring atoms. We have repulsive (electron - electron) and attractive (electron - nuclei) Coulomb interactions of the charge densities. Bonding and anti-bonding orbitals are formed, electronic charge is transferred and so on. The resulting system can be understood as a mixture of covalent (overlapping charge densities) and ionic (Coulomb interactions of point charges) bonding.

This in mind, we split the transformation from isolated to 'clustered' atoms in two steps:

1. We deform the charge density of the isolated atom such as they will be deformed during embedding in the cluster (this deformed atom will be referred to as *deformed ion* or simply *ion* in the following). *Deformation* thereby refers to

the change in shape and charged state. The deformation effect of embedding will be described by a potential, referred to as v^{emb}. The embedding potential thereby has contributions from the individual neighbors of the embedded atom. Although not exactly representing the Pauli repulsion[1], we will refer to these contributions as *Pauli potentials* v^{pauli}. As a consequence of the potential formulation of the embedding process, the ion does not have the possibility to interact with neighboring densities. Loosely spoken, we force the atom in a shape, which reflects the vicinity when embedded in the cluster without allowing the formation of bonding and anti-bonding states with the neighbors. Due to the increase of the kinetic energy, the total energy of the deformed ion will be above the atomic energy.

2. We then bring the deformed ions together, now allowing the charge densities to interact. The formation of bonds brings the total energy down (usually well below the energy of the isolated atoms).

It is common knowledge, that relative energies determined from DFT calculations usually compare much better than absolute. This is, because, for relative expressions, the linear contribution of systematic errors cancel. The numerical effort for a sufficiently accurate description of a combination of two contributions to the total energy may be much less than for individual handling. Error cancellation therefore plays an important role in our formulation. We will discuss this in more detail in the context of numerical implementation.

The new functional addresses the atomization energy in the following way[2]:

$$\Delta E \;\; = \;\; \underbrace{\sum_i \left(E_i^{ion} - E_i^{at} \right)}_{step\,1} + \underbrace{E^{cry} - \sum_i E_i^{ion}}_{step\,2} \tag{3.1}$$

The index i thereby runs over all n members of the unit cell.

3.2.2 Full core expression

Ionic contributions

Suppose embedding effects could be condensed in a potential v^{emb}. We could then solve the ion self-consistently in a potential $\bar{v}$, which includes the usual potential $v[n]$ for the isolated ion defined in (2.34) and the embedding effects of the neighbors v^{emb}:

$$\bar{v} = v[n] + v^{emb}$$

---

[1] Our *Pauli potentials* represent the predominantly repulsive interaction between the electrons. Besides the Pauli repulsion, this includes e.g. the Coulomb repulsion between electrons.

[2] The energy of the cluster (molecule or crystal) will be written as E^{cry}.

This approach corresponds to an exact Kohn-Sham calculation as well as to a self-consistent solution of the Harris-Foulkes Functional (2.40). The ion state however is a theoretical concept. The explicit contribution of the energy E^{ion} in (3.1) drops out. The effect of embedding is inherent in the altered shape - reflected in the kinetic energy - and total charge of the density. We therefore define the total energy for a specific ion, excluding the explicit contribution of the embedding potential, as follows:

$$
\begin{aligned}
E^{ion}[n] \quad &:= \quad E^{'}[n'[\bar{v}], \bar{v}] - \int n(\mathbf{r})\bar{v}(\mathbf{r})d^3r + E_{pot}[n] \\
&= \quad E^{'}[n'[\bar{v}], \bar{v}] - \int n(\mathbf{r})\bar{v}(\mathbf{r})d^3r + E_{coul}[n] + E_{xc}[n] \quad (3.2)
\end{aligned}
$$

For self-consistency, $n' = n$. Note that the potential $E_{pot}[n]$ defined in (2.18) does not include the embedding potential. The embedding potential contribution of the first and the second term in (3.2) cancel each other. This definition makes sense because we are interested in what could be referred to as the *cost of deformation* and not in the interaction energy with the embedding potential. Consequently, the ionic band structure energy is defined excluding the embedding potential:

$$
\begin{aligned}
\varepsilon_{n,i} \quad &:= \quad \sum_{i,n} f_{i,n}^{ion} \langle \psi_{i,n}^{ion} | -\frac{1}{2}\nabla^2 + \bar{v}[\bar{n}_i(\mathbf{r})] - v^{emb} | \psi_{i,n}^{ion} \rangle \\
&= \quad \tilde{\varepsilon}_{i,n} - \sum_{i,n} f_{i,n}^{ion} \langle \psi_{i,n}^{ion} | v^{emb} | \psi_{i,n}^{ion} \rangle \quad (3.3)
\end{aligned}
$$

In (3.2) and in the following, we split the potential energy $E_{pot}[n]$ in the Coulomb and exchange-correlation contribution:

$$
\begin{aligned}
E_{pot}[n] \quad &= \quad E_{pot}[n] + E_{xc}[n] \\
&\text{with} \\
E_{coul}[n] \quad &= \quad \int n(\mathbf{r})V_{ext}(\mathbf{r})\,d\mathbf{r} + \frac{1}{2}\iint \frac{n(\mathbf{r})n(\mathbf{r}')}{|\mathbf{r} - \mathbf{r}'|}\,d\mathbf{r}\,d\mathbf{r}'
\end{aligned}
$$

The above expressions hold for a single ion and therefore should carry an index i, which we left out for the sake of readability. To be explicit, we will denote the n'th self-consistent one-particle state of ion i and its occupation by $\psi_{i,n}^{ion}$ and $f_{i,n}$, respectively.

In the following section, we will use the superposition of the deformed ionic densities as approximation of the crystals total density $\bar{n}$, which we define as follows:

$$
\begin{aligned}
\bar{n}_i \quad &:= \quad n_i = \sum_i f_{i,n}^{ion} \langle \psi_{i,n}^{ion} | \psi_{i,n}^{ion} \rangle \\
\bar{n} \quad &:= \quad \sum_i \bar{n}_i \quad (3.4)
\end{aligned}
$$

The total ionic contribution is then given by:

$$
\begin{aligned}
\sum_i E_i^{ion} \;=\;& \sum_{i,n} f_{i,n}^{ion} \langle \psi_{i,n}^{ion} | -\frac{1}{2}\nabla^2 + \bar{v}[\bar{n}_i(\mathbf{r})] | \psi_{i,n}^{ion} \rangle \\
&- \sum_{i,n} f_{i,n}^{ion} \langle \psi_{i,n}^{ion} | \bar{v}[\bar{n}_i(\mathbf{r})] | \psi_{i,n}^{ion} \rangle \\
&+ \sum_i E_{coul}[\bar{n}_i] + \sum_i E_{xc}[\bar{n}_i] \\
=\;& \sum_{i,n} f_{i,n}^{ion} \langle \psi_{i,n}^{ion} | -\frac{1}{2}\nabla^2 | \psi_{i,n}^{ion} \rangle \\
&+ \sum_i E_{coul}[\bar{n}_i] + \sum_i E_{xc}[\bar{n}_i] \qquad (3.5)
\end{aligned}
$$

Crystal contribution

For the ground-state total energy of the crystal $E^{cry}[n_0]$, we use the approximate formulation according to (2.40). With the trial-density defined in (3.4):

$$
\begin{aligned}
E^{cry}[n_0] \;=\;& E^{'}[n'[v], v[\bar{n}]] - \int \bar{n}(\mathbf{r}) v([\bar{n}],\mathbf{r}) d^3r + E_{coul}[\bar{n}] + E_{xc}[\bar{n}] \\
&+ O((n_0 - n')^2) + O((n_0 - \sum_i \bar{n}_i)^2) \qquad (3.6) \\
=\;& E^{'}[n'[v], v[\sum_i \bar{n}_i]] - \sum_{i,n} f_{i,n}^{ion} \langle \psi_{i,n}^{ion} | v[\sum_i \bar{n}_i(\mathbf{r})] | \psi_{i,n}^{ion} \rangle \\
&+ E_{coul}[\sum_i \bar{n}_i] + E_{xc}[\sum_i \bar{n}_i] \\
&+ O((n_0 - n')^2) + O((n_0 - \sum_i \bar{n}_i)^2) \qquad (3.7)
\end{aligned}
$$

Assembling the energy expression

Bringing the ionic and crystal energies together, equation (3.1) can be written as follows:

$$
\begin{aligned}
\Delta E \;\;=\;\; & \sum_i \left(E_i^{ion} - E_i^{at} \right) \\
& + E^{'}[n'[v], v[\sum_i \bar{n}_i]] - \sum_{i,n} f_{i,n}^{ion} \langle \psi_{i,n}^{ion} | - \frac{1}{2}\nabla^2 + v[\sum_i \bar{n}_i(\mathbf{r})] | \psi_{i,n}^{ion} \rangle \\
& + E_{coul}[\sum_i \bar{n}_i] - \sum_i E_{coul}[\bar{n}_i] \\
& + E_{xc}[\sum_i \bar{n}_i] - \sum_i E_{xc}[\bar{n}_i] \\
& + O((n_0 - n')^2) + O((n_0 - \sum_i \bar{n}_i)^2)
\end{aligned}
$$

In order to be able to extract some information about the ionic character of the bonds, we define an atomic charge as follows:

$$
\begin{aligned}
Q_i \;\; &:= \;\; \int \bar{n}_i(\mathbf{r}) + Z_i(\mathbf{r}) \mathrm{d}^3 r \\
Z_i(\mathbf{r}) \;\; &:= \;\; -z_i \delta(\mathbf{r} - \mathbf{R}_i)
\end{aligned}
$$

and split the long-range point-charge from the short-range Coulomb interaction:

$$
\begin{aligned}
\Delta E \;\;=\;\; & \sum_i \left(E_i^{ion} - E_i^{at} \right) \\
& + E^{'}[n'[v], v[\sum_i \bar{n}_i]] - \sum_{i,n} f_{i,n}^{ion} \langle \psi_{i,n}^{ion} | - \frac{1}{2}\nabla^2 + v[\sum_i \bar{n}_i(\mathbf{r})] | \psi_{i,n}^{ion} \rangle \\
& + \frac{1}{2} \sum_{i \neq j} \left[\int \int \frac{(\bar{n}_i(\mathbf{r}) + Z_i(\mathbf{r}))(\bar{n}_j(\mathbf{r}') + Z_j(\mathbf{r}'))}{|\mathbf{r} - \mathbf{r}'|} \mathrm{d}^3 r \mathrm{d}^3 r' - \frac{Q_i Q_j}{|\mathbf{R}_i - \mathbf{R}_j|} \right] \\
& + \frac{1}{2} \sum_{i \neq j} \frac{Q_i Q_j}{|\mathbf{R}_i - \mathbf{R}_j|} \\
& + E_{xc}[\sum_i \bar{n}_i] - \sum_i E_{xc}[\bar{n}_i] \\
& + O((n_0 - n')^2) + O((n_0 - \sum_i \bar{n}_i)^2) \tag{3.8}
\end{aligned}
$$

The individual energy contributions to the functional will be referenced by the following abbreviations (see section 3.3 for a detailed discussion):

$$E_{def} \quad := \quad \sum_i \left(E_i^{ion} - E_i^{at} \right) \tag{3.9}$$

$$E_{tb} \quad := \quad E^{'}[n'[v], v[\sum_i \bar{n}_i]] \tag{3.10}$$

$$E_{diag} \quad := \quad \sum_{i,n} f_{i,n}^{ion} \langle \psi_{i,n}^{ion} | -\frac{1}{2}\nabla^2 + v[\sum_i \bar{n}_i(\mathbf{r})] | \psi_{i,n}^{ion} \rangle \tag{3.11}$$

$$E_{coup} \quad := \quad \frac{1}{2} \sum_{i \neq j} \left[\int \int \frac{(\bar{n}_i(\mathbf{r}) + Z_i(\mathbf{r}))(\bar{n}_j(\mathbf{r}') + Z_j(\mathbf{r}'))}{|\mathbf{r} - \mathbf{r}'|} \mathrm{d}^3r\mathrm{d}^3r' \right.$$
$$\left. -\frac{Q_i Q_j}{|\mathbf{R}_i - \mathbf{R}_j|} \right] \tag{3.12}$$

$$E_{mad} \quad := \quad \frac{1}{2} \sum_{i \neq j} \frac{Q_i Q_j}{|\mathbf{R}_i - \mathbf{R}_j|} \tag{3.13}$$

$$\Delta E_{xc} \quad := \quad E_{xc}[\sum_i \bar{n}_i] - \sum_i E_{xc}[\bar{n}_i] \tag{3.14}$$

3.3 The full picture

Although exaggerated, a resume of the *state of the art electronic structure methods* discussion in part one of this thesis could state:

> The main numerical effort in common electronic structure methods is spent in the setup and diagonalization of the Hamiltonian. Without further approximations, this effort scales cubic with the number of particles involved. The complexity of quantum mechanics thereby usually requires an iterative approach. This is unfavorable, because the bad scaling system of equations needs to be solved several times in order to reach sufficiently accurate results. Over the years, there have been several more or less sophisticated approaches to circumvent these problems. The effort in reducing the numerical demands usually either results in less intelligible approaches, theoretically not well funded approximations or representations which make it hard to extract the physical meaning.

The approach presented in this work is focused on a formulation which is consistent with the physico-chemical intuition. We thereby apply theoretically well funded and straight forward approximations. In our view, intuition, well controlable approximations and numerical efficiency do not have to be mutually exclusive, but can lead to synergetic effects.

We split the transformation from isolated to 'clustered' atoms in two steps: deformation from the atomic to a reference state, which shall be referred to as *ionic state,* and clustering (see section 3.2.1 for further details). The numerical most demanding part is the determination of the clusters total energy. This effort can be reduced by application of the Harris-Foulkes approximation. This approximation however depends on a good approximation of the clusters total density. The deformation process therefore will be formulated such, that it provides a good approximation of the clusters total density. In addition, it can be handled on a per atom basis, which leads to almost linear scaling with the number of atoms in the cluster. In other words: We split the problem in two and work as much as possible on the almost linear scaling first part. This in turn allows to reduce the numerical effort of the most demanding second part. Aside from this, the relative energy expressions permit to play error cancellation to its strength. Historically, there has been an ongoing discussion about the role of potential and kinetic energy in bonding processes. This discussion basically has been settled by Ruedenberg [76]. He pointed out that bonding processes in principle may best be understood when splitted in two steps, which correspond to our deformation and clustering. To our knowledge, an appropriate formulation of the deformation so far has not been presented.

Let us therefore take a closer look at our deformation process. The effect of embedding will be described by a potential. This potential can be thought of as a superposition of nearest neighbor contributions representing the deformation effects due to e.g. Pauli repulsion and Coulomb interaction. In order to be able to formulate the embedding potential, a new representation of so called *nodeless wavefunctions* has been introduced in previous works at our institute [77, 78, 79]. An introduction will be given in section 4.3.3. The embedding potential will then be discussed in section 4.3.7. The neighbor-dependent deformation potential allows to generate nonspherical input densities, which reflect the spatial structure of the vicinity in the crystal. The repulsive character thereby leads to a localization. Although the Harris-Foulkes approximation is widely used, this approach, to our knowledge, is the first to apply nonspherical input densities. See chapter 2 for a detailed discussion of the state of the art. We suppose the superposition of deformed densities to be a good approximation of the clusters density. The corresponding one particle states consequently should be a good guess of a minimal and localized basis set.

So far, the discussion of the deformation potential has been focused on the interaction of neighboring atoms. The technique however can also be applied on the interaction between core and valence states. This allows an numerical efficient formulation of valence only expressions.

The deformation process requires the solution of nonspherical Schrödinger equations. Our approach, based on radial, logarithmic grids, is illustrated in appendix B.5.

The basic total-energy functional in frozen-core formulation will be derived in section 4.1.

In the following, we will discuss the individual contributions (3.9- 3.14) to the energy functional (3.8):

- The first line is the energy needed to convert atoms into the proper reference ions. The energy related to the deformation potential was subtracted out in the definition of E^{ion} (3.2). The energy $\sum_i \left(E_i^{ion} - E_i^{at} \right)$ therefore could be referred to as real costs of deformation and is denoted by E_{def}.

- In the second line, we subtract the sum of one particle energies (E_{diag}) of the deformed ions from the crystal's sum (E_{tb}). The resulting energy gain corresponds to the stabilization of the crystal due to covalent-bond formation. It is considerably smaller than the sum of one-particle energies of the crystal. This has been pointed out by Robert Mulliken already in 1935 [80] in the context of LCAO. He showed that the eigenvalues $\lambda_{1,2}$ of H_2 in LCAO may not be written as[3] $\lambda_{1,2} = H_{aa} \pm H_{ab}$. Assuming a negligible overlap S, this result indeed can be obtained from the more general expression $\lambda_{1,2} = H_{aa} \pm \beta/(1+S)$, with $\beta = H_{ab} - H_{aa}S$. β usually is referred to as *reduced resonance integral*. The approximation however is not valid. Mulliken stated that the essential contribution to the covalent bond corresponds to the reduced resonance integral and not simply to the off-diagonal element of the Hamiltonian. The line two of (3.2) corresponds to Mullikans expression$\beta/(1+S)$.

- The third line is a short-ranged pair-potential (E_{coup}). The short-range character arises from the subtraction of the long-ranged point-charge interaction and the fact that the deformed densities are localized. Note that the subtraction of the ionic contributions from the crystal expression is reflected in the missing self-interaction $i = j$. Unlike in traditional Harris-Foulkes formulations, this pair-potential is not only repulsive, but exhibits a minimum for a certain value of $|\mathbf{r} - \mathbf{r}'|$. This value however lies above the bond length. The bond length corresponds to the minimum of the complete functional with respect to the fragment separation. As will turn out in the discussion on the basis of H_2 in part III, the energy gain due to covalent and ionic bonding (line two and four) as well as the contribution of the exchange correlation energy (line five) are attractive up to very short distances. This attraction is mainly balanced by the repulsive character of the pair-potential term and the bond length therefore is smaller than the minimum separation of line three.

- The fourth line corresponds to the Madelung energy (E_{mad}). It is a measure of the ionic character of the bonding. The point-charge formulation furthermore allows to handle the long-range Coulomb interaction in a numerically efficient way.

---

[3]Here, $H_{aa} = \int \phi_a(\mathbf{r}) H \phi_a(\mathbf{r}) d^3r$ and $S = \int \phi_a(\mathbf{r}) \phi_b(\mathbf{r}) d^3r$. ϕ_a and ϕ_b correspond to the atomic orbitals.

- The fifth line is the change in exchange correlation energy (ΔE_{xc}) during cluster formation. The trend of this contribution can easily be approximated. Suppose we would have a diatomic system. The overlapping part of the densities will increase if we bring the two fragments together. In local density approximation, the energy of exchange and correlation for a given density can be estimated as follows: $E_{xc} = -C \int n^{\frac{4}{3}}(\mathbf{r}) d^3 r$. For increasing overlap, the difference $(\sum_i n_i)^{4/3} - \sum_i (n_i)^{4/3}$ will become more and more positive. The exchange and correlation contribution in line five therefore should be zero for large distances and become more and more attractive for decreasing fragment separation.

- The error terms in line six have extensively been discussed in section 2.4 (see e.g. equations (2.30) and (2.35) and the corresponding text). In conclusion, the functional (3.8) is stationary at the exact ground-state density, but does not necessarily correspond to a minimum.
  It is however worth taking a closer look at our choice of the trial potential $\bar{v}$, as it directly influences $O((n_0 - n')^2)$. During the derivation of the non self-consistent functional (2.38), which enters (3.8), we already mentioned, that the trial potential $\bar{v}$ should be chosen reasonably. In the transition to the Harris-Foulkes functional (2.40), as well as in the above approach, we choose the trial potential to be equal to the potential $v[\bar{n}]$. One may ask if this choice - besides the further simplification of the equations - is reasonable. In order to illustrate this, suppose $\sum_i \bar{n}_i$ to be a good approximation of the self-consistent crystal density, that is $O((n_0 - \sum_i \bar{n}_i)^2)$ is small. The potential $v[\sum_i \bar{n}_i(\mathbf{r})]$ then is close to the self-consistent crystal potential, which, for exact self-consistency produces $\sum_i \bar{n}_i$ as output density of the non interacting Schrödinger equation. Therefore $O((n_0 - n')^2)$ is small.

The error discussion leads us to another interesting point: The deformed orbitals, which form the correct crystal density, should be a good choice for a basis set. It therefore seems natural to determine $E'[n'[v], v[\sum_i \bar{n}_i]]$ approximately, using a tight-binding ansatz in the deformed basis. The fact that the deformed basis is localized leads to a sparse Hamiltonian, which is numerically convenient. Moreover, the interpretation of the crystals orbitals, built from atom centered deformed atomic orbitals is quite intuitive.

In conclusion, a possible program flow would go through the following steps:

- Determine the embedding potential contribution once per chemical element. These potentials are structure-independent and can be predetermined.

- Loop over all unique atoms of a given unit cell and setup the embedding potential, determine the ionic (deformed) orbitals and densities.

- Superimpose the ionic densities to the crystals trial density.

- Determine the contributions in line one and three to five.

- Setup the potential $v[\bar{n}]$.

- Determine the contribution in line two from a tight-binding approach in the deformed basis. Note that the second term corresponds to the sum of the corresponding Hamilton matrix diagonal elements.

The above stated guideline surely misses several theoretical and practical subtleties, which will be discussed in the following sections.

4 Theoretical details

4.1 Frozen core formulation of the fundamental functional

The basic idea of the approach is to introduce the frozen core approximation in the selfconsistent calculation of the ions. The frozen core approximation results in an energy functional of the one-particle wave functions, which is stationary and variational. The resulting ionic densities are then superimposed to provide the trial density for the crystal part of the total energy functional. The variationality of the crystal's band-structure energies furthermore allows to cancel the core contributions to first order. The basics have been discussed in section 2.7.

Note that we do not introduce an explicit notation to distinguish the frozen core from the full core expressions. We e.g. use the same symbols $f_{i,n}^{ion}$ and $\varepsilon_{i,n}^{ion}$ for the occupations and the band-structure energy of the ion in both cases. We do this, because the basic meaning is the same. Nevertheless, the actual numbers in the full core and frozen core case may be different.

Ionic contributions

Let $\psi_{i,n}^{ion}$ be the nth one-particle frozen core wave function of the ith ion. The core wave functions ($n \in c$) should be fixed (e.g. to the atomic solutions). The valence wave functions ($n \in v$) should be determined self-consistently using equation (2.48). The ionic contribution can then be written in terms of the functional (2.46) as follows:

$$
\begin{aligned}
\sum_i E_i^{ion} &= \sum_{i,n \in c} f_{i,n}^{ion} \langle \psi_{i,n}^{ion} | -\frac{1}{2}\nabla^2 | \psi_{i,n}^{ion} \rangle + \sum_{i,n \in v} f_{i,n}^{ion} \langle \psi_{i,n}^{ion} | -\frac{1}{2}\nabla^2 | \psi_{i,n}^{ion} \rangle \\
&+ E_{pot}[\sum_i \bar{n}_i] \\
&- \sum_i \sum_{j,k} \lambda_{i,j,k} \left[\langle \psi_{i,j}^{ion} | \psi_{i,k}^{ion} \rangle - \delta_{j,k} \right]. \\
&+ O((\psi_{i,n}^{ion} - \psi_{i,n}^0)^2)
\end{aligned}
\tag{4.1}
$$

Crystal contribution

Splitting the core from the valence kinetic energy, the crystal total energy expression (3.6) can be written as follows:

$$
\begin{aligned}
E^{cry}[n_0] \;=\;& \sum_{i,n\in c} f_{i,n}\langle \psi'_{i,n}| -\frac{1}{2}\nabla^2 |\psi'_{i,n}\rangle \\
&+ \sum_{i,n\epsilon v} f_{i,n}\varepsilon_{i,n} - \int \bar{n}^v(\mathbf{r})v([\bar{n}],\mathbf{r})d^3r + E_{pot}[\bar{n}] \\
&+ O((n_0-n')^2) + O((n_0-\sum_i \bar{n}_i^{fc})^2) \quad\quad\quad (4.2)
\end{aligned}
$$

The trial density thereby was divided in the core and valence contribution according to:

$$
\bar{n}(\mathbf{r}) \;=\; \bar{n}^c(\mathbf{r}) + \bar{n}^v(\mathbf{r}). \quad\quad\quad (4.3)
$$

The one-particle energies $\varepsilon_{i,n}$ correspond to the output wave functions $\psi'_{i,n}$ of the potential $v[\bar{n}]$. Due to the variationality of $E'[n'[v],v[\bar{n}]]$, the following relation holds (see equation (2.49) and related text for details):

$$
\sum_{i,n\in c} f_{i,n}\langle \psi'_{i,n}| -\frac{1}{2}\nabla^2 |\psi'_{i,n}\rangle \;=\; \sum_{i,n\in c} f_{i,n}\langle \psi_{i,n}| -\frac{1}{2}\nabla^2 |\psi_{i,n}\rangle + O((\psi_{i,n}-\psi'_{i,n})^2)
$$

$$(4.4)$$

and (4.2) can be written as follows:

$$
\begin{aligned}
E^{cry}[n_0] \;=\;& \sum_{i,n\in c} f_{i,n}\langle \psi_{i,n}| -\frac{1}{2}\nabla^2 |\psi_{i,n}\rangle \\
&+ \sum_{i,n\epsilon v} f_{i,n}\varepsilon_{i,n} - \int \bar{n}^v(\mathbf{r})v([\bar{n}],\mathbf{r})d^3r + E_{pot}[\bar{n}] \\
&+ O((n_0-n')^2) + O((n_0-\sum_i \bar{n}_i)^2) + O((\psi_{i,n}-\psi'_{i,n})^2) \quad (4.5)
\end{aligned}
$$

Assembling the energy expression

The frozen core formulation of (3.8) is then given by:

$$
\begin{aligned}
\Delta E \;=\; & \sum_{i,n\in v} \left(f_{i,n}^{ion}\varepsilon_{i,n}^{ion} - f_{i,n}^{at}\varepsilon_{i,n}^{at} \right) \\
& + \sum_{i,n\epsilon v} f_{i,n}\varepsilon_{i,n} - \sum_{i,n\in v} f_{i,n}^{ion}\langle\psi_{i,n}^{ion}| - \frac{1}{2}\nabla^2 + \bar{v}[\sum_i \bar{n}_i(\mathbf{r})]|\psi_{i,n}^{ion}\rangle \\
& + \frac{1}{2}\sum_{i\neq j}\left[\int\int \frac{(\bar{n}_i(\mathbf{r})+Z_i(\mathbf{r}))(\bar{n}_j(\mathbf{r}')+Z_j(\mathbf{r}'))}{|\mathbf{r}-\mathbf{r}'|}\mathrm{d}^3r\mathrm{d}^3r' - \frac{Q_iQ_j}{|\mathbf{R}_i-\mathbf{R}_j|}\right] \\
& + \frac{1}{2}\sum_{i\neq j}\frac{Q_iQ_j}{|\mathbf{R}_i-\mathbf{R}_j|} \\
& + E_{xc}[\sum_i\bar{n}_i] - \sum_i E_{xc}[\bar{n}_i] \\
& + O((n_0-n')^2) + O((n_0-\sum_i\bar{n}_i)^2) + O((\psi_{i,n}^{ion}-\psi_{i,n}')^2) \\
& + O((\psi_{i,n}^{ion}-\psi_{i,n}^0)^2)
\end{aligned}
\tag{4.6}
$$

In the first and second line, the core contribution can be removed because the occupations of the core states are fixed and the ionic core wave functions have been assumed to be frozen atomic :

$$
f_{i,n}^{at} = f_{i,n}^{ion} = f_{i,n} \quad \text{for} \quad i,n\in c \tag{4.7}
$$
$$
\varepsilon_{i,n}^{ion} = \varepsilon_{i,n}^{at} \quad \text{for} \quad i,n\in c \tag{4.8}
$$

Alternatively, the ionic core wave functions could be frozen to e.g. localized atomic wave functions. The first row in (4.6) then however needs to include the difference in the core energies (the sum need to extend over $i,n\in c$). Note that the ionic band-structure energy $\varepsilon_{i,n}^{ion}$ was defined excluding the embedding potential (see (3.3)). The orthogonality constraint in the third line of (4.1) occurs twice and can be removed from (4.6). Nevertheless, the orthogonality has to be fulfilled. This naturally is the case, when the ionic wave functions were determined in solving Schrödingers equation derived from 4.1, which includes the constraints.

Except for the removed core contribution in the first two rows, the meaning of the term is just as already discussed in the context of the full core expression (see section 3.3 for a discussion).

A word about the sequence in which we introduced the approximations: we could just as well have started with the fully selfconsistent frozen core expression for the crystal and introduce the Harris-Foulkes approximation for the valence only. This however would result in almost unmanageable orthogonality constraints. Inter ionic core orthogonality and the orthogonality of the valence to all core wave functions would need to be satisfied. As discussed in section 2.7, the orthogonality constraint between valence and frozen core usually can be relaxed to first order. This however

is not obvious.

Our formulation of the frozen core atomization energy in contrast is straightforward. It complies to our philosophy to put as much as possible work in the linear scaling ionic contribution and to use well defined approximations.

4.2 Error cancellation in the fundamental functional

The new functional (3.8) is formulated in terms of energy differences (3.9-3.14), to achieve best possible error cancellation on implementation. Obviously, the corresponding terms should be handled on the same level of numerical approximation. Besides these, there are however several more concealed connections across the individual differences (3.9-3.14), which result from the reformulation of the kinetic energy (2.24) and the approximations (2.29) and (2.33). The second term in (2.33), $\int v([\bar{n}], \mathbf{r}) \, (n(\mathbf{r}) - \bar{n}(\mathbf{r})) \, d^3r$, e.g. partly enters in the coupling (E_{coup}) and diagonal (E_{diag}) energy, respectively. Because this integral, together with the potential energy $E_{pot}[\bar{n}]$ needs to cancel the first order errors in (2.33), the potential $v([\bar{n}], \mathbf{r})$ should not be handled differently in the implementation of E_{coup} and E_{diag}.

The following list provides some facts about the connections between individual terms and should be helpful when trying to disentangle the error cancellations:

- The E^{ion} contribution is handled exactly (with respect to DFT) and therefore includes no trial potential. The original kinetic energy expression is used (see equation (3.5)). The electrostatic and exchange correlation terms of the ion and crystal are treated in the same way.

- The electrostatic energy and the energy of exchange and correlation are connected, as E_{xc} (in the usual formulation of exchange and correlation functionals) cancels the self interaction of the electronic density. This, in particular, needs to be taken into account when generating the potential for the tight-binding calculation. It is e.g. not valid to approximate the potential of exchange and correlation (μ_{xc}) by a superposition of fragment contributions ($\mu_{xc}[\sum_i n_i] \approx \sum_i \mu_{xc}[n_i]$), while including interference contributions in the electrostatic potential.

- The potential $v[\sum_i \bar{n}_i]$, in which the energy E_{tb} (3.10) needs to be determined originates from the approximation (2.36) and the choice of the trial potential (2.39). Note the n in the second term of (2.36). The approximation of the potential energy (2.33) in the crystal's expression (3.6) contributes $\int v([\bar{n}], \mathbf{r}) \, (n(\mathbf{r}) - \bar{n}(\mathbf{r})) \, d^3r$, which cancels the corresponding term in (2.36). The final $\int \bar{n}(\mathbf{r}) v([\bar{n}], \mathbf{r}) d^3r$ in E_{diag} therefore traces back to the potential energy of the crystal.

- The potential $v[\sum_i \bar{n}_i]$ is the same for both, E_{tb} and E_{diag} as long as the approximation of the crystal density in terms of fragment densities (3.4) is valid. The

ion contributes only the kinetic energy of the trial (=ionic) wave functions to the energy E_{diag}. Therefore, the Hamiltonians for the diagonal and tight-binding energies are the same, provided (3.4) holds.

Taking the interference contribution of the deformed wave functions into account (which we did for testing reasons), this however is not the case and needs to be compensated (see equation (6.1) and the related discussion for details).

- If numerical errors occur in $v[\bar{n}]$, this contributes to both, E_{diag} and E_{tb} and therefore partly cancels. Note however that the remaining error, according to (2.37) scales linearly, and therefore, in general cannot be neglected. Section (10.2) illustrates this for the potential of exchange and correlation.

Concerning the frozen core expression:

- The frozen core approximation outlined in section 4.1 alters the trial density, which however enters all terms of the above discussion in the same way. The arguments therefore stay the same.

- In the crystal expression, we split the kinetic energy of the core from the valence, and expand it about the ionic core wave functions (4.4). This term therefore cancels to first order with the corresponding ionic term.

4.3 Embedding potentials in node-less representation

4.3.1 Historical background

In this section, the Pauli repulsion and embedding potentials, outlined in chapter (3), will be derived. The underlying methods have been proposed by Prof. Blöchl [77]. First aspects of the node-less wave function formulation have been studied in the diploma thesis of Mike Thieme [78]. The work of Thieme has been continued in the PhD-thesis of Clemens Först [79]. The compilation of definitions and conditional equations in sections 4.3.3 to 4.3.5 are mainly based on the formulation introduced by Clemens Först.

4.3.2 The role of the energy derivative

The basic problems in the derivation of a numerically convenient formulation of embedding potentials can be illustrated by a simple, one dimensional model system shown in figure 4.1. It consist of two identical atoms A and B. Following the commonly known LMTO approach, we identify the regions near the atom A (Ω_A) and B (Ω_B), as well as the interstitial region between both atoms (Ω_{int}). From a mathematical point of view, any given molecular orbital $\phi(r)$ (full line in the lower panel), can be regarded as built from the quasi-atomic orbitals $\chi_A(r)$ and $\chi_B(r)$ (dashed line in the
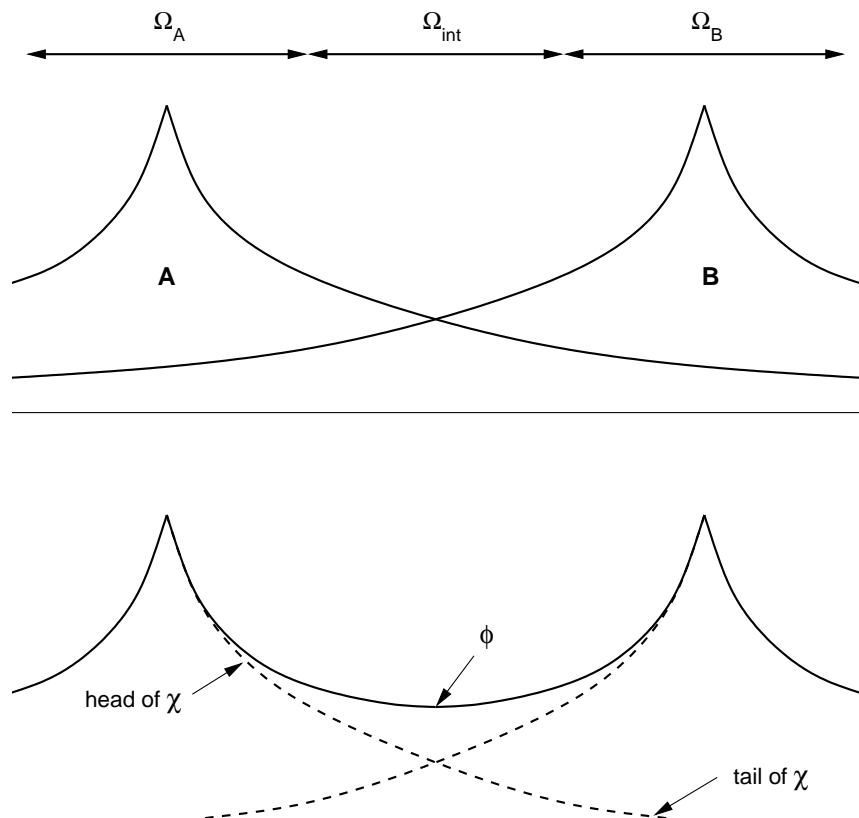
Figure 4.1: Model system of two identical atoms A and B. The regions near the atom A and B, as well as the interstitial region between both atoms (Ω_{int}) are denoted by Ω_A, Ω_B and Ω_{int}, respectively. The upper panel shows a sketch of atomic orbitals. A molecular orbital (full line) and the corresponding quasi-atomic orbitals (dashed line) are shown in the lower panel. See the text for further details.

lower panel) as follows:

$$\phi(r,\varepsilon) = a\chi_A(r,\varepsilon) + b\chi_B(r,\varepsilon) \tag{4.9}$$

The orbital χ_i thereby dominates the region Ω_i and has a minor contribution in the region $\Omega_{j\neq i}$. Due to the shape of the quasi-atomic orbitals, the contributions of χ_i in Ω_i and $\Omega_{j\neq i}$ are denoted by *head* and *tail*, respectively. Once determined, the molecular orbitals and hence the total crystal density can be build from the quasi-atomic orbitals. We will therefore refer to the corresponding orbitals and densities as *fragment orbitals* and *fragment densities*.

Our aim is to find formation rules which allow to determine the quasi-atomic orbitals and hence the molecular orbitals in a numerically efficient way. An approach applied by so called *linear methods* is based on the fact that the molecular potential in the atomic regions Ω_A and Ω_B are mainly dominated by the corresponding atomic potentials. It is therefore reasonable, to describe the solutions in these regions by perturbed atomic wave functions:

$$\phi^{@\Omega_A}(r,\varepsilon) = \phi^{at,A}(r,\varepsilon_\nu) + \dot{\phi}^{at,A}(r,\varepsilon_\nu)(\varepsilon - \varepsilon_\nu) + O((\varepsilon - \varepsilon_\nu)^2) \tag{4.10}$$

$\phi^{at,A}(r,\varepsilon_\nu)$ denotes the atomic orbital of A and $\dot{\phi}^{at,A}$ the corresponding energy derivative. Rewriting equation (4.9) as follows:

$$\phi^{@\Omega_A}(r,\varepsilon) = a\left(\chi_A^{@\Omega_A}(r,\varepsilon) + \frac{b}{a}\chi_B^{@\Omega_A}(r,\varepsilon)\right) \tag{4.11}$$

allows to relate the head and tail of χ with the corresponding atomic wave function and its energy derivative, respectively. Explicitly:

$$\chi_A^{@\Omega_A} \sim \phi^{at,A} \tag{4.12}$$

$$\chi_A^{@\Omega_B} \sim \dot{\phi}^{at,B} \tag{4.13}$$

$$\chi_B^{@\Omega_B} \sim \phi^{at,B} \tag{4.14}$$

$$\chi_B^{@\Omega_A} \sim \dot{\phi}^{at,A}. \tag{4.15}$$

A basis build from atomic orbitals and their energy derivatives therefore allows to solve the molecular Schrödinger equation, at least to linear order. It can be shown, that the energy derivative $\dot{\phi}^{at}$ is orthogonal to the corresponding atomic core and valence wave functions. The above approach therefore ensures the orthogonality of the molecular orbitals among each other, as well as to the atomic core. The orthogonality to the core wave functions allows to easily apply the frozen core approximation.

As a first step towards the formulation of embedding potentials, one can state that the difference between the isolated atom and an embedded fragment could be described in terms of atomic wave functions and their energy derivatives. The energy

derivative in principle can be determined from the energy derivative of Schrödingers equation:

$$\left[-\frac{1}{2}\nabla^2 + v - \varepsilon \right] \dot{\phi}(r,\varepsilon) = \phi(r,\varepsilon). \tag{4.16}$$

This can be written in terms of a homogeneous Schrödinger equation including an additional potential:

$$\left[-\frac{1}{2}\nabla^2 + v + \eta(r,\varepsilon) - \varepsilon \right] \dot{\phi}(r,\varepsilon) = 0$$

$$\text{with}$$

$$\eta(r,\varepsilon) = -\frac{\phi(r,\varepsilon)}{\dot{\phi}(r,\varepsilon)}.$$

Due to the nodal character[1] of $\dot{\phi}$, such a potential however is numerically inconvenient. Blöchl, Thieme and Först introduced *node-less wave functions* to solve this problem. The idea is to decompose the wave function and its energy derivative in a superposition of several contributions from node-less functions. The language of node-less wave functions thereby not only circumvents the numerical problems stated above. It furthermore allows to derive so called Pauli repulsion potentials, which describe the interaction between valence- and core-states. In addition, the connection between the energy derivative character of the tail and the Pauli repulsion potential becomes evident.

4.3.3 Node-less wave functions

The node-less wave functions are derived from isolated atoms. Due to the sphericity of the potential, the angular momentum channels can be separated. In the following, we will therefore drop the indices for the angular (l) and magnetic (m) momentum.

A given atomic wave function can be decomposed in node-less contributions as follows (for further details see [79]):

$$|\phi_n(\varepsilon)\rangle = \sum_{i=1}^{n-1} |u_i\rangle c_{i,n} + |q_n(\varepsilon)\rangle c_{n,n} \tag{4.17}$$

$$\text{with}$$

$$|u_i\rangle = |q_i(\varepsilon_i)\rangle \tag{4.18}$$

The index n thereby refers to the n-th state for a given angular momentum channel[2].

---

[1] $\dot{\phi}$, just as well as the atomic wave function, exhibits nodes for all but the first wave function for a given angular momentum l.

[2] For e.g. $l = 1$, the sequence $2p, 3p, \ldots$ corresponds to $n = 1, 2, \ldots$ etc.
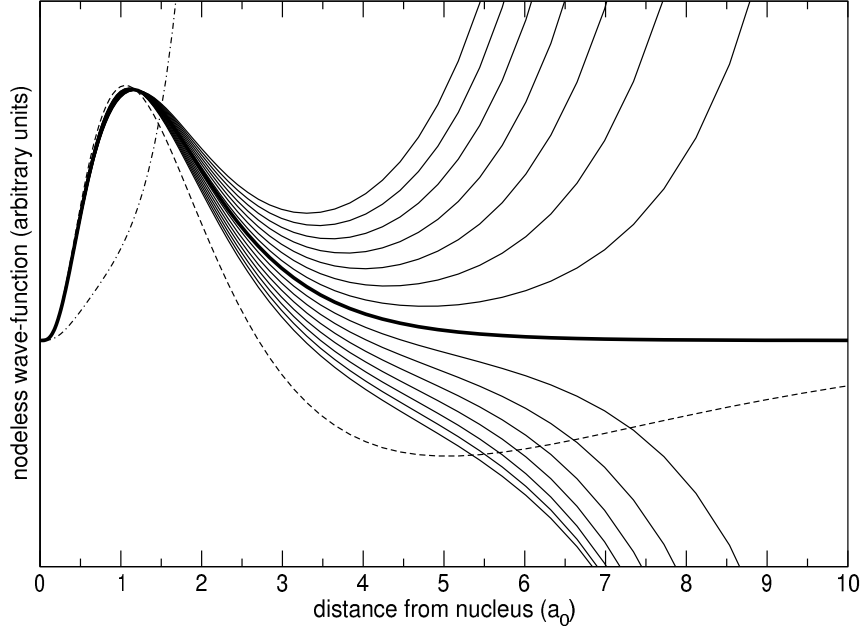
Figure 4.2: $|q_3(\varepsilon)\rangle$ for the Si s-channel in an energy window of ± 0.15 H around the atomic eigenvalue ε_3. The bound state $|u_3\rangle = |q_3(\varepsilon_3)\rangle$ is indicated by the bold line. The dash dotted and dashed curves show $|q_3(\varepsilon_2)\rangle$ and $|q_3(\varepsilon_4)\rangle$, respectively. Figure courtesy of Clemens Först.

The energy ε_i denotes the i-th atomic eigenvalue. The node-less wave functions are defined as follows:

$$(\hat{H} - \varepsilon)|q_n(\varepsilon)\rangle = |u_{n-1}\rangle \tag{4.19}$$

$$(\hat{H} - \varepsilon_i)|u_i\rangle = |u_{i-1}\rangle \tag{4.20}$$

with

$$|u_0\rangle = 0 \tag{4.21}$$

Equation (4.20) follows from (4.19) and (4.18). The first node-less wave function per angular momentum channel (u_1) corresponds to the atomic wave function.

The expansion coefficients are given by:

$$c_i = c_1 \prod_{j=1}^{i-1} (\varepsilon - \varepsilon_j). \tag{4.22}$$

Note that the index n has been dropped here.

Figure 4.2 shows $|q_3(\varepsilon)\rangle$ for the Si s-channel in an energy window of ± 0.15 H around the atomic eigenvalue ε_3. The bound state $|u_3\rangle = |q_3(\varepsilon_3)\rangle$ is indicated by

index i	$|\phi_i\rangle$	$|u_i\rangle$	$|\dot{u}_i\rangle$
1	r^l	r^l	r^{l+2}
2	r^l	r^{l+2}	r^{l+4}
$\vdots$	$\vdots$	$\vdots$	$\vdots$
n	r^l	$r^{l+2(n-1)}$	r^{l+2n}

Table 4.1: The behavior of the atomic node-less wave function $|u\rangle$ and the corresponding energy derivative $|\dot{u}\rangle$ compared to the atomic wave functions $|\phi\rangle$ for $r \rightarrow 0$. The energy derivative is discussed in section 4.3.5.

the bold line. The dash dotted and dashed curves show $|q_3(\varepsilon_2)\rangle$ and $|q_3(\varepsilon_4)\rangle$, respectively. Apparently, the node-less character of $|q_n(\varepsilon)\rangle$ only applies in the energy interval $\varepsilon_{n-1} \leq \varepsilon \leq \varepsilon_{n+1}$. With this in mind, the choice to absorb the energy dependence of the wave function only in the expansion coefficients and the highest node-less wave function becomes reasonable. In this way, all expansions for a given angular momentum channel share the same, energy independent basis $\{u\}$. Furthermore, the node-less character of each individual contribution is ensured.

A typical approach in the work with node-less wave functions is to determine the basis $\{u\}$ per angular momentum channel from bottom up, repeatedly solving the inhomogeneous Schrödinger equation (4.20). The atomic wave functions $|\phi_n(\varepsilon)\rangle$ can be reconstructed from the node-less wave functions via the expansion (4.17) and the coefficients (4.22) or, alternatively, by an orthogonalization to all $|\phi_j(\varepsilon_j)\rangle$ with $j < n$ (see appendix B.1 for further details):

$$|\phi_n(\varepsilon)\rangle = \left(1 - \sum_{j=1}^{n-1} |\phi_j(\varepsilon_j)\rangle\langle\phi_j(\varepsilon_j)|\right) c_{n,n}|q_n(\varepsilon)\rangle \tag{4.23}$$

Figure 4.3 shows the $3s$ wave function of silicon decomposed into the contributions from the node-less wave function $|u_i\rangle$ times the corresponding weights c_i. Each node-less wave function is responsible for one local extremum of the atomic wave function. The extrema of the atomic wave function $|\phi_3\rangle$ are slightly shifted to larger r values compared to those of the node-less wave functions.

The first three node-less wave functions $|u_1\rangle$, $|u_2\rangle$ and $|u_3\rangle$ for the silicon s-channel, scaled to have a common maximum, are plotted in figure 4.4. The behavior of the atomic node-less compared to the atomic wave functions for $r \rightarrow 0$ is listed in table 4.1. For large radii, the $|u_i\rangle$ become identical to the corresponding $|\phi_i\rangle$. The corresponding derivations can be found in appendix D.1 of [79]. The node-less wave functions may be parametrized by Slater type orbitals [15]. A sufficiently accurate representation however requires at least two polynomial and two exponential parameters per radial part [78, 79].
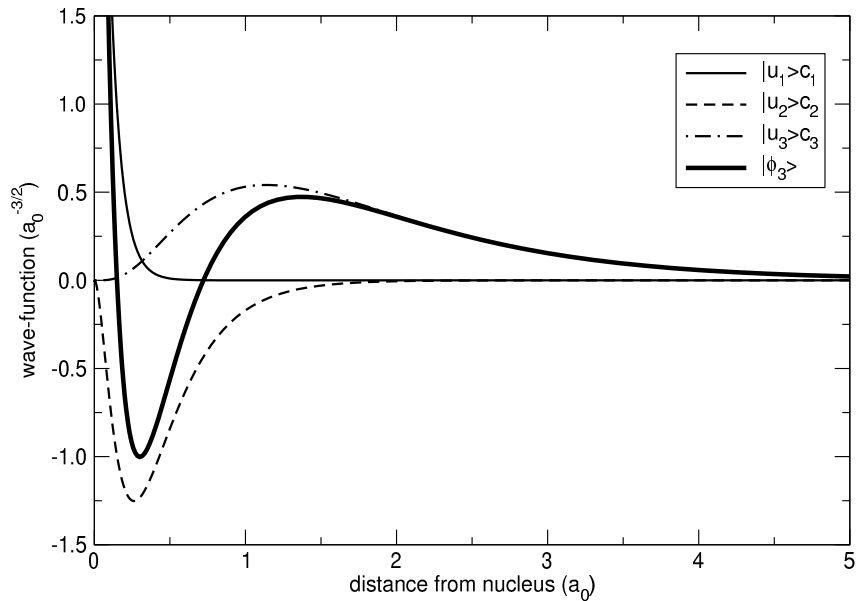
Figure 4.3: The $3s$ wavefunction of silicon decomposed into the contributions from the node-less wave function $|u_i\rangle$ times the corresponding weights c_i. Each node-less wave function is responsible for one local extremum of the atomic wave function. The extrema of the atomic wave function $|\phi_3\rangle$ are slightly shifted to larger r values compared to those of the node-less wave functions. Figure courtesy of Clemens Först.
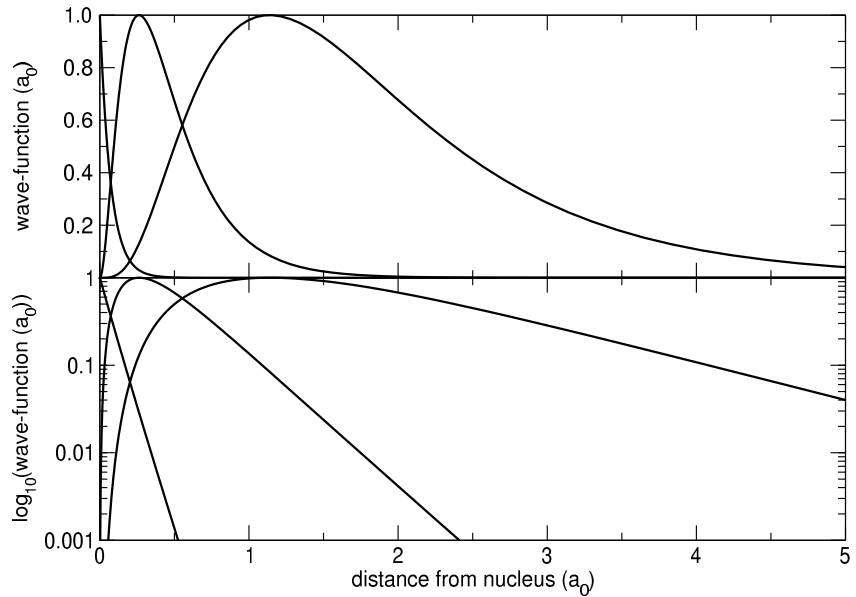
Figure 4.4: The first three node-less wave functions $|u_1\rangle$, $|u_2\rangle$ and $|u_3\rangle$ for the silicon s-channel, scaled to have a common maximum. The lower panel shows the node-less wave functions on a logarithmic scale. Figure courtesy of Clemens Först.

4.3.4 Potentials for the node-less wave functions

Rewriting (4.19) into a homogeneous equation

$$\left[-\frac{1}{2}\nabla^2 + v + \eta_n(r,\varepsilon) - \varepsilon \right] q_n(r,\varepsilon) \;\; = \;\; 0 \tag{4.24}$$

defines $\eta_n(\varepsilon)$ as follows:

$$\eta_n(r,\varepsilon) \;\; = \;\; -\frac{u_{n-1}(r,\varepsilon)}{q_n(r,\varepsilon)}. \tag{4.25}$$

Any atomic wave function may be expanded in node-less wave functions. Therefore, and due to the node-less character of $q_n(r,\varepsilon)$ in the energy interval $\varepsilon_{n-1} \le \varepsilon \le \varepsilon_{n+1}$, (4.25) corresponds to a numerically convenient ab initio pseudo potential. The additional potential term $\eta_n(r,\varepsilon)$ mimics the presence of the lower shells and thus has been identified with a *Pauli repulsion potential.*

The energy dependence of η however renders the numerical solution of Schrödingers equation cumbersome. Linearization in energy around some energy $\bar{\varepsilon}$ leads to:

$$\eta_n(r,\varepsilon) \;\; = \;\; v_n^{pauli}(r,\bar{\varepsilon}) - o_n(r,\bar{\varepsilon}) \cdot \varepsilon + O((\varepsilon - \bar{\varepsilon})^2) \tag{4.26}$$

with

$$\dot{\eta}_n(r,\bar{\epsilon}) \;\; := \;\; \left.\frac{\partial \eta_n}{\partial \varepsilon}\right|_{\bar{\epsilon}} \tag{4.27}$$

$$v_n^{pauli}(r,\bar{\varepsilon}) \;\; := \;\; \eta_n(r,\bar{\varepsilon}) - \bar{\varepsilon}\dot{\eta}_n(r,\bar{\epsilon}) \tag{4.28}$$

$$o_n(r,\bar{\varepsilon}) \;\; := \;\; -\dot{\eta}_n(r,\bar{\epsilon}) \tag{4.29}$$

$v_n^{pauli}(r,\bar{\varepsilon})$ is denoted by *energy independent Pauli repulsion potential.* The energy dependence is, to linear order, absorbed in the so called *overlap times energy* ($o_n(r,\bar{\varepsilon}) \cdot \varepsilon$) term. This is common practice in linear methods and results in a generalized eigenvalue problem:

$$\left[-\frac{1}{2}\nabla^2 + v + v_n^{pauli}(r,\bar{\varepsilon}) - \varepsilon(1 + o_n(r,\bar{\varepsilon})) \right] q_n(r,\varepsilon) \;\; = \;\; 0.$$

The Pauli repulsion potential and overlap term, explicitly expressed in node-less wave functions, read as follows:

$$v_n^{pauli}(r,\bar{\epsilon}) \;\; = \;\; -\frac{u_{n-1}(r)}{q_n(r,\bar{\varepsilon})}\left[1 + \bar{\varepsilon}\frac{\dot{q}_n(r,\bar{\varepsilon})}{q_n(r,\bar{\varepsilon})} \right] \tag{4.30}$$

$$o_n(r,\bar{\varepsilon}) \;\; = \;\; -\frac{\dot{q}_n(r,\bar{\varepsilon})u_{n-1}}{q_n^2(r,\bar{\varepsilon})}. \tag{4.31}$$

The energy derivative of the node-less wave function $\dot{q}_n(r,\varepsilon)$ will be discussed in the following section.

4.3.5 The energy derivative of node-less wave functions

The energy derivative of atomic wave functions plays an important role in linear methods (see section 4.3.2 for details). A decomposition in node-less wave functions can be achieved in analogy to (4.17) :

$$|\dot{\phi}_n(\varepsilon)\rangle \;\; = \;\; \sum_{i=1}^{n} |u_i\rangle d_{i,n} + |\dot{q}_n(\varepsilon)\rangle d_{n,n}. \tag{4.32}$$

A differential equation defining the energy derivative of the node-less wave function can be obtained from the corresponding derivative of (4.19):

$$(\hat{H} - \varepsilon)|\dot{q}_n(\varepsilon)\rangle \;\; = \;\; |q_n(\varepsilon)\rangle \tag{4.33}$$

Comparison of (4.19) and (4.33) leads to:

$$|q_{n+1}(\varepsilon_n)\rangle \;\; = \;\; |\dot{q}_n(\varepsilon_n)\rangle. \tag{4.34}$$

This expression can be generalized to higher derivatives (see appendix D.3 in [79]):

$$|q_{n+1}^{(j)}(\varepsilon_n)\rangle \;\; = \;\; \frac{1}{j+1}|q_n^{(j+1)}(\varepsilon_n)\rangle. \tag{4.35}$$

In accordance to the atomic wave function, $|\dot{\phi}_n(\varepsilon)\rangle$ can be reconstructed from the node-less wave functions by an orthogonalisation to all $|\phi_j(\varepsilon_j)\rangle$ with $j < n$ (see appendix B.1 for further details):

$$|\dot{\phi}_n(\varepsilon)\rangle \;\; = \;\; \left(1 - \sum_{j=1}^{n-1} |\phi_j(\varepsilon_j)\rangle\langle\phi_j(\varepsilon_j)| \right) c_{n,n}|\dot{q}_n(\varepsilon)\rangle. \tag{4.36}$$

4.3.6 Potentials for $|\dot{q}(\varepsilon)\rangle$

In analogy to (4.24), we rewrite (4.33) as follows:

$$\left[-\frac{1}{2}\nabla^2 + v + \tilde{\eta}_n(r,\varepsilon) - \varepsilon \right] \dot{q}_n(r,\varepsilon) \;\; = \;\; 0 \tag{4.37}$$

with

$$\tilde{\eta}_n(r,\varepsilon) \;\; = \;\; -\frac{q_n(r,\varepsilon)}{\dot{q}_n(r,\varepsilon)}. \tag{4.38}$$

Linearisation of $\tilde{\eta}_n(r, \varepsilon)$ in energy can be written as:

$$\tilde{\eta}_n(r, \varepsilon) \quad = \quad \tilde{v}_n(r, \bar{\varepsilon}) - \varepsilon \tilde{o}_n(r, \bar{\varepsilon}) + (\bar{\varepsilon} - \varepsilon) + O((\varepsilon - \bar{\varepsilon})^2) \tag{4.39}$$

with

$$\tilde{v}_n(r, \bar{\varepsilon}) \quad := \quad -\frac{q_n(r, \bar{\varepsilon})}{\dot{q}_n(r, \bar{\varepsilon})}\left[1 + \bar{\varepsilon}\frac{\ddot{q}_n(r, \bar{\varepsilon})}{\dot{q}_n(r, \bar{\varepsilon})}\right] \tag{4.40}$$

$$\tilde{o}_n(r, \bar{\varepsilon}) \quad := \quad -\frac{q_n(r, \bar{\varepsilon})}{\dot{q}_n^2(r, \bar{\varepsilon})}\ddot{q}_n(r, \bar{\varepsilon}). \tag{4.41}$$

The extra term $(\bar{\varepsilon} - \varepsilon)$ in (4.39), when compared to (4.26) results from the energy dependent denominator in (4.38).

Comparison of (4.25) and (4.38) shows an interesting connection between the Pauli repulsion potential η and the potential generating the $\dot{q}$-character ($\tilde{\eta}$). For the energy ε_n, the Pauli repulsion potential (4.25) for the first exited state (using the substitution $n \to n+1$)

$$\eta_{n+1}(\varepsilon_n) \quad = \quad -\frac{|u_n\rangle}{|q_{n+1}(\varepsilon_n)\rangle}$$

corresponds to the potential $\tilde{\eta}_n$

$$\tilde{\eta}_n(\varepsilon_n) \quad = \quad -\frac{|q_n(\varepsilon_n)\rangle}{|\dot{q}_n(\varepsilon_n)\rangle}$$
$$\quad = \quad -\frac{|u_n\rangle}{|q_{n+1}(\varepsilon_n)\rangle}.$$

We used the relation (4.18) and (4.34) in the last step. Note however, that this exclusively holds for the energy ε_n. The energy dependence of the potentials is different, as can be seen from the energy linearisations (4.26) and (4.39).

4.3.7 Embedding potentials

Before we return to the model system, let us introduce the following definition of terms: in the context of the deformation process, we divide the atoms of the crystal in two classes. We distinguish the *central atom,* the one which actually gets deformed, from all the other atoms, which build the embedding surrounding. These are referred to as *off-central.* Contributions arising from central or off-central sites, usually carry the adverb *on-site* or *off-site*, respectively.

The node-less representation introduced in the preceding sections, allows to access the fragment orbitals discussed in section (4.3.2) in a numerically convenient way. The repulsion potential η (4.25) mimics the Pauli repulsion of the lower shells. The off-center electrons approaching the central atom should feel the repulsion of the central valence electrons. It is therefore physically consistent to generate the tails from $\eta_{n+1}(r, \varepsilon)$. This results in the tails having $q_{n+1}(r, \varepsilon)$-character. In the desired

energy range $\varepsilon < \varepsilon_{n+1}$, the functions $q_{n+1}(r, \varepsilon)$ - and therefore the influence of the neighbors - vanish at the central atom (see Figure 4.2).

Our new formulation of the tail function however differs from the construction (4.10), which corresponds to a $\dot{q}_n(r, \varepsilon)$-character of the tails. As discussed in section (4.3.6), the energy of the atomic bound-state, ε_n, is special. For this energy, the potential $\tilde{\eta}_n(r, \varepsilon)$ (generating $\dot{q}_n(r, \varepsilon)$) corresponds to $\eta_{n+1}(r, \varepsilon)$ (which in turn is related to $q_{n+1}(r, \varepsilon)$). According to (4.35), the energy derivative $\dot{q}_n(r, \varepsilon_n)$ becomes equal to $q_{n+1}(r, \varepsilon_n)$. Our new construction therefore corresponds to a more general formulation, which includes the linear methods approach (4.10) as special case.

In the following, we will illustrate the procedure of generating atomic fragments, firstly neglecting the energy and angular momentum dependence of the potential η.

Suppose we want to determine the fragment orbital residing on atom A. Atom A therefore refers to the *central* atom. In the node-less representation, it is possible to achieve the required character of the tail in the off-site region Ω_B by application of the corresponding potential[3] η_{m+1}^B. In our example, we would need to add the potential η_{m+1}^B to the total crystal potential. The index B thereby indicates the origin of η_{m+1}.

In electronic structure calculations, it is common practice to apply the frozen core approximation (see section 2.7 for further details). The Pauli repulsion potential of the node-less representation allows to determine the valence wave function in frozen core approximation in a numerically efficient way. Application of the potential η_n at the central atom, with n corresponding to the valence, results in a node-less character of the fragment orbital in this region.

The general procedure to determine a valence fragment orbital therefore implies the following steps:

- Estimate the total potential (e.g. as superposition of atomic potentials)

- On the central atom add the corresponding Pauli repulsion potential for the valence η_n

- On all off-site atoms I, add the corresponding off-center potentials η_{m+1}^I

The resulting atomic fragment obeys $q_n(r, \varepsilon)$-character in the central region, and the corresponding $q_{m+1}(r, \varepsilon)$-character in all off-center regions. As a consequence, the crystal solution in a given atomic region Ω_A (in the following denoted by $f^{@\Omega_A}(r, \varepsilon)$) can be written in terms of the unperturbed atomic node-less solution u_n and energy dependent function q_{n+1} as follows:

$$f^{@\Omega_A}(r, \varepsilon) \;\; = \;\; u_n(r) + (\varepsilon - \varepsilon_n)q_{n+1}(r, \varepsilon). \tag{4.42}$$

This equation corresponds to equation (4.11) with $a = 1$ and $b = (\varepsilon - \varepsilon_n)$. Note however, that $f^{@\Omega_A}(r, \varepsilon)$ solves the unperturbed Schrödinger equation exactly, whereas $\phi^{@\Omega_A}$ solves the corresponding Schrödinger equation only to linear order.

---

[3] m corresponds to the valence state of the off-center orbital. It may be different from n, which refers to the valence of the central atom.

So far, the angular momentum dependence of the potential η has been neglected. The equation (4.25) holds for a specific angular momentum channel. Due to the non-sphericity of the crystals potential, the fragment orbitals in general have contributions from several angular momenta. We thus have to set up potentials which probe the angular momentum character of the wave function and then provide the correct radial potential:

$$\hat{\eta}_i(\varepsilon) \quad = \quad \sum_{lm} |Y_{lm}\rangle \eta_{i,lm}(\varepsilon) \langle Y_{lm}|$$

with i now referencing a certain atom. This is a so called nonlocal potential, which, in explicit form reads as follows:

$$\begin{aligned}
\eta_i(\varepsilon, \mathbf{r}, \mathbf{r}') &= \langle \mathbf{r}|\hat{\eta}_i(\varepsilon)|\mathbf{r}'\rangle \\
&= \sum_{lm} Y_{lm}(\widehat{\mathbf{r} - \mathbf{R}_i}) \left(\eta_{i,lm}(\varepsilon, |r|) \frac{\delta(|\mathbf{r}| - |\mathbf{r}'|)}{r^2} \right) Y_{lm}^*(\widehat{\mathbf{r}' - \mathbf{R}_i})
\end{aligned} \quad (4.43)$$

where $\widehat{\mathbf{r} - \mathbf{R}_i}$ denotes the direction of the vector $\mathbf{r} - \mathbf{R}_i$ and $\mathbf{R}_i$ corresponds to the i-th atomic position. The potential η is energy dependent and therefore needs to be redetermined in each step of a self-consistent cycle.

We finally define the embedding potential $v^{embed}(\varepsilon)$ for atom i as the potential which needs to be added to the selfconsistent potential of the crystal $(v^{ae,cry})$, in order to produce the appropriately shaped atomic fragment $|\chi_i\rangle$:

$$\left[-\frac{1}{2}\nabla^2 + v^{cry,ae} + v^{embed}(\varepsilon) - \varepsilon \right] |\chi_i\rangle \quad = \quad 0. \quad (4.44)$$

In the node-less representation, the embedding potential can be written as follows:

$$v^{embed}(\varepsilon, \mathbf{r}, \mathbf{r}') \quad := \quad \eta_i(\varepsilon, \mathbf{r}, \mathbf{r}') + \sum_{j \neq i} \eta_j^{off}(\varepsilon, \mathbf{r}, \mathbf{r}') \quad (4.45)$$

with the index off denoting the off-site valence repulsion potential η_{n+1}.

4.3.8 Linearized and localized embedding potentials

In principle, the fragment orbital approach in node-less formulation is more general than the linear approach discussed in section 4.3.2. The energy dependence of the repulsion potential η however is numerically cumbersome. We will therefore in the following make use of the linearized repulsion potentials derived in (4.26- 4.29). As can be seen from equation (4.42), the tail contribution to the crystal solution is explicitly energy dependent. A comparable degree of approximation can be achieved by taking the on-site potential to linear order and the off-site repulsion potential only to zero order into account.

The deformation process in the above construction implies the estimation of the self-consistent crystal potential $v^{ae,cry}$. Following the basic idea of the new method discussed in section 3.3, we split the crystal expression in contributions originating from the individual members of the crystal:

$$v^{cry,ae} = \sum_i v^{i,ae}$$

The total potential in the vicinity of the central atom is mainly dominated by the nearest neighbor contributions. The sum therefore may be limited to nearest neighbors.

The contributions of the neighbors could be estimated from self-consistent, atomic calculations. The atomic orbitals of isolated atoms and hence the resulting selfconsistent potential however are well extended. For usual crystal and molecular separations of the fragments, the potentials derived from isolated atoms therefore are inappropriate. We propose to derive the neighbors contributions from atoms confined in a spherical box. At the walls of the box, the potential rises to infinity. This ensures strict localization within the sphere. The radius of the box (r_t), which corresponds to a free parameter, will be chosen relative to the covalent radius of the chemical element. From a physical point of view, this approach meets the situation in crystals or molecules much better than the isolated atom. In addition, the above construction allows to estimate the energy $\bar{\varepsilon}$, at which the potentials will be expanded. We suppose the valence total energy to be dominated by bonding orbitals. This is, because the valence anti-bonding orbitals will in general be occupied to a much lesser extend. The expansion energy $\bar{\varepsilon}$ therefore should be close to the energy of the bonding valence orbitals. The bonding valence orbitals however are characterized by a zero spatial derivative of the wave function in the bonding region. We will therefore choose the energy, at which the derivative of the wave function at the walls of the box vanishes, as expansion energy $\bar{\varepsilon}$.

Following the approach illustrated in figure 4.1, the off-site valence repulsion potentials η^{off} shall induce the desired tail shape in the atomic region of the neighbors. It is important to determine these potentials from atoms confined in a box such, that they do not lap into the interstitial region. We therefore introduce a second free parameter r_p, which corresponds to the radius of the box used for the calculation of the repulsion potentials. The radius r_p will, just as r_t, be chosen relative to the covalent radius. The embedding potential contributions per chemical element can then be precalculated as setups. The setup for a chemical element thereby is fully determined by the radii r_t and r_p and will in the following be coded in the form $(\tilde{r}_p : \tilde{r}_t)$ with

$$\begin{aligned} r_p &= \tilde{r}_p \times r_{covalent}. \\ r_t &= \tilde{r}_t \times r_{covalent} \end{aligned} \tag{4.46}$$

The central potential contribution to the embedding potential finally will be de-

termined self-consistently during the deformation process. In this way, no artificial localization is applied to the deformed fragment density which is used as trial density for the energy functional. Hence, the localization of the trial density is only due to the repulsion of the neighbors and therefore reflects the symmetry of the crystal. This is different from the spherically localized frozen atomic fragment approach usually applied by other groups. In part III, the difference of the approaches and the results will be discuss in more detail.

Part III

First applications

5 Introduction

5.1 The H_2 reference system

In the preceding sections, a new approach to non self-consistent electronic structure calculations has been introduced. It basically consists of two main aspects: a new formulation of a non self-consistent energy functional and an ab initio construction of non-spherical input densities for such functionals. As discussed in section 2.4.4, atomic densities, so called *frozen atomic fragments*, as well as spherically localized atomic densities have been successfully applied in connection with non-selfconsistent functionals for certain systems classes, such as weakly interacting fragments [25, 29]. They however fail for more sophisticated systems such as defect structures, surfaces and vacancies [30, 31, 32]. In order to point out the reasons for these limitations, I will, first of all, discuss some results obtained from the new non self-consistent functional when applied to spherical input densities for the hydrogen dimer. This molecule has been chosen for several reasons. The most important lies in the nature of the node-less wave functions. Per construction, in the nodeless picture, the first member per angular momentum channel (e.g. 1s, 2p, 3d,...) corresponds to the atomic wave function. The embedding potentials and obtained non-spherical densities can therefore be compared to usual potentials and densities without an additional transformation (see section 4.3 for further details).

Furthermore, the H_2 molecule does not possess any core electrons which, in our formulation, would imply the application of onsite Pauli repulsion potentials. From a physical point of view, the offsite repulsion potentials are of much more interest. They give rise to the non-sphericity of the fragment densities. Following a divide and conquer approach, it is therefore reasonable to initially concentrate on the valence repulsion only.

5.2 Approximations

In order to make a first attempt towards non-spherical input densities, we apply several additional approximations in all calculations presented in this work. Unless otherwise stated, the following approximations are understood:

1. The linearized and localized formulation of the repulsion potentials discussed in section 4.3.8 is applied. For some calculations we however determine the repulsion potentials at the energy of the crystal state. It therefore corresponds to the exact repulsion potential.

2. A local form of the repulsion potentials is used. As shown in equation (4.43), the repulsion potentials have contributions from several angular momenta and therefore are non local. As a first approximation, we either keep only the spherical part or the spherical average of the repulsion potential. The central atom therefore gets deformed by spherical neighbors. We suppose the relative position and deformational strength of the neighbors to be the most dominating effects. The deformed fragment densities obtained from spherical offcenter deformation potentials therefore should provide an appropriate approximation of the crystal density.

3. The total potential for the deformation process is estimated by a superposition of individual fragment contributions (see the discussion in section 4.3.8 for more details). As a consequence, the nonlinear contribution to the exchange and correlation potential, which is due to overlap of the neighboring and onsite density, is missing ($\mu_{xc}[\sum_i n_i] \neq \sum_i \mu_{xc}[n_i]$). For overlapping densities, this contribution is of repulsive character. Its maximum is located in the bonding region. The deformed fragment densities therefore might be overestimated in the interstitial region. This effect however partly cancels with the approximation discussed next.
The difference between superimposed exchange and correlation potentials and potentials of superimposed densities is illustrated in figure 7.5.

4. The interference contribution of the fragment wave functions to the total density is not taken into account. In order to illustrate this, I will once again pick up the model system shown in figure 4.1. Let the deformed wave functions (including head and tail) of atom A and B be χ_A and χ_B, respectively. The total density approximated by a superposition of the fragment contributions consequently would correspond to $(\chi_A + \chi_B)^2/C$, with C corresponding to a normalization factor[1]. In our formulation, we however superimpose the fragment densities. This corresponds to the density $\chi_A^2 + \chi_B^2$ and therefore misses the interference contribution $2\chi_A\chi_B$. The effect of the interference contribution will be discussed in the following sections for both, spherical atomic fragments and deformed densities. Neglecting the interference contribution shifts density from the interstitial to the atomic region. This approximation therefore partly cancels with the previous one, concerning the exchange and correlation potential.

5. The Perdew Zunger parametrization [81] of the local density approximation is used.

6. Spinpolarization is not explicitly taken into account. For the binding energy studies, a spinpolarization correction to the total energy of the isolated fragments is applied. This correction is obtained from fully converged PAW cal-

---

[1]$C = \frac{1}{2}\int (\chi_A(\mathbf{r}) + \chi_B(\mathbf{r}))^2 d^3r$ for χ_A and χ_B being normalized.

culations for non- and spinpolarized systems (see section 5.4 for computational details of the PAW calculations).

It should be noted that the approximations 1-4 discussed above only affect the quality of the input density. Apart from numerical errors, no further approximations to the non self-consistent functional (3.8) are applied.

5.3 Computational Details

5.3.1 Preface

The aim of this part of the thesis is to allow an evaluation of the theoretical basis of the new approach. In this context, numerical convergence and reproducibility of results is much more important than numerical efficiency. The implementation and level of convergence applied in the following - with errors usually below 1 mH - therefore certainly might not be the first choice for all day work applications, but ensures as much comparability of individual contributions as possible. Details concerning other possible numerical implementations of the new approach, discussion of the corresponding subtleties and convergence studies can be found in part IV.

5.3.2 Grid representations

The deformation potential calculation and the deformation itself are carried out on logarithmic, atom-centered, radial grids with 1000 support points in the range $1.056 \cdot 10^{-4} \leq r \leq 26.96\, a.u.$. The offcenter deformation potentials are re-expanded at the central site, using the spherical harmonics re-expansion algorithm discussed in section 8.2. Unless otherwise stated, the expansion of the deformed fragment density is truncated at $l = 3$. The truncation for all other expressions are chosen such, that the selection rules for the products of spherical harmonics are fulfilled (in the present case, the potential e.g. needs to be expanded up to $l = 6$). We found that noncompliance of the selection rules strongly affects the numerical convergence. This is discussed in more detail in section 8.4.

After deformation, Poisson's equation for the deformed density is solved on the radial grid. The resulting potential as well as the fragment densities are then transformed to a cylinder grid representation. We exploit here the cylinder symmetry of the dimer molecules. The z-axis of the grid is aligned parallel to the molecule-axis at $r = 0$. We keep the data on a representative two-dimensional plane with the side length $l_r = \frac{1}{2}l_z$ and $n_r = \frac{1}{2}n_z$ equispaced support points. Typical values are $l_z = 30\, a.u.$ and $n_z = 2000$. The first grid point in r resides at $r_1 = \frac{1}{2}d_r$, with $d_r = \frac{l_r}{n_r}$. For intermediate values, a third order polynomial interpolation is applied. The interpolation is based on the function and the numerical first and second derivative values of two adjacent support points.

The cylinder grid allows to evaluate the exchange and correlation energy and potential point by point in 3D space and therefore results in accurate results for densities of arbitrary symmetry. In the context of the new functional we found this approach superior to the common approach with the densities held as spherical expansions (see section 9 for a detailed discussion).

5.3.3 Tight-binding approximation, potential of exchange and correlation

In line two of equation (3.8), we subtract the sum of one particle energies of the deformed ions from the crystal's sum. This is solved in a tight-binding approach. The deformed ions contributions (part two of line 2) then corresponds to the diagonal sum of the tight-binding Hamiltonian. For all calculations presented in this part of the work, we use an extended basis set. The combination of the deformed orbitals with three spherical basis-functions of the form $e^{-\lambda r}$ ($\lambda = 1.0$, 1.5 and 2.0), one $2p_z$ function has been found to be sufficient (see section 10.1 for further details).

Unlike in the deformation process, the exchange and correlation potential contribution to the total potential $v[\sum_i \bar{n}_i]$ cannnot be approximated by a superposition of atomic contributions of the form $\sum_i V_{xc}[n_i]$. Figure 10.1 shows the resulting binding energy for deformed atomic fragments, once applying the exact potential $V_{xc}[\sum_i n_i]$ (dashed black line) and once the approximate potential $\sum_i V_{xc}[n_i]$ (grey line) in the tight-binding calculation. At the lda equilibrium separation of H_2 ($1.41\,a.u.$), the error introduced in the tight-binding energy (3.10) by the approximation of the exchange and correlation potential has been found to be in the range of $415\,mH$, which corresponds to $225\,\%$ of the binding energy ($E_{bond} \approx 185\,mH$). Due to the afforded error cancellation in line two of (3.8), the effective deviation is reduced to about $21\,\%$ of the binding energy ($\sim 38\,mH$), which however is still far too large.

The reason for the success of the approximation in the context of deformation (section 5.2, item three) and the failure in the tight-binding calculation is the following: in the deformation process, the approximation of the exchange and correlation potential affects the trial density. For the trial density however, a variational principle holds. This is not the case for the potential of the tight-binding calculation. As can be seen from equation (2.38), errors in the potential linearly enter the total energy.

5.3.4 Grid transformations, density splitting and interference contribution

In order to evaluate the effect of the interference contribution discussed in section 5.2, calculations for the total density including the interference term have been carried out. This implies the solution of Poisson's equation for the interference density, which can not easily be converged on the standard cylinder grid. The interference density therefore has been transformed to a spherical expansion centered at the mid of the bond as outlined below. Poisson's equation can then be solved on the radial

logarithmic grid just as for the atomic contributions.

In a first step, the data-points are transformed from the cylinder grid onto an equispaced 3d grid, which then is Fourier-transformed into G-space. The side length of the 3d box thereby is chosen such, that the artificial periodic image contributions in G-space can be neglected ($30\,a.u.$ have been found to be sufficient). The separation of support points in 3d and G are determined by a plane wave cutoff energy. A cutoff of $200\,Ry$ usually leads to converged results. In order to center the expansion at the origin, the corresponding structure factor is applied in G-space. Applying an inverse spherical Bessel-transformation on a per plane wave basis then allows to determine the corresponding spherical harmonics expansion (for a detailed derivation see section B.3.3).

The tight-binding calculation for the self-consistent PAW density of the H_2 dimer shown in figure 6.1 follows a similar approach. The PAW density is imported on a 3d grid. It is then splitted in two symmetric atomic contributions which add up to the total density. This is achieved by application of a fading proportional to cos^2 along the bond axis in the direction of the neighbor[2]. The tight-binding potential can then be determined in the way discussed above.

In order to determine the selfconsistent density for the hydrogen dimer in the representation of the new method, the tight-binding term has been solved selfconsistently, applying a potential mixing. The output density, written in terms of the occupied output wave function, can be splitted in atom-centered and interference contributions. This allows to determine the output potential following the above approach.

5.4 PAW reference calculations

Selfconsistent reference calculations are performed based on the projector augmented wave (PAW) method [82, 83]. The PAW method is a frozen-core all-electron method. Like other plane-wave based methods, the PAW method leads to the occurrence of artificial periodic images of the structures. This effect was avoided by explicit subtraction of the electrostatic interaction between them [84]. Wave function overlap was avoided by choosing the unit cell large enough to keep a distance of more than 6 between atoms belonging to different periodic images. We used a plane wave cutoff of $50\,Ry$ for the auxiliary wave functions of the PAW method. The following sets of projector functions were employed, N 2s2p, H 2s, which provides the number of projector functions per angular momentum magnetic quantum number m in each main angular momentum channel l.

---

[2]Let the dimer be aligned parallel to the z-axis, with z_1 and z_2 being the z-position of atom one and two, respectively (we suppose $z_2 > z_1$). The fading function f_1 for atom one is then given as

$$f_1(x,y,z) = \begin{cases} 1 & for & z \leq z_1 \\ cos^2\phi & for & z_1 < z \leq z_2 \\ 0 & for & z > z_2 \end{cases} \text{, with } \phi = \frac{\pi(z-z_1)}{2(z_2-z_1)}.$$ The fragment density for atom one can then be determined by multiplication of the total density by f_1 on the 3d grid.

	E_{tot}(H)	E_{tot}(eV)
H nonspinpolarized	-0.445	-12.11
H spinpolarized	-0.478	-13.01
spinpolarization correction per H_2	-0.066	-1.79

Table 5.1: The total energy for the spin- and nonspinpolarized hydrogen atom, as well as the spinpolarization correction used in the following calculations obtained from self-consistent PAW calculations.

Atomic structures were optimized by damped Car-Parrinello [46] molecular dynamics. We used a time-step of 10 a.u. (2.5 fs) for all calculations. The convergence was tested by monitoring if the total energy change remains below $10^{-5} H$ during a simulation of 500 time steps. During the simulation for the convergence test, no friction was applied to the atomic motion and the friction on the wave function dynamics was chosen sufficiently low to avoid a noticeable effect on the atomic motion.

The total energy for the spin- and non-spinpolarized hydrogen atom, as well as the spinpolarization correction used in the following are listed in table 5.1.

6 Spherical atomic fragments

6.1 Selfconsistent reference calculations

In order to determine the selfconsistent density for the hydrogen dimer at the lda equilibrium spacing (1.45 a.u.) in the representation of the new method, the tight-binding term has been solved self-consistently, applying a potential mixing. The output density, written in terms of the occupied output wave function, can be splitted in atom-centered and interference contributions. This allows to determine the output potential following the approach discussed in section 5.3.4. The deformed orbital basis functions have been replaced by the output molecular wave functions in each step of the selfconsistent iteration. Figure 6.1 compares the resulting selfconsistent density (full line) to the PAW selfconsistent density (dashed). The dash dotted line corresponds to the output density obtained using the self-consistent PAW density as input density in a tight-binding cycle. The numerical implementations of both methods follow a completely different approach. The applied approximations, namely the limited number of real-space grid points in the tight-binding and the limited number of plane waves in the PAW calculation, lead to small differences in the selfconsistent density.

Table 6.1 provides the energy contributions to the self-consistent total energy for both calculations. The energy terms of the SESM representation correspond to the crystal contribution (3.6) of the new functional (3.8).

	PAW (H)	SESM (H)	Difference (mH)
E_{kin}	1.0740	1.0817	7.7
E_{coul}	-1.5656	-1.5780	-12.4
E_{xc}	-0.6445	-0.6442	0.3
E_{tot}	-1.1360	-1.1406	-4.6

Table 6.1: The energy contributions to the selfconsistent total energy determined from a PAW and a selfconsistent SESM calculation. The provided energy terms of the SESM representation correspond to the crystal contribution (3.6) of the new functional (3.8).

The energy differences are in accordance with the different shape of the selfconsistent densities: compared to PAW, in the SESM representation density is shifted from the bonding into the atomic region. This, on the one hand, is electrostatically favorable but leads to an increased kinetic energy due to the higher curvature of the wave function in the bonding region.
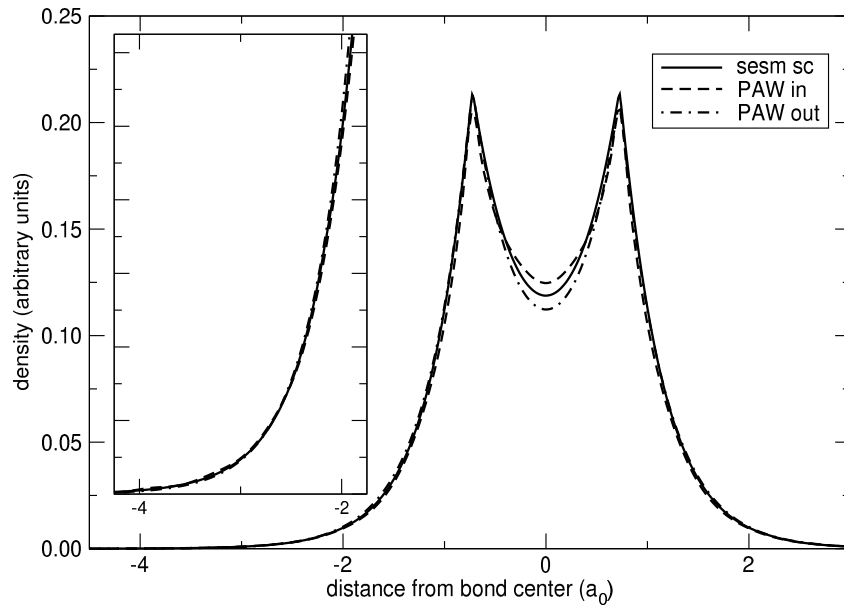
Figure 6.1: The PAW selfconsistent density (dashed) and the resulting output density (dash dotted) compared to the selfconsistent SESM density (full line) along the molecular axis for a hydrogen dimer at the lda equilibrium spacing (1.45 a.u.). The input and output densities correspond to the trial density $\bar{n}$ defined in (3.4) and the density n', defined in (2.25), respectively. All densities integrate to the same number of electrons. The ordinate of the inset is scaled by a factor of 20.

	Energy (H)
E_{tb}	-0.7455
E_{diag}^{inter}	-0.4456
$E_{tb} - E_{diag}$	-0.2999
E_{coup}	0.0418
ΔE_{xc}	-0.0653

Table 6.2: The energy contributions (3.12-3.14) to the selfconsistent SESM energy ΔE (3.8).

Table 6.1 lists the SESM functional energies (3.12-3.14) obtained for the selfconsistent density. These will be plotted in the following figures for comparison with the energies obtained from deformed fragments. It should however be noted, that the values do not correspond to a reference (such as e.g. the self-consistent total energy). This is, because the energies listed in table are relative to the deformed ion, which however is not unique.

The output and hence the selfconsistent wave functions in our implementation is given in terms of superimposed, atom-centered contributions. The selfconsistent density therefore needs to include interference contributions. For the selfconsistent as well as for all other calculations including interference contributions, equation (3.4), $\bar{n} = \sum_i \bar{n}_i$, is not fulfilled. As a consequence,

$$\int \bar{n}(\mathbf{r})v([\bar{n}],\mathbf{r})d^3r \quad \neq \quad \sum_{i,n} f_{i,n}^{ion}\langle\psi_{i,n}^{ion}|v[\sum_i \bar{n}_i(\mathbf{r})]|\psi_{i,n}^{ion}\rangle.$$

The energy contribution E_{diag} defined in (3.11) therefore needs to be replaced by:

$$E_{diag}^{inter} \quad := \quad \sum_{i,n} f_{i,n}^{ion}\langle\psi_{i,n}^{ion}| - \frac{1}{2}\nabla^2|\psi_{i,n}^{ion}\rangle + \int \bar{n}(\mathbf{r})v([\bar{n}],\mathbf{r})d^3r. \qquad (6.1)$$

Let me stress another subtle point. The deformed ion reference is not unique. The actual shape is arbitrary, except that it needs to result in the correct crystal density. The individual SESM energy contributions for two different reference systems therefore may be different. Because a unique reference does not exist, neither of them is more or less exact. The only reference energies which can be used to estimate the quality of a trial density are the crystal energy contributions listed in table 6.1 and the SESM total energy ΔE.

The results shown in table 6.1 correspond to a selfconsistent calculation which does not follow the two step deformation/clustering approach. The deformed ion reference therefore is not self-similar to the deformed ions discussed in the following. The energies therefore may differ.

6.2 Frozen atomic fragments

Figure 6.2 shows the binding energy of the H_2 dimer as a function of inter-atomic spacing. The full line corresponds to the selfconsistent PAW reference. The dashed line shows the results for the frozen atomic fragment density (FAF) approach determined in the representation of the new method. The single data points correspond to frozen atomic fragment results published by Kobayashi et. al. [85], Averill and Painter [34] and Foulkes and Haydock [27]. The ground state binding energy (-5.61 eV) and bond length (1.31 a.u.) obtained by the new method are in good agreement with the results of Kobayashi et. al. (the deviation in binding energy is below 4 mH, the bond lengths agree exactly). Averill and Painter unfortunately did not provide the binding energy of the FAF ground state, but fixed the bond length to the selfconsistent value (1.45 a.u.). The binding energy is however close to our finding for this inter-atomic spacing (the deviation is about 3 mH). Foulkes and Haydocks ground state results obviously deviate in both, binding energy and bond length. They follow a tight-binding approach with a basis consisting of just two s functions on each hydrogen atom. Convergence tests with respect to the basis set showed, that, at least in our implementation, convergence can only be achieved adding three extra s and one p_z function per atom to the FAF orbital. Reducing the number of basis functions, the ground state binding energy and length shift towards Foulkes results, which we therefore regard as unconverged.

Figure 6.3 compares the frozen atomic fragment input (dashed) and corresponding output density (dash dotted) to the selfconsistent density (full line) along the molecular axis for a hydrogen dimer at the lda equilibrium spacing (1.45 a.u.). The input and output densities correspond to the trial density $\bar{n}$ defined in (3.4) and the density n', defined in (2.25), respectively. All densities integrate to the same number of electrons. The ordinate of the inset is scaled by a factor of 20.The FAF trial density significantly deviates from the selfconsistent one. It underestimates the density in the molecular, and overestimates it in the outer region. Generally, the crystal potential overcompensates the kinetic energy costs of localization. This is, because the electrons feel the attraction of both nuclei. From an energetic point of view, it is therefore favorable to shift electronic density closer to the molecule. In the isolated atom with only one nucleus, the driving force for localization is much smaller. Hence, a superposition of atomic densities is no adequate estimate of the crystal density. An artificial localization can be introduced by a spherical localization of the atomic density. This will be discussed in the following section.

6.3 Spherically localized FAF

As discussed in the previous section, a superposition of frozen atomic densities is not a good estimate of the crystal density. The missing localization can however artificially be introduced, applying a localization potential to the isolated atom potential. All
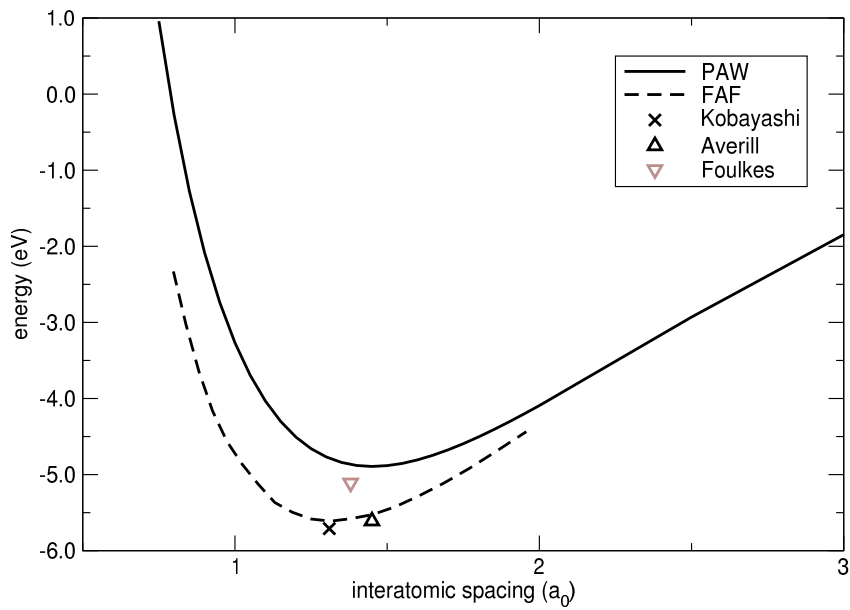
Figure 6.2: Binding energy of the H_2 dimer as a function of inter-atomic spacing. The full line corresponds to the selfconsistent reference. The dashed line shows the results for the frozen atomic fragment density approach determined in the representation of the new method. The single data points correspond to published results of other groups for frozen atomic fragments. Foulkes results (grey triangle) seem to be unconverged. For details see the text.
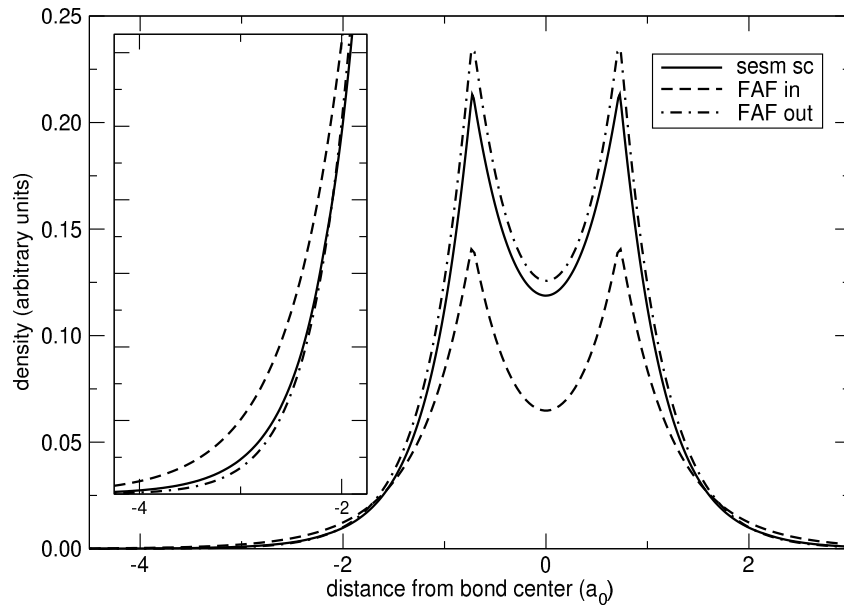
Figure 6.3: The frozen atomic fragment input (dashed) and output density (dash dotted) compared to the selfconsistent density (full line) along the molecular axis for a hydrogen dimer at the lda equilibrium spacing (1.45 a.u.). The input and output densities correspond to the trial density $\bar{n}$ defined in (3.4) and the density n', defined in (2.25), respectively. All densities integrate to the same number of electrons. The ordinate of the inset is scaled by a factor of 20.

flavors of localization potentials, from harmonic to exponential shape, have been used in the past decades. See section 2.4.4 and 2.5 for further details.

Figure 6.4 shows the binding energy of H_2 for spherically localized atomic fragments at the lda equilibrium spacing (1.45 a.u.), using an additional exponential potential of the form:

$$V^{loc}(|\mathbf{r}|) \quad = \quad \min\left(V_{max} \cdot e^{-\frac{r_c}{|\mathbf{r}|}+1}, V_{max}\right).$$

V_{max} has been fixed to a value of 1000, the cutoff radius r_c, at which $V^{loc} = V_{max}$ served as free parameter. The dashed and dash dotted line correspond to trial densities composed from superimposed localized atomic fragments excluding and including the interference contribution, respectively.

In common implementations, the interference contribution is not taken into account, because it is numerically demanding and, in general, does not lead to better results. This will become clear in the following analysis. Excluding the interference contribution, the lda ground state binding energy (full line) is achieved for $r_c = 2.10$ a.u. and 3.69 a.u.. Taking it into account, best results are obtained for $r_c = 2.09$ a.u. and 4.65 a.u..

Table 6.3 references the corresponding trial densities to abbreviations used in the following. It includes an additional density (F-2) for which E_{tb}, which corresponds to the eigenvalue of the occupied molecular orbital, is equal to the selfconsistent value.

	r_c (a.u.)	Trial density referenced as
no interference contribution	2.10	(F-1)
	3.28	(F-2)
	3.69	(F-3)
including interference contribution	2.09	(F-4)
	4.65	(F-5)

Table 6.3: List of trial density identification code used in the this section. For details see the text.

Figure 6.5 shows the crystal total energy contributions over cutoff radius for H_2 at the lda equilibrium spacing (1.45 a.u.). No interference has been taken into account. The horizontal lines mark the self-consistent reference values given in table 6.1. The vertical lines denote the densities (F-1) - (F-3). The corresponding in- and output densities are given in figure 6.6. Although the correct binding energy is achieved for the trial densities (F-1) and (F-3) (see figure 6.4 for details), the individual crystal energy contributions deviate from the selfconsistent values. The cutoff radii, for which the non- and selfconsistent energy contributions coincide are close (E_{kin} : 3.10 , E_{coul} : 3.04, E_{xc} : 3.30) but not the same. From this follows, that it is impossible to represent the selfconsistent crystal density in spherically localized atomic fragments. Only for $r_c = 2.10$ (F-1) and 3.69 a.u. (F-3), the individual errors - although quite
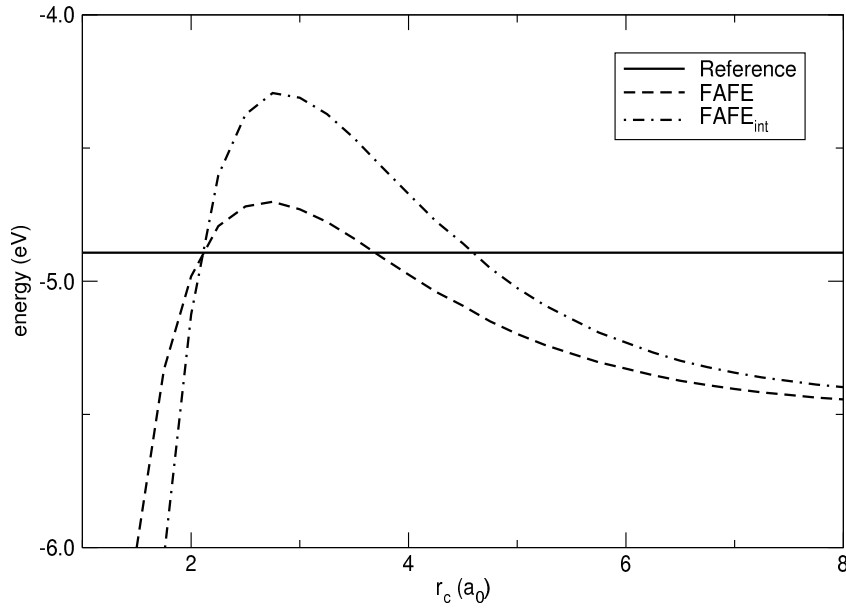
Figure 6.4: The binding energy of H_2 for spherically localized atomic fragments at the lda equilibrium spacing (1.45 a.u.), using an additional exponential potential of the form $V^{loc}(|\mathbf{r}|) = \min\left(V_{max}e^{-\frac{r_c}{|\mathbf{r}|}+1}, V_{max}\right)$. V_{max} has been fixed to a value of 1000, the cutoff radius r_c, at which $V^{loc} = V_{max}$ served as free parameter. The dashed and dash dotted line correspond to trial densities composed from superimposed localized atomic fragments excluding and including the interference contribution, respectively. The lda ground state binding energy (full line) is achieved for $r_c = 2.10$ a.u. and 3.69 a.u. (no interference contribution) and $r_c = 2.09$ a.u. and 4.65 a.u. (including the interference contribution). Table 6.3 references the corresponding trial densities to the abbreviations used in the text.
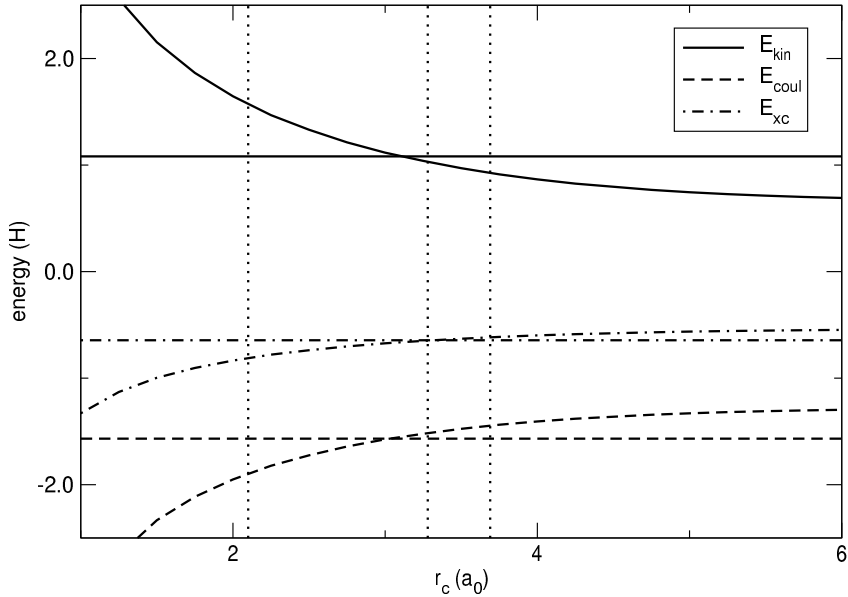
Figure 6.5: The crystal total energy contributions over cutoff radius for H_2 at the lda equilibrium spacing (1.45 a.u.). No interference has been taken into account. The horizontal lines mark the self-consistent reference values given in table 6.1. The vertical lines denote the densities (F-1) - (F-3) (from left to right). The corresponding in and output densities are given in figure 6.6. Although the correct binding energy is achieved for the trial densities (F-1) and (F-3) (see figure 6.4 for details), the individual crystal energy contributions deviate from the selfconsistent values. The cutoff radii, for which the non- and selfconsistent energy contributions coincide are close (E_{kin} : 3.10 , E_{coul} : 3.04, E_{xc} : 3.30) but not the same. From this follows, that it is impossible to represent the selfconsistent crystal density in spherically localized atomic fragments.

large - cancel exactly. The corresponding densities (dashed and dash dotted line in figure (6.6) are not even close to the selfconsistent one. This reflects the stationarity of the total energy functional.

Figure 6.7 compares the SESM functional energies (3.12-3.14) over cutoff radius r_c to the selfconsistent values listed in table 6.1. As discussed above, the differences are due to the different deformation strategies used in generation of the input density. This most significantly can be seen for the coupling energy (double dash dotted lines), which do not even cross.

For trial densities including the interference contribution, one intuitively would expect better results. This is, because the trial densities excluding interference (shown in figure 6.6) generally underestimate the density in the bond region with respect to the atomic region. The interference term mainly contributes to the bond region. Taking it into account therefore corresponds to shifting density from the atomic into the
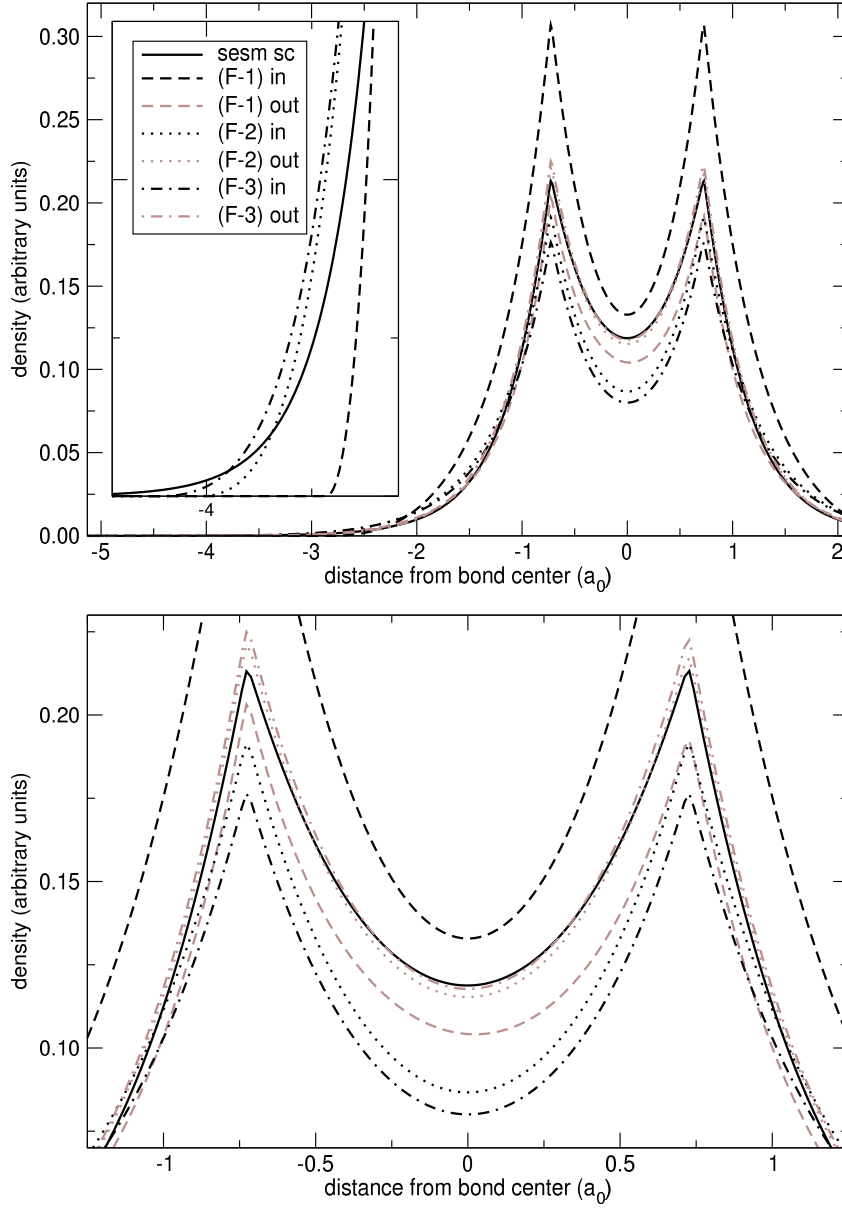
Figure 6.6: The spherically localized frozen atomic fragment input (black) and output densities (grey) (mnemonics defined in table 6.3) compared to the selfconsistent density (full line) along the molecular axis for a hydrogen dimer at the lda equilibrium spacing (1.45 a.u.). All densities integrate to the same number of electrons. The ordinate of the inset in the upper panel is scaled by a factor of 100. It can be seen that no trial density composed from atomic fragments can accurately represent the selfconsistent density in the bond and atomic region at the same time. Even the decay for larger separation from the bond center is qualitatively wrong. The latter is the reason for the failure of this approach e.g. for defect structures. See the text for further details.
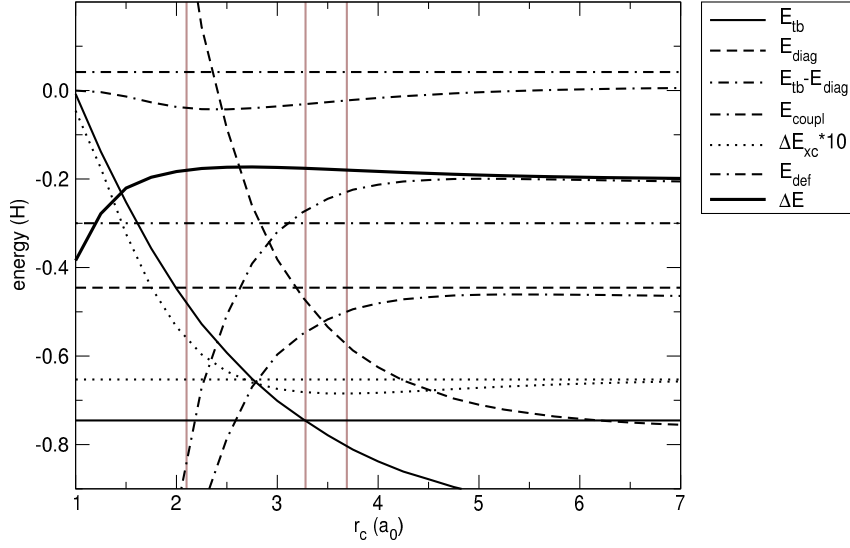
Figure 6.7: The SESM functional energies (3.9-3.14) over cutoff radius r_c compared to the selfconsistent values (horizontal lines) listed in table 6.1 for H_2 at the lda equilibrium spacing (1.45 a.u.). No interference has been taken into account. The vertical lines denote the densities (F-1) - (F-3) (from left to right).

bond region[1]. For spherically localized atomic fragments, this effect however is much stronger than for the selfconsistent crystal and the densities including interference therefore overestimate the density in the bond region. This is illustrated in figure 6.8.

Figure 6.9 compares the binding energy of the H_2 dimer as a function of inter atomic spacing for the spherically localized atomic densities (F-1) - (F-3) defined in table 6.3 to the selfconsistent PAW result. The binding energy converges to the spinpolarization correction (1.79 eV), discussed in the context of table 5.1. For the cases (F-1) and (F-3), the cutoff radius r_c and hence the atomic densities have been fitted such, that the correct binding energy is achieved at the lda ground state separation (1.45 a.u.). Although the errors in binding energy are small for a wide range of inter-atomic separations, the plots emphasize a general drawback of this approach: once r_c is chosen, the shape of each atomic fragment is held fixed for all inter-atomic separations. A set of fixed atomic fragments can however not represent the crystal density for arbitrary bond lengths. This is most obvious for large inter-atomic separations: the spherically localized atomic densities deviate strongly from the free atom densities. For regions not dominated by the bond, this mismatch however is present, independent from the actual fragment separation. This can be seen in the insets of figure 6.6 and 6.8. The decay of the trial density on the opposite side of the bond corresponds to the decay of the spherically localized atom, whereas the selfconsistent density corresponds

---

[1]Due to norm conservation $(\int \chi_A^2 + \chi_B^2 d^3r = \int \chi_A^2 + 2\chi_A\chi_B + \chi_B^2 d^3r = N)$, the density in the atomic region is scaled down for included interference contribution $(2\chi_A\chi_B)$.
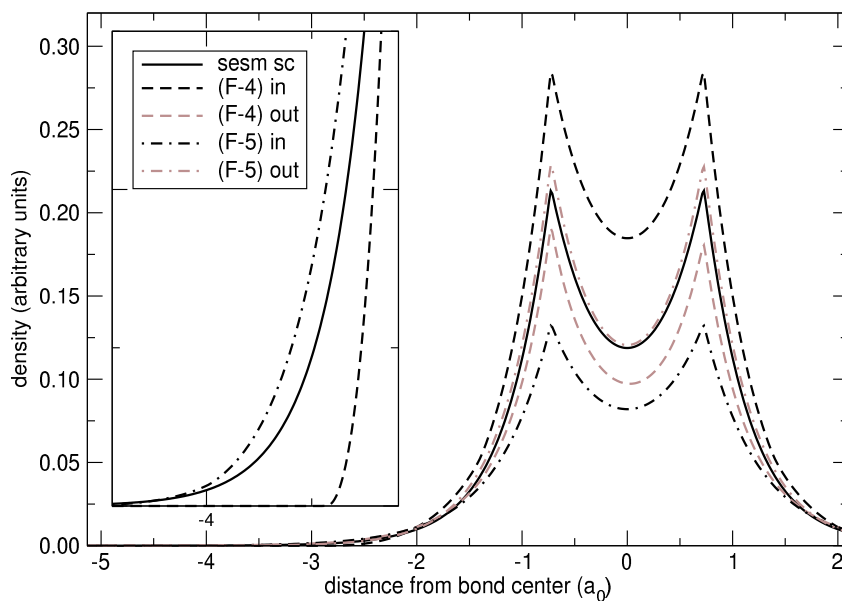
Figure 6.8: The spherically localized frozen atomic fragment input (black) and output densities (grey) including the interference contribution (mnemonics defined in table 6.3) compared to the selfconsistent density (full line) along the molecular axis for a hydrogen dimer at the lda equilibrium spacing (1.45 a.u.). All densities integrate to the same number of electrons. The ordinate of the inset in the upper panel is scaled by a factor of 100. See the text for further details.

to the free atom's density. This is the reason for the failure of the atomic fragment approach for more complex systems such as defect structures and surfaces.

Our new approach, discussed in the following section, allows to determine non-spherically deformed fragments reflecting the crystal structure and therefore overcomes these problems.
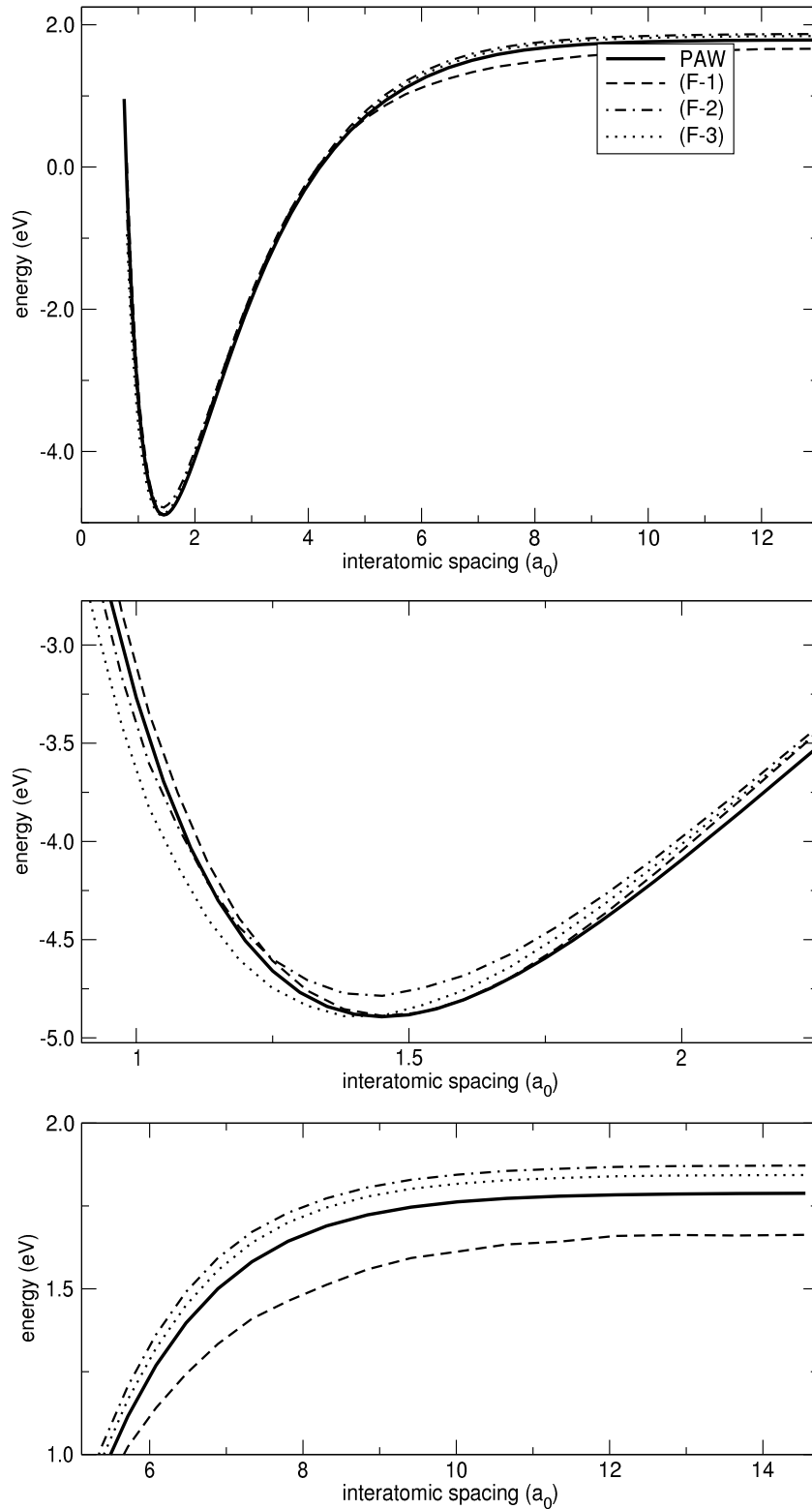
Figure 6.9: Binding energy of the H_2 dimer as a function of inter-atomic spacing for spherically localized atomic densities, defined in table 6.3. The full line corresponds to the selfconsistent PAW reference. The selfconsistent binding energy converges to the spinpolarization correction (1.79 eV), discussed in the context of table 5.1. See the text for further details.

7 Non-spherical deformed atomic fragments

7.1 Deformed atomic density and binding energy

The embedding potentials introduced in section 4.3 allow to determine non-spherically deformed atomic fragments, which reflect the crystal structure and therefore overcome the limitations of frozen atomic fragments. The contribution per chemical element to the embedding potential thereby is fully characterized by the radii r_t and r_p defined in subsection 4.3.7. In the following, we refer to individual setups in the form $(\tilde{r}_p : \tilde{r}_t)$ (see equation 4.46 and the corresponding text for further details).

Figure 7.1, 7.2 and 7.3 compare the binding energy of the H_2 dimer as a function of inter-atomic spacing for trial densities obtained from different embedding potentials, to the self-consistent result (full line). For large inter-atomic spacing, the bond energies for all trial densities (except the FAF calculation (F-1)) converge to the spin-polarization correction (1.79 eV), discussed in the context of table 5.1. Keeping r_p fixed to $\frac{1}{8}r_{covalent}$, best results are obtained for $r_t = 3$. A further increasing of r_t has only a little effect (upper panel of figure 7.2). The results for $r_t = 5$ (not plotted) in fact are equal to those obtained for $r_t = 4$.

Confining the repulsion potential in a box with $r_p = \frac{1}{4}r_{covalent}$ (lower panel of figure 7.2), the binding energy for $r_t = 4$ comes closest to the self-consistent result. Comparing the upper and lower panel of figure 7.2, one finds that for $r_p = \frac{1}{8}$, the exact result can be reproduced much better than for $\frac{1}{4}$. The curves for the latter seem to be somewhat tilted to the left. Choosing $r_p = \frac{1}{4}$ and r_t such, that the binding energy at the lda equilibrium spacing (1.45 a.u.) would corresponds to the correct value (which is almost exactly obtained from (1/8:3)), the binding energy would be overestimated for inter-atomic separations smaller than 1.45 a.u.. This effect is due to the repulsion potential reaching further in the bonding region. As shown in figure 7.3, the effect gets stronger for increased r_p.

The setup (1/8:3) leads to an accuracy which is achieved by the best frozen atomic fragment calculation (F-1) only near the inter-atomic spacing, for which it has been optimized.

Figure 7.4 compares the trial densities obtained for different setups to the self-consistent density (full line) along the molecular axis for a hydrogen dimer at the lda equilibrium spacing (1.45 a.u.). All densities integrate to the same number of electrons. The ordinate of the inset in the upper panel is scaled by a factor of 100. Following the sequence $r_t = 2$ to $r_t = 4$ for $r_p = \frac{1}{8}$ (black) and $r_p = \frac{1}{4}$ (grey), it is
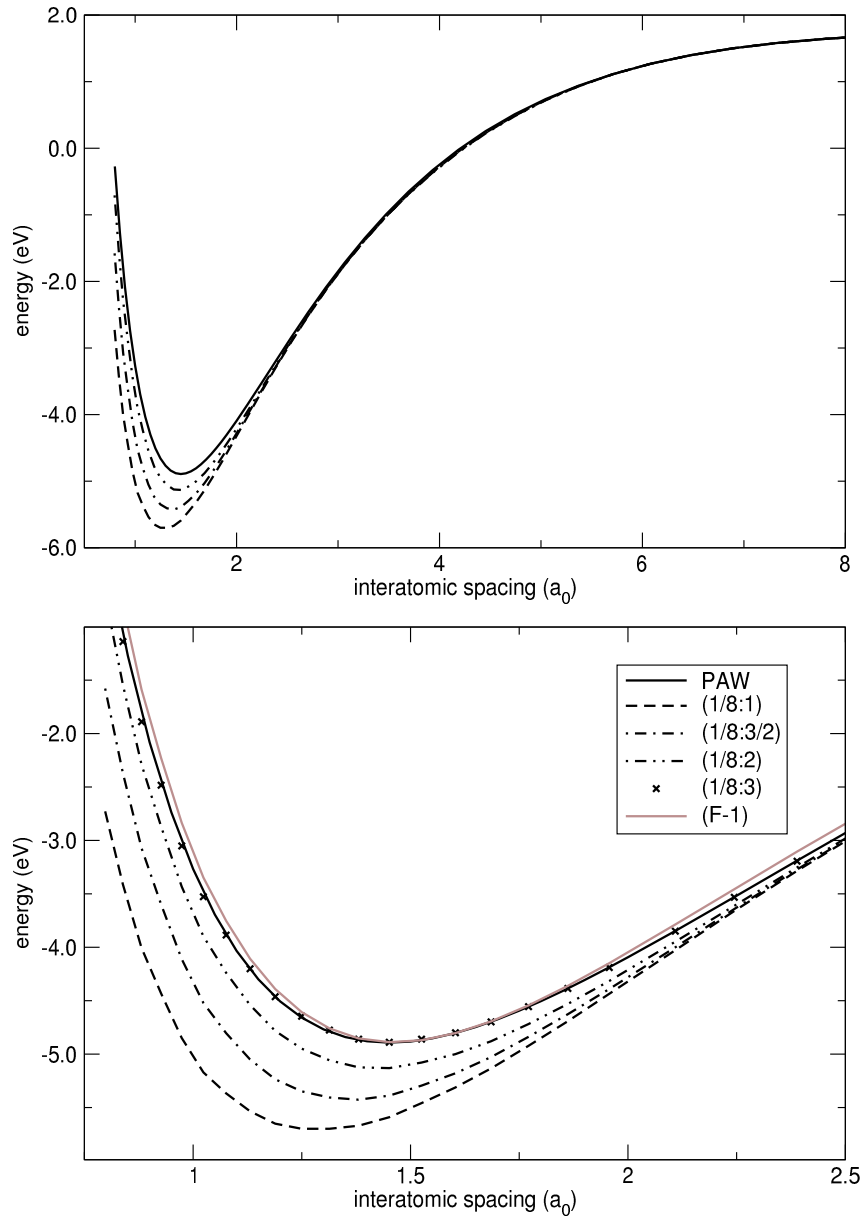
Figure 7.1: Binding energy of the H_2 dimer as a function of inter-atomic spacing for trial densities obtained from different embedding potentials, compared to the self-consistent result (full line). For large inter-atomic spacing, the bond energies for all trial densities (except the FAF calculation (F-1)) converge to the spinpolarization correction (1.79 eV), discussed in the context of table 5.1. The FAF density has been defined in table 6.3. The setups for the nonspherical deformation are coded in the form $(\tilde{r}_p : \tilde{r}_t)$ (see equation 4.46 and the corresponding text for further details). See the text for a discussion.
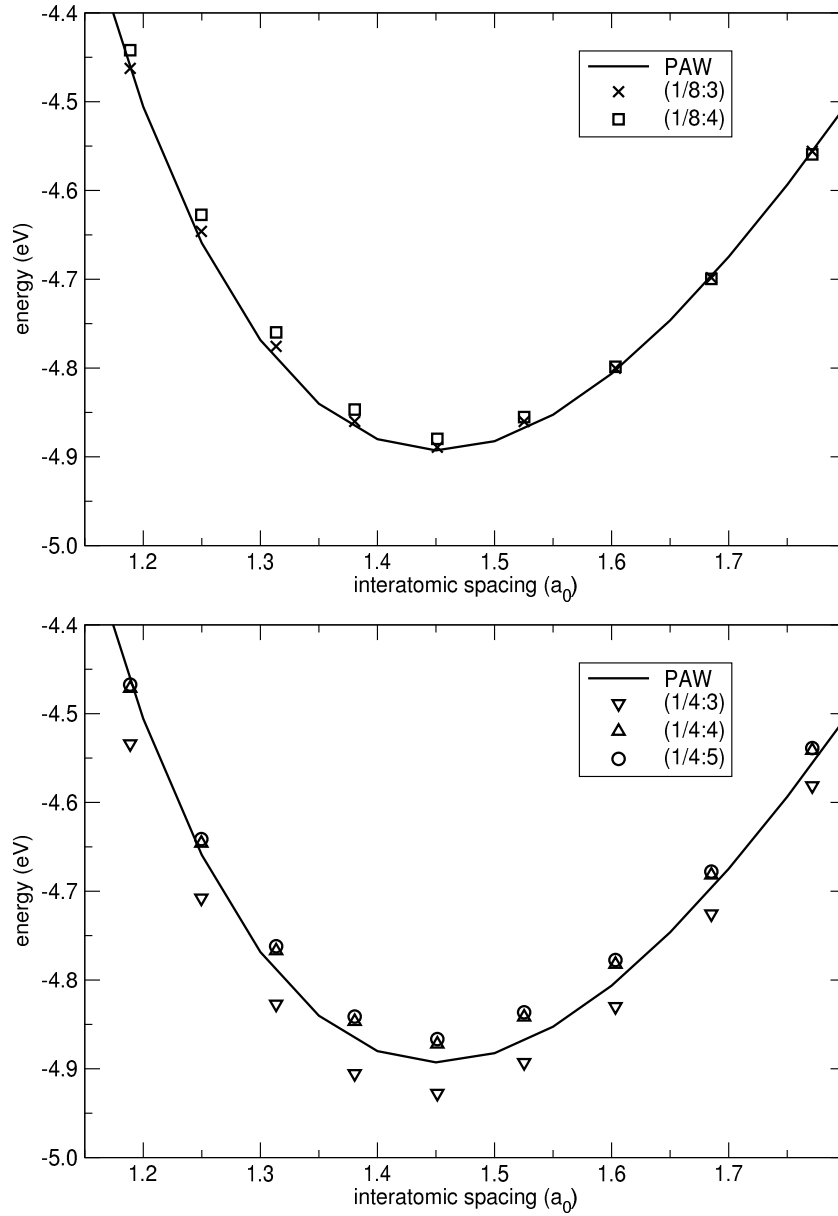
Figure 7.2: Binding energy of the H_2 dimer as a function of inter-atomic spacing for trial densities obtained from different embedding potentials, compared to the self-consistent result (full line). The setups for the nonspherical deformation are coded in the form $(\tilde{r}_p : \tilde{r}_t)$ (see equation 4.46 and the corresponding text for further details). See the text for a discussion.
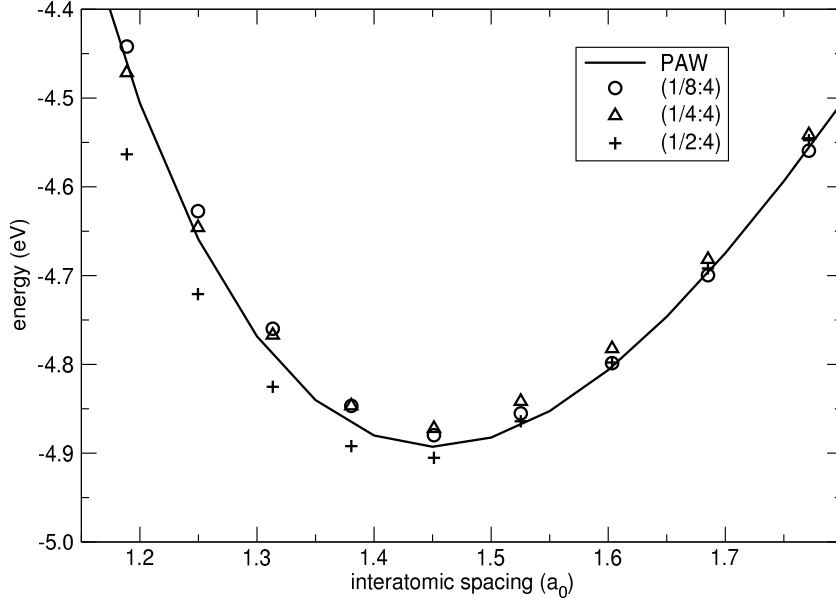
Figure 7.3: Binding energy of the H_2 dimer as a function of inter-atomic spacing for trial densities obtained from different embedding potentials, compared to the self-consistent result (full line). The setups for the nonspherical deformation are coded in the form $(\tilde{r}_p : \tilde{r}_t)$ (see equation 4.46 and the corresponding text for further details). See the text for a discussion.

found that the density at the atomic position is mainly influenced by the box radius for the total potential of the neighbor's (r_t), whereas the density in the bond region is dominated by the localization of the repulsion potential (r_p). For increasing r_t, density is shifted from the outer to the molecular region and the decay of the density for larger distances from the bond center becomes equal to the selfconsistent one (see the inset on the top panel of figure 7.4). The curve (1/4:4) (grey, dotted line) mimics the shape of the selfconsistent density (black, full line) the best. It is almost parallel to the exact density in the bond and and equal to it in the outer region. Nevertheless, it does not lead to the best accordance with the selfconsistent result in terms of binding energy. The reason for this seeming contradiction lies in the error cancellation. As shown in figure 7.7, the individual deviation in the kinetic, electrostatic and exchange and correlation energy for (1/4:4) is, for wide ranges of inter-atomic separations, smaller than those of (1/8:3). The quality of the total energy approximation however does not depend on the absolute values of the individual errors, but on the remaining error when added up.

Following the sequence $r_t = 2$ to $r_t = 4$, the amount of density in the molecular region increases, but does not approach the selfconsistent reference. One could think that a further increase of r_t could bring the trial density for $r_p = \frac{1}{4}$ to exact accordance with the selfconsistent one. As discussed above, the influence of r_t however is minimal for values larger than 4.
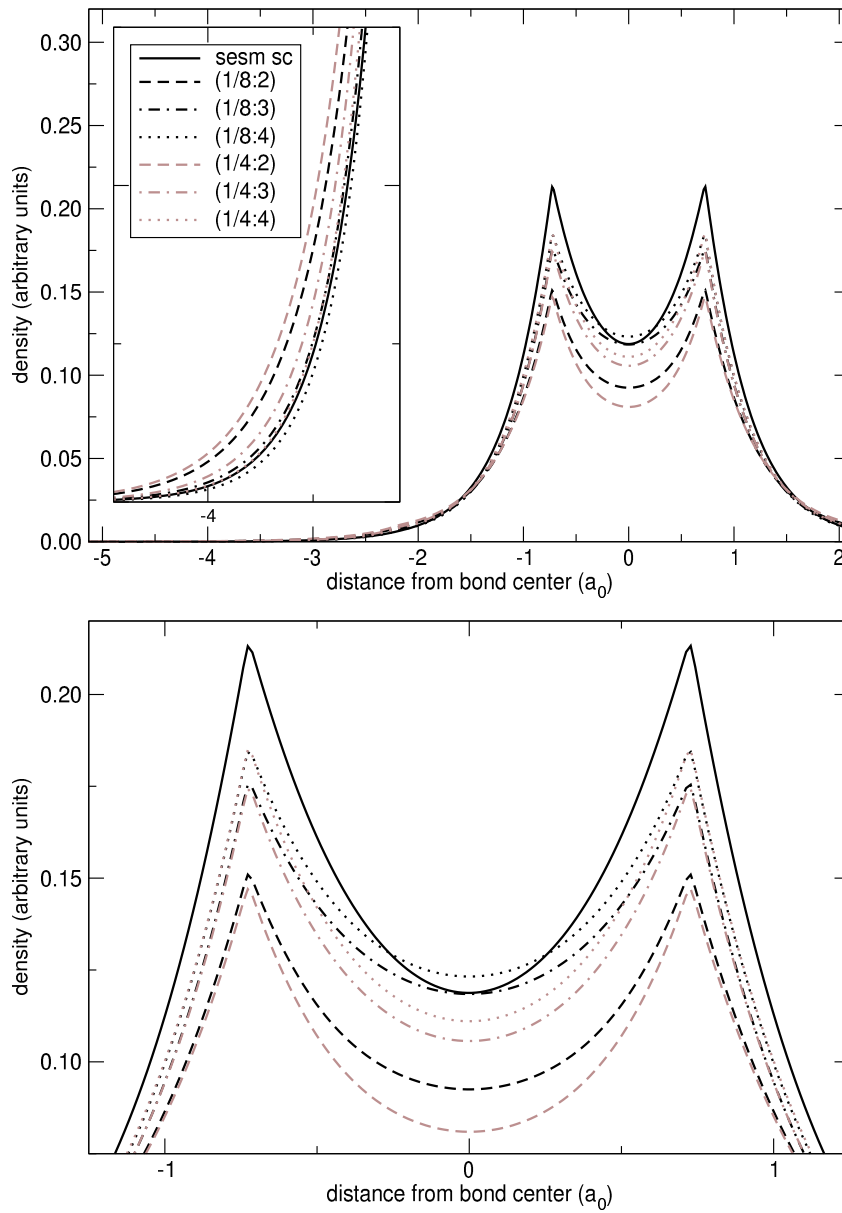
Figure 7.4: Trial densities obtained for different setups compared to the selfconsistent density (full line) along the molecular axis for a hydrogen dimer at the lda equilibrium spacing (1.45 a.u.). All densities integrate to the same number of electrons. The ordinate of the inset in the upper panel is scaled by a factor of 100. The setups for the nonspeherical deformation are coded in the form $(\tilde{r}_p : \tilde{r}_t)$ (see equation 4.46 and the corresponding text for further details). See the text for a discussion.
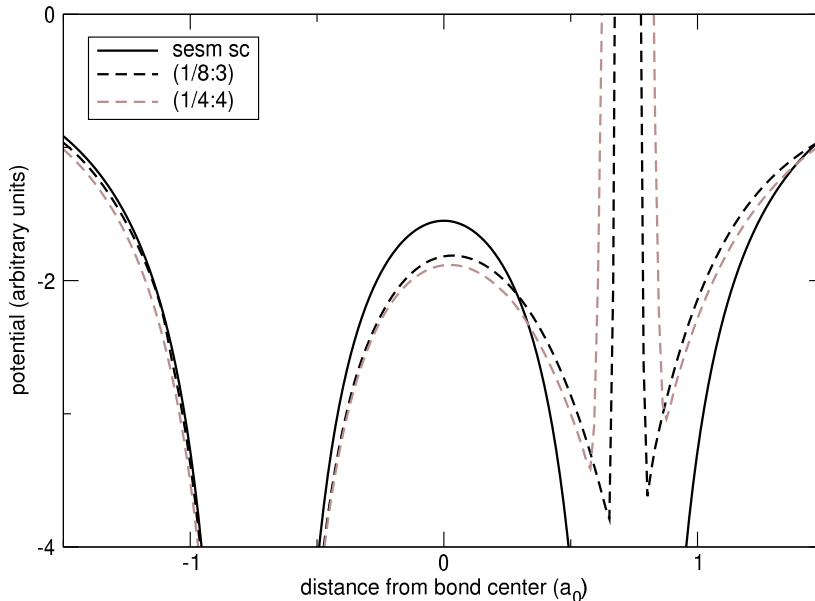
Figure 7.5: The embedding potential for the atom residing at -0.725 a.u. along the molec-
ular axis for a hydrogen dimer at the lda equilibrium spacing (1.45 a.u.) compared to the
selfconsistent total potential (full line). The setups for the nonspeherical deformation are
coded in the form $(\tilde{r}_p : \tilde{r}_t)$ (see equation 4.46 and the corresponding text for further details).
See the text for a discussion.

The remaining deviation arises from the approximation of the total potential used
in the deformation process. The approximation of the exchange and correlation po-
tential (item 3 in 5.2) as superposition of the individual contributions ($V_{xc}[\sum_i n_i] \approx$
$\sum_i V_{xc}[n_i]$) thereby deviates from the selfconsistent crystal potential because of two
reasons: first, it misses a repulsion due to the overlap of the fragment densities, which
is mainly located in the bond region. The embedding potential (plotted in figure 7.5)
hence is more attractive in these regions. This leads to density being shifted from
the atomic in the interstitial region. In addition, the exchange correlation potential
of the self-consistent crystal results from the superposition of the selfconsistent frag-
ment densities. In the embedding potential, we however use the density localized in a
spherical box with radius r_t for all neighbors. The effects of these approximations mu-
tually interact. The difference between the embedding potentials (1/8:3) and (1/4:4)
therefore can not easily be explained.

In composition of the total density, we furthermore neglect the interference part
of the fragments. In the selfconsistent case including interference, a non negligible
contribution to the density in the atomic region however arises just therefrom (see
figure 7.8 for more details).

Figure 7.6 and 7.7 emphasize the basic difference between the spherically localized
frozen and deformed atomic fragment approach. The approximated densities for the
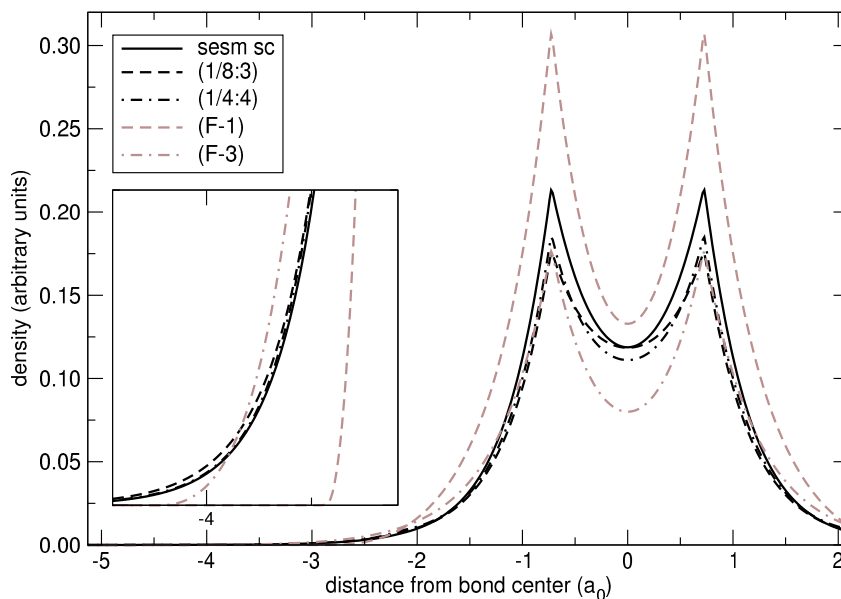
Figure 7.6: Trial densities obtained for different setups compared to FAF and the selfconsistent density (full line) along the molecular axis for a hydrogen dimer at the lda equilibrium spacing (1.45 a.u.). All densities integrate to the same number of electrons. The ordinate of the inset is scaled by a factor of 100. The FAF density has been defined in table 6.3. The setups for the nonspeherical deformation are coded in the form $(\tilde{r}_p : \tilde{r}_t)$ (see equation 4.46 and the corresponding text for further details). See the text for a discussion.

FAF are much worse, in particular for the regions not being part of a bond. The decay of the selfconsistent crystal density, which is satisfactorily reproduced by the deformed fragment densities, can not be described in terms of spherically localized atomic fragments (see the inset in figure 7.6). The FAF densities lead to considerable errors in the kinetic, electrostatic and exchange and correlation energy plotted in figure 7.7. Due to the stationarity of the total energy functional, these errors mainly cancel for small molecules and small deviations from the inter-atomic separation, the FAF density has been optimized for. In the case of more complicated systems, such as defect structures and surfaces, errors due to the wrong decay of the trial density play an important role and the FAF approach breaks down.

7.2 Deformed atomic wave functions

Figure 7.8 shows the self-consistent trial density (full line) along the molecular axis for a hydrogen dimer at the lda equilibrium spacing (1.45 a.u.) decomposed in atomic (dashed line) and interference contributions (dotted line). The superposition of the atomic contributions (dash dotted line) and the interference part (dotted line) add up to the self-consistent density (full line). The interference density considerably
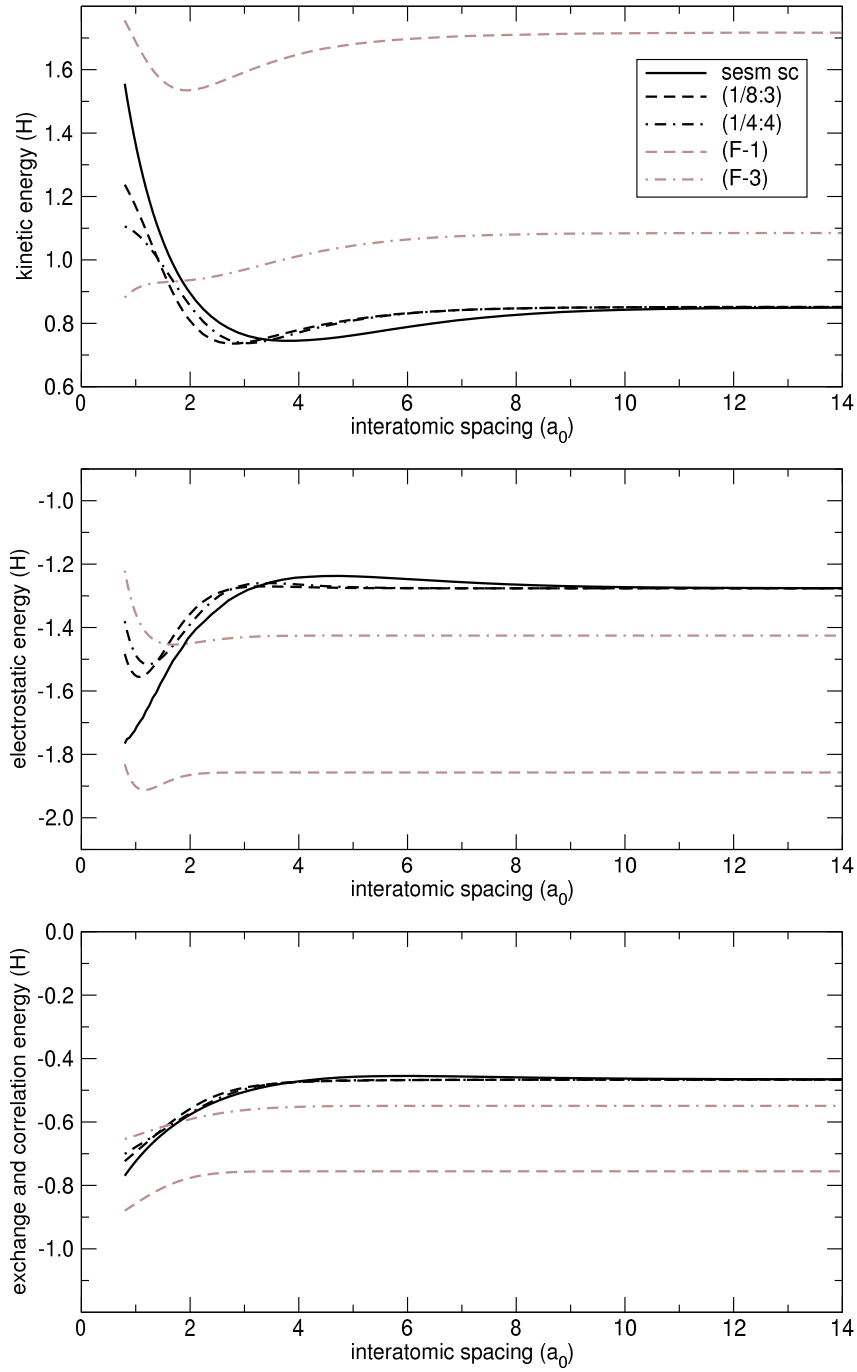
Figure 7.7: Kinetic, electrostatic and exchange and correlation energy of the H_2 dimer as a function of inter-atomic spacing for trial densities obtained from different embedding potentials, compared to FAF and self-consistent results (full line). The FAF density has been defined in table 6.3. The setups for the nonspeherical deformation are coded in the form $(\tilde{r}_p : \tilde{r}_t)$ (see equation 4.46 and the corresponding text for further details). See the text for a discussion.
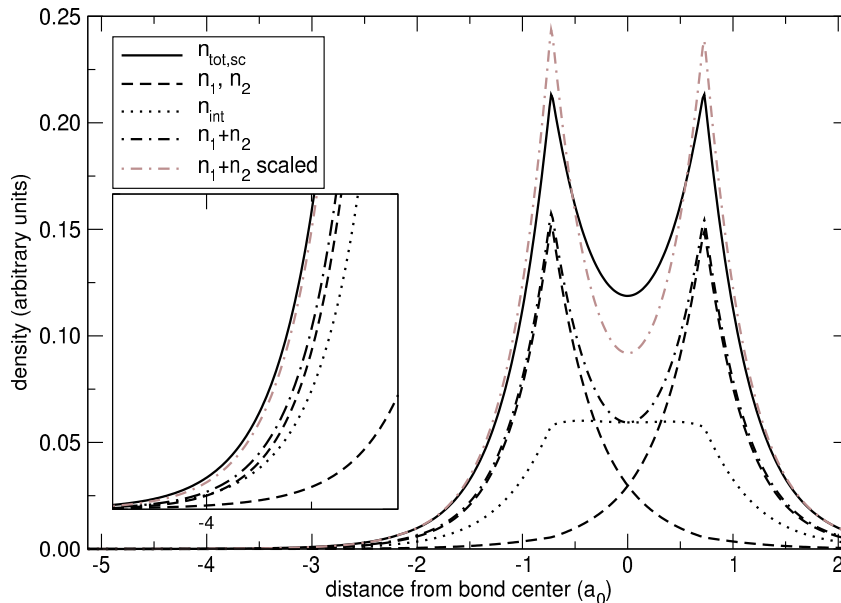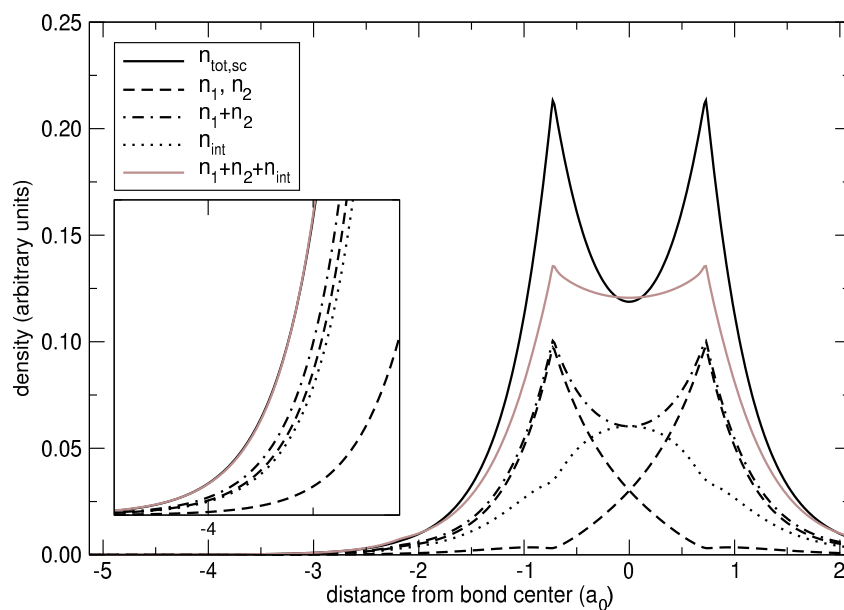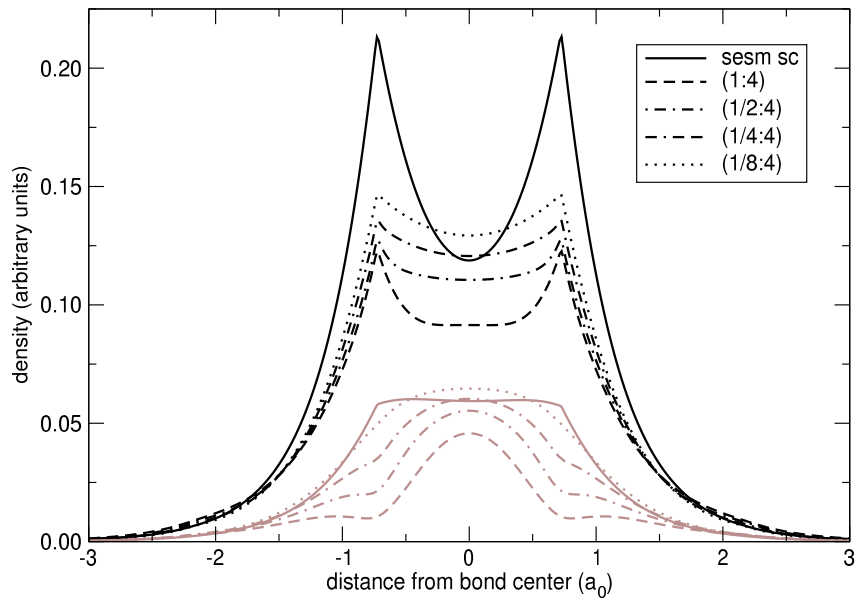
Figure 7.8: The self-consistent trial density (full line) along the molecular axis for a hydrogen dimer at the lda equilibrium spacing (1.45 a.u.) decomposed in atomic (dashed line) and interference contributions (dotted line). The superposition of the atomic contributions (dash dotted line) and the interference part (dotted line) add up to the self-consistent density (full line). Excluding the interference contribution from the trial density, the atomic contributions need to be rescaled in order to integrate to the same amount of electrons (dash dotted gray line). The ordinate of the inset is scaled by a factor of 100. See the text for a discussion.

contributes to the density in the atomic region. Excluding the interference contribution from the trial density, the atomic contributions need to be rescaled in order to integrate to the same amount of electrons (dash dotted gray line). Because the selfconsistent density has been optimized including the interference contribution, the scaled atomic superposition can not reproduce the selfconsistent density satisfactory.

The trial densities, which lead to the best approximations of the binding energy (see figure 7.2 and the related discussion for details) when interference contributions were excluded, are plotted in figure 7.9 (results obtained from (1/4:4) correspond to the black and (1/8:3) to the grey dashed and dash dotted lines). In order to reproduce the selfconsistent crystal density in the bond region from atomic contributions solely, the atomic fragments need to extend into this region. As a result, the overlap and hence the interference contribution (relative to the atomic contribution) of these fragments is larger than in the selfconsistent case (compare figure 7.18 and 7.8).

Figure 7.10 shows the fragment wave functions for the setups (1/4:4) (black dashed lines) and (1/8:3) (gray dashed lines) along the molecular axis for a hydrogen dimer at the lda equilibrium spacing (1.45 a.u.) compared to the occupied selfconsistent molecular orbital (full line). The small wriggles at −2.25 a.u. from the bond center in
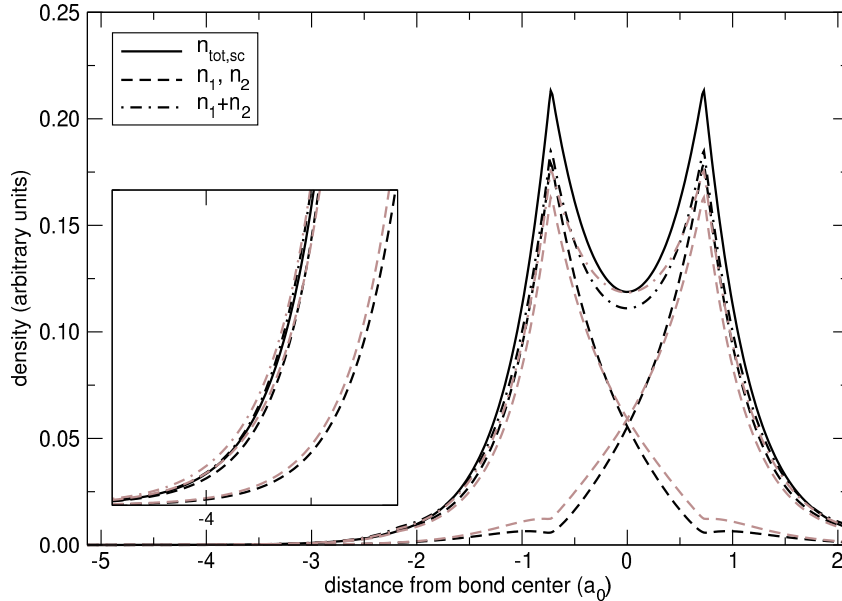
Figure 7.9: The trial density for the setups (1/4:4) (black) and (1/8:3) (grey) along the molecular axis for a hydrogen dimer at the lda equilibrium spacing (1.45 a.u.) decomposed in atomic contributions (dashed line) compared to self-consistent trial density (full line). See the text for a discussion.

the on-site branch are due to an artifact in the embedding potential (shown in figure 7.11). During the deformation calculation, the Pauli repulsion peak of the neighbor is described in a spherical harmonics expansion. The strong localization and finite angular momentum cutoff lead to Gauss oscillations (see section 8.3 for a detailed discussion) in the potential.

The amplitude of the fragment wave function in the tail region is considerably reduced (compare the lower dashed lines with the full line at the atomic positions) but does not exactly approach zero for the neighbors position. This might be due the tunnel effect because the Pauli repulsion peak is strongly localized and finite. Nevertheless, the desired localization effect of the neighbor is present. This is emphasized in the inset of figure 7.12, which compares the decay of the off-site fragments density to that of the molecular orbital. When applied to crystal systems, the new approach should allow to decompose the density of delocalized states in localized, atom centered contributions, as sketched in figure 7.13.

7.3 Transferability of the embedding potentials

Figure 7.14 shows the hydrogen s- (black), p- (grey), and d- (light grey) radial function of the valence repulsion potential, determined from atoms compressed in spherical boxes with box radius $r_p = \frac{1}{8}$, $\frac{1}{4}$, and $\frac{1}{2}r_{covalent}$, respectively (see section 4.3 for
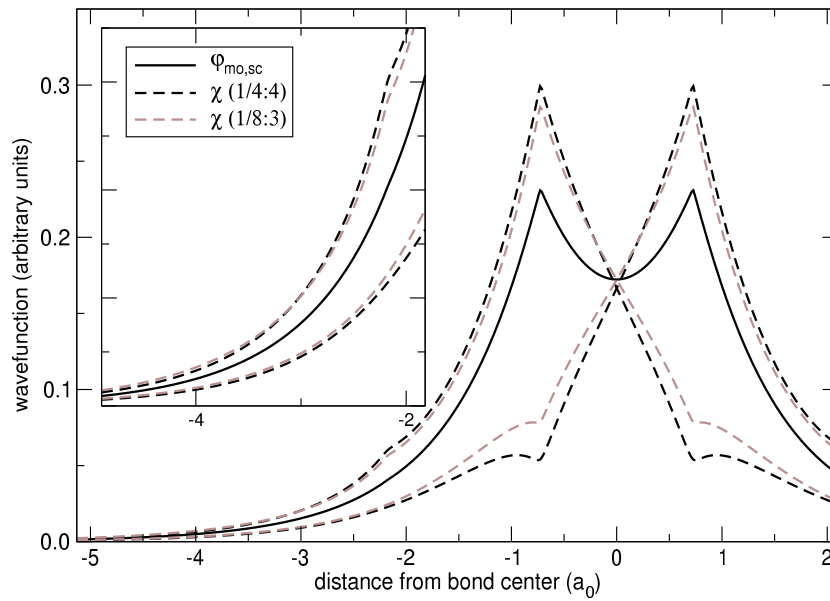
Figure 7.10: The fragment wave functions for the setups (1/4:4) (black dashed lines) and (1/8:3) (gray dashed lines) along the molecular axis for a hydrogen dimer at the lda equilibrium spacing (1.45 a.u.) compared to the occupied selfconsistent molecular orbital (full line). The ordinate of the inset is scaled by a factor of 5. The setups for the nonspeherical deformation are coded in the form $(\tilde{r}_p : \tilde{r}_t)$ (see equation 4.46 and the corresponding text for further details). See the text for a discussion.
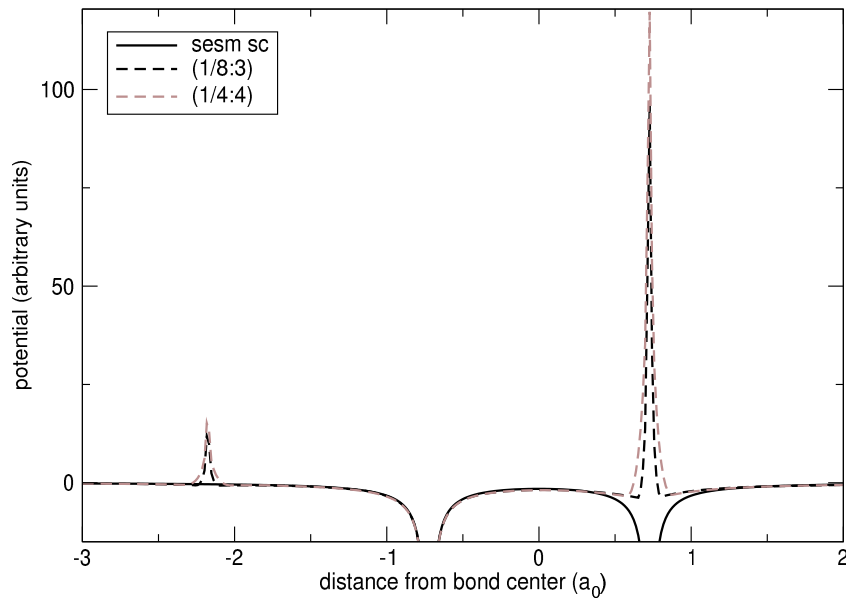
Figure 7.11: The embedding potential for the atom residing at -0.725 a.u. along the molecular axis for a hydrogen dimer at the lda equilibrium spacing (1.45 a.u.) compared to the selfconsistent total potential (full line). The small peak at -2.25 a.u. corresponds to Gauss oscillations originating from the limited angular momentum cutoff in the spherical harmonic expansion of the peak residing at 0.725 a.u.. The setups for the nonspeherical deformation are coded in the form $(\tilde{r}_p : \tilde{r}_t)$ (see equation 4.46 and the corresponding text for further details). See the text for a discussion.
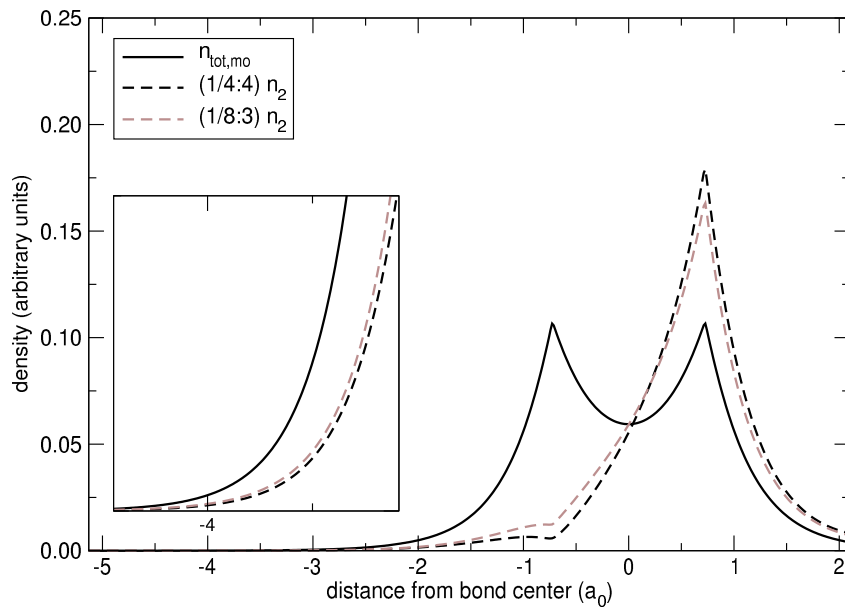
Figure 7.12: The off-site trial density for the setups (1/4:4) (black) and (1/8:3) (grey) along the molecular axis for a hydrogen dimer at the lda equilibrium spacing (1.45 a.u.) compared to self-consistent density of the occupied molecular orbital (full line). The ordinate of the inset is scaled by a factor of 100. The setups for the nonspeherical deformation are coded in the form $(\tilde{r}_p : \tilde{r}_t)$ (see equation 4.46 and the corresponding text for further details). See the text for a discussion.
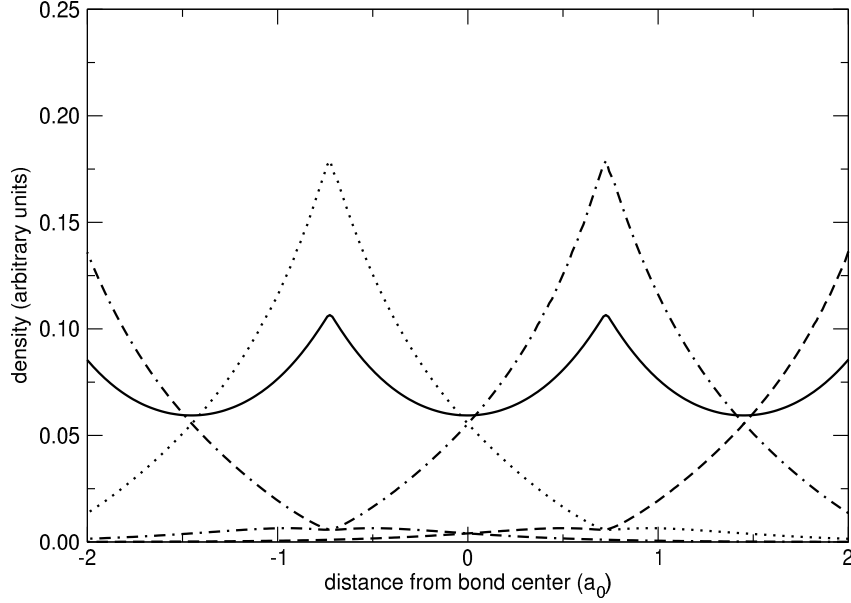
Figure 7.13: A sketch of the decomposition of a localized crystal density (full line) in local contributions for the setup (1/4:4). See the text for a discussion.

theoretical details). For all calculations shown in the upper panel, the expansion energy $\bar{\varepsilon}$ has been chosen to be equal to the energy of the crystal state at the lda ground state separation (-0.37 H). Thus, the potentials correspond to the exact potentials for this separation. In the lower panel, the repulsion potentials determined at the corresponding bond energies in the spherical box ($E^s_{bond} = -4.23$ H, $E^p_{bond} = 92.97$ H, $E^d_{bond} = 244.95$ H) are compared to the exact potentials for $r_p = \frac{1}{4}r_{covalent}$.

The corresponding densities are shown in figure 7.15. Following the argumentation in section 4.3.8, the densities have been calculated, applying only the spherical part of the repulsion potentials. The sole exception is the result labeled by (1/4:4 p), for which the spherical symmetrized p-channel has been used.

Picking up the discussion in 7.1, it can be stated that the density in the atomic region is dominated by the approximation of the fragments total potential contribution, whereas the valence repulsion potential affects the bond region. The changes in the trial density due to neglect of the spherical symmetrized contributions of higher angular momentum channels can be balanced by an adaption of the spherical box radii r_t and r_d. The lower panel of figure 7.14 emphasizes the fact that the energy-dependence of the repulsion potentials is minimal. Besides, it should be noted that the error in binding energy at the lda ground state separation of H_2 for all trial densities plotted in figure 7.15 - except (1/2:1) - is in the range of 1 mH. The setup (1/2:1) leads to a deviation of 38 mH.

The approach based on spherically approximated and energy linearized valence repulsion potentials outlined in section 4.3.8 therefore is well justified and should be

applicable in all day work.

7.4 Results for included interference

Taking the interference contribution in the composition of the trial density into account, the setups (1/8:3) and (1/4:4) still lead to the best accordance with the self-consistent binding energy. The four most accurate results are shown in Figure 7.16. The corresponding trial densities, plotted in figure (7.17), however dramatically underestimate the density in the atomic region. This is, because the overlap and hence the interference contribution of these fragments is large. In order to integrate to the same amount of electrons, the atomic contribution needs to be scaled down, when interference is taken into account (see figure 7.18 for a decomposition of the trial density into the individual contributions). This weighting shifts density from the atomic into the regions where the fragments overlap. Due to the approximation of V_{xc} and the resulting underestimated repulsion in these regions (for details see the discussion in the preceding sections), the density relocation is additionally fortified. It should be noted that the regions with large overlap are located on a plane perpendicular to the bond, subtending the molecular axis at the mid of the bond. All densities plotted in figure 7.17 in 3d integrate to the same value.

Figure 7.19 shows the trial densities and interference contributions obtained for different setups including interference, compared to the selfconsistent density (full line) along the molecular axis for a hydrogen dimer at the lda equilibrium spacing (1.45 a.u.). For stronger localized valence repulsion, the shape of the interference part becomes similar to the selfconsistent one. Due to the unbalanced ratio between interference and atomic contribution, the absolute height however is not the same. Figure 7.20 shows the corresponding atomic contributions.

7.5 Deformed atomic fragments as minimal basis

One goal of the SESM approach was to allow a representation of the selfconsistent crystal density in atom-centered contributions, because it is numerically convenient and facilitates the interpretation of results. The results discussed above (see e.g. figure 7.1 and 7.6) showed, that the non-spherical deformation allows to access the binding energy as well as the self-consistent density sufficiently accurate. The trial density from non-spherical atomic fragments thereby is much closer to the selfconsistent one than in the case of spherically localized atomic fragments. The remaining difference is due to the approximation of the total potential used during the deformation process. The errors are in particular dominated by the neglect of the overlap contribution to the exchange and correlation potential (see figure 7.5 and the related discussion for further details).

The deformed orbitals χ, optimized for the representation of the crystal density from atomic contributions solely (e.g. in the case of H_2: $n_{H_2}(\mathbf{r}) \approx \chi_1^2(\mathbf{r}) + \chi_2^2(\mathbf{r})$),
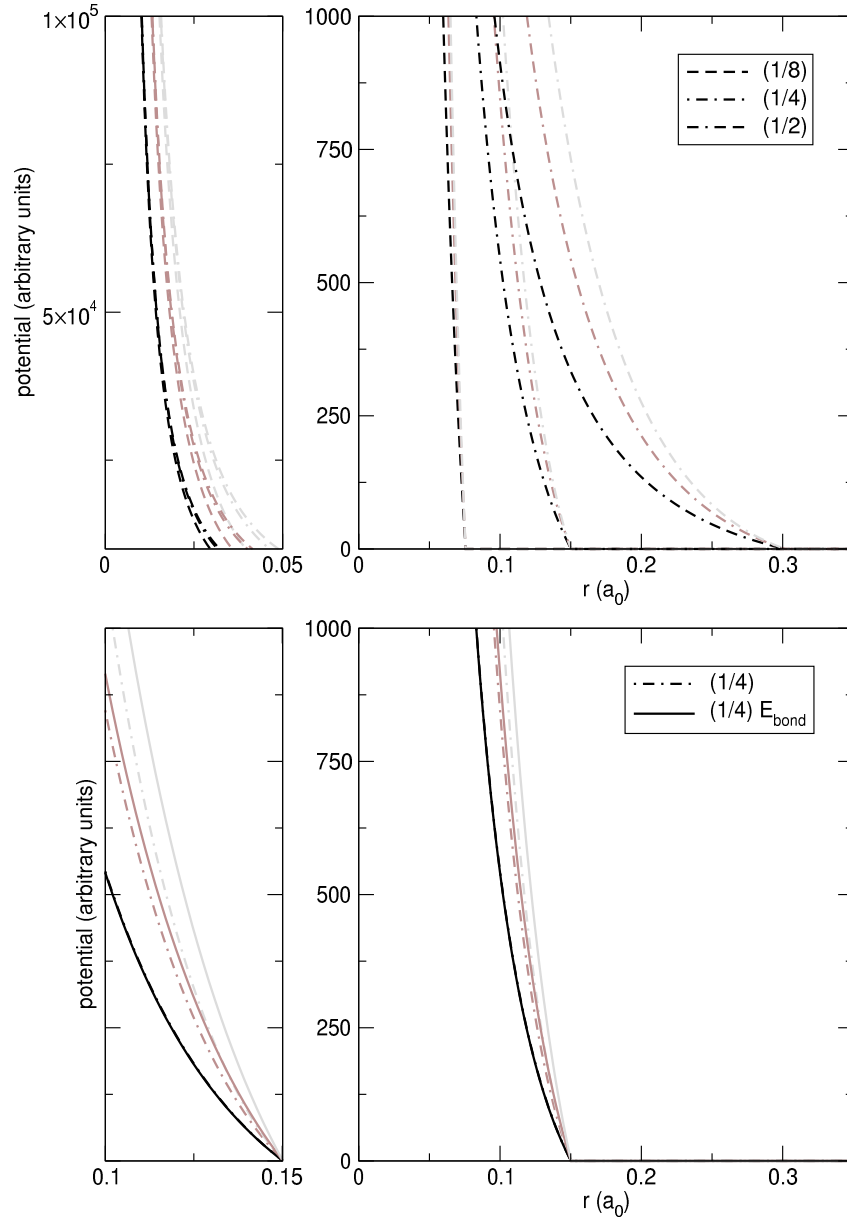
Figure 7.14: The hydrogen s- (black), p- (grey), and d- (light grey) radial function of the valence repulsion potential, determined from atoms compressed in spherical boxes with box radius $r_p = \frac{1}{8}$, $\frac{1}{4}$, and $\frac{1}{2}r_{covalent}$, respectively (see section 4.3 for theoretical details). For all calculations shown in the upper panel, the expansion energy $\bar{\varepsilon}$ has been chosen to be equal to the energy of the crystal state at the lda ground state separation (-0.37 H). Thus, the potentials correspond to the exact potentials for this separation. In the lower panel, the repulsion potentials determined at the corresponding bond energies in the spherical box ($E_{bond}^s = -4.23$ H, $E_{bond}^p = 92.97$ H, $E_{bond}^d = 244.95$ H) are compared to the exact potentials for $r_p = \frac{1}{4}r_{covalent}$. The repulsion potentials are coded in the form ($\tilde{r}_p : \tilde{r}_t$) (see equation 4.46 and the corresponding text for further details). See the text for a discussion.
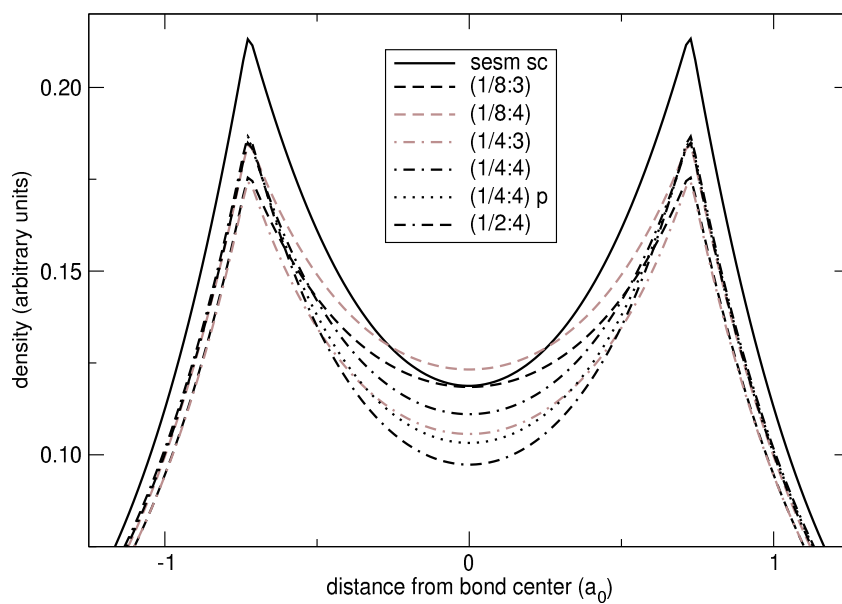
Figure 7.15: The trial densities obtained for the Pauli repulsion potentials plotted in figure 7.14 along the molecular axis for a hydrogen dimer at the lda equilibrium spacing (1.45 a.u.), compared to the selfconsistent density (full line). The setups for the nonspeherical deformation are coded in the form $(\tilde{r}_p : \tilde{r}_t)$ (see equation 4.46 and the corresponding text for further details). See the text for a discussion.
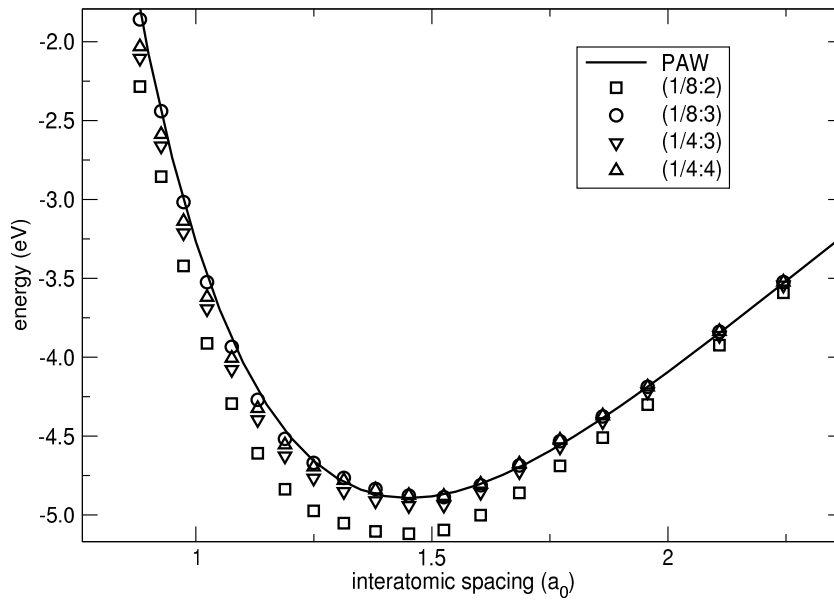
Figure 7.16: Binding energy of the H_2 dimer as a function of inter-atomic spacing for trial densities including interference obtained from different embedding potentials, compared to the self-consistent result (full line). The setups for the nonspeherical deformation are coded in the form $(\tilde{r}_p : \tilde{r}_t)$ (see equation 4.46 and the corresponding text for further details). See the text for a discussion.
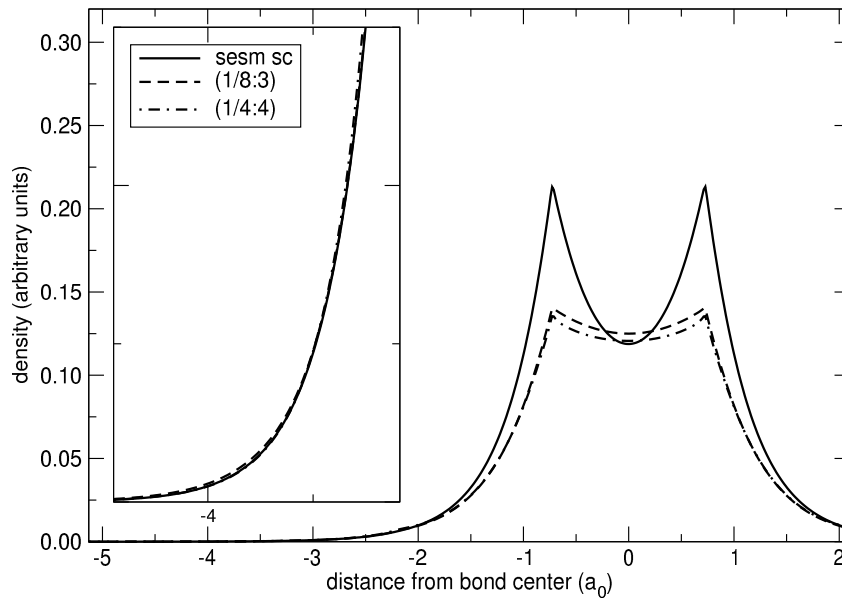
Figure 7.17: Trial densities obtained for the setups (1/8:3) and (1/4:4) including interference, compared to the selfconsistent density (full line) along the molecular axis for a hydrogen dimer at the lda equilibrium spacing (1.45 a.u.). All densities integrate to the same number of electrons. The ordinate of the inset is scaled by a factor of 100. The setups for the nonspeherical deformation are coded in the form $(\tilde{r}_p : \tilde{r}_t)$ (see equation 4.46 and the corresponding text for further details). See the text for a discussion.

Figure 7.18: The trial density, including the interference contribution, for the setup (1/4:4) (grey line) along the molecular axis for a hydrogen dimer at the lda equilibrium spacing (1.45 a.u.) compared to the selfconsistent density (full line) and decomposed in atomic (dashed line) and interference contributions (dotted line). The superposition of the atomic contributions (dash dotted line) and the interference part (dotted line) add up to the grey line. The ordinate of the inset is scaled by a factor of 100. The setups for the nonspeherical deformation are coded in the form $(\tilde{r}_p : \tilde{r}_t)$ (see equation 4.46 and the corresponding text for further details). See the text for a discussion.

Figure 7.19: Trial densities and interference contribution obtained for different setups including interference, compared to the selfconsistent density (full line) along the molecular axis for a hydrogen dimer at the lda equilibrium spacing (1.45 a.u.). The setups for the nonspeherical deformation are coded in the form $(\tilde{r}_p : \tilde{r}_t)$ (see equation 4.46 and the corresponding text for further details). See the text for a discussion.
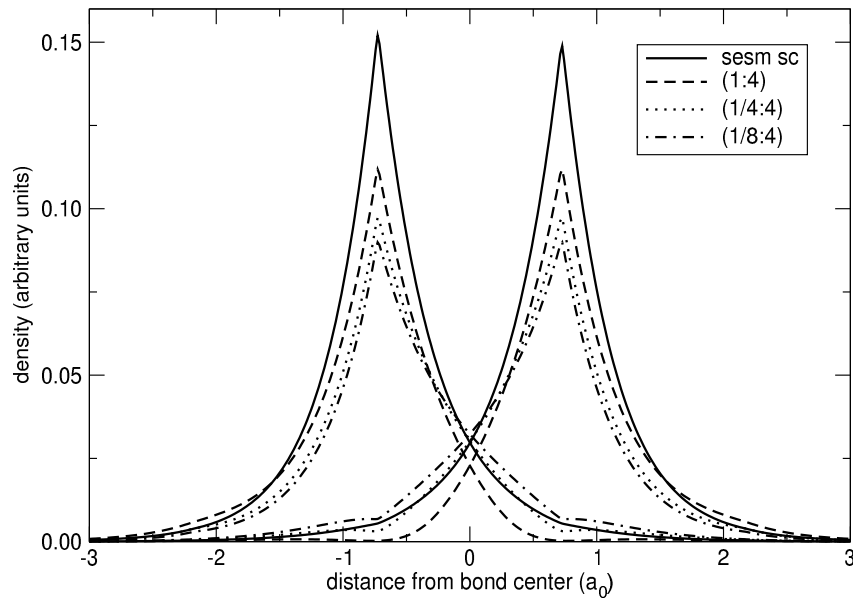
Figure 7.20: The atomic contribution of the trial density for different setups along the molecular axis for a hydrogen dimer at the lda equilibrium spacing (1.45 a.u.) compared to the selfconsistent density (full line). The setups for the nonspeherical deformation are coded in the form $(\tilde{r}_p : \tilde{r}_t)$ (see equation 4.46 and the corresponding text for further details). See the text for a discussion.

however can not be used as *minimal* basis for the solution of the crystals Schrödinger's equation. This is, because the process of solving Schrödinger's equation operates on the level of wave functions. The corresponding density and energy contributions are connected to the square of the wavefunction, which automatically includes the interference contribution. Applying a minimal basis which includes the interference in the atomic contibution, therefore leads to a overstimation of interference.

In order to illustrate this, one may think of two minimal bases $\{\chi\}$ and $\{\tilde{\chi}\}$ for the H_2 system. The first ($\{\chi\}$) corresponds to the deformed orbitals, optimized to reproduce the groundstate density from superposition of atomic contributions according to

$$n_{H_2}(\mathbf{r}) = \chi_1^2(\mathbf{r}) + \chi_2^2(\mathbf{r}). \tag{7.1}$$

The latter ($\{\tilde{\chi}\}$) may correspond to a correct description of the H_2 groundstate wavefunction:

$$\varphi_{H_2}(\mathbf{r}) = \tilde{\chi}_1(\mathbf{r}) + \tilde{\chi}_2(\mathbf{r}).$$

The groundstate density obtained from a tight-binding approach in the basis $\{\tilde{\chi}\}$ can be written as follows:

$$
\begin{aligned}
n_{H_2}(\mathbf{r}) &= \varphi_{H_2}^2(\mathbf{r}) \\
&= (\tilde{\chi}_1(\mathbf{r}) + \tilde{\chi}_2(\mathbf{r}))^2 \\
&= \left(\tilde{\chi}_1^2(\mathbf{r}) + \tilde{\chi}_2^2(\mathbf{r}) + 2\tilde{\chi}_1(\mathbf{r})\tilde{\chi}_2(\mathbf{r})\right),
\end{aligned}
\tag{7.2}
$$

and corresponds to the true density.

Solving the H_2 system in a tight-binding approach in the minimal basis $\{\chi\}$ however results in the following groundstate wavefunction and density:

$$\phi_{H_2}(\mathbf{r}) = C\left(\chi_1(\mathbf{r}) + \chi_2(\mathbf{r})\right)$$

$$
\begin{aligned}
n_{H_2}^{(\chi)}(\mathbf{r}) &= \phi_{H_2}^2(\mathbf{r}) \\
&= C^2\left(\chi_1^2(\mathbf{r}) + \chi_2^2(\mathbf{r}) + 2\chi_1(\mathbf{r})\chi_2(\mathbf{r})\right),
\end{aligned}
\tag{7.3}
$$

with C corresponding to a normalization constant such, that $\int \phi_{H_2}^2(\mathbf{r})d^3r = 2$.

Per construction (7.1), the deformed orbitals $\{\chi\}$ however include the interference in the atomic contribution. From (7.1) and (7.3) therefore follows:

$$
\begin{aligned}
n_{H_2}^{(\chi)}(\mathbf{r}) &= C^2\left(\chi_1^2(\mathbf{r}) + \chi_2^2(\mathbf{r}) + 2\chi_1(\mathbf{r})\chi_2(\mathbf{r})\right) \\
&= C^2\left(n_{H_2}(\mathbf{r}) + 2\chi_1(\mathbf{r})\chi_2(\mathbf{r})\right).
\end{aligned}
$$

This is a strange density explicitely including the interference $\chi_1(\mathbf{r})\chi_2(\mathbf{r})$ of two basisfunctions, which themselves implicitely include the interference $\tilde{\chi}_1(\mathbf{r})\tilde{\chi}_2(\mathbf{r})$.

When following a tight-binding approach in an extended deformed basis, the interference contribution $\chi_1(\mathbf{r})\chi_2(\mathbf{r})$ can be compensated by additional basis functions.

	χ	$\sim e^{-1.0\lvert\mathbf{r}\rvert}$	$\sim e^{-1.5\lvert\mathbf{r}\rvert}$	$\sim e^{-2.0\lvert\mathbf{r}\rvert}$	$\sim e^{-5.0\lvert\mathbf{r}\rvert}$	$\sim \lvert\mathbf{r}\rvert e^{-0.5\lvert\mathbf{r}\rvert}$
centered at $\mathbf{R}_A$	0.375	0.513	0.279	0.098	-0.005	0.059
centered at $\mathbf{R}_B$	0.384	0.525	0.258	0.107	-0.005	-0.060

Table 7.1: The expansion coefficients for a hydrogen dimer at the lda equilibrium spacing (1.45 a.u.). The deformed orbitals χ have been determined, using the setup (1/8:3). The expansion coefficients are normalized such that the orbitals density is equal to one. It can be seen that a considerable mixing of additional basis functions occurs. The setup is coded in the form ($\tilde{r}_p : \tilde{r}_t$) (see equation 4.46 and the corresponding text for further details). See the text for a discussion.

From a physical point of view, this is unproblematic, as long as the addition of further basis functions leads to a complete basis set. The numerical costs however increase. Table 7.1 provides the expansion coefficients for a hydrogen dimer at the lda equilibrium spacing (1.45 a.u.). The deformed orbitals χ have been determined, using the setup (1/8:3). The expansion coefficients are normalized such that the orbitals density is equal to one. It can be seen that a considerable mixing of additional basis functions occurs.

It should be noted, that the accurate determination of E_{tb} (defined in equation (3.10)), which implies the solution of Schrödinger's equation, is indispensable. An artificial neglect of interference contributions in this step would affect the error cancellation and hence the accuracy of the density functional (3.8).

Nevertheless, non-spherical deformed atomic orbitals, in principle, should be suitable as minimal basis set. They simply need to be determined such, that the crystal density is represented most accurate with included interference contribution (which would correspond to the basis $\{\tilde{\chi}\}$ introduced above). It is therefore not possible to determine atomic fragments which allow to split the crystal density in atomic contributions - excluding interference - and serve as minimal basis set at the same time.

From the discussion of the interference contribution in section 7.4 follows, that the approximation of the exchange and correlation potential in the deformation process heavily affects the quality of the basis functions. Due to the stationarity of the SESM functional, the derived density nevertheless leads to quite accurate results. In order to determine deformed wavefunctions suitable as minimal basis ($\{\tilde{\chi}\}$), the quality of the deformed wavefunctions and hence the approximation of the exchange and correlation potential needs to be enhanced.

7.6 Detailed discussion of the self-consistent deformation method of Boyer et. al.

Recently, a self-consistent method for the deformation of atomic orbitals has been published by Boyer et. al. [51]. This approach, just as the Car-Parrinello dynamic localized orbital scheme, applies an additional localization potential on the electrons.

The localization potentials are however derived from the overlap contribution to the kinetic energy. The kinetic energy is approximated as follows:

$$T_s[n(\mathbf{r})] \approx \sum_i T_0[n_i(\mathbf{r})] + T_k[n(\mathbf{r})] - \sum_i T_k[n_i(\mathbf{r})] \tag{7.4}$$

where $T_0[n_i(\mathbf{r})]$ is the kinetic energy of non-interacting electrons of density n_i in a potential v_i, centered at the atomic position $\mathbf{R}_i$, which shall be chosen such, that

$$n(\mathbf{r}) = \sum_i n_i(\mathbf{r}).$$

T_k is a functional to account for the non interacting kinetic energy due to the overlapping of electronic densities from neighboring sites. It corresponds to the Thomas-Fermi form

$$T_k[n(\mathbf{r})] = T_{TF}[n(\mathbf{r})] = A \int n^{\frac{5}{3}}(\mathbf{r})d^3r$$

and generalizations thereof for non-local functionals. See Appendix A.3 for the theoretical details of the Thomas Fermi approach.

The condition for the many particle energy (2.17) to be a minimum with respect to the many particle density:

$$0 = \frac{\delta E[n]}{\delta n} = \frac{\delta}{\delta n}\left(T_s[n] + E_{coul}[n] + E_{xc}[n]\right)$$

allows to solve for the potential v_i, which however depends on the actual crystal density. This introduces the need for self-consistent iterations with respect to the total crystal. This is totally different from our approach, which allows to derive embedding potential contributions on an chemical element basis in the form of setups. The deformed fragment is then indeed calculated self-consistently, but only with respect to the fragments density. The embedding potential itself is not explicitly dependent on the self-consistent density of the crystal, in which the fragment is embedded. A self-consistent determination therefore is dispensable.

In addition, in our density functional approach, all approximations operate on the level of total energies. The stationarity of ground state total energies with respect to the density ensures the cancellation of first order errors. Furthermore, closed expressions for the second order errors can be derived (see section 2.4.2 for details).

Boyer et. al. however approximate the kinetic energy for which no stationarity principle exists. This impedes the error cancellation. The resulting errors in the total energy therefore usually are orders of magnitude larger than for balanced error cancellations. In addition, the quality of the approximation of the kinetic energy is not enhanced during the self-consistent iteration. This leads to a non-vanishing error, even for self-consistency. Our method in contrast for self-consistency approaches the exact many-particle ground state. See figures 6.5 and 7.7 and the related discussion for

more details about the error cancellation. Boyer et.al. in [51] besides owe a discussion of the introduced errors.

The authors state that the numerical implementation is based on the re-transformation of spherical harmonic expansions. It should suffer from Gauß-oscillations discussed in section 8.3. This problem is however not discussed in the publication. It is therefore unclear if the authors are aware of it.

Part IV

Implementational details

8 Spherical harmonics basis set

8.1 Advantages

The spherical harmonics basis set, with its decomposition in radial function times spherical harmonics:

$$f(\mathbf{r}) = \sum_{l,m} f_{l,m}(|\mathbf{r}|) Y_{l,m}(\hat{\mathbf{r}}),$$

is the natural basis of isolated atoms. For spherically symmetric potentials, Schrödinger's equation can easily be solved in this representation (see standard textbooks for details). In numerical implementations, the radial functions thereby are usually held on logarithmic radial grids:

$$
\begin{aligned}
r(x) &= r_1 e^{(x-1)\alpha}, x = 1 \ldots nr \\
r(x+1) &= r(x) e^{\alpha}
\end{aligned}
$$

with typical values of $nr = 250$, $r_1 = 1.056 \cdot 10^{-4} a_0$ and $\alpha = 1/20$, respectively. This allows a high resolution near the nucleus, where the potential and wave functions are steep, and a description of the smooth long-range behavior with a limited number of mesh-points. This representation is therefore numerically convenient. Poisson's equation can e.g. be solved with considerable reduced numerical costs compared to standard 3D grid implementations.

An alternative approach is the commonly used plane wave basis. For a numerically sensible application, the decomposed functions however need to be smooth. This is not the case for our new method, in which we deal with extremely steep potential contributions, originating from the Pauli repulsion discussed in section 4.3. Figure 8.1 compares the radial part of the embedding potential contribution $v^{emb,H} = v^{H,ae} + \eta_H^{off}$ of hydrogen for the setup (1/4:4) (grey line), to the corresponding radial functions obtained from plane wave decompositions with different plane-wave cutoff (black lines). The high curvature of the potential makes it almost impossible to decompose it in a numerically convenient number of plane waves, which would correspond to ~ 30 Ry.

We therefore decided to use a real-space implementation based on atom centered spherical harmonics expansions, which may be combined with other real-space approaches such as star-burst meshes.
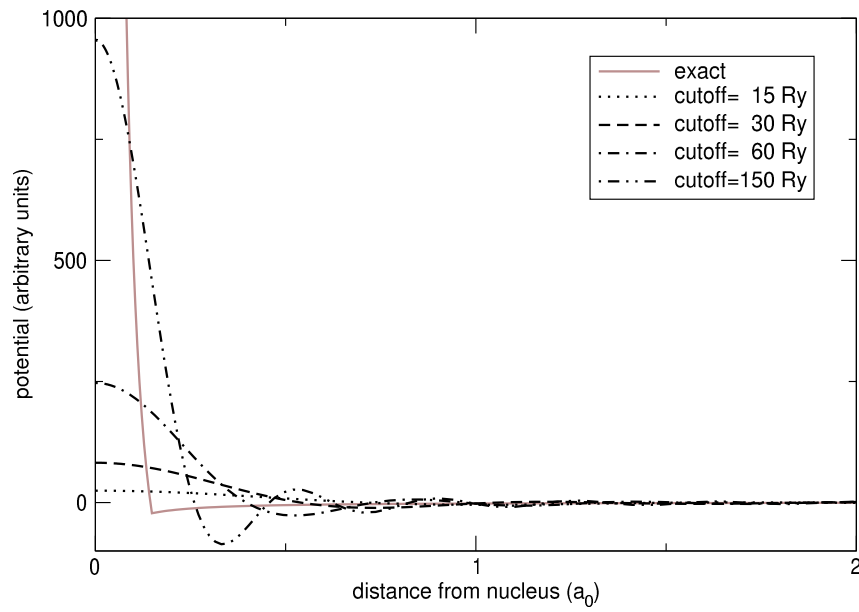
Figure 8.1: The radial part of the embedding potential contribution $v^{emb,H} = v^{H,ae} + \eta_H^{off}$ of hydrogen for the setup (1/4:4) (grey line), compared to the corresponding radial functions obtained from plane wave decompositions with different plane-wave cutoff (black lines). The setup is coded in the form $(\tilde{r}_p : \tilde{r}_t)$ (see equation 4.46 and the corresponding text for further details). See the text for a discussion.

8.2 Expansion center transformation

In the context of the new method, multi-center integrals need to be solved. The embedding potential, applied for the deformation of the fragments e.g. has contributions from several neighbors. The neighbor contributions thereby are given as spherical harmonics expansion, centered at the corresponding nuclei. A possible approach is to transform the expansion center from the offsite to the central atom. Two alternative general expressions for a transformation in 3D are derived in section B.4.3 and B.4.4, respectively. For numerical implementations, it is however preferable to divide the transformation in three steps. In a first step, the spherical harmonics expansion is rotated such, that the connecting vector between old and new center resides on the z-axis. In a second step, the center of the rotated expansion is transformed along the z-axis. Finally, the result is rotated back into the original orientation. The advantage of this approach is, that, in step two, we can exploit that all components for which $m \neq 0$ do not contribute and that the integration along $d\phi$ can be carried out analytically. The spherical harmonics expansion of a function $f(\mathbf{r})$, centered at $\mathbf{R} = (0, 0, R)$ can then be expanded at the origin as follows[1]:

$$f(\mathbf{r}) = \sum_L f_L(|\mathbf{r} - \mathbf{R}|) Y_L(\mathbf{r} - \mathbf{R}) = \sum_{L'} g_{L'}(|\mathbf{r}|) Y_{L'}(\mathbf{r}) \tag{8.1}$$

with

$$g_{L'}(|\mathbf{r}|) = \sum_L 2\pi \delta_{m,m'} \int_0^\pi f_L(\sqrt{R^2 + r^2 - 2rR\cos\theta}) \bar{P}_{L'}(cos\theta) \bar{P}_L(cos(h(\theta))) sin\theta d\theta \tag{8.2}$$

The definition of $\bar{P}$ and $h(\theta)$ and a detailed derivation can be found in section B.4 and B.4.5.

8.3 Gauß oscillations

The finite angular momentum cutoff of transformed expansions leads to virtual reflections of the transformed function. According to the oscillations emerging when decomposing a given functions in plane waves (see e.g. figure 8.1), we refer to this effect as *Gauß oscillations* or *shadows*.

Figure 8.2 and 8.3 illustrate this effect. On the left panel, the transformed 1s orbital, with origin on the right atom, expanded at the left atom is plotted for $l^{max} = 0 \ldots 5$ (top $\rightarrow$ down). On the right panel, the corresponding difference between the exact and the transformed function is shown. The scale is the same for all plots. Blue color corresponds to negative, red to positive values. The errors due to finite angular momentum cutoff in the transformation leads to error contributions, located on a

---

[1]The indices l, m are in the following combined in a single index L.

sphere with a radius corresponding to the distance of transformation ($2 \cdot 1.45$ a.u.).

When calculating multi-center integrals this effect can dramatically influence the result. Figure 8.4 shows the hydrogen 1s wave function of two atoms (left/rightmost ball) at the lda ground-state separation of H_2 (1.45 a.u.), when transformed to the center of gravity (ball in the mid) applying a cutoff $l^{max} = 2$ (top- and mid-panel). The corresponding overlap (bottom) is dominated by the Gauss oscillations. Figure 8.5 compares the analytic overlap (full line) over inter-atomic spacing for a hydrogen dimer in lcao to the results obtained from transformed orbitals with $l^{max} = 2$ (dashed) and $l^{max} = 3$ (dash dotted). The errors can only be suppressed by application of selection rules (see section 8.4 for details).

8.4 Selection rules

The transformed expansion (8.1) in principle has contributions from infinitely high angular momentum components L'. The number of angular momentum contributions needed to achieve a certain numerical accuracy increases with a stronger localization in angle space. Therefore, a stronger localization at the original expansion center, or a transformation over a larger distance (R) requires a higher cutoff. A convergence with respect to angular momentum components for an individual expansion can, in practical implementations, however not be achieved. It is therefore indispensable to make use of the selection rules for the product of spherical harmonics (B.71).

Two-center integrals

For two-center integrals, the selection rules allow to derive an angular momentum cutoff when one expansion is transformed in the other center. This can be illustrated by the overlap of two wave functions residing on two different nuclei[2]:

$$\langle \varphi^{(1)} | \phi^{(2)} \rangle \quad = \quad \int \sum_{lm,lm'} \varphi^{(1)}_{lm}(|\mathbf{r}|) \phi^{(2)}_{lm'}(|\mathbf{r}|) Y_{lm}(|\mathbf{r}|) Y_{lm'}(|\mathbf{r}|) d^3r$$

$$\overset{B.65}{=} \quad \int \sum_{lm} \varphi^{(1)}_{lm}(|\mathbf{r}|) \phi^{(2)}_{lm}(|\mathbf{r}|) r^2 dr$$

For two transformed expansions, the summation in principle has no upper limit. If we however transform one function to the center of the second, the limited angular momentum contribution of the onsite expansion naturally limits the maximum angular momentum needed for the transformation. Suppose $\varphi^{(1)}$ to have contributions up to $l = 3$. The highest angular momentum channel of $\phi^{(2)}$, when re-expanded at $\mathbf{r}_1$, which contributes to the integral therefore is also $l = 3$. Table 8.1 illustrates this for two wave functions with hydrogen $1s$ and $2p_z$ contributions, separated at 1.45a.u. along z.

---

[2]Here, we suppose to deal with real spherical harmonics. The notation (i) denotes the original expansion center.
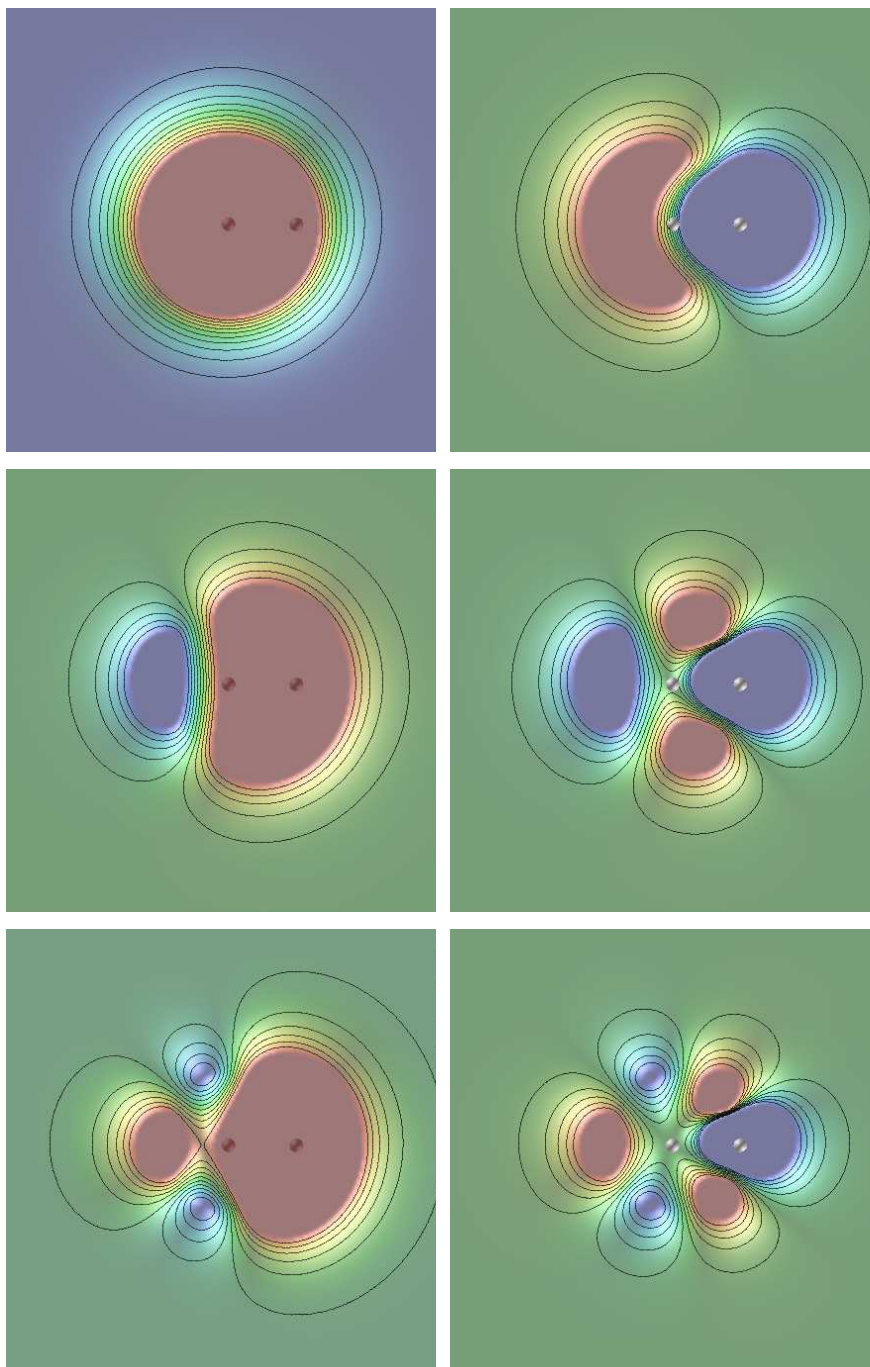
Figure 8.2: The transformed 1s orbital, with origin on the right atom, expanded at the left atom for $l^{max} = 0 \ldots 2$ (top $\rightarrow$ down,left panel). On the right panel, the corresponding difference between the exact and the transformed function is shown. The scale is the same for all plots. Blue color corresponds to negative, red to positive values. The errors due to finite angular momentum cutoff in the transformation leads to error contributions, located on a sphere with a radius corresponding to the distance of transformation ($2 \cdot 1.45$ a.u.).
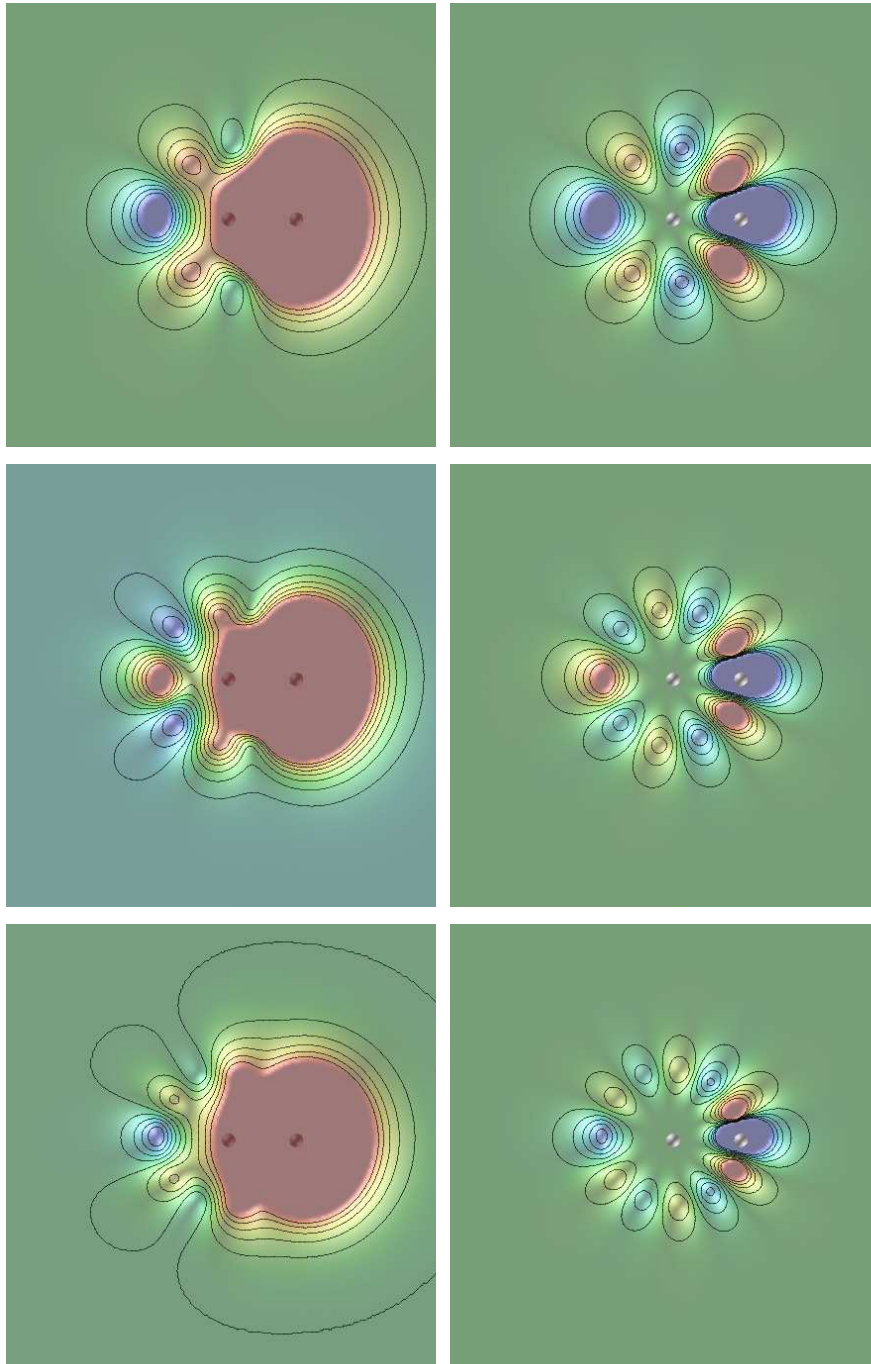
Figure 8.3: The transformed 1s orbital, with origin on the right atom, expanded at the left atom for $l^{max} = 3 \ldots 6$ (top $\rightarrow$ down,left panel). On the right panel, the corresponding difference between the exact and the transformed function is shown. The scale is the same for all plots. Blue color corresponds to negative, red to positive values. The errors due to finite angular momentum cutoff in the transformation leads to error contributions, located on a sphere with a radius corresponding to the distance of transformation ($2 \cdot 1.45$ a.u.).
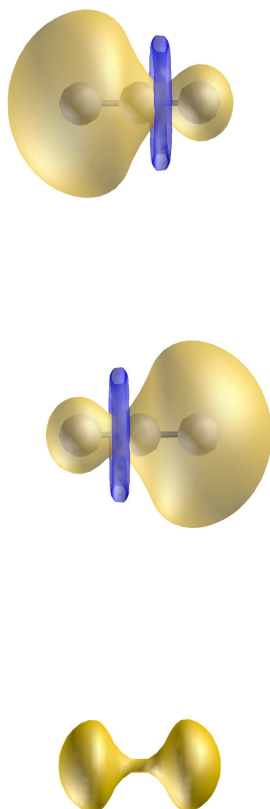
Figure 8.4: The hydrogen 1s wave function of two atoms (left/rightmost ball) at the lda ground-state separation of H_2 (1.45 a.u.), when transformed to the center of gravity (ball in the mid) applying a cutoff $l^{max} = 2$ (panel on top and in the mid). The corresponding overlap (bottom) is dominated by the Gauss oscillations.
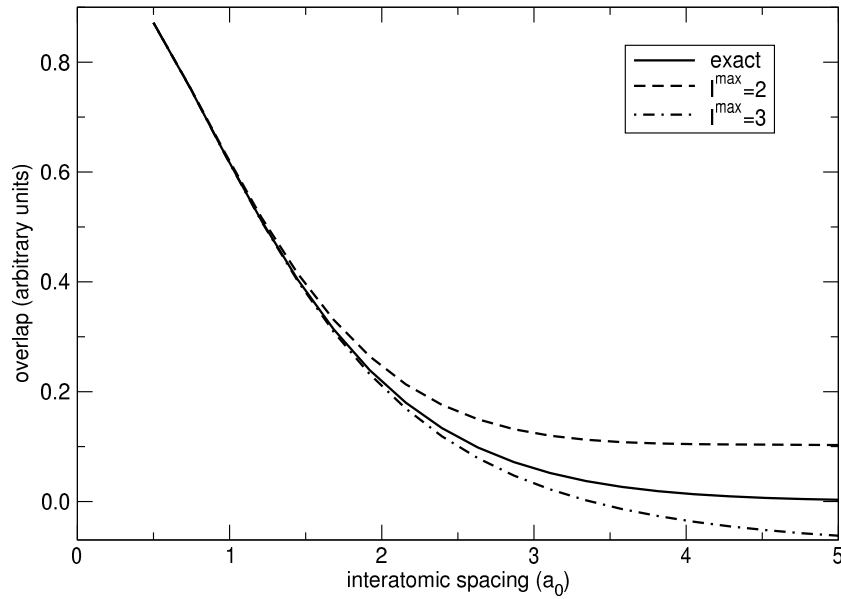
Figure 8.5: The analytic overlap (full line) over inter-atomic spacing for a hydrogen dimer in lcao compared to the results obtained from transformed orbitals with $l^{max} = 2$ (dashed) and $l^{max} = 3$ (dash dotted). See the text for details.

The angular momentum cutoff for the transformation is given in column one. Column two and three provide the calculated overlap, once with one transformed center (wavefunction two into the center of the first) and once with two transformed centers (both wave functions in the center of gravity). Due to the natural cutoff in the case of one transformed center, the result converges to the exact value at the highest angular momentum contribution of the onsite function ($l = 1$). For two transformed centers, the overlap hardly converges. Note that this effect gets worse for larger separations and more complex wave functions.

l^{max}	one transformed center	two transformed centers
0	0.38823	0.81651
1	1.59196	1.61325
2	1.59196	1.59249
3	1.59196	1.59180
4	1.59196	1.59201
5	1.59196	1.59195

Table 8.1: Calculated overlap for two wave functions with hydrogen $1s$ and $2p_z$ contributions, separated at 1.45a.u. along z. The angular momentum cutoff for the transformation is given in column one. Column two and three provide the calculated overlap, once with one transformed center (wave-function two into the center of the first) and once with two transformed centers (both wave functions in the center of gravity). See text for details.

Three-center integrals with at least two identical centers

For three-center integrals, with two expansions residing at the same center, the third function should be transformed to the center of the first and second function. In this way, the maximum angular momentum from the transformation gets naturally limited by the limited untransformed expansions (see equation (B.71) for details):

$$\int f^{(1)}_{lm'}(|\mathbf{r}|)h^{(1)}_{lm''}(|\mathbf{r}|)u^{(2)}_{lm'''}(|\mathbf{r}|)Y_{lm'}(\mathbf{r})Y_{lm''}(\mathbf{r})Y_{lm'''}(\mathbf{r})d^3r$$

$$l'''_{max} = l'_{max} + l''_{max}$$

This situation e.g. occurs in calculation of tight-binding potential matrix elements of the form $\langle \varphi^{(1)}|V^{(2)}|\phi^{(1)}\rangle$.

This class of cutoff can also be applied, when solving Schrödinger's equation. Suppose to have a maximum cutoff for the wave function (l^{max}_ψ). The density and the therefrom derived potential in selfconsistent calculations should then take contributions up to $l^{max}_v = 2 \cdot l^{max}_\psi$ into account. Table 8.2 illustrates this for the eigenvalue of the deformed hydrogen atom (setup (1/4:4)). The wave-function cutoff has been held fixed to $l^{max}_\psi = 3$.

l^{max}_v	eigenvalue (H)
3	-0.38729
4	-0.38845
5	-0.38711
6	-0.38583
7	-0.38583

Table 8.2: The eigenvalue of the deformed hydrogen atom (setup (1/4:4)). The wave-function cutoff has been held fixed to $l^{max}_\psi = 3$. See text for details.

Three-center integrals without identical centers

The numerically most demanding contributions in electronic structure calculations come from real three-center integrals of the form $\langle f^{(1)}|h^{(2)}|u^{(3)}\rangle$. For these integrals, the application of selection rules is absolutely indispensable. The transformation of two functions to the center of the remaining however does not lead to a natural limitation in angular momenta. This usually not only leads to *slow* convergence, but to totally wrong results (the reason will be illustrated in the following). Table 8.3 provides the result for an integral of the form

$$\int f_{lm'}^{(1)}(|\mathbf{r}|)h_{lm''}^{(2)}(|\mathbf{r}|)u_{lm'''}^{(3)}(|\mathbf{r}|)Y_{lm'}(\mathbf{r})Y_{lm''}(\mathbf{r})Y_{lm'''}(\mathbf{r})d^3r, \tag{8.3}$$

with f, h and u corresponding to wave functions with contributions from hydrogen $1s$ and $2p_z$ residing at $\mathbf{r}_1 = (0,0,0)$, $\mathbf{r}_2 = (0,0,1.45)$, and $\mathbf{r}_3 = (0,0,2\cdot1.45)$, respectively.

l^{max}	result
2	0.23582
3	0.27596
4	0.28437
5	0.28630
exact	0.07545

Table 8.3: The result for an integral of the form (8.3). The expansion center of $h^{(2)}$ and $u^{(3)}$ have been transformed to $\mathbf{r}_1$, using a cutoff l^{max}. Even for increased cutoff, the exact result is not achieved. See text for details.

The expansion center of $h^{(2)}$ and $u^{(3)}$ have been transformed to $\mathbf{r}_1$, using a cutoff l^{max}. Even for increased cutoff, the exact result is not achieved. The reason is that a transformation always leads to so called Gauß oscillations (see section 8.3). Without effective limitation of angular momentum contributions to the integral, the Gauß oscillations are included and the result therefore can be far from the exact value.

A better convergence can be achieved applying a divide and conquer approach. In a first step, we transform the function $u^{(3)}$ to $\mathbf{r}_2$ and determine a new function $g^{(2)}$, centered at $\mathbf{r}_2$ as follows:

$$
\begin{aligned}
g^{(2)}(\mathbf{r}) &= \sum_{lm'lm_t'''} h_{lm'}^{(2)}(|\mathbf{r}-\mathbf{r}_2|)u_{lm_t'''}^{(3@\mathbf{r}_2)}(|\mathbf{r}-\mathbf{r}_2|)Y_{lm'}Y_{lm_t'''} \\
&= \sum_{lm_g}\underbrace{\sum_{lm''lm_t'''} h_{lm'}^{(2)}(|\mathbf{r}-\mathbf{r}_2|)u_{lm_t'''}^{(3@\mathbf{r}_2)}(|\mathbf{r}-\mathbf{r}_2|)c_{lm'',lm_t''',lm_g}}_{g_{lm_g}(|\mathbf{r}-\mathbf{r}_2|)}Y_{lm_g} \qquad (8.4) \\
&= \sum_{lm_g} g_{lm_g}^{(2)}(|\mathbf{r}-\mathbf{r}_2|)Y_{lm_g} \qquad (8.5)
\end{aligned}
$$

The notation $u^{(3@\mathbf{r}_2)}$ and the index t thereby accounts for the fact that the radial part and angular momentum contributions of $u^{(3)}$, when transformed to $\mathbf{r}_2$ are different from the original function.

Transformation of g to $\mathbf{r}_1$ then allows to rewrite the integral in the following way (without any loss of generality, we suppose $f^{(1)}$ to reside at the origin):

$$\int f^{(1)}(\mathbf{r})h^{(2)}(\mathbf{r})u^{(3)}(\mathbf{r})d^3r$$

$$= \int f^1(\mathbf{r})g^{(2)}(\mathbf{r})d^3r$$

$$= \int \sum_{lm'lm_{gt}} f_{lm'}^{(1)}(|\mathbf{r}|)g_{lm_{gt}}^{(2@\mathbf{r}_1)}(|\mathbf{r}|)Y_{lm'}Y_{lm_{gt}}d^3r \tag{8.6}$$

$$= \int \sum_{lm'} f_{lm'}^{(1)}(|\mathbf{r}|)g_{lm'}^{(2@\mathbf{r}_1)}(|\mathbf{r}|)r^2dr \tag{8.7}$$

In this way, a cutoff similar to the two-center cutoff discussed above emerges for the transformation of g. Note however that this cutoff limits lm_{gt} and does not hold for the expansion (lm_g) of g in (8.5). The important point is, that, provided we have a given function g, centered at $\mathbf{r}_2$, we can determine (8.7) without applying an artificial cutoff for the second transformation. This step therefore does not introduce contributions from Gauß oscillations.

The expansion of $g^{(2@\mathbf{r}_2)}$ in principle has infinitely high angular momentum contributions. Nevertheless, we can introduce a cutoff lm_g^{max}. Together with the cutoff lm''_{max} for $h^{(2)}$ (remember: the function $h^{(2)}$ has a limited angular momentum expansion, because it is onsite), the selection rules for the Gaunt coefficients in (8.4) then allow to derive a cutoff for the transformation of $u^{(3)}$ to $\mathbf{r}_2$ as follows:

$$|l'' - l_g| \leq l_t''' \leq |l'' + l_g|$$

$$\Rightarrow l_{t,max}''' = l_{max}'' + l_g^{max}$$

Table 8.4 shows the result for the three center integral used for table 8.3, this time determined following the double transformation approach. The functions $f^{(1)}$, $h^{(2)}$ and $u^{(3)}$ have contributions up to $l = 1$. The cutoff for the transformations therefore are:

$$\begin{aligned} l_{gt}^{max} &= l_{max}' \\ l_{t,max}''' &= l_g^{max} + 1 \end{aligned}$$

Table 8.5 illustrates the natural limitation of $l_{t,max}'''$ for given l_g^{max}.

l_g^{max}	$l_{t,max}'''$	result	|deviation|
1	2	0.07136	0.00409
2	3	0.07732	0.00187
3	4	0.07489	0.00056
4	5	0.07564	0.00019
exact		0.07545	

Table 8.4: The result for an integral of the form (8.3), applying the double transformation approach discussed in the text. This approach makes use of selection rules to suppress Gauß oscillation effects arising from re-expansion. The quality of the result is directly related to the angular momentum cutoff l_g^{max}.

l_g^{max}	$l_{t,max}'''$	result
2	2	0.07683
2	3	0.07732
2	4	0.07732

Table 8.5: Demonstration of the naturally emerging angular momentum cutoff for l_t''', when applying the double transformation approach discussed in the text.

Following the direct transformation approach, two re-expansions need to be artificially limited in angular momenta. The advantage of the double transformation approach is, that only one cutoff, namely l_g^{max} needs to be introduced. The resulting selection rules then allow to transform the expansion centers exactly.

9 Energy of exchange and correlation

The exchange and correlation energy contribution (3.14) to the new functional (3.8)

$$\Delta E_{xc} = E_{xc}[\sum_i \bar{n}_i] - \sum_i E_{xc}[\bar{n}_i]$$

has been approached by cluster expanding $E_{xc}[\sum_i \bar{n}_i]$. In the following, I use a short hand notation of the form:

$$
\begin{aligned}
E_{xc}[\bar{n}_i] &= E_i \\
E_{xc}[\bar{n}_i + \bar{n}_j] &= E_{ij} \\
E_{xc}[\bar{n}_i + \bar{n}_j + \bar{n}_k] &= E_{ijk} \\
&\vdots
\end{aligned}
$$

$$
\begin{aligned}
E_{xc}[\sum_i \bar{n}_i] - \sum_i E_{xc}[\bar{n}_i] =\ & \underbrace{\sum_i E_i - \sum_i E_i}_{=0} \\
& + \frac{1}{2!} \sum_{i \neq j} E_{ij} - E_i - E_j \\
& + \frac{1}{3!} \sum_{i \neq j \neq k} \{ E_{ijk} - E_i - E_j - E_k \\
& - (E_{ij} - E_i - E_j) \\
& - (E_{ik} - E_i - E_k) \\
& - (E_{jk} - E_j - E_k) \} \\
& + \cdots
\end{aligned}
\tag{9.1}
$$

The rule fore the n-th term is: inside the sum over n indices we have one n order term and subtract all possible lower order terms[1]. The idea of the cluster expansion

---

[1] All possible means that one has to take $\begin{pmatrix} i \\ n \end{pmatrix}$ terms for the i-th order. This corresponds to writing down all index combinations without double counting (ijk, ikj etc. is used only once) or doing double counting and using a prefactor of $\frac{1}{i!}$.

can be explained best using an example. Think of a 5 particle cluster. Particle 1,2 and 3,4 should overlap. The three groups should be separated in such a way, that the densities do not overlap. The 5-particle term then 'degenerates' into two 2-particle and a 1-particle term. The terms that are not compensated directly in the order-5 expression are compensated by lower-order terms. Writing down all terms, one can see that there will remain exactly two two-order (1,2 and 2,3) and one one-order (5) term. The deformed densities $\bar{n}_i$ are localized (see figure 7.13 and related text). The highest order contribution to the cluster expansion therefore should correspond to the number of nearest neighbors.

For each n-order summand (e.g. the expression in curly brackets in line 3-6 of (9.1)), the densities of the n contributing atoms should be transformed onto a 3d grid centered at the center of gravity. In order to minimize numerical errors (error cancellation), it is important that all contributions (even the first order terms) share the same grid. The resolution of the 3d representation may be increased near the center of gravity (e.g. using a star-burst mesh with logarithmic radial spacing), because these regions actually contributions to the difference (3.14).

It is not possible to use the transformation of spherical harmonics expansions discussed in section 8.2. This is because the energy of exchange and correlation expression does not allow to apply selection rules (see section 8.4 for a detailed discussion). The Gauß oscillations therefore heavily distort the result.

For the dimer calculations presented in part III, the cluster expansion becomes trivial: $E_{xc}[\sum_i \bar{n}_i] - \sum_i E_{xc}[\bar{n}_i] = E_{12} - E_1 - E_2$. The difference has been calculated on the cylinder grid discussed in section 5.3.

10 Tight binding

10.1 Basis set convergence

Table 10.1 shows the basis set convergence of the total energy in the tight-binding calculation (E_{tb}) for H_2 at the lda ground-state separation (1.45 a.u.). The deformed orbitals basis thereby is extended by atomic orbitals of the following radial shape:

$$
\begin{aligned}
1s^\lambda &\sim e^{-\lambda r} \\
2p_z &\sim re^{-\frac{1}{2}r} \\
3p_z &\sim (6-r)re^{-\frac{1}{3}r} \\
3d_{z^2} &\sim r^2 e^{-\frac{1}{3}r}
\end{aligned}
$$

A combination of deformed orbitals with three $1s$ orbitals and one $2p_z$ function has been found to be sufficiently accurate.

extra basis functions	E_{tb} (H)
no	-0.72902
all above $+1s^{1.0}$	-0.74389
all above $+1s^{1.5}$	-0.76693
all above $+1s^{2.0}$	-0.76694
all above $+1s^{5.0}$	-0.76705
all above $+2p_z$	-0.76720
all above $+3p_z$	-0.76720
all above $+3d_{z^2}$	-0.76734
$+(1s^{1.0},1s^{1.5},1s^{2.0},2p_z)$	-0.76710

Table 10.1: The basis set convergence of the total energy in the tight-binding calculation (E_{tb}) for H_2 at the lda ground-state separation (1.45 a.u.). See the text for details.

10.2 V_{xc} of fragment densities

Unlike in the deformation process, the effect on the total energy of an approximation of the exchange and correlation potential $V_{xc}[\sum_i n_i]$ by a superposition of atomic contributions of the form $\sum_i V_{xc}[n_i]$ can not be neglected. Figure 10.1 shows the resulting binding energy for deformed fragments, once applying the exact potential $V_{xc}[\sum_i n_i]$ (dashed black line) and once the approximate potential $\sum_i V_{xc}[n_i]$ (grey

	E_{tb} (H)	E_{diag} (H)	$E_{tb} - E_{diag}$ (H)
$V_{xc}[\sum_i n_i]$	-0.76719	-0.57537	-0.19182
$\sum_i V_{xc}[n_i]$	-1.18165	-1.02781	-0.15383
delta (H)	0.41446	0.45244	-0.03799
delta (% of E_{bond})	225	245	21

Table 10.2: The effect of the approximation of the exchange and correlation potential $V_{xc}[\sum_i n_i]$ by a superposition of atomic contributions of the form $\sum_i V_{xc}[n_i]$ for the lda equilibrium separation of H_2 (1.41 a.u.). See the text for details.

line) in the tight-binding calculation. Table 10.2 provides detailed information for the lda equilibrium separation of H_2 (1.41 a.u.). The error introduced in the tight-binding energy by the approximation of the exchange and correlation potential has been found to be in the range of $415\,mH$, which corresponds to $225\,\%$ of the binding energy ($E_{bond} \approx 185\,mH$). Due to the afforded error cancellation in line two of (3.8), the effective deviation is reduced to about $21\,\%$ of the binding energy ($\sim 38\,mH$), which however is still far too large. The reason for the success of the approximation in the context of deformation (section 5.2, item three) and the failure in the tight-binding calculation is the following: in the deformation process, the approximation of the exchange and correlation potential affects the trial density. For the trial density however, a variational principle holds. This is not the case for the potential of the tight-binding calculation. As can be seen from equation (2.38), errors in the potential linearly enter the total energy.

For the dimer calculations presented in part III, the exchange and correlation potential has been calculated on the cylinder grid discussed in section 5.3. For a numerically efficient and general implementation, the following two approaches may be applicable. Due to the localized character of the deformed density, the cluster expansion approach discussed in section 9 should lead to sufficiently accurate results. An alternative, but more involved approach is the application of selection rules as follows: Suppose we want to determine a matrix element of the form $\langle \varphi_i | V_{xc} | \varphi_j \rangle$. First, the expansion centers of the densities of the nearest neighbors are transformed to $\mathbf{r}_j$. Then, V_{xc} is determined as spherical harmonics expansion centered at $\mathbf{r}_j$. Following the double transformation approach discussed in 8.4, a new expansion, which may be limited in the number of angular momenta, is determined from the product $V_{xc} | \varphi_j \rangle$ and then transformed to $\mathbf{r}_i$.
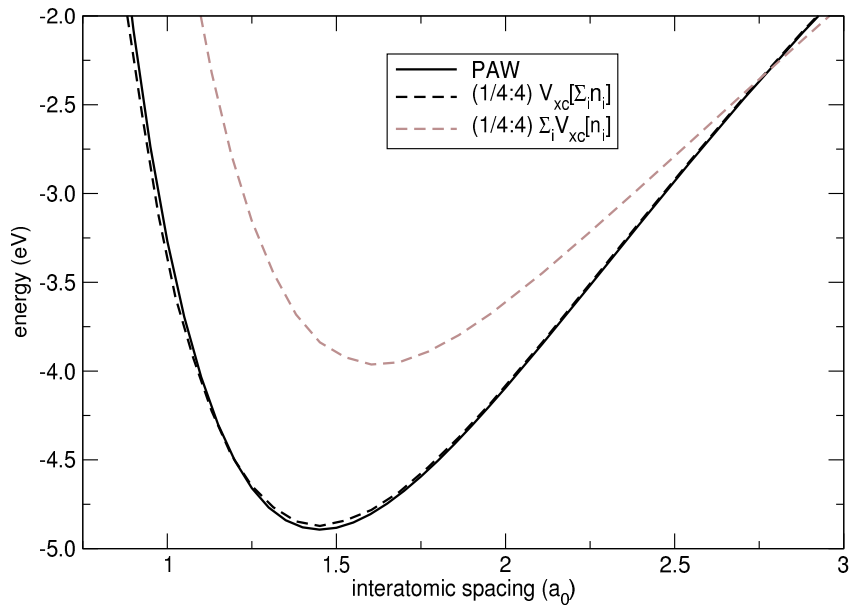
Figure 10.1: The binding energy for deformed fragments, once applying the exact potential $V_{xc}[\sum_i n_i]$ (dashed black line) and once the approximate potential $\sum_i V_{xc}[n_i]$ (grey line) in the tight-binding calculation. The setup for the nonspeherical deformation is coded in the form $(\tilde{r}_p : \tilde{r}_t)$ (see equation 4.46 and the corresponding text for further details). See the text for a discussion.

11 Summary & Outlook

The main numerical effort in common electronic structure methods is spent in the setup and diagonalization of the Hamiltonian. Without further approximations, this effort scales cubicly with the number of particles involved. The complexity of quantum mechanics thereby usually requires an iterative approach. This is unfavorable, because the badly scaling system of equations needs to be solved several times in order to reach sufficiently accurate results. Over the years, there have been several more or less sophisticated approaches to circumvent these problems. The effort in reducing the numerical demands usually either results in less intelligible approaches, theoretically not well funded approximations or representations which make it hard to extract the physical meaning.

The approach presented in this work is focused on a formulation which is consistent with the physico-chemical intuition. Theoretically well funded and straight forward approximations and numerical efficiency thereby are not mutually exclusive, but lead to synergetic effects.

The transformation from isolated to 'clustered' atoms is splitted in two steps: deformation from the atomic to a reference state, and clustering. The numerical most demanding part is the determination of the clusters total energy. This effort has been reduced by the application of a new formulation of a non-selfconsistent density functional. Furthermore, an ab initio based construction of embedding potentials has been introduced. The embedding potentials reflect the crystal structure and allow to determine non-spherically deformed fragment densities as input densities for non-selfconsistent functionals. Due to the non-spherical character of the fragment densities, the new construction overcomes the limitations of frozen atomic fragments.

The following listing is a sketch of the steps that need to be taken next in order to generalize the new approach to a full fledged electronic structure method:

- A node-less formulation of the tight-binding expressions, which allows to apply the frozen core approximation needs to be derived. It is recommended to follow the sequence of Harris-Foulkes and frozen core approximation discussed in section (4.1). The actual formulation thereby should take the possible implementation of the exchange and correlation potential, discussed in the next item, into account. Following an approach based on atom-centered spherical harmonics expansions, the application of selection rules discussed in section (8.4) is indispensable.

- Detailed studies of the core embedding potentials, according to the valence potential studies presented in the main part of this thesis, need to be carried

out. In particular, the effect of the frozen core approximation in the deformation process should be studied. The transformation from the node-less picture to real densities implies an orthogonalization to the corresponding core states. The core states obtained in the selfconsistent deformation potential however are different from the frozen core states. The significance of this deviation for the quality of the trial density needs to be checked. In addition, the pros and cons of free and spherically localized atomic states as frozen core states should be examined.

- The logarithmic radial mesh applied in the deformation process should be extended to provide a higher radial resolution in the neighbors region. The neighbors valence deformation potential is quite localized. This may lead to a radial egg-box effect for standard logarithmic grids. A possible approach, discussed in [51], is to omit contributions for a selected number of points on either side of the neighbors distances in integration. The missing contribution is then obtained from a finer mesh which covers this region.

- A three dimensional real-space mesh for the determination of the exchange and correlation energy (3.14) in a cluster-expansion approach (discussed in section 9) needs to be introduced. The effective contribution thereby comes from the regions in which the neighboring densities overlap and should be smooth. A coarse radial grid, centered at the center of gravity of the cluster, should be sufficient. The directions and weights for solid angles (Ω) may be generated following Pederson and Jackson's approach [86]. Alternatively, an equispaced star-burst mesh could be applied.

- For the determination of the exchange and correlation potential in the tight-binding calculation, a 3D-mesh similar to the one discussed in the previous item could be applied. The potential however has the full atomic contribution and therefore requires a higher resolution near the nuclei. It might be numerically advantageous to apply the double transformation approach based on atom-centered spherical harmonics expansions discussed in section 10.2.

- Charge transfer.

- Forces.

In order to reduce the numerical costs, further approximations usually applied in the context of empirical tight-binding - such as parametrization of three center integrals - might be introduced [12, 13].

12 Dimer Method

12.1 Change log

The dynamical dimer method for the determination of transition states, introduced by the author in the framework of a diploma thesis [87] has been expanded and published [88] (see appendix C). The derivations have been reworked for better readability. Besides several minor extensions, the optimized friction control has been extended by the possibility to limit the kinetic energy for the rotational, perpendicular and parallel motion individually (see appendix C for details). The code finally has been merged into the release branch of the CP-PAW simulation package.

12.2 Handling the dimer method in CP-PAW

12.2.1 File names, start-up

The dynamical dimer method requires the parallel calculation of two coupled systems, referred to as 'monomers'. Each monomer has its own control-, structure-, and output files. The name convention is case_mi.ending, with i being the identifier of the monomer. 'case_m2.strc' e.g. specifies the structure input file for monomer 2. The parallelization code in principle allows for a higher number of polymers (e.g. for future implementation of the nudged elastic band method). For technical reasons, a polymer calculation has to be triggered using a special command:

./paw_fast.x case_polymer.cntl

In future versions, the case_polymer.cntl will only contain control settings which are specific for the polymer parallelization. All usual control settings (the traditional 'case.cntl') are kept in 'case_mi.cntl'. In the actual implementation (which is limited to dimer calculations), the case_polymer.cntl file is not read by the program and therefore does not have to exist physically. The above command simply triggers the read-in of case_m1.cntl and case_m2.cntl. Even though it is possible to use different control setting for the individual monomers of the dimer, it is not recommended. Best practice is to link 'case_m1.cntl' and 'case_m2.cntl' with one file called 'case.cntl'. The structure files 'case_m1.strc' and 'case_m2.strc' have to be present, and need to differ in the atomic positions. Dimer specific information is reported to 'case_mi.dimer_prot' and to stdout (in the following referd to as 'out').

12.2.2 Control-file parameters

Table 12.1 and 12.2 list the dimer method specific control-file parameters.

Parameter	Description
DIMERDIST	the constrainde dimer length in massweighted coordinates
KDLENGTH	keeps the dimer-length fixed to the value resulting from strc or restart files
STRETCHDIST	the dimer length which sould be achieved during stretch mode
CONSTRSTEP	the steplength in massweighted coordinates for the couple constraint
COUPLE ATOM	the given atom is constrained to the same coordinates on monomer 1 and 2.
DFOLLOWDOWN	=F: normal dimer calculation; =T: parallel paw calculation with usual equation of motion
INHIBITUP	the motion parallel to the dimer axis is constrained to 0
INHIBITPERP	the motion perpendicular to the dimer axis is constrained to 0
ONLYROT	allows only rotation of the dimer
ONLYPERP	allows only perpendicular motion
WDOWN	(developer option) scales the atomic masses of monomer 1 by WDOWNFACT
WDOWNFACT	scaling factor for the masses of monomer 1
FMPARA	fictitiuos mass for the parallel motion (typically -1.)
FMPERP	fictitiuos mass for the perpendicular motion (typically 0.5)
FMROT	fictitiuos mass for the rotational motion (typically 0.25)
FRICPARA	fricion for the parallel motion
FRICPERP	fricion for the perpendicular motion
FRICROT	fricion for the rotational motion
OPTFRICPARA	should estimated optimal friction be used for this type of motion
OPTFRICPERP	should estimated optimal friction be used for this type of motion

Table 12.1: Description of the dimer specific control parameters. All lengths in mass-weighted coordinates.

Parameter	Description
OPTFRICROT	should estimated optimal friction be used for this type of motion
TMAXPARA	max. Temperature for this type of motion (estimated via $\langle E_{kin} \rangle = \frac{f}{2} k_B T$); only active for optfric=T
TMAXPERP	max. Temperature for this type of motion (estimated via $\langle E_{kin} \rangle = \frac{f}{2} k_B T$); only active for optfric=T
TMAXROT	max. Temperature for this type of motion (estimated via $\langle E_{kin} \rangle = \frac{f}{2} k_B T$); only active for optfric=T
FAUTO[PARA/PERP/ROT]	enables the force autopilot, which increases the friction to FRIX(+)[PARA/PERP/ROT] if the dimer moves opposite to the direction of the forces
FRIC(+)[PARA/PERP/ROT]	see FAUTO
DLFLEX	allow the dimers length to change (shortened/stretched by DSTEP per simulation step until the dimers length equals DTOBE as long as NSTEPS is not present; if NSTEPS is present, DSTEP gives the limits the maximal stepwidth)
LCS	see CENTERDIFFMIN
CENTERDIFFMIN	only shorten/stretch the dimer's lenth if the center of gravity moved less than this value for LCS steps
DSTEP	see DLFLEX
DTOBE	see DLFLEX
NSTEPS	on the presence of NSTEPS, the dimerlength is reduced percentual in such a way, that DTOBE is achieved after NSTEPS
!ITERATION	(developers options controlling the internal iteration)
!OUTPUT	enables ENERGYTRA output. should be disabledS
ENERGYTRA	(developers option) write the actual total energy and distance from RTS to a file
NATOMS	3*NATOMS determines the dimension of RTS
RTS	coordinates of the transition state

Table 12.2: Description of the dimer specific control parameters. All lengths in mass-weighted coordinates.

The following is a sample control file. The parameters may be mutually exclusive.

```
!CONTROL
!DIMER
  DIMERDIST=2.0
  KDLENGTH=T
  STRETCHDIST=100.0
  !CONSTRAINTS CONSTRSTEP=0.5
    !COUPLE ATOM='H_1' !END
    !COUPLE ATOM='H_5' !END
  !END
  !MOTION
    DFOLLOWDOWN=F
    INHIBITUP=F
    INHIBIPTERP=F
    ONLYROT=F
    ONLYPERP=F
    WDOWN=F
    WDOWNFACT=2.000
    FMPARA=-1.0
    FMPERP=0.5
    FMROT=0.25
    FRICPARA=0.05
    FRICPERP=0.05
    FRICROT=0.05
    OPTFRICPARA=T
    OPTFRICPERP=T
    OPTFRICROT=T
    TMAXPARA=100.
    TMAXPERP=100.
    TMAXROT=100.
    FAUTOPARA=T
    FAUTOPERP=T
```

```
      FAUTOROT=T
      FRIC(+)PARA=0.05
      FRIC(+)PERP=0.05
      FRIC(+)ROT=0.05
    !END
    !FLEXLENGTH
      DLFLEX=F
      LCS=0
      CENTERDIFFMIN=0.2
      DSTEP=0.1
      DTOBE=100.0
      NSTEPS=1000
    !END
    !ITERATION
      LITERMAX=100
      DLAMBDA=0.000001
      VITER=100
      DVELOCITY=0.00001
    !END
    !OUTPUT
      ENERGYTRA=0.0001
      NATOMS=6
    RTS= 9.17391413148942 6.94296002500009 17.0181424401132 10.6780092163608
      10.1572547830354 17.0327995478249 7.14274321484992 9.85239646799042
      17.0317177501930 8.99698614125294 8.96184528623900 21.4880576000447
      8.99608836545232 9.00108048192150 12.5578511945098 8.99836684655655
      8.98406664039175 17.0361651787350
    !END
  !END
```

12.2.3 Recipes

Using DIMERDIST

- provide two strc files

- DIMERDIST=val; KDLENGTH=F

- rdyn off

- dimer block present in cntl file

- start with electron minimization

Monomer 2 will be placed according to[1]

$$\mathbf{x}_1^{start} = \mathbf{x}^{strc}{}_1$$

$$\mathbf{x}_2^{start} = \mathbf{x}^{strc}{}_1 + a(\mathbf{x}_2^{strc} - \mathbf{x}_1^{strc})$$

with a such that the dimers length equals DIMERDIST.

The 'case_mi.dimer_prot' file states :

'DIMER: DIMER_PROPAGATE: WE PLACED THE DIMER AND NOW HAVE A DISTANCE OF'

Using KDLENGTH

- provide two strc files

- KDLENGTH=T

- rdyn off

- dimer block present in cntl file

- start with electron minimization

$\mathbf{x}_i^{start} = \mathbf{x}^{strc}{}_i$. The dimers length is constrained to the value resluting from the given strc.

The 'case_mi.dimer_prot' file states:

'DIMER: DIMER_PROPAGATE: WE KEPT THE DIMERLENGTH AND NOW HAVE A DISTANCE OF'

Using STRETCHDIST

- provide the same restart file for both monomers

- do not provide DIMERDIST, set KDLENGTH=F, set STRETCHDIST=val

- rdyn on

---

[1]$\mathbf{x}^{strc}{}_i$ refers to the mass-weighted coordinates read from the strc file for monomer i; $\mathbf{x}_i^{start}$ refers to the mass-weighted coordinates used as initial position for monomer i

Monomer 2 will follow down the potential energy surface (as usual) until the dimers length equals STRETCHDIST. Monomer 1 is fixed to its original position.

The out file states:

DIMER STRETCH : d should be", stretchdist," and is", sqrt(sqdimerdist)

General Hints

Do not start with optfric, but with a fixed value for the friction to damp stiff modes. Best practice is to use some steps with ONLYROT=T, follwed by INHIBITUP=T. Then switch to normal dimer calculation and limit the max. allowed temperature for the parallel, perpendicular and roattional motion of the dimer.

Appendices

A Electronic structure methods at length

A.1 The Hartree approximation

An early approximative approach solving Schrödinger's equation for a many particle system was developed by Hartree. He assumed the electrons to be non interacting ("independent electron approximation"). In addition, the fact that the electron experiences the electric fields of all other electrons was (approximately) incorporated by treating the remaining electrons as a smooth distribution of negative charge with the charge density[1]

$$n(\mathbf{r}) \;=\; \sum_i |\psi_i(\mathbf{r})|^2 \; . \tag{A.1}$$

The potential energy of a given electron can then be written as:

$$V_e(\mathbf{r}) \;=\; -\int \frac{n(\mathbf{r}')}{|\mathbf{r} - \mathbf{r}'|} \, d\mathbf{r}' + V_{ext}(\mathbf{r}). \tag{A.2}$$

Placing (A.2) in the one-electron Schrödinger equation leads to the so called Hartree equations:

$$\left[-\frac{1}{2} \nabla_{\mathbf{r}}^2 - \int \frac{n(\mathbf{r}')}{|\mathbf{r} - \mathbf{r}'|} \, d\mathbf{r}' + V_{ext}(\mathbf{r}) \right] \psi_i(\mathbf{r}) \;=\; \varepsilon_i \psi_i(\mathbf{r}). \tag{A.3}$$

Note that these equations can also be obtained by applying the variational principle to the expectation value of the energy

$$E[\Psi] \;=\; \frac{\langle \Psi | \hat{H} | \Psi \rangle}{\langle \Psi | \Psi \rangle} \, ,$$

where Ψ is written as product of one electron wave functions in the above manner. They are practically solved iteratively by assuming a charge density for the electrons, solving Schrödinger's equation and then recalculating an improved charge density using the one-electron wave functions until the potential is converged. Methods which approximate the electron-electron interaction by the interaction of an electron with

---

[1]The sum extends over all occupied one-electron levels except the one of the considered electron. Note that $\langle \psi_i | \psi_j \rangle = \delta_{ij}$.

a field (of the remaining electrons) and iteratively solve the problem in the above described manner are called "self consistent field approximations" (SCF) [89]. These approximations in general fail to describe the effect of a particular electron on the electron under consideration.

A.2 The Hartree-Fock approximation

The requirement of the wave function being antisymmetric with respect to the interchange of two of its arguments

$$\Psi\left(\mathbf{x}_1, ..., \mathbf{x}_i, ..., \mathbf{x}_j, ..., \mathbf{x}_n\right) \quad = \quad -\Psi\left(\mathbf{x}_1, ..., \mathbf{x}_j, ..., \mathbf{x}_i, ..., \mathbf{x}_n\right)$$

can be satisfied by replacing it by a so called Slater determinant of one-electron wave functions[2]:

$$\Psi^{HF}\left(\mathbf{x}_1, ..., \mathbf{x}_i, ..., \mathbf{x}_j, ..., \mathbf{x}_n\right) \quad = \quad \frac{1}{\sqrt{n!}}\begin{vmatrix} \psi_1\left(\mathbf{x}_1\right) & \cdots & \psi_n\left(\mathbf{x}_1\right) \\ \vdots & \ddots & \vdots \\ \psi_1\left(\mathbf{x}_n\right) & \cdots & \psi_n\left(\mathbf{x}_n\right) \end{vmatrix}$$

This approach exploits the nature of determinants. They change their sign when any two columns or rows are interchanged.

Minimization of the expectation value of the energy[3]

$$E[\Psi^{HF}] \quad = \quad \langle\Psi^{HF}|\hat{H}|\Psi^{HF}\rangle$$

with respect to the one-electron wave functions ψ_i leads to the Hartree-Fock equations[4] [89]:

$$\underbrace{\left[-\frac{1}{2}\nabla_{\mathbf{r}}^2 - \int \frac{n(\mathbf{r}')}{|\mathbf{r} - \mathbf{r}'|}\, d\mathbf{r}' + V_{ext}(\mathbf{r})\right]}_{Hartree\ operator}\psi_i(\mathbf{r}) - \sum_j \int \frac{\psi_j^*(\mathbf{r}')\psi_i(\mathbf{r}')\psi_j(\mathbf{r})}{|\mathbf{r} - \mathbf{r}'|}\delta_{s_i s_j}\, d\mathbf{r}' \quad = \quad \varepsilon_i\psi_i(\mathbf{r})$$

---

[2] In a simplistic way, $\psi_j\left(\mathbf{x}_i\right)$ can be understood as " electron i in the jth one-electron state".

[3] Note that Ψ^{HF} is normalized: $\langle\Psi^{HF}|\Psi^{HF}\rangle = 1$.

[4] The terms with $i = j$ are usually not included in the Hartree/Coulomb and exchange terms, even though they cancel each other. The exchange term excluding the case $i = j$ is also called "Fock operator".

Using (A.1) this can be rewritten as follows:

$$\left[-\frac{1}{2}\nabla_{\mathbf{r}}^2 + \sum_j \int \frac{\psi_j^*(\mathbf{r}')\psi_j(\mathbf{r}')}{|\mathbf{r}-\mathbf{r}'|}\,d\mathbf{r}' + V_{ext}(\mathbf{r}) \right]\psi_i(\mathbf{r}) - \sum_j \int \frac{\psi_j^*(\mathbf{r}')\psi_i(\mathbf{r}')\psi_j(\mathbf{r})}{|\mathbf{r}-\mathbf{r}'|}\delta_{s_i s_j}\,d\mathbf{r}'$$

$$= \left[-\frac{1}{2}\nabla_{\mathbf{r}}^2 + V_{ext}(\mathbf{r}) \right]\psi_i(\mathbf{r}) + \underbrace{\sum_j \int \frac{\psi_j^*(\mathbf{r}')\psi_j(\mathbf{r}')\psi_i(\mathbf{r})}{|\mathbf{r}-\mathbf{r}'|}\,d\mathbf{r}'}_{Coulomb\,term}$$

$$- \underbrace{\sum_j \int \frac{\psi_j^*(\mathbf{r}')\psi_i(\mathbf{r}')\psi_j(\mathbf{r})}{|\mathbf{r}-\mathbf{r}'|}\delta_{s_i s_j}\,d\mathbf{r}'}_{exchange\,term}$$

$$= \varepsilon_i\psi_i(\mathbf{r}). \tag{A.4}$$

The Hartree-Fock equations differ from the Hartree equations by the exchange term. The three most noticeable effects of the exchange term are the following:

1. For $i = j$ the exchange term cancels the Coulomb term exactly and therefore suppresses the self interaction of the electrons.

2. For $i \neq j$ and $s_i = s_j$ (different electrons with the same spin) the exchange term contributes to the potential.

3. For $i \neq j$ and $s_i \neq s_j$ (different electrons with different spin) the exchange term vanishes.

The exchange term thus describes the interaction between electrons with the same spin. Since an exact wave function usually can not be formed using a single determinant, the Hartree-Fock approach gives a ground state energy that differs from the exact energy. The Hartree-Fock energy always is higher than the real energy. The difference between the exact (nonrelativistic) and the Hartree-Fock energy is called the "correlation energy".

There exist approaches using a higher number (up to millions) of determinants, which achieve a higher accuracy at the expense of computing time. These methods are referred to as configuration interaction (CI) calculations. For further details see [22].

A.3 The Thomas-Fermi theory

Solving the Schrödinger equation for a multi particle system, even approximatively, as shown above, is a considerable task because one has to deal with i×N dimensional wave

functions (i=3 for nuclei and i=4 for electronic wave functions including a discrete spin coordinate). There is a long history of approaches (starting with the works of Thomas and Fermi around 1927) trying to replace these many-body wave functions (at least partly) by the much simpler (electron) density function $n(\mathbf{r})$, which solely depends on 3 spatial coordinates. Thomas and Fermi realized that statistical considerations can be used to approximate the distribution of electrons in atoms in the following way[5] [22]:

- One divides the space in many small cubes of the volume ΔV, containing a fixed number of electrons ΔN_i[6].

- Assume the electrons in each cell to be independent fermions at 0 K.

- Considerations concerning the 3 dimensional, infinite well $\begin{pmatrix} V = 0 & ,\mathbf{r} < \mathbf{r}_w \\ V = \infty & ,\mathbf{r} > \mathbf{r}_w \end{pmatrix}$ allow to determine the density of states $g(\varepsilon)$ for a given energy ε.

- The probability for the state with the energy ε to be occupied is Fermi-Dirac distributed[7]: $f(\varepsilon) = \frac{1}{1+e^{\beta(\varepsilon-\mu)}} \stackrel{T \to 0K}{=} \begin{cases} 1, & \varepsilon < \varepsilon_F \\ 0, & \varepsilon > \varepsilon_F \end{cases}$.

- Summing the contributions from the occupied energy states gives the total kinetic energy of the cell (with $n = \Delta N/\Delta V$).

$$T_{cube}(n) \quad = \quad \frac{3}{10} \left(3\pi^2\right)^{\frac{2}{3}} \Delta V n^{\frac{5}{3}}$$

- Taking the limit $\Delta V \to 0$ and integration over all (infinitesimal small) cubes gives the Thomas-Fermi energy functional [8]:

$$T_{TF}[n] \quad = \quad C_F \int n^{\frac{5}{3}}(\mathbf{r}) \, d\mathbf{r} \tag{A.5}$$

Combining this result with the considerations of the foregoing sections one can write the energy for one atom as follows:

$$E_{TF}\left[n(\mathbf{r})\right] \quad = \quad C_F \int n^{\frac{5}{3}}(\mathbf{r}) \, d\mathbf{r} - Z \int \frac{n(\mathbf{r})}{|\mathbf{r} - \mathbf{R}|} \, d\mathbf{r} + \frac{1}{2} \iint \frac{n(\mathbf{r})n(\mathbf{r}')}{|\mathbf{r} - \mathbf{r}'|} \, d\mathbf{r} \, d\mathbf{r}' \tag{A.6}$$

---

[5]In the following, the kinetic energy of the electrons is determined as functional of the electron density by applying locally relations appropriate for a homogeneous electronic system. This idea can be used to determine other electronic properties as well and is called "local density approximation". See section 2.3.5 for further details.

[6]There may be different numbers of electron in different cells.

[7]With $\beta = \frac{1}{k_b T}$, and μ being the chemical potential. ε_F is the zero-temperature limit of the chemical potential and is called "Fermi energy".

[8]With $C_F = \frac{3}{10}(3\pi^2)^{\frac{2}{3}}$.

This is the Thomas-Fermi energy functional for atoms, which of course omits exchange and correlation terms but depends solely on the electron density. Minimization of (A.6) with respect to the electron density under the constraint of a fixed number of electrons yields the Euler-Lagrange equation for the Thomas-Fermi model of the atom. Because exchange and correlation terms were neglected, the accuracy for atoms is not as high as with other methods. Furthermore, the method fails in describing molecular bonds. Even so, the underlying idea of this approach is remarkable.

A.4 Standard implementations of DFT

A.4.1 Basis sets

In section 2.3, the density functional theory was introduced. It allows to (numerically) solve quantum mechanical many-body problems approximatively[9]. For that purpose a basis set of one electron wave functions called "Kohn-Sham orbitals" has to be chosen. These basis sets have to reproduce the real behavior of wave functions in the atomic *and* the bonding region.

In the atomic region near the nucleus the kinetic energy of the electrons becomes large and the wave function therefore oscillates rapidly. In numerical calculations one has to discretize the wave function. Drastic changes of the wave function (as in the near nucleus region) require a fine grid for a proper numerical representation. On the other hand, the large kinetic energy leads to a small influence of the chemical environment on the wave function. Therefore a small basis set suffices to describe the behavior in the atomic region.

In the bonding region the wave function is highly dependent on the environment because the kinetic energy of the electrons is small. This requires large, almost complete basis sets. In addition, a larger grid for discretization can be used because the wave function is smooth.

Various approaches try to combine these different requirements. In the following, I will introduce three main routes before going into detail of the projector augmented wave (PAW) method [82, 90].

- Atomic orbital methods use basis sets similar to real atomic orbitals. The bonding is described by the overlapping tails of these orbitals. A compromise between functions which yield good results but are not easily handled in numerical simulations, such as Slater-type orbitals [91], on the one hand and numerically convenient basis functions such, as Gaussians [92], which have the wrong asymptotic behavior far from, and near the nucleus, has to be made.

- Pseudo-potentials regard an atom as a pertubation of free electron gas. The wave functions are constructed of plane waves. A large number of basis functions is needed to describe the wave function. In exchange, plane waves are

---

[9]Note that density functional theory is an exact theory until one approximates the exchange and correlation functional.

easily handled within numerical calculations. A shortcoming of finite plane wave expansions is, that they can not describe correctly the strong oscillations in the near-nucleus region. Therefore the Pauli repulsion of the core electrons is described by an effective potential that expels the valence electrons from the core region. Thus all information on wave function and the charge density near the nucleus is inaccessible.

• Augmented wave methods compose their basis functions out of atom-like partial waves in the atomic regions and a set of functions, called envelope functions, appropriate for the bonding in between. The partial solutions of the atom and binding region were matched at the interface between them. The linear muffin thin orbital (LMTO) method for example uses solutions to the $\frac{1}{r}$-potential of the nucleus as envelope function [35]. The linear augmented plane wave (LAPW) and the augmented spherical wave (ASW) methods use plane waves and spherical waves respectively for this purpose. [8, 93].

A.4.2 The PAW formalism

The projector augmented wave (PAW) method [82, 90] provides a formalism to combine the advantages of the pseudopotential and the augmented wave methods. It introduces energy and potential independent basis sets as required by the Car-Parrinello molecular dynamics method [46].

As mentioned above, the wavefunctions have a nodal structure in the atomic region. The main idea of the PAW formalism is a transformation of the true wavefunction into auxiliary wave functions, which are also smooth in the near nucleus region and equal to the true wavefunction beyond a certain distance from the nucleus. The resulting wave functions have a rapidly convergent plane wave expansion and can therefore be expanded into a convenient basis set. This numerical favorable basis set is used for the simulation. The related true wavefunction can be reconstructed from the auxiliary one to extract the physical properties of the system. Let the transformation operator, which transforms the auxiliary one electron wave function (denoted by $|\tilde{\psi}_i\rangle$) into the physical wave function, be $\hat{\mathcal{T}}$:

$$
\begin{aligned}
|\psi_i\rangle &= \hat{\mathcal{T}}|\tilde{\psi}_i\rangle \\
\langle\psi_i| &= \langle\tilde{\psi}_i|\hat{\mathcal{T}}^\dagger.
\end{aligned}
$$

Substituting this in the total energy functional (2.12), the Kohn-Sham equation for the auxiliary wave function can be derived according to (2.21):\

$$
\hat{\mathcal{T}}^\dagger \left[-\frac{1}{2}\nabla_{\mathbf{r}_i}^2 + V_{ext}(\mathbf{r}) + \int \frac{n(\mathbf{r}')}{|\mathbf{r}-\mathbf{r}'|}\,d\mathbf{r}' + \frac{\delta E_{xc}[n(\mathbf{r})]}{\delta n(\mathbf{r})} \right] \hat{\mathcal{T}}|\tilde{\psi}_i\rangle = \hat{\mathcal{T}}^\dagger\hat{\mathcal{T}}|\tilde{\psi}_i\rangle\varepsilon_i.
$$

The expectation values which correspond to physical quantities can be determined

using the physical or the auxiliary wave function:

$$\langle \hat{A} \rangle \;\; = \;\; \sum_i f_i \langle \psi_i | \hat{A} | \psi_i \rangle = \sum_i f_i \langle \tilde{\psi}_i | \underbrace{\hat{\mathcal{T}}^\dagger \hat{A} \hat{\mathcal{T}}}_{\tilde{A}} | \tilde{\psi}_i \rangle \tag{A.7}$$

with the occupation number f_i. The transformed operator $\tilde{A}$ is the Operator $\hat{A}$ in the auxiliary-wave-function representation[10].

How is the transformation defined? I will show this in more detail in the following.

As the auxiliary wavefunction equals the true wavefunction beyond a certain distance from the nucleus, the transformation can be written as:

$$\hat{\mathcal{T}} \;\; = \;\; 1 + \sum_R S_R \tag{A.8}$$

where S_R stands for the contribution within a sphere around the nucleus R. Therefore S_R is a local term. One can express the wavefunction in the atomic region around nucleus R in terms of partial solutions of the isolated atom[11] here denoted by $|\phi_i\rangle$:

$$|\Psi\rangle \;\; = \;\; \sum_i |\phi_i\rangle c_i \;\; for \;\; |\mathbf{r} - \mathbf{R}_R| < r_{c,R} \tag{A.9}$$

with the so called "cutoff radius" $r_{c,R}$. The local contribution S_R is then defined in the following way:

$$|\phi_i\rangle \;\; = \;\; (1 + S_R)\, |\tilde{\phi}_i\rangle \tag{A.10}$$
$$\Rightarrow S_R|\tilde{\phi}_i\rangle \;\; = \;\; |\phi_i\rangle - |\tilde{\phi}_i\rangle \tag{A.11}$$

or in more detail:

$$S_R|\tilde{\Psi}\rangle \;\; = \;\; \sum_i S_R|\tilde{\psi}_i\rangle = \sum_i S_R|\tilde{\phi}_i\rangle c_i = \sum_i \left(|\phi_i\rangle - |\tilde{\phi}_i\rangle \right) c_i, \tag{A.12}$$

with i extending over the one electron orbitals of nuclei R. Equations (A.10)-(A.12) are still limited to $|\mathbf{r} - \mathbf{R}_R| > r_{c,R}$.

Since S_R should not change the auxiliary wave function $|\tilde{\Psi}\rangle$ beyond the cut-off radius ($S_R|\tilde{\Psi}\rangle = 0 \;\; for \;\; |\mathbf{r} - \mathbf{R}_R| > r_{c,R}$), the partial wave and the auxiliary partial wave have to be identical outside the atomic region:

$$|\phi_i\rangle \;\; = \;\; |\tilde{\phi}_i\rangle \;\; for \;\; |\mathbf{r} - \mathbf{R}_R| > r_{c,R}$$

The coefficients c_i are determined by projecting the wave function onto projector

---

[10]For a deeper insight concerning transformed operators and expectation values see [82, 90].

[11]Note that the sum extends over the one electron orbitals of the nucleus R at position $\mathbf{R}_R$. The partial waves are not necessarily bound states and can be non normalizable for $|\mathbf{r} - \mathbf{R}_R| > r_{c,R}$.
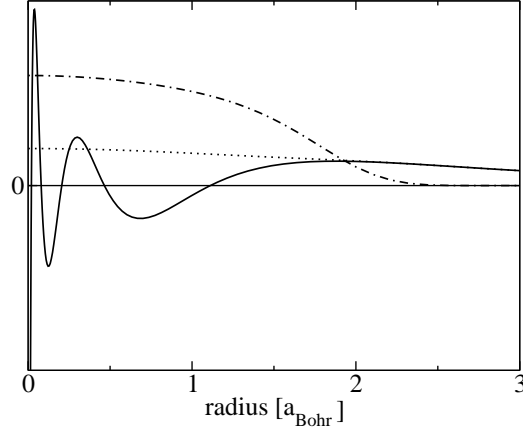
Figure A.1: The radial part of the all electron 6s wave function of gold (full line), its auxiliary wave function (dashed line) and a projector function (chain dotted line).

functions $|\tilde{p}_i\rangle$ which fulfill the following condition:

$$\langle \tilde{p}_i|\tilde{\phi}_j\rangle = \delta_{ij}.$$

Using projector functions that probe only the local character of a wave function (which means $\langle \tilde{p}_i|\tilde{\Psi}\rangle = 0 \; for \; |\mathbf{r} - \mathbf{R}_R| > r_{c,R})$[12] allows to write (A.12) as follows

$$S_R|\tilde{\Psi}\rangle = \sum_i S_R|\tilde{\phi}_i\rangle \underbrace{\langle \tilde{p}_i|\tilde{\Psi}\rangle}_{c_i} = \underbrace{\sum_i \left(|\phi_i\rangle - |\tilde{\phi}_i\rangle \right) \langle \tilde{p}_i |\tilde{\Psi}\rangle}_{S_R}$$

without limiting it to the atomic region[13]. The transformation operator (A.8) therefore becomes:

$$\hat{\mathcal{T}} = 1 + \sum_R \sum_i \left(|\phi_{R,i}\rangle - |\tilde{\phi}_{R,i}\rangle \right) \langle \tilde{p}_{R,i}|$$

and the true wavefunction can be written as:

$$|\Psi\rangle = |\tilde{\Psi}\rangle + \sum_R \sum_i \left(|\phi_{R,i}\rangle - |\tilde{\phi}_{R,i}\rangle \right) \langle \tilde{p}_{R,i}|\tilde{\Psi}\rangle$$

Figure (A.1) shows the radial part of the all electron 6s wave function of gold with its nodal structure. The smooth auxiliary wavefunction becomes equal to the real wave function even before the projector function becomes zero.

---

[12]Otherwise partial waves (which are not limited to bound states and therefore not equal to zero outside the atom) of atom R could contribute neighboring atoms. This would violate the assumption of local contributions.

[13]The exact derivation of the projector functions can be found in [82].

A.4.3 Approximations in the PAW method

Actual implementations of the PAW method use three approximations. They will be discussed in the following.

- The so called "frozen core electron approximation" treats the density and energy of the core electrons as identical to those in the isolated atom. This approximation decreases the numerical costs and introduces only small errors, because the core electrons do not spread out into bonding regions and therefore are not influenced much by neighboring atoms. If this approximation is used, the pseudo partial waves $|\tilde{\phi}_i\rangle$ have to be orthogonal to the core electron wave functions $|\phi^c\rangle$. The transformation Operator $\hat{\mathcal{T}}^\dagger$ therefore transforms the wave function $|\Psi\rangle$ into a pseudo wavefunction $|\tilde{\Psi}\rangle$ which is orthogonal to the core electron wave functions. The true wavefunction for all electrons then has to be written as:

$$|\Psi\rangle = |\tilde{\Psi}\rangle + \sum_R \sum_i \left(|\phi_{R,i}\rangle - |\tilde{\phi}_{R,i}\rangle \right) \langle \tilde{p}_{R,i} | \tilde{\Psi}\rangle + \sum_{n=1}^{N_c} |\phi_n^c\rangle$$

- The auxiliary wave function $|\tilde{\Psi}\rangle$ is expanded in plane waves. In numerical simulations this expansion can not be complete. It is usually truncated at $E_{PW} = \frac{1}{2}\hbar^2 G_{max}^2 = 30\,Ry$. Higher accuracy (at the expense of computational costs) can easily be obtained by increasing the plane wave cutoff.

- The auxiliary wave function $|\tilde{\Psi}\rangle$ is expanded in pseudo partial waves ($|\tilde{\phi}\rangle$) in the atomic region. For this expansion typically one or two partial waves per angular momentum (l, m) and site are used[14].

---

[14]It should be noted that the partial wave expansion is not variational, because the partial wave expansion changes the total energy functional and not only the basis set[82].

B Derivations

B.1 Core orthogonalisation of node-less wave functions

The following outline of the proof of (4.23):

$$|\phi_n(\varepsilon)\rangle \quad = \quad \left(1 - \hat{P}_c\right) c_{n,n} |q_n(\varepsilon)\rangle$$

$$\text{with}$$

$$\hat{P}_c \quad := \quad \sum_{j=1}^{n-1} |\phi_j(\varepsilon_j)\rangle\langle\phi_j(\varepsilon_j)|$$

makes use of the relations:

$$|\phi_i\rangle \quad := \quad |\phi_i(\varepsilon_i)\rangle$$

$$(1 - \hat{P}_c)|\phi_k\rangle \quad = \quad 0 \,, \text{for } k \in c$$

$$(1 - \hat{P}_c)|\phi_k\rangle \quad = \quad |\phi_k\rangle \,, \text{for } k \notin c$$

$$|u_i\rangle \quad = \quad \sum_{j=1}^{i} |\phi_j\rangle\tilde{c}_{j,i}$$

Multiplication of (4.23) with $(1 - \hat{P}_c)$ leads to:

$$|\phi_n(\varepsilon)\rangle \quad = \quad \underbrace{\left(1 - \hat{P}_c\right)\sum_{i=1}^{n-1} |u_i\rangle c_{i,n}}_{*^1} + \left(1 - \hat{P}_c\right)|q_n(\varepsilon)\rangle c_{n,n}$$

For the relation (4.23) to hold, $*^1$ needs to vanish. The sum will be equal to zero if each summand vanishes. For $i < n$:

$$\left(1 - \hat{P}_c\right)|u_i\rangle c_{i,n}$$

$$= \quad \left(1 - \hat{P}_c\right)\sum_{j=1}^{i<n} |\phi_j\rangle\tilde{c}_{j,i}c_{i,n}$$

$$= \quad 0$$

The corresponding orthogonalization for the energy derivatives $|\dot{q}(\varepsilon)\rangle$ can be obtained

from (4.23) as follows:

$$\frac{d}{d\varepsilon}\left[\frac{1}{c_{n,n}}|\phi_n(\varepsilon)\rangle\right] \quad = \quad \frac{d}{d\varepsilon}\left[\left(1-\hat{P}_c\right)|q_n(\varepsilon)\rangle\right]$$

$$|\dot{\phi}_n(\varepsilon)\rangle + \alpha_n|\phi_n(\varepsilon)\rangle \quad = \quad \left(1-\hat{P}_c\right)c_{n,n}|\dot{q}_n(\varepsilon)\rangle \qquad\qquad \text{(B.1)}$$

$$\text{with}$$

$$\alpha_n \quad = \quad \frac{d}{d\varepsilon}\frac{1}{c_{n,n}}$$

$|\phi_n(\varepsilon)\rangle$ however corresponds to a solution of the homogeneous differential equation (4.16). Any linear-combination of $|\dot{\phi}_n(\varepsilon)\rangle$ and $|\phi_n(\varepsilon)\rangle$ therefore solves the inhomogeneous equation (4.16). The exact amount of the homogeneous solution mixed into the inhomogeneous can usually be determined from boundary conditions. With this in mind, we can reduce (B.1) as follows:

$$|\dot{\phi}_n(\varepsilon)\rangle \quad = \quad \left(1-\hat{P}_c\right)c_{n,n}|\dot{q}_n(\varepsilon)\rangle.$$

B.2 The plane wave basis

B.2.1 Norm in plane-wave basis

We use

$$\langle G|G'\rangle \quad = \quad \int_{cell} \underbrace{\langle G|r\rangle}_{e^{-iGr}}\underbrace{\langle r|G'\rangle}_{e^{iG'r}}\,d^3r = V\delta_{G,G'} \qquad\qquad \text{(B.2)}$$

which deviates from the usual definition

$$\langle G|G'\rangle \quad = \quad \delta_{G,G'}\,,$$

leading to prefactors of $e^{\pm iGr}$. The unity operator then looks then like[1]

$$1 \quad = \quad \int\limits_{cell} |r\rangle\langle r|d^3r \tag{B.3}$$

$$1 \quad = \quad \int\limits_{cell} |G\rangle\frac{1}{V}\langle G|d^3G \tag{B.4}$$

$$1 \quad = \quad \sum_i |r_i\rangle\frac{V}{\sum_{r_i}1}\langle r_i| \tag{B.5}$$

$$1 \quad = \quad \sum_i |G_i\rangle\frac{1}{V}\langle G_i| \tag{B.6}$$

The factor $\frac{V}{\sum_{r_i}1}$ for the discrete 1 can be shown in the following way: We know that $\langle G|G'\rangle$ has to have the same value, independent of the 1 we introduce. We are sure about the continuous case $1 = \int\limits_{cell} |r\rangle\langle r|d^3r$, which leads to $\langle G|G'\rangle = V\delta_{G,G'}$. Using the discrete Fourier transformation, we can then determine the factor for the discrete case. It's even better to start from $\langle 1|1\rangle = V$, with $\langle r_i|1\rangle = 1$.

B.2.2 Scalar products in plane waves

$$\langle G|\psi\rangle \quad = \quad V\psi(G) \tag{B.7}$$

This can be derived in the following way:

$$\langle r|\psi\rangle \quad = \quad \sum_G \langle r|G\rangle\frac{1}{V}\langle G|\psi\rangle \tag{B.8}$$

$$= \quad \sum_G e^{iGr}\underbrace{\frac{1}{V}\langle G|\psi\rangle}_{\psi(G)} \tag{B.9}$$

According to equation (B.2), we choose

$$\langle G|G'\rangle \quad = \quad \int\limits_{cell} \underbrace{\langle G|r\rangle}_{e^{-iGr}}\underbrace{\langle r|G'\rangle}_{e^{iG'r}} d^3r = V\delta_{G,G'} . \tag{B.10}$$

---

[1] Note that we always have to start from $1 = \int |x\rangle\frac{1}{\langle x|x\rangle}\langle x|$. For orthonormal $|x\rangle$ the fraction becomes 1

For the total charge, the following relation holds:

$$\langle \psi | \psi \rangle \quad = \quad \int_{V_{cell}} \langle \psi | r \rangle \langle r | \psi \rangle d^3 r \tag{B.11}$$

$$= \quad \sum_{G,G'} \int_{V_{cell}} \frac{1}{V^2} \langle \psi | G \rangle \langle G | r \rangle \langle r | G' \rangle \langle G' | \psi \rangle d^3 r \tag{B.12}$$

$$= \quad \sum_{G,G'} \int_{V_{cell}} \frac{1}{V^2} \langle \psi | G \rangle \langle G | r \rangle \langle r | G' \rangle \langle G' | \psi \rangle d^3 r \tag{B.13}$$

$$= \quad \sum_{G,G'} \int_{V_{cell}} \psi^*(G) e^{-iGr} e^{iG'r} \psi(G') d^3 r \tag{B.14}$$

$$= \quad \sum_{G,G'} \psi^*(G) \psi(G') \int_{V_{cell}} e^{-i(G-G')r} d^3 r \tag{B.15}$$

$$= \quad \sum_{G,G'} \psi^*(G) \psi(G') V_{cell} \delta_{G,G'} \tag{B.16}$$

$$= \quad \sum_{G} V \psi^*(G) \psi(G) \tag{B.17}$$

For the density, we have to start from the density operator

$$\hat{\rho} \quad = \quad | \psi \rangle \langle \psi | \tag{B.18}$$

with

$$\rho(r, r') \quad = \quad \langle r | \psi \rangle \langle \psi | r' \rangle \tag{B.19}$$

$$\rho(r) \quad = \quad \rho(r, r') \delta(r - r') = \langle r | \psi \rangle \langle \psi | r \rangle \tag{B.20}$$

follows

$$\rho(r) \quad = \quad \frac{1}{V^2} \sum_{G,G'} \langle r | G' \rangle \langle G' | \psi \rangle \langle \psi | G \rangle \langle G | r \rangle \tag{B.21}$$

$$\overset{B.12}{=} \quad \sum_{G,G'} \psi^*(G) \psi(G') e^{-i(G-G')r} \tag{B.22}$$

This function now depends on G and G'. Because $\max\{G - G'\} = 2G_{max}$, we have to use a finer grid for the density. If we want to calculate the kinetic energy, we do

this in G-space:

$$
\langle\psi| - \frac{1}{2}\nabla^2|\psi\rangle = \sum_{G,G'} \int\int \frac{1}{V^2}\langle\psi|G\rangle\langle G|r\rangle\langle r| - \frac{1}{2}\nabla^2|r'\rangle\langle r'|G'\rangle\langle G'|\psi\rangle d^3r d^3r' \tag{B.23}
$$

$$
= \sum_{G,G'} \int \frac{1}{V^2}\langle\psi|G\rangle e^{-iGr}\frac{1}{2}G'^2 e^{iG'r}\langle G'|\psi\rangle d^3r \tag{B.24}
$$

$$
= \sum_{G,G'} \frac{1}{V^2}\langle\psi|G\rangle\frac{1}{2}G'^2\langle G'|\psi\rangle \int e^{-i(G-G')r}d^3r \tag{B.25}
$$

$$
= \sum_{G,G'} \frac{1}{V^2}\langle\psi|G\rangle\frac{1}{2}G'^2\langle G'|\psi\rangle V\delta_{G,G'} \tag{B.26}
$$

$$
= \sum_{G} \frac{1}{V}\langle\psi|G\rangle\frac{1}{2}G^2\langle G|\psi\rangle \tag{B.27}
$$

$$
= \sum_{G} V\psi^*(G)\frac{1}{2}G^2\psi(G) \tag{B.28}
$$

Note that we can introduce a discrete 1 in G-space, if we have periodic boundary conditions (otherwise this is not exact). But we have to use a continuous 1 for the real space, because the complete basis in real space corresponds to the integral formulation! Therefore, the following formulation is *buggy*:

$$
\langle\psi| - \frac{1}{2}\nabla^2|\psi\rangle \approx \sum_{G,G',r,r'} \frac{1}{V^2}\frac{V^2}{N_r^2}\langle\psi|G\rangle\langle G|r\rangle\langle r| - \frac{1}{2}\nabla^2|r'\rangle\langle r'|G'\rangle\langle G'|\psi\rangle \tag{B.29}
$$

$$
\overset{??}{=} \sum_{G,G',r,} \frac{1}{N_r^2}\langle\psi|G\rangle e^{-iGr}\frac{1}{2}G'^2 e^{iG'r}\langle G'|\psi\rangle \tag{B.30}
$$

$$
= \frac{1}{2}\frac{1}{N_r^2}\sum_{G,G'}\langle\psi|G\rangle G'^2\langle G'|\psi\rangle \underbrace{\sum_{r} e^{-i(G-G')r}}_{N_r\delta_{G,G'}} \tag{B.31}
$$

$$
= \frac{1}{2}\frac{1}{N_r}\sum_{G}\langle\psi|G\rangle G^2\langle G|\psi\rangle \tag{B.32}
$$

If we want to be exact, we have to make the transition to the Integral!

It's even more elegant to derive this with the following argument: We know that $-\frac{1}{2}\nabla^2|G\rangle = \frac{1}{2}G^2|G\rangle$ (this follows from the definition $\hat{P}|G\rangle = p|G\rangle$ for the momentum

operator. For periodic boundary conditions then follows:

$$\langle\psi| -\frac{1}{2}\nabla^2|\psi\rangle \;=\; \sum_{G,G'} \frac{1}{V^2}\langle\psi|G\rangle\langle G| -\frac{1}{2}\nabla^2|G'\rangle\langle G'|\psi\rangle \tag{B.33}$$

$$=\; \sum_{G,G'} \frac{1}{V^2}\langle\psi|G\rangle\langle G|\frac{1}{2}G'^2|G'\rangle\langle G'|\psi\rangle \tag{B.34}$$

$$=\; \sum_{G,G'} \frac{1}{V^2}\frac{1}{2}G'^2\langle\psi|G\rangle\underbrace{\langle G|G'\rangle}_{\delta_{G,G'}V}\langle G'|\psi\rangle \tag{B.35}$$

$$=\; \sum_{G,G'} \frac{1}{V}\frac{1}{2}G^2\langle\psi|G\rangle\langle G|\psi\rangle \tag{B.36}$$

In the same way follows:

$$\langle G| -\frac{1}{2}\nabla^2|\psi\rangle \;=\; \sum_{G'} \frac{1}{V}\langle G| -\frac{1}{2}\nabla^2|G'\rangle\langle G'|\psi\rangle \tag{B.37}$$

$$=\; \sum_{G'} \frac{1}{V}\langle G|\frac{1}{2}G'^2|G'\rangle\langle G'|\psi\rangle \tag{B.38}$$

$$=\; \sum_{G'} \frac{1}{V}\frac{1}{2}G'^2\underbrace{\langle G|G'\rangle}_{\delta_{G,G'}V}\langle G'|\psi\rangle \tag{B.39}$$

$$=\; \frac{1}{2}G^2\langle G|\psi\rangle \tag{B.40}$$

$$=\; V\frac{1}{2}G^2\psi(G) \tag{B.41}$$

From all the above written, we see, that we can write the scalar product in G-space for periodic boundary conditions as:

$$\langle x|y\rangle \;=\; \sum_{G}\langle x|G\rangle\frac{1}{V}\langle G|y\rangle \tag{B.42}$$

$$=\; \sum_{G} x^*(G)Vy(G) \tag{B.43}$$

Note that we always work with $x(G)$ in the grid representation (the values stored refer to $\frac{1}{V}\langle G|x\rangle$)

B.2.3 Fourier transformation

We use the discrete Fourier transformation as follows:

$$
f(r) = \sum_{G_i=G_1}^{G_{max}} e^{iG_i r} f(G_i)
$$

$$
f(G) = \frac{1}{\sum_{r_i} 1} \sum_{r_i=r_1}^{r_{max}} e^{-iG r_i} f(r_i)
$$

Note that, for continuous Fourier transformations, we have to distinguish between transformations concerning a finite or an infinite part of the space:

$$
f(r) = \int_{cell} e^{iGr} f(G) \, d^3G \tag{B.44}
$$

$$
f(G) = \frac{1}{V_{cell}} \int_{cell} e^{-iGr} f(r) \, d^3r \tag{B.45}
$$

$$
\tag{B.46}
$$

$$
f(r) = \frac{1}{(2\pi)^{n/2}} \int_{\infty} e^{iGr} f(G) \, d^nG \tag{B.47}
$$

$$
f(G) = \frac{1}{(2\pi)^{n/2}} \int_{\infty} e^{-iGr} f(r) d^nr \tag{B.48}
$$

Note that I choose the prefactors of the Fourier transformation over infinite space to be symmetric. The following identities are noticeable:

$$
\int e^{iG(r-r')} \, d^3G = C\delta(r - r') \tag{B.49}
$$

$$
\int e^{-i(G-G')r} \, d^3r = C\delta(G - G') \tag{B.50}
$$

$$
\sum_i e^{iG_i(r-r')} = C\delta_{r,r'} \tag{B.51}
$$

$$
\sum_i e^{-i(G-G')r_i} = C\delta_{G,G'} \tag{B.52}
$$

C can be $(2\pi)^{\frac{n}{2}}$ or V_{cell}, depending on the integration limits in the continuous case - or $\sum_{i=1}^{r_{max}} 1$, the number of r-components, in the discrete case.

A closer look at the prefactors:

The factor 2π comes from $\Delta G = \frac{2\pi}{L}$ during transition to infinite integrals. One can

test the prefactor $\frac{1}{V_{cell}}$ by inserting $\psi(r)$ in the expression for the kinetic energy:

$$E_{kin} \;=\; -\frac{1}{2}\int\limits_{cell} \psi^*(r)\nabla^2\psi(r)\,dr \tag{B.53}$$

$$=\; -\frac{1}{2}\int\limits_{cell} \sum_{G_i=G_1}^{G_{max}} e^{-iG_i r}\psi^*(G_i)\nabla^2 \sum_{G_i'=G_1}^{G_{max}} e^{iG_i' r}\psi(G_i')\,dr \tag{B.54}$$

$$=\; \frac{1}{2}\sum_{G_i=G_1}^{G_{max}}\sum_{G_i'=G_1}^{G_{max}}\int\limits_{cell} e^{-iG_i r}f^*(G_i)G_i'^2 e^{iG_i' r}f(G_i')\,dr \tag{B.55}$$

$$=\; \frac{1}{2}\sum_{G_i=G_1}^{G_{max}}\sum_{G_i'=G_1}^{G_{max}} \psi^*(G_i)G'^2_i\psi(G_i')\int\limits_{cell} e^{-iG_i r}e^{iG_i' r}\,dr \tag{B.56}$$

$$=\; \frac{1}{2}\sum_{G_i=G_1}^{G_{max}}\sum_{G_i'=G_1}^{G_{max}} \psi^*(G_i)G'^2_i\psi(G_i')\int\limits_{cell} e^{-i(G_i-G_i')r}\,dr \tag{B.57}$$

$$=\; \frac{1}{2}\sum_{G_i=G_1}^{G_{max}}\sum_{G_i'=G_1}^{G_{max}} \psi^*(G_i)G'^2_i\psi(G_i')V_{cell}\delta_{G,G'} \tag{B.58}$$

$$=\; \frac{1}{2}V_{cell}\sum_{G_i=G_1}^{G_{max}} G^2_i|\psi(G_i)|^2 \tag{B.59}$$

<u>FFT scaling:</u>

The costs for a fast Fourier Transformation scale with $n\log n$, with n being the number of G-Vectors (G-Points). Therefore, a FFT for atomic wave functions is impossible, because we need a plane-wave cutoff of about 1000 Ry instead of 30 Ry. The number of G-vectors (scaling with about $E^{\frac{3}{2}}$ is immense.)

B.2.4 Bessel transformation

B.2.4.1 Some formulas

Expanding a plane-wave into spherical harmonics and spherical Bessel functions of first kind

$$e^{iGr} \;=\; 4\pi\sum_{\ell,m} i^\ell j_\ell(|G||r|)Y_{lm}^*(\mathbf{G})Y_{lm}(\mathbf{r}) \tag{B.60}$$

$$e^{-iGr} \;=\; 4\pi\sum_{\ell,m} \left(i^\ell\right)^* j_\ell(|G||r|)Y_{lm}(\mathbf{G})Y_{lm}^*(\mathbf{r}) \tag{B.61}$$

Formulas related to spherical harmonics

$$P_\ell(\cos\gamma) = \frac{4\pi}{2\ell+1} \sum_{m=-\ell}^{\ell} Y_{lm}^*(\mathbf{G}) Y_{lm}(\mathbf{G}') \tag{B.62}$$

$$\cos\gamma = \frac{G \cdot G'}{|G||G'|} \tag{B.63}$$

$$Y_{lm}(G) = (-1)^m \sqrt{\frac{2\ell+1}{4\pi} \frac{(\ell-m)!}{(\ell+m)!}} sin^m\theta_G \times$$
$$\frac{d^m}{d(\cos\theta_G)^m} P_\ell(\cos\theta_G) e^{im\phi_G} \tag{B.64}$$

B.2.4.2 From radial grids to a plane-wave representation

This section deals with transforming a function given in terms of radial part times spherical harmonics

$$f(\mathbf{r}) = \sum_{\ell m} f_{\ell m}(|r|) Y_{\ell m}(\mathbf{r})$$

into G space

$$f(\mathbf{r}) = \int d^3 G f(\mathbf{G}) e^{i\mathbf{Gr}}.$$

Mind that we are using a continuous set of G vectors, since we do not require periodic boundary conditions at this point. Using the prerequisites introduced so far we thus write

$$
\begin{aligned}
f(\mathbf{G}) &= \frac{1}{(2\pi)^3} \int_\infty d^3r \, f(\mathbf{r}) e^{-i\mathbf{G}\mathbf{r}} \\
&= \frac{4\pi}{(2\pi)^3} \int_\infty d^3r \left[\sum_{\ell m} f_{\ell m}(|r|) Y_{\ell m}(\mathbf{r}) \right] \left[\sum_{\ell' m'} (-i)^{\ell'} j_{\ell'}(|G||r|) Y_{\ell' m'}(\mathbf{G}) Y^*_{\ell' m'}(\mathbf{r}) \right] \\
&= \frac{4\pi}{(2\pi)^3} \sum_{\ell' m'} (-i)^{\ell'} \left[\int_\infty d^3r \sum_{\ell m} f_{\ell m}(|r|) j_{\ell'}(|G||r|) Y_{\ell m}(\mathbf{r}) Y^*_{\ell' m'}(\mathbf{r}) \right] Y_{\ell' m'}(\mathbf{G}) \\
&= \frac{4\pi}{(2\pi)^3} \sum_{\ell' m'} (-i)^{\ell'} \Bigg[\sum_{\ell m} \underbrace{\int_\infty d\Omega \, Y_{\ell m}(\mathbf{r}) Y^*_{\ell' m'}(\mathbf{r})}_{\delta_{\ell \ell'} \delta_{m m'}} \\
&\qquad \int_\infty d|r| r^2 f_{\ell m}(|r|) j_{\ell'}(|G||r|) \Bigg] Y_{\ell' m'}(\mathbf{G}) \\
&= \frac{4\pi}{(2\pi)^3} \sum_{\ell' m'} (-i)^{\ell'} \left[\int_0^\infty d|r| r^2 f_{\ell' m'}(|r|) j_{\ell'}(|G||r|) \right] Y_{\ell' m'}(\mathbf{G})
\end{aligned}
$$

The expression for a periodic function and thus discrete G vectors is obtained by multiplying with

$$
\frac{(2\pi)^3}{V}.
$$

The final expression for periodic boundary conditions is thus

$$
f(\mathbf{G}) = \frac{4\pi}{V} \sum_{\ell' m'} (-i)^{\ell'} \underbrace{\left[\int_0^\infty d|r| r^2 f_{\ell' m'}(|r|) j_{\ell'}(|G||r|) \right]}_{\text{BESSELTRANSFORM} = f_{\ell' m'}(|G|)} Y_{\ell' m'}(\mathbf{G}).
$$

In all applications in the SESM context we always transform functions which can be expressed in terms of a single radial times spherical harmonics expression. The sum over ℓ' and m' is thus removed. We store the Bessel-transformed function with the prefactor $\frac{4\pi}{V} f_{\ell' m'}(|G|)$ on a radial G grid and apply $\sum_{\ell' m'} (-i)^{\ell'} Y_{\ell' m'}(\mathbf{G})$ when we need $f(\mathbf{G})$. We actually use a matrix with one index referring to the g components ($ig \to ng$) and the second index corresponding to the lmx (s, p_x, p_y, p_z,...). $Y_{\ell' m'}(\mathbf{G})$ means that we just depend on the angle of the vector G. Therefore we can use the same PAW routine `getylm` as for $Y_{\ell' m'}(\mathbf{r})$. The expression in square brackets is called spherical Bessel transform of order ℓ and is calculated on radial grids [94]. The corresponding subroutine in the PAW library is `besseltransform`.

B.3 Spherical harmonics expansion

B.3.1 Some facts about spherical harmonics

The spherical harmonics have some noticeable properties:

$$
\begin{aligned}
\hat{L}^2 Y_{lm}(\mathbf{r}) &= l(l+1)Y_{lm}(\mathbf{r}) \\
\hat{L}_z Y_{lm}(\mathbf{r}) &= m Y_{lm}(\mathbf{r})
\end{aligned}
$$

$$
\oint Y_{lm}^*(\mathbf{r})Y_{l'm'}(\mathbf{r})\,dA = \underbrace{\mathbf{r}^2}_{=1\,if\,\mathbf{r}=\mathbf{e}} \delta_{l,l'}\delta_{m,m'} \tag{B.65}
$$

$$
f(\mathbf{r}) = \sum_{l,m} R_{lm}(|\mathbf{r}|) \cdot Y_{lm}(\mathbf{r})
$$

$$
\Rightarrow R_{lm}(|\mathbf{r}|) = \oint_{|\mathbf{r}|=|\mathbf{r}'|} \frac{1}{|\mathbf{r}|^2} f(\mathbf{r}')Y_{lm}^*(\mathbf{r'})\,dA' \tag{B.66}
$$

$$
= \int f(\mathbf{r}')Y_{lm}^*(\mathbf{r}')\frac{\delta(|\mathbf{r}|-|\mathbf{r}'|)}{|\mathbf{r}|^2}\,d^3r' \tag{B.67}
$$

There exist cubic spherical harmonics $\bar{Y}_{lm} = \sqrt{2}\mathcal{R}[Y_{l|m|}]$ and $\bar{Y}_{l,-m} = \sqrt{2}\mathcal{I}[Y_{l|m|}]$ that are only real or imaginary and fulfill the above relations except the second one. One should at least remember $Y_{00} = \frac{1}{\sqrt{4\pi}}$. This comes from

$$
\begin{aligned}
\oint Y_{lm}^* Y_{lm} dA &= \int\int \frac{1}{4\pi}\mathbf{r}^2 sin\theta d\theta d\phi \\
&= \mathbf{r}^2 \frac{1}{4\pi} 4\pi
\end{aligned}
$$

B.3.2 Clebsch and Gaunt coefficients, selection rules

When working in the spherical harmonics basis, so called Gaunt-integrals occur:

$$
\langle L''|L|L'\rangle := \int Y_{L''}^* Y_L Y_{L'} d\Omega. \tag{B.68}
$$

For real spherical harmonics ($\int \bar{Y}_{L''}\bar{Y}_L\bar{Y}_{L'}d\Omega$), this integral can be solved analytically, applying the Wigner Eckart theorem [95]. The more general integral (B.68) can also be solved analytically [96, 97] and is parametrized by so called Gaunt coefficients:

$$
c_{L'',L,L'} = \int Y_{L''}^* Y_L Y_{L'} d\Omega \tag{B.69}
$$

The product of two spherical harmonics is parametrized by Clebsch-Gordon coefficients[2]:

$$Y_L Y_{L'} = \sum_{L''} c_{L'',L,L'} Y_{l''m''} \tag{B.70}$$

Both sets of coefficients satisfy the selection rule:

$$m_3 = m_1 + m_2$$
$$|l_1 - l_2| \leq l_3 \leq |l_1 + l_2| \tag{B.71}$$

Note however, that the m specific selection rule only holds for complex spherical harmonics.

B.3.3 Spherical harmonics and Fourier transformation

We start from the usual spherical harmonics expansion and project onto a specific spherical harmonic[3]:

$$f(\mathbf{r}) = \sum_{\ell m} f_{\ell m}(|r|) Y_{\ell m}(\mathbf{r})$$

$$\int Y_{\ell'm'}^*(\mathbf{r}) f(\mathbf{r}) \mathrm{d}A = \sum_{\ell m} f_{\ell m}(|r|) \underbrace{\int Y_{\ell'm'}^*(\mathbf{r}) Y_{\ell m}(\mathbf{r}) \mathrm{d}A}_{|r|^2 \delta_{\ell\ell'} \delta_{mm'}}$$

$$\int Y_{\ell'm'}^*(\mathbf{r}) f(\mathbf{r}) \mathrm{d}A = |r|^2 f_{\ell m}(|r|)$$

Now we use the Fourier transform and the spherical harmonic expansion for plane waves [4]:

$$|r|^2 f_{\ell m}(|r|) = \int Y_{\ell'm'}^*(\mathbf{r}) \int f(\mathbf{G}) e^{i\mathbf{Gr}} \mathrm{d}^3 G \mathrm{d}A$$

$$|r|^2 f_{\ell m}(|r|) = \int Y_{\ell'm'}^*(\mathbf{r}) \int f(\mathbf{G}) 4\pi \sum_{\ell m} i^l j_\ell(|G||r|) Y_{\ell m}^*(\mathbf{G}) Y_{\ell m}(\mathbf{r}) \mathrm{d}^3 G \mathrm{d}A$$

$$|r|^2 f_{\ell m}(|r|) = 4\pi \int f(\mathbf{G}) \sum_{\ell m} i^l j_\ell(|G||r|) Y_{\ell m}^*(\mathbf{G}) \underbrace{\int Y_{\ell'm'}^*(\mathbf{r}) Y_{\ell m}(\mathbf{r}) \mathrm{d}A}_{|r|^2 \delta_{\ell\ell'} \delta_{mm'}} \mathrm{d}^3 G$$

$$f_{\ell m}(|r|) = 4\pi \int i^l f(\mathbf{G}) j_\ell(|G||r|) Y_{\ell m}^*(\mathbf{G}) \mathrm{d}^3 G$$

---

[2]Both relations also hold for real spherical harmonics.
[3]Note that $\mathrm{d}A = r^2 \mathrm{d}\Omega$. We can get $f_{\ell m}(|r|)$ out of the integral, because it is not angular dependent.
[4]Note that we can get the $\int \mathrm{d}A$ inside, because j_ℓ does not depend on the angle, but just on the length of $\mathbf{r}$.

For numerical reasons, we are using the following steps in the code:

- determine $Y_{\ell m}^*(\mathbf{G})$ as a vector containing all lmx $Y(lmx)$

- take the product $i^\ell f(\mathbf{G}) Y_{\ell m}^*(\mathbf{G})$, store the result in a matrix $xbar(lmx, ng)$

- sort that matrix for $|\mathbf{G}|$ and add the contributions with same $|\mathbf{G}|$ up

- take $\sum_{|\mathbf{G}|} xbar(lmx, ng) \cdot j_\ell(|G||r|)$

- multiply by 4π

In that way, we split the $\int \mathrm{d}^3 G$ (which has to be replaced by $\sum_{\mathbf{G}}$ for a grid representation) in such a way, that we need the minimal amount of calls for j_ℓ, the spherical Bessel-function of first kind. The calculation of the latter is done according to Abramowitz and Stegun, formula 10.1.2 for $\ell < 8$ and formula 10.1.8 and 10.1.9 for $\ell > 8$, and is numerically demanding (find the code in `numeric$bessel`).

B.4 Spherical harmonics re-expansion

B.4.1 General expressions

We use the following definitions and relations[5]

$$\tilde{Y}_{l,m}(\theta, \phi) = P_{l,m}(\cos\theta)e^{im\phi} \tag{B.72}$$

$$P_{l,m}(x) = \frac{1}{2^l l!}(1 - x^2)^{\frac{m}{2}}\frac{d^{l+m}}{dx^{l+m}}(x^2 - 1)^l$$

$$Y_{l,m} = (-1)^m\sqrt{\frac{(2l+1)(l-m)!}{4\pi(l+m)!}}\tilde{Y}_{l,m} \tag{B.73}$$

$$\bar{P}_{l,m}(x) = (-1)^m\sqrt{\frac{(2l+1)(l-m)!}{4\pi(l+m)!}}P_{l,m}(x) \tag{B.74}$$

$$\int Y_{l,m}^* Y_{l',m'} d\Omega = \delta_{l,l'}\delta_{m,m'}$$

$$\int Y_{l,m}^* Y_{l',m'} dA = r^2\delta_{l,l'}\delta_{m,m'}$$

$$S_{l,m}(\mathbf{x}) = (-1)^m(l-m)!\frac{1}{|\mathbf{x}|^{l+1}}\tilde{Y}_{l,m}(\mathbf{x}) \tag{B.75}$$

$$R_{l,m}(\mathbf{x}) = (-1)^m\frac{1}{(l+m)!}|\mathbf{x}|^l\tilde{Y}_{l,m}(\mathbf{x}) \tag{B.76}$$

The inverse distance $\frac{1}{|\mathbf{r}-\mathbf{\Delta}|}$ can be expanded in spherical harmonics[6] [98, 99]

$$\frac{1}{|\mathbf{r}-\mathbf{\Delta}|} = \sum_L R_L^*(\mathbf{\Delta})S_L(\mathbf{r}) \ \text{ for } |\mathbf{\Delta}| \leq |\mathbf{r}| \tag{B.77}$$

We make further use of Van Gelderens expression[7] (26) :

$$S_{l,m}(\mathbf{x}+\mathbf{y}) = \sum_{L'}(-1)^{l'+m'-m}R_{l'-l,m-m'}(\mathbf{y})S_{l',m'}(\mathbf{x})$$

---

[5]Note that $dA = r^2 dr d\Omega = r^2 \sin\theta dr d\theta d\phi$.

[6]Van Gelderen writes $|\mathbf{\Delta}| < |\mathbf{r}|$, this has to be an error. In other publications we find $\leq$. We do not follow Van Gelderen here.

[7]Note that we have $l' - l$ and $m - m'$.

We can use this to write

$$
\begin{aligned}
S_{l,m}(\mathbf{r}) &= S_{l,m}(\mathbf{r} - \boldsymbol{\Delta} + \boldsymbol{\Delta}) \\
&= \sum_{L'} (-1)^{l'+m'-m} R_{l'-l,m-m'}(\boldsymbol{\Delta}) S_{l',m'}(\mathbf{r} - \boldsymbol{\Delta})
\end{aligned}
\tag{B.78}
$$

In addition we use Van Gelderens shift expression for the normalized spherical harmonics:

$$
\begin{aligned}
Y_L(\mathbf{x} - \mathbf{y}) &= \frac{1}{|\mathbf{x} - \mathbf{y}|^l} \sum_{L'} (-1)^{l'} \frac{\sqrt{\frac{4\pi(2l+1)}{(2l-2l'+1)(2l'+1)}} \sqrt{\frac{(l-m)!(l+m)!}{(l'-m')!(l'+m')!}}}{\sqrt{(l-l'-m+m')!(l-l'+m-m')!}} \\
&\quad |\mathbf{y}|^{l'} Y_{L'}(\mathbf{y}) |\mathbf{x}|^{l-l'} Y_{l-l',m-m'}(\mathbf{x})
\end{aligned}
\tag{B.79}
$$

B.4.2 Transformation in 3D

We have a function expanded in spherical harmonics[8] around the origin

$$
f(\mathbf{r}) = \sum_L f_L(|\mathbf{r}|) Y_L(\mathbf{r})
\tag{B.80}
$$

and want to have the expansion shifted to a new center $\boldsymbol{\Delta}$:

$$
f(\mathbf{r}) = \sum_L f_L(|\mathbf{r} - \boldsymbol{\Delta}|) Y_L(\mathbf{r} - \boldsymbol{\Delta}) .
$$

We start with (B.80) and multiply by 1:

$$
f(\mathbf{r}) = \sum_L f_L(|\mathbf{r}|) \frac{1}{|\mathbf{r} - \boldsymbol{\Delta}|} |\mathbf{r} - \boldsymbol{\Delta}| Y_L(\mathbf{r})
$$

Using the expansion (B.77) and the substitution (B.78) leads to:

$$
\begin{aligned}
f(\mathbf{r}) \stackrel{(B.77)}{=}& \sum_{LL'} f_L(|\mathbf{r}|) R_{L'}^*(\boldsymbol{\Delta}) S_{L'}(\mathbf{r}) |\mathbf{r} - \boldsymbol{\Delta}| Y_L(\mathbf{r}) \\
\stackrel{(B.78)}{=}& \sum_{LL'L''} f_L(|\mathbf{r}|) R_{L'}^*(\boldsymbol{\Delta}) (-1)^{l''+m''-m'} R_{l''-l',m'-m''}(\boldsymbol{\Delta}) \\
& \times S_{l'',m''}(\mathbf{r} - \boldsymbol{\Delta}) |\mathbf{r} - \boldsymbol{\Delta}| Y_L(\mathbf{r}) \\
& \sum_{L''} \left[\sum_{LL'} (-1)^{l''+m''-m'} f_L(|\mathbf{r}|) R_{l',m'}^*(\boldsymbol{\Delta}) R_{l''-l',m'-m''}(\boldsymbol{\Delta}) Y_L(\mathbf{r}) |\mathbf{r} - \boldsymbol{\Delta}| \right] \\
=& \times S_{l'',m''}(\mathbf{r} - \boldsymbol{\Delta})
\end{aligned}
\tag{B.81}
$$

---

[8]With $\sum\limits_L = \sum\limits_l \sum\limits_{m=-l}^{l}$.

The expression in brackets defines the expansion coefficients for the expansion with center $\boldsymbol{\Delta}$.

B.4.3 Transition to normalized spherical harmonics

We can express (B.81) in terms of normalized spherical harmonics:

$$
\begin{aligned}
f(\mathbf{r}) &\overset{(B.75)}{=} \sum_{LL'L''} (-1)^{l''+m''-m'} f_L(|\mathbf{r}|) R_{L'}^*(\boldsymbol{\Delta}) R_{l''-l',m'-m''}(\boldsymbol{\Delta}) \\
&\qquad Y_L(\mathbf{r}) |\mathbf{r}-\boldsymbol{\Delta}| (-1)^{m''}(l''-m'')! \frac{1}{|\mathbf{r}-\boldsymbol{\Delta}|^{l''+1}} \tilde{Y}_{l'',m''}(\mathbf{r}-\boldsymbol{\Delta}) \\
&= \sum_{LL'L''} (-1)^{l''+m''-m'} f_L(|\mathbf{r}|) R_{L'}^*(\boldsymbol{\Delta}) R_{l''-l',m'-m''}(\boldsymbol{\Delta}) \\
&\qquad Y_L(\mathbf{r})(l''-m'')! \left(\frac{(2l''+1)(l''-m'')!}{4\pi(l''+m'')!} \right)^{-\frac{1}{2}} \frac{|\mathbf{r}-\boldsymbol{\Delta}|}{|\mathbf{r}-\boldsymbol{\Delta}|^{l''+1}} Y_{l'',m''}(\mathbf{r}-\boldsymbol{\Delta}) \\
&= \sum_{LL'L''} \frac{(-1)^{l''+m''-m'}}{\left(\frac{(2l''+1)(l''-m'')!}{4\pi(l''+m'')!} \right)^{\frac{1}{2}}} f_L(|\mathbf{r}|) R_{L'}^*(\boldsymbol{\Delta}) R_{l''-l',m'-m''}(\boldsymbol{\Delta}) \\
&\qquad Y_L(\mathbf{r})(l''-m'')! \frac{1}{|\mathbf{r}-\boldsymbol{\Delta}|^{l''}} Y_{l'',m''}(\mathbf{r}-\boldsymbol{\Delta}) \\
&= \sum_{L''} \sum_{LL'} \frac{(-1)^{l''+m''-m'}}{\left(\frac{(2l''+1)(l''-m'')!}{4\pi(l''+m'')!} \right)^{\frac{1}{2}}} f_L(|\mathbf{r}|) R_{L'}^*(\boldsymbol{\Delta}) R_{l''-l',m'-m''}(\boldsymbol{\Delta}) \\
&\qquad Y_L(\mathbf{r})(l''-m'')! \frac{1}{|\mathbf{r}-\boldsymbol{\Delta}|^{l''}} Y_{l'',m''}(\mathbf{r}-\boldsymbol{\Delta})
\end{aligned}
$$

B.4.4 Alternative transformation expression

We start with (B.80):

$$
f(\mathbf{r}) = \sum_L f_L(|\mathbf{r}|) Y_L(\mathbf{r})
$$

and rewrite $Y_L(\mathbf{r}) = Y_L(\mathbf{r}-\boldsymbol{\Delta}+\boldsymbol{\Delta})$ using (B.79):

$$
\begin{aligned}
f(\mathbf{r}) = \sum_L f_L(|\mathbf{r}|) \frac{1}{|\mathbf{r}|^l} \sum_{L'} (-1)^{l'} \frac{\sqrt{\frac{4\pi(2l+1)}{(2l-2l'+1)(2l'+1)}} \sqrt{\frac{(l-m)!(l+m)!}{(l'-m')!(l'+m')!}}}{\sqrt{(l-l'-m+m')!(l-l'+m-m')!}} \\
\times |\boldsymbol{\Delta}|^{l'} Y_{L'}(\boldsymbol{\Delta}) |\mathbf{r}-\boldsymbol{\Delta}|^{l-l'} Y_{l-l',m-m'}(\mathbf{r}-\boldsymbol{\Delta})
\end{aligned}
$$

We can now expand the radial part $\frac{1}{|\mathbf{r}|^l}f_L(|\mathbf{r}|)$ around the new center $\boldsymbol{\Delta}$:

$$\frac{1}{|\mathbf{r}|^l}f_L(|\mathbf{r}|) = \sum_{L''} g_{L,L''}(|\mathbf{r}-\boldsymbol{\Delta}|)Y_{L''}(\mathbf{r}-\boldsymbol{\Delta})$$

$$\int \frac{1}{|\mathbf{r}|^l}f_L(|\mathbf{r}|)Y^*_{L'''}(\mathbf{r}-\boldsymbol{\Delta})\mathrm{d}\Omega = \sum_{L''} g_{L,L''}(|\mathbf{r}-\boldsymbol{\Delta}|)\int Y^*_{L'''}(\mathbf{r}-\boldsymbol{\Delta})Y_{L''}(\mathbf{r}-\boldsymbol{\Delta})\mathrm{d}\Omega$$

$$\int \frac{1}{|\mathbf{r}|^l}f_L(|\mathbf{r}|)Y^*_{L''}(\mathbf{r}-\boldsymbol{\Delta})\mathrm{d}\Omega = g_{L,L''}(|\mathbf{r}-\boldsymbol{\Delta}|)$$

and get:

$$
\begin{aligned}
f(\mathbf{r}) &= \sum_{L}\sum_{L''} g_{L,L''}(|\mathbf{r}-\boldsymbol{\Delta}|)Y_{L''}(\mathbf{r}-\boldsymbol{\Delta})\sum_{L'}(-1)^{l'}\\
&\quad \times \frac{\sqrt{\frac{4\pi(2l+1)}{(2l-2l'+1)(2l'+1)}}\sqrt{\frac{(l-m)!(l+m)!}{(l'-m')!(l'+m')!}}}{\sqrt{(l-l'-m+m')!(l-l'+m-m')!}}\\
&\quad \times |\boldsymbol{\Delta}|^{l'}Y_{L'}(\boldsymbol{\Delta})|\mathbf{r}-\boldsymbol{\Delta}|^{l-l'}Y_{l-l',m-m'}(\mathbf{r}-\boldsymbol{\Delta})\\[2ex]
&= \sum_{L}\sum_{L''} g_{L,L''}(|\mathbf{r}-\boldsymbol{\Delta}|)\sum_{L'}(-1)^{l'}\frac{\sqrt{\frac{4\pi(2l+1)}{(2l-2l'+1)(2l'+1)}}\sqrt{\frac{(l-m)!(l+m)!}{(l'-m')!(l'+m')!}}}{\sqrt{(l-l'-m+m')!(l-l'+m-m')!}}\\
&\quad \times |\boldsymbol{\Delta}|^{l'}Y_{L'}(\boldsymbol{\Delta})|\mathbf{r}-\boldsymbol{\Delta}|^{l-l'}Y_{L''}(\mathbf{r}-\boldsymbol{\Delta})Y_{l-l',m-m'}(\mathbf{r}-\boldsymbol{\Delta})
\end{aligned}
$$

Let's try to get rid of the $l - l'$:

$$
\begin{aligned}
= & \sum_{L'''} \sum_{L'} \sum_{L''} g(|\mathbf{r} - \boldsymbol{\Delta}|) \, (-1)^{l'} \frac{\sqrt{\frac{4\pi(2l'+l'''+1)}{(2l'''+1)(2l'+1)}} \sqrt{\frac{(l'+l'''-m'-m''')!(l'+l'''+m'+m''')!}{(l'-m')!(l'+m')!}}}{\sqrt{(l'''-m''')!(l'''+m''')!}} \\
& \times |\boldsymbol{\Delta}|^{l'} Y_{L'}(\boldsymbol{\Delta}) |\mathbf{r} - \boldsymbol{\Delta}|^{l'''} Y_{L''}(\mathbf{r} - \boldsymbol{\Delta}) Y_{l''',m'''}(\mathbf{r} - \boldsymbol{\Delta})
\end{aligned}
$$

$$
\begin{aligned}
= & \sum_{L'''} \sum_{L'} \sum_{L''} g(|\mathbf{r} - \boldsymbol{\Delta}|) \, (-1)^{l'} \frac{\sqrt{\frac{4\pi(2l'+l'''+1)}{(2l'''+1)(2l'+1)}} \sqrt{\frac{(l'+l'''-m'-m''')!(l'+l'''+m'+m''')!}{(l'-m')!(l'+m')!}}}{\sqrt{(l'''-m''')!(l'''+m''')!}} \\
& \times |\boldsymbol{\Delta}|^{l'} Y_{L'}(\boldsymbol{\Delta}) |\mathbf{r} - \boldsymbol{\Delta}|^{l'''} \sum_{L''''} c_{L'',L''',L''''} Y_{L''''}(\mathbf{r} - \boldsymbol{\Delta})
\end{aligned}
$$

$$
\begin{aligned}
= & \sum_{L''''} \sum_{L'} \sum_{L''} \sum_{L'''} g(|\mathbf{r} - \boldsymbol{\Delta}|) \, (-1)^{l'} \frac{\sqrt{\frac{4\pi(2l'+l'''+1)}{(2l'''+1)(2l'+1)}} \sqrt{\frac{(l'+l'''-m'-m''')!(l'+l'''+m'+m''')!}{(l'-m')!(l'+m')!}}}{\sqrt{(l'''-m''')!(l'''+m''')!}} \\
& \times |\boldsymbol{\Delta}|^{l'} Y_{L'}(\boldsymbol{\Delta}) |\mathbf{r} - \boldsymbol{\Delta}|^{l'''} c_{L'',L''',L''''} \, Y_{L''''}(\mathbf{r} - \boldsymbol{\Delta})
\end{aligned}
$$

Note however, that these expressions are explicit, but numerically inconvenient. For numerical implementations, the rotate - expand - rotate algorithm discussed in the following subsection is preferable.

B.4.5 Rotate - expand - rotate algorithm

The explicit transformations in 3D, derived above are numerically demanding. For numerical implementations, it is preferable to divide the transformation in three steps. In a first step, we rotate the spherical harmonics such, that the connecting vector between old and new center lie on the z-axis. In a second step we expand the rotated expansion in the new center and finally, we rotate the result back. The advantage is that in step two, we can exploit that all components for which $m \neq 0$ do not contribute and that the integration along $d\phi$ can be carried out analytically (this will be explained in the following).

Recursion formulas for the determination of rotation matrices for real spherical harmonics can be found in [100]. This is common knowledge, we therefore will not go into detail here[9].

In the following, we suppose the (rotated) spherical harmonics expansion of a given

---

[9]The numerical implementation of the rotation is based on the routine `rotateylm` of the PAW library.

function in 3D to be located at $\mathbf{R} = (0, 0, R)$:

$$f(\mathbf{r}) \;\; = \;\; \sum_L f_L(|\mathbf{r} - \mathbf{R}|) Y_L(\mathbf{r} - \mathbf{R})$$

The new expansion center shall be located in the origin:

$$\sum_L f_L(|\mathbf{r} - \mathbf{R}|) Y_L(\mathbf{r} - \mathbf{R}) \;\; = \;\; \sum_{L'} g_{L'}(|\mathbf{r}|) Y_{L'}(\mathbf{r}).$$

We can access the radial part of the new expansion for a given distance $|\mathbf{r}|$, by projection onto $Y_{L'}^*(\mathbf{r})$ and surface integration at constant $|\mathbf{r}|$, which we denote by $d\Omega_{\mathbf{r}}$:

$$\sum_L \int f_L(|\mathbf{r} - \mathbf{R}|) Y_{L'}^*(\mathbf{r}) Y_L(\mathbf{r} - \mathbf{R}) d\Omega_{\mathbf{r}} \;\; = \;\; \sum_{L'} g_{L'}(|\mathbf{r}|) \int \underbrace{Y_{L'}^*(\mathbf{r}) Y_{L'}(\mathbf{r}) d\Omega_{\mathbf{r}}}_{\overset{B.65}{=} \delta_{L,L'}}$$

$$\sum_L \int f_L(|\mathbf{r} - \mathbf{R}|) Y_{L'}^*(\mathbf{r}) Y_L(\mathbf{r} - \mathbf{R}) d\Omega_{\mathbf{r}} \;\; = \;\; g_{L'}(|\mathbf{r}|) \tag{B.82}$$

Note that the distance $|\mathbf{r} - \mathbf{R}|$ changes during integration over Ω. We can now switch to spherical coordinates centered at $\mathbf{R}$ ($|\mathbf{r} - \mathbf{R}|, \alpha, \phi$) and the origin ($|\mathbf{r}|, \theta, \phi$). We can now exploit, that the expansion center of the original and final expansion is only shifted along z. Applying the law of cosine, the following relations

$$|\mathbf{r} - \mathbf{R}| \;\; = \;\; \sqrt{R^2 + r^2 - 2rR\cos\theta}$$

$$\alpha \;\; = \;\; \underbrace{arccos\left(\frac{r\cos\theta - R}{\sqrt{R^2 + r^2 - 2rR\cos\theta}} \right)}_{:=h(\theta)},$$

with $r = |\mathbf{r}|$ and $R = |\mathbf{R}|$ hold. Insertion in (B.82) leads to:

$$g_{L'}(|\mathbf{r}|) \;\; = \;\; \sum_L \int_0^\pi \int_0^{2\pi} f_L(\sqrt{R^2 + r^2 - 2rR\cos\theta}) Y_{L'}^*(\theta, \phi) Y_L(h(\theta), \phi) d\phi \sin\theta d\theta$$

$$= \;\; \sum_L 2\pi \delta_{m,m'} \int_0^\pi f_L(\sqrt{R^2 + r^2 - 2rR\cos\theta}) \bar{P}_{L'}(\cos\theta) \bar{P}_L(\cos(h(\theta))) \sin\theta d\theta. \tag{B.83}$$

In the second line we used that f_L is constant for ϕ integration, and that the product $Y_{L'}^* Y_L$ only contributes for equal magnetic quantum numbers. The latter follows from

the definition of the spherical harmonics (B.72):

$$\int\limits_{0}^{2\pi} Y_{L'}^*(\theta,\phi)Y_L(h(\theta),\phi)d\phi = \bar{P}_{L'}(cos\theta)\bar{P}_L(cos(h(\theta)))\int\limits_{0}^{2\pi} e^{(m-m')i\phi}d\phi$$

$$= \bar{P}_{L'}(cos\theta)\bar{P}_L(cos(h(\theta)))2\pi\delta_{m,m'}$$

We perform the θ integration on an equispaced grid with 300 grid points. Further reduction of numerical costs may be achieved by application of Gaussian quadrature (choosing optimized grid points and integration weights) with spherical harmonics as generating functions [86].

B.5 Numerical integration of Schrödinger's equation

B.5.1 Logarithmic grid

The spherical harmonics basis set, with its decomposition in radial function times spherical harmonics:

$$f(\mathbf{r}) = \sum_{l,m} f_{l,m}(|\mathbf{r}|)Y_{l,m}(\mathbf{r}),$$

is the natural basis of isolated atoms. In numerical implementations, the radial functions thereby are usually held on logarithmic radial grids:

$$r(x) = r_1 e^{(x-1)\alpha}, x = 1\ldots nr$$
$$r(x+1) = r(x)e^{\alpha}$$

with typical values of $nr = 250$, $r_1 = 1.056 \cdot 10^{-4} a_0$ and $\alpha = 1/20$, respectively. This allows a high resolution near the nucleus, where the potential and wave functions are steep, and a description of the smooth long-range behavior with a limited number of mesh-points.

When switching to logarithmic radial grids, the integration limits, integration variables and derivatives can be expressed in terms of grid points (x) as follows:

$$x = \frac{ln\frac{r}{r_1}}{\alpha} + 1$$

$$dr = \alpha r(x)dx$$

$$\frac{\partial}{\partial r} = \frac{\partial}{\alpha r(x)\partial x}$$

$$\frac{\partial^2}{\partial r^2} = -\frac{1}{\alpha r(x)^2}\frac{\partial}{\partial x} + \frac{1}{\alpha^2 r(x)^2}\frac{\partial^2}{\partial x^2}$$

B.5.2 Schrödinger's equation in spherical harmonics

We expand an arbitrary basis set $|\Phi\rangle$ in spherical harmonics:

$$\langle r|\Phi\rangle \;\; = \;\; \sum_{l,m} \varphi_{lm}(|\mathbf{r}|) \cdot Y_{lm}(\mathbf{r})$$

and insert this in the inhomogeneous Schrödinger equation

$$\left(\frac{1}{2}\hat{P}^2 + \hat{V}_{loc} - \varepsilon\right)|\Phi\rangle = |I\rangle$$

$$\int\int|r'\rangle\langle r'|\left(\frac{1}{2}\hat{P}^2 + \hat{V}_{loc} - \varepsilon\right)|r\rangle\langle r|\Phi\rangle dr'dr = \int|r\rangle\langle r|I\rangle dr$$

$$\int|r\rangle\left(-\frac{1}{2}\nabla^2 + \sum_{l,m}V_{lm}(|\mathbf{r}|)\cdot Y_{lm}(\mathbf{r}) - \varepsilon\right)$$

$$\sum_{l',m'}\varphi_{l'm'}(|\mathbf{r}|)\cdot Y_{l'm'}(\mathbf{r})d\Omega = \int|r\rangle\sum_{l,m}I_{lm}(|\mathbf{r}|)\cdot Y_{lm}(\mathbf{r})d\Omega$$

$$both\ sides\ \cdot\ \langle Y_{l'''m'''},|\mathbf{r}||$$

$$\int Y^*_{l'''m'''}(\mathbf{r})\left(-\frac{1}{2}\nabla^2 + \sum_{l,m}V_{lm}(|\mathbf{r}|)\cdot Y_{lm}(\mathbf{r}) - \varepsilon\right)$$

$$\sum_{l',m'}\varphi_{l'm'}(|\mathbf{r}|)\cdot Y_{l'm'}(\mathbf{r})d\Omega = \sum_{l,m}I_{lm}(|\mathbf{r}|)$$

$$\underbrace{\int Y^*_{l'''m'''}(\mathbf{r})\cdot Y_{lm}(\mathbf{r})d\Omega}_{\delta_{l,l'''}\delta_{m,m'''}}$$

$$\int Y^*_{l'''m'''}(\mathbf{r})\left(-\frac{1}{2}\nabla^2_\mathbf{r} - \varepsilon\right)\sum_{l',m'}\varphi_{l'm'}(|\mathbf{r}|)\cdot Y_{l'm'}(\mathbf{r})d\Omega$$

$$+\sum_{l',m'}\sum_{l,m}\int Y^*_{l'''m'''}(\mathbf{r})Y_{l'm'}(\mathbf{r})Y_{lm}(\mathbf{r})d\Omega V_{lm}(|\mathbf{r}|)\varphi_{l'm'}(|\mathbf{r}|) = I_{l'''m'''}(|\mathbf{r}|)$$

$$\int Y^*_{l'''m'''}(\mathbf{r})\left(\frac{1}{2}\cdot\underbrace{(-\nabla^2_\mathbf{r})}_{=-\frac{1}{r}\partial^2_r r+\frac{1}{r^2}\hat{L}^2} - \varepsilon\right)$$

$$\sum_{l',m'}\varphi_{l'm'}(|\mathbf{r}|)\cdot Y_{l'm'}(\mathbf{r})d\Omega$$

$$+\sum_{l',m'}\sum_{l,m}\underbrace{c_{l'''m'''l'm'lm}}_{Gaunt\,coefficient}V_{lm}(|\mathbf{r}|)\varphi_{l'm'}(|\mathbf{r}|) = I_{l'''m'''}(|\mathbf{r}|)$$

$$\sum_{l',m'}\int Y^*_{l'''m'''}(\mathbf{r})Y_{l'm'}(\mathbf{r})$$

$$\left(-\frac{1}{2r}\partial^2_r r + \frac{l'(l'+1)}{2r^2} - \varepsilon\right)\varphi_{l'm'}(|\mathbf{r}|)\cdot d\Omega$$

$$+\sum_{l',m'}\sum_{l,m}c_{l'''m'''l'm'lm}V_{lm}(|\mathbf{r}|)\varphi_{l'm'}(|\mathbf{r}|) = I_{l'''m'''}(|\mathbf{r}|)$$

$$\left(-\frac{1}{2r}\partial^2_r r + \frac{l'''(l'''+1)}{2r^2} - \varepsilon\right)\varphi_{l'''m'''}(|\mathbf{r}|)$$

$$+\sum_{l',m'}\sum_{l,m}c_{l'''m'''l'm'lm}V_{lm}(|\mathbf{r}|)\varphi_{l'm'}(|\mathbf{r}|) = I_{l'''m'''}(|\mathbf{r}|)$$

$$\frac{1}{r}\left(-\frac{1}{2}\partial^2_r + \frac{l'''(l'''+1)}{2r^2} - \varepsilon\right)r\varphi_{l'''m'''}(|\mathbf{r}|)$$

with $r = |\mathbf{r}|$. $\langle Y_{l'''m'''}, |\mathbf{r}||$is a bra, that projects on the sphere surface and then onto a spherical harmonic. In real space this corresponds to a multiplication with $Y^*_{l''m''}(\mathbf{r}')\delta(|\mathbf{r}| - |\mathbf{r}'|)$ and projects onto the radial part for a given $\mathbf{r}$.

We now rewrite[10] $\frac{1}{r}\partial_r^2 r = \frac{1}{r}\partial_r(1 + \partial_r) = \frac{1}{r}(2\partial_r + r\partial_r^2) = \frac{2}{r}\partial_r + \partial_r^2$. This expression is more convenient for the numerical integration than the usual approach where we get r to the right side.

$$\left[-\frac{1}{r}\partial_r - \frac{1}{2}\partial_r^2 + \frac{l(l+1)}{2r^2} - \varepsilon \right] \psi_{lm}(|\mathbf{r}|)$$
$$+ \sum_{l'm',l''m''} c_{lm,l'm',l''m''} V_{l'm'}(|\mathbf{r}|)\psi_{l''m''}(|\mathbf{r}|) = I_{lm}(|\mathbf{r}|)$$

What is the meaning of this equation? We started from Schrödinger's equation including a non-spherical potential. This potential does not allow to decouple the solutions with respect to their angular momentum. A solution in a non-spherical potential has (at least in principle) contributions from all angular momenta. Therefore, we need to write the solution as spherical harmonics expansion $\psi(\mathbf{r}) = \sum_{lm} \psi_{lm}(|\mathbf{r}|)Y_{lm}(\mathbf{r})$. In order to determine a solution to the non-spherical Schrödinger equation, we need to solve the above equation for all present lm channels at the same time (we have a coupled system of differential equations)! But before we focus on this aspect, we'll discuss how to solve one of those equations by numerical integration using Verlet's algorithm.

B.5.3 Discretized Schrödinger's equation

First, we switch to the logarithmic grid as discussed above:

$$\left[-\frac{1}{2\alpha r(x)^2}\partial_x - \frac{1}{2\alpha^2 r(x)^2}\partial_x^2 + \frac{l(l+1)}{2r(x)^2} - \varepsilon \right] \psi_{lm}(x)$$
$$+ \sum_{l'm',l''m''} c_{lm,l'm',l''m''} V_{l'm'}(x)\psi_{l''m''}(x) = I_{lm}(x) \quad \text{(B.84)}$$

Now we can discretize the equation using Verlet's differential operators

$$\partial_x f(x) = \frac{f(x+\Delta) - f(x-\Delta)}{2\Delta}$$
$$\partial_x^2 f(x) = \frac{f(x+\Delta) - 2f(x) + f(x-\Delta)}{\Delta^2}$$

---

[10]We simply use the product rule for derivation: $\frac{1}{r}\partial_r^2 rf(r) = \frac{1}{r}\partial_r(\partial_r rf(r)) = \frac{1}{r}\partial_r(f(r)\partial_r r + r\partial_r f(r)) = \frac{1}{r}\partial_r(1 + r\partial_r)f(r)$ and so on.

with $\Delta = 1$ because we work in the equispaced index space.

$$-\frac{\psi_{lm}(x+1) - \psi_{lm}(x-1)}{4\alpha r(x)^2} - \frac{\psi_{lm}(x+1) - 2\psi_{lm}(x) + \psi_{lm}(x-1)}{2\alpha^2 r(x)^2} + \frac{l(l+1)}{2r(x)^2}\psi_{lm}(x)$$

$$-\varepsilon\psi_{lm}(x) + \sum_{l'm',l''m''} c_{lm,l'm',l''m''} V_{l'm'}(x)\psi_{l''m''}(x)$$

$$= I_{lm}(x)$$

We solve this for $\psi(x+1)$ and $\psi(x-1)$ in order to be able to integrate from inside out and vice versa.

$$\psi_{lm}(x+1) = -\frac{4\alpha^2 r(x)^2}{\alpha + 2}\left(I_{lm}(x) - \sum_{l'm',l''m''} c_{lm,l'm',l''m''} V_{l'm'}(x)\psi_{l''m''}(x)\right.$$

$$\left.-\frac{l(l+1)}{2r(x)^2}\psi_{lm}(x) + \varepsilon\psi_{lm}(x)\right) + \frac{4}{\alpha+2}\psi_{lm}(x) + \frac{\alpha-2}{\alpha+2}\psi_{lm}(x-1)$$

$$\psi_{lm}(x-1) = \frac{4\alpha^2 r(x)^2}{\alpha - 2}\left(I_{lm}(x) - \sum_{l'm',l''m''} c_{lm,l'm',l''m''} V_{l'm'}(x)\psi_{l''m''}(x)\right.$$

$$\left.-\frac{l(l+1)}{2r(x)^2}\psi_{lm}(x) + \varepsilon\psi_{lm}(x)\right) + \frac{\alpha+2}{\alpha-2}\psi_{lm}(x+1) - \frac{4}{\alpha-2}\psi_{lm}(x)$$

Spherical potentials

For strictly spherical potentials[11], the lm channels do not mix. We have

$$\sum_{l'm',l''m''} c_{lm,l'm',l''m''} V_{l'm'}(x)\psi_{l''m''}(x) \to V_{l'm'=1}(x)\psi_{lm}(x)$$

and the discretized equations become decoupled with respect to the angular momenta:

$$\psi_{lm}(x+1) = -\frac{4\alpha^2 r(x)^2}{\alpha+2}\left(I_{lm}(x) - V_s(x)\psi_{lm}(x) - \frac{l(l+1)}{2r(x)^2}\psi_{lm}(x) + \varepsilon\psi_{lm}(x)\right)$$

$$+\frac{4}{\alpha+2}\psi_{lm}(x) + \frac{\alpha-2}{\alpha+2}\psi_{lm}(x-1)$$

$$\psi_{lm}(x-1) = \frac{4\alpha^2 r(x)^2}{\alpha-2}\left(I_{lm}(x) - V_s(x)\psi_{lm}(x) - \frac{l(l+1)}{2r(x)^2}\psi_{lm}(x) + \varepsilon\psi_{lm}(x)\right)$$

$$+\frac{\alpha+2}{\alpha-2}\psi_{lm}(x+1) - \frac{4}{\alpha-2}\psi_{lm}(x)$$

---

[11] Do not forget the factor $\frac{1}{\sqrt{4\pi}}$: $V(\mathbf{r}) = V(r) = V_s(r)\frac{1}{\sqrt{4\pi}}$!

Choosing the correct boundary conditions and an approximated energy ε_{app}, this equations allow to integrate Schrödinger's equation from inside out ($x = 1 \rightarrow x = x_{max}$) and outside in ($x = x_{max} \rightarrow x = 1$). The two solutions usually are matched at the classical return point. For ε_{app} not being the energy of the exact solution, this leads to a kink at the matching point, which is proportional to the deviation in energy. A better estimate of the exact energy can therefore be obtained from the miss-match in the logarithmic derivatives at the matching point for at least two different energies.

Non-spherical potentials

For non-spherical potentials, the angular momenta do not decouple. It is therefore necessary to solve all equations step by step in parallel. The basic approach thereby is similar to the spherical case: all equations are solved in parallel from outside in and inside out (note the mixing of angular momenta for a given channel only depends on the information of all other angular momenta channels from the previous mesh points). Matching inside and outside solutions at the classical return-point however leads to a matrix equation in ε.

C Publication

Due to copyright issues, the publication *Dynamical dimer method for the determination of transition states with ab initio molecular dynamics*, J. Chem. Phys. 128, 044107 (2008) is not included in this version of the thesis.

D Symbols and Constants

D.1 Symbols used

Γ	Transition Rate
ε	Dielectric constant
λ	Lagrange Multiplier
ρ	Density
τ	Average Lifetime
$\tilde{\phi}$	Auxiliary Partial Wave Function
ϕ^c	Core Electron Wave Function
ψ	Single Particle Wave Function
$\tilde{\psi}$	Auxiliary Single Particle Wave Function
Ψ	Total Wave Function
$\tilde{\Psi}$	Auxiliary Total Wave Function
a_0	Bohr Radius
AIMD	Ab Initio Molecular Dynamic
ASW	Augmented Spherical Wave
au	atomic units
CI	Configuration Interaction (methods)
CP	Car Parrinello
d	constraint dimer distance
DFT	Density Functional Theory
E	Energy
E_{PW}	Plane Wave Cutoff Energy
E_{TF}	THOMAS-FERMI energy for atoms
f_i	Occupation Number
$\mathbf{F}$	Force Vector
$\bar{\mathbf{F}}$	Velocity Dependent Force Vector
G	Constraint Function
G_{max}	Maximum Value of the Wave Vector for Plane Wave Expansions
GGA	General Gradient Approximation
$\hat{H}$	Hamiltonian operator
H	Hamiltonian
$\mathbb{H}$	Hessian matrix
I	Flux

$\underline{\mathbf{I}}$	Matrix that projects out the direction parallel to the dimer
J	Exchange Interaction in the LEPS Potential
k	Boltzmann's constant
l	angular momentum
$\mathcal{L}$	Lagrange Function
LDA	Local Density Approximation
LEPS	London-Eyring-Polanyi-Sato
LMTO	Linear Muffin Thin Orbital
LAPW	Linear Augmented Plane Wave
LSDA	Local Spin Density Approximation
m_e	Mass of the electron
m_{ni}	Mass of the nuclei i
$\underline{\mathbf{m}}$	Mass Matrix
$\underline{\mathbf{M}}$	$\frac{1}{2}\underline{\mathbf{m}} - \underline{\mathbf{m}}^{\frac{1}{2}}\,\underline{\mathbf{I}}\,\underline{\mathbf{m}}^{\frac{1}{2}}$
$\bar{M}_{ij}$	$M_{ij} + M_{ji}$
M_o	Fictitious Mass-factor for the rotational Velocity of the Dimer
$M_\parallel$	Fictitious Mass-factor for the parallel Velocity of the Dimer
$M_\perp$	Fictitious Mass-factor for the perpendicular Velocity of the Dimer
MPI	Message Passing Interface
MPICH	MPI implementation of the University of Chicago
n	Number of electrons in a given system
N	Number of nuclei in a given system
$\tilde{p}_R$	Projector Function for atom R in PAW
PAW	Projector Augmented Wave
Q	Coulomb Interaction in the LEPS Potential
$\mathbf{r}$	Space coordinate of the electrons
$\mathbf{R}$	Space coordinate of the nuclei
$\mathbf{R}_+$	Space Coordinate at the next Time-step
$\mathbf{R}_-$	Space Coordinate at the last Time-step
$\mathbf{R}_{TS}$	Space Coordinate of the Transition State
$r_{c,R}$	Cutoff radius for atom R
S_R	Local contribution around nuclei R in PAW
s	Spin coordinate of the electrons
S_N2	Substitution Nucleophilic Bipolar
SCF	Self Consistent Field
SI	International system (for units)
$\hat{\mathcal{T}}$	Transformation Operator in the PAW method
T_{TF}	THOMAS-FERMI kinetic energy
$\hat{T}_e$	Kinetic energy operator for the electrons
$\hat{T}_n$	Kinetic energy operator for the nuclei
V	Volume
v_o	Rotational Velocity of the Dimer

$v_\parallel$	Parallel Velocity of the Dimer
$v_\perp$	Perpendicular Velocity of the Dimer
V_{eff}	Effective Potential
$\hat{V}_{ee}$	Electron-electron interaction potential operator
$\hat{V}_{en}$	Electron-nuclei interaction potential operator
$\hat{V}_{ext}$	External-potential operator
$\hat{V}_{nn}$	Nuclei-nuclei interaction potential operator
$\mathbf{x}$	Coordinate (space and spin) of the electrons in DFT
$\mathbf{x}$	$\underline{\mathbf{m}}^{\frac{1}{2}}\mathbf{R}$ in Dimer Calculations
Z	Nuclear charge in au

D.2 Physical Constants

$$
\begin{aligned}
a_0 &= 0.529177\,\text{Å} \\
c_{vac} &= 2.99792 \cdot 10^8\,\tfrac{m}{s} \\
\varepsilon_0 &= 8.85419 \cdot 10^{-12}\,\tfrac{C^2}{Jm} \\
\hbar &= 1.05457 \cdot 10^{-34}\,Js \\
h &= 6.62608 \cdot 10^{-34}\,Js \\
k &= 1.30866 \cdot 10^{-23}\,\tfrac{J}{K} \\
m_e &= 9.10939 \cdot 10^{-31}\,kg \\
m_p &= 1.67262 \cdot 10^{-27}\,kg \\
m_n &= 1.67493 \cdot 10^{-27}\,kg
\end{aligned}
$$

E CV

Curriculum Vitae

Alexander Poddey

Persönliche Daten

Name:	Alexander Poddey
Geburtsdaten:	20.08.1976, in Karlsruhe
Familienstand:	verheiratet
Anschrift:	Adolf-Eystr. 14
	38678 Clausthal
Tel.(dienstl.):	+49 (0) 5323 - 72 25 80
Tel.(privat):	+49 (0) 176 - 43 12 00 87
Email:	alexander.poddey@gmx.net

Hochschulbildung

06/2004–dato **Promotion**, Abteilung für theoretische Physik - Technische Universität Clausthal

- Theoretische Untersuchung und Ableitung von Methoden zur numerischen Simulation physikalischer Systeme (Quanten- & klassische Mechanik; u.a. dynamische Strukturoptimierung).
- Numerische Implementierung als eigenständiges Programmpaket (FORTRAN 90, mehrere 10-tausend Zeilen, objektorientiert).
- Pflege und Weiterentwicklung eines wissenschaftlichen Simulationspaketes, Multilevel-Parallelisierung auf Beowulf-Clustern (MPI, InfiniBand), Administration der Cluster
- Einführung von Methoden zur Qualitätssicherung in der Softwareentwicklung innerhalb der Arbeitsgruppe
- Lehr- und Diplomandenbetreuung. Einführung eines neuen Übungssystems für Studenten.

10/2002–05/2004 **Dipl.-Phys. (Uni), mit Auszeichnung**, Schwerpunkt: theoretische Physik - Technische Universität Clausthal (Gesamtschnitt: 1,0)
Diplomarbeit angefertigt am Institut für theoretische Physik, Titel 'A Dimer Method for the Determination of Transition States in Ab Initio Molecular Dynamics Simulations'
Theoretische Ableitung und numerische Implementierung molekulardynamischer Algorithmen (Euler-Lagrange Mechanik, Car-Parrinello Dynamik; Stabilitätsanalyse, Dämpfung instationärer Systeme)

10/1999–08/2002 **Dipl.-Ing. (FH)**, Maschinentechnik/Zukunftsenergien - Fraunhofer Institut für Solare Energiesysteme & Technische Fachhochschule Bochum (Diplomarbeit: 1,0; Diplomprüfung: 1,0; Gesamtschnitt: 1,8)
Diplomarbeit angefertigt am Fraunhofer Institut für Solare Energiesysteme in Gelsenkirchen, Titel 'Isotrope und anisotrope Texturierung von Silizium zur Reflexionsminderung von Solarzellen'

- Einführung von Oberflächenätzverfahren im Industriemasstab
- Programmierung von Modellierungs- und Simulationssoftware

10/1997–10/1999 Chemie, Technische Universität Karlsruhe

Praktika / Berufserfahrung

06/2004–dato	**Institut für theoretische Physik** - Technische Universität Clausthal, *Wissenschaftlicher Mitarbeiter (Promotion vorauss. 12/2008)*, Kernaufgabengebiete s. Promotion.
10/2005–12/2007	**tec::sol - Technical Solutions** - Ötigheim, *Gründer und Geschäftsführer,* Unternehmung zum Zweck der Entwicklung einer Methode zur Leistungsmessung im Sport (eingereichtes Patent DE 10 2005 052 445.1, Zuteilungsfähigkeit bestätigt, Verfahren läuft); Demonstration der technischen Machbarkeit.

- Patentrecherche, Marktanalyse, Businessplanerstellung, Finanzplanung
- Konzeption und Programmierung von Mikrocontrollersystemen zur Messdatenerfassung und Visualisierung (u.a. 8-Bit RISC, 32-Bit ARM Architektur; Entwicklungsumgebung u.a. Linux GNU ARM toolchain; Sprachen: Assembler, C, C++)
- Entwicklung und Konstruktion mechanischer Komponenten (2D, 3D in MEGACAD)

09/2002–05/2004	**Institut für theoretische Physik** - Technische Universität Clausthal, *Wissenschaftlicher Mitarbeiter (1/4 Stelle),* Ab initio Simulation quantenmechanischer Systeme.
08/2000–08/2002	**Fraunhofer Institut für Solare Energiesysteme** - Gelsenkirchen, *Wissenschaftlicher Mitarbeiter (1/2 Stelle),* Messaufbauten (z.B. Steuerung eines Spektrometers mittels LABVIEW, C, C++, WinAPI).
03/2001–02/2002	**TFH Bochum**, *'Auftragnehmerseitige' Projektleitung (ca. 8 'Teammitglieder'),* Studienprojekt Elektronische Raumüberwachung.
07/2000–08/2000	**Fraunhofer Institut für Solare Energiesysteme** - Gelsenkirchen, *Praktikum.*
02/2000–04/2000	**Siemens KWU** - Mülheim a.d. Ruhr, *Praktikum,* Programmierung eines Systems zur Auftragsverfolgung (Visual Basic, Microsoft Office).

Fremdsprachen

Englisch	Sicher in Wort und Schrift (ständiger beruflicher Gebrauch, Sprache der 2. Diplomarbeit und der Dissertation)
Französisch	Grundkenntnisse

Stipendien / Förderungen

06/2004–dato	e-fellows Online-Stipendium

10/2005–10/2006	Teilnehmer an der 'KMU Patentaktion' des Bundesministeriums für Bildung und Forschung (Förderleistung: 6750 Euro)
01/2005	Marie Curie Fellowship zur Teilnahme am Workshop 'Advanced Monte-Carlo Methods', CECAM, Lyon, France

SCHULBILDUNG / ZIVILDIENST

07/1996–07/1997	Zivildienst im Rettungsdienst, DRK Rastatt
09/1987–06/1996	Tulla Gymnasium Rastatt, Abschluss Abitur
09/1983–06/1987	Grundschule Ötigheim

INTERESSEN

	Triathlon (z.B. IRONMAN Schweiz 2006, Quelle Challenge Roth 2007)
	Bergsteigen, Eisklettern
07/1997–9/1997	Reisen, z.B. mit dem Fahrrad von Südschweden zum Nordkap
03/1994	Prüfung zum Amateurfunker (DG4UAU)

ENGAGEMENT

2006	Initiator der Spendenaktion 'Strong for Human Rights', Sportler zu Gunsten von Amnesty International
05/1988–10/1996	Mitglied im Musikverein Ötigheim (Saxophon und Klarinette)
05/1988–10/1994	Amateurschauspieler an 'Deutschlands größter Freilichtbühne', Ötigheim (z.B. Hofer's Sohn in 'Andreas Hofer', Georg in 'Götz von Berlichingen')

Clausthal-Zellerfeld, August 2008

Vorträge · Publikationen · Seminare

Alexander Poddey

Vorträge

- **The Fictitious Lagrangian Dimer Method and it's Applications**,
  Erster Studentenworkshop TU-Clausthal/TU Ilmenau,
  Clausthal; Jul. 2004

- **A Dimer Method for the Determination of Transition States**,
  Seminar of the Computational Quantum Theory Group at the Institute of Materials Chemistry,
  TU Wien, Österreich; Sep. 2004.

- **A Dimer Method for the Determination of Transition States**,
  Probing Potential Energy Surfaces (PPES-III),
  Zermatt, Schweiz; Apr. 2005,
  eingeladen.

- **An- & Isotrope Texturierung von Silizium zur Reflexionsminderung bei Solarzellen**,
  Q.Cells AG,
  Thalheim; Dez. 2005,
  eingeladen.

- **A Fictitious Lagrangian Formulation of the Dimer Method for the Determination of Transition States**,
  State of the Art, Developements and Perspectives of Electronic Structure Calculations in the Frame of the Projector Augmented Wave (PAW) Method,
  CECAM Lyon, Frankreich; Jun. 2006,
  eingeladen.

- **Dynamical Dimer Method for the Determination of Transition States**,
  1. Harzer Ab Initio Workshop,
  Clausthal-Zellerfeld, Germany; Okt.2006,
  eingeladen.

Veröffentlichungen / Druckschriften

- **Dynamical dimer method for the determination of transition states with ab initio molecular dynamics**,
  A. Poddey and P. E. Blöchl,
  J. Chem. Phys., 128, 044107 (2008).

- **Interaction of NaCl with solid water**,
  A. Borodin, O. Höfft, U. Kahnert, and V. Kempter,
  A. Poddey and P. E. Blöchl,
  J. Chem. Phys. 121, 9671 (2004).

- **A Dimer Method for Finding Transition States in ab initio molecular-dynamics simulations**,
  A. Poddey, Diplomarbeit, Technische Universität Clausthal (2004).

- **Comparison of Texturing Methods for Monocrystalline Silicon Solar Cells using KOH and Na$_2$CO$_3$**,
  W. Sparber, O. Schultz, D. Biro, G. Emanuel, R. Preu,
  A. Poddey and D. Borchert,
  Conference Proceeding: 3rd World Conference Photovoltaic Energy Conversion, Osaka - Japan, (2003)

- **Isotrope und Anisotrope Texturierung von Silizium zur Reflexionsminderung bei Solarzellen**,
  A. Poddey, Diplomarbeit, Fraunhofer Institut für solare Energiesysteme und Technische Fachhochschule Bochum (2002).

Patente

- **Verfahren zum Betrieb eines Trainingsgerätes**,
  Alexander Poddey, DE 10 2005 052 445.1, Zuteilungsfähigkeit bestätigt.

Weiterbildung / Trainings / Seminare

10/2007	2. Harzer ab initio Workshop, Goslar (3 Tage).
10/2006–03/2007	Teilnahme an der Ringvorlesung 'Existenzgündung und Unternehmensführung'.

- Existenzgründung
- Finanzierung und Investition
- Kosten- und Leistungsrechnung
- Buchführung und Bilanzierung
- Recht und Steuern
- Personalwesen
- Arbeitsrecht

10/2006	1. Harzer ab initio Workshop (gemeinsamer Workshop der Abteilung für theoretische Physik TU Clausthal und des Max-Planck-Instituts für Eisenforschung Düsseldorf), Clausthal-Zellerfeld (3 Tage).
06/2006	Workshop 'State of the Art, Developements and Perspectives of the PAW method (DFT)', CECAM, Lyon, Frankreich (3 Tage).
12/2005	Besuch bei Q.Cells AG, Thalheim (2 Tage).
04/2005	Probing Potential Energy Surfaces (PPES-III) Zermatt, Schweiz (6 Tage).
01/2005	Workshop 'Advanced Monte-Carlo Methods', CECAM, Lyon, Frankreich (14 Tage).
09/2004	Besuch der Forschergruppe 'Computational Quantum Chemistry', Institut für Materialchemie, TU Wien, Österreich (6 Tage).
02/2004	19. Workshop 'Novel Materials and Superconductor', Planneralm, Österreich (7 Tage).

F Danksagung

Abschließend möchte ich mich bei all jenen bedanken, die zum Gelingen dieser Arbeit beigetragen haben, insbesondere bei:

Meinem Betreuer, Herrn Prof. Peter Blöchl für die Vergabe eines Themas, welches meine Hartnäckigkeit und Zähigkeit sehr effektiv auf die Probe gestellt hat, sowie für hervorragende Arbeitsbedingungen.
Prof. Tom Kirchner für die Übernahme der Zweitbegutachtung, sowie die vielen mehr oder weniger politischen, aber immer sehr unterhaltsamen Gespräche.
Jürgen Noffke, für seine hervorragende Einführung in die theoretische Festkörperphysik und viele wichtige Diskussionen und Anregungen.
Meinem Vorgänger im Thema und Freund Clemens Först für die Einführung ins Themengebiet, und so manche Unterstützung entlang des Weges.
Dem "Leidensgenossen" Sascha Hemmen, für die vielen Diskussionen, gemeinsamen Squash-Stunden und Croque-Inn Besuche.
Frau Frömmel, für so manche Erleichterung in formalen Dingen.
Allen anderen Mitarbeitern der Abteilung für ihre Unterstützung.

Der Linux- und Open-Source Gemeinde (insbesondere Andy Vaught für die Entwicklung des g95, sowie den Debian Entwicklern), ohne deren großartigen Werkzeuge die Arbeit wohl nicht zu bewältigen gewesen wäre.

Kein Dank geht an die bildungspolitisch Verantwortlichen für das zu Grunde richten der Diplomstudiengänge und der Forschungslandschaft in Deutschland im Allgemeinen, sowie für die Torpedierung der grundlagenorientierten, theoretisch ausgerichteten Fachbereiche. Grundlagenforschung von heute ist der Nährboden für die Anwendung von morgen. Zukunftsorientierte Bildungpolitik sollte daher meiner Meinung nach einen Schwerpunkt auf die theoretischen Fachdisziplinen legen.

Meinen Freunden im Badischen, die mich trotz andauernder Absenz nicht vergessen haben.

Besonderer Dank gilt meinen Eltern, die mich, unabhängig von meinen Entscheidungen immer unterstützt haben. Sie haben mir dadurch Gelegenheit gegeben meinen "Wissensdurst" in verschiedenen Fachgebieten zu befriedigen.
Herzlich bedanken möchte ich mich bei meiner Frau Alice, die mich auch in schwierigen Stunden immer liebevoll unterstützt, und so viele Stunden auf meine Anwesenheit

verzichtet hat.

Vorschlag Dissertationsprüfung

Alexander Poddey

Freitag 28. November 2008 10:00 Uhr

Freitag 21. November 2008 10:00 Uhr

Seminarraum der theoretischen Physik, Leibnizstr.10 Raum 327

List of Figures

List of Tables

Bibliography

[1] E. Fick: *Einführung in die Grundlagen der Quantentheorie* Akademische Verlagsgesellschaft Frankfurth am Main, 1. Auflage (1968).

[2] C. Cohen-Tannoudji, B. Diu, and F. Laloe: *Quantenmechanik* W. de Gruyter Verlag (1999).

[3] D.R. Hartree: The Wave Mechanics of an Atom with a Non-Coulomb Central Field. Part I-Theory and Methods. *Proc. Cam. Phil. Soc.* **24**, 89 (1928) Hartree approximation.

[4] J.C. Slater and G.F. Koster: Simplified LCAO method for the periodic potential problem. *Phys. Rev.* **94**, 1498 (1954).

[5] F. Bloch: Über die Quantenmechanik der Elektronen in Kristallgittern. *Zeitschr. Phys.* **52**, 555 (1929) Original paper on the Bloch theorem.

[6] P. Loewdin: On the Non-Orthogonality Problem Connected with the Use of Atomic Wave Functions in the Theory of Molecules and Crystals. *J. Chem. Phys.* **18**, 365 (1950).

[7] O.K. Andersen and O. Jepsen: Explicit, First-principles Tight-Binding Theory. *Phys. Rev. Lett* **53**, 2571 (1984) Original paper on Tight-binding LMTO.

[8] O. K. Andersen: Linear Methods in band theory. *Phys. Rev. B* **12**, 3060 (1975) Original paper on Linear methods (LMTO,LAPW etc.).

[9] R. Hoffmann: An Extended Hückel Theory. I. Hydrocarbons. *J. Chem. Phys.* **39**, 1397 (1963).

[10] P. Ordejón, D. A. Drabold, M. P. Grumbach, and R. M. Martin: Unconstrained minimization approach for electronic computations that scales linearly with system size. *Phys. Rev. B* **48**, 14646 (1993).

[11] X. P. Li, R. W. Nunes, and D. Vanderbilt: Density-matrix electronic-structure method with linear system-size scaling. *Phys. Rev. B* **47**, 10891 (1993).

[12] O. F. Sankey and D. J. Niklewski: Ab initio multicenter tight-binding model for molecular-dynamics simulations and other applications in covalent systems. *Phys. Rev. B* **40**, 3979 (1989).

[13] C. M. Goringe, D. R. Bowler, and E. Hernández: . *Rep. Prog. Phys.* **60**, 1447 (1997).

[14] V. Fock: . *Z. Phys.* **61**, 126 (1930).

[15] J. C. Slater: Atomic Shielding Constants. *Phys. Rev.* **36**, 57–64 (1930).

[16] L. H. Thomas: The Calculation of Atomic Fields. *Proc. Camb. Philos. Soc.* **23**, 542 (1927).

[17] E. Fermi: Un metodo statistico per la determinazione di alcune priorieta dell'atome. *Rend. Accad. Naz. Lincei* **6**, 602 (1927).

[18] P. Hohenberg and W. Kohn: Inhomogeneous electron gas. *Phys. Rev.* **136**, B864 (1964).

[19] M. Levy: Universal variational functionals of electron densities, first order density matrixes and natural spin-orbitals and solution of the v-representability problem. *Proc. Nat'l Acad. Sci. USA* (1979).

[20] M. Levy: Electron densities in search of Hamiltonians. *Phys. Rev. A* **26**, 1200 (1982).

[21] M. Levy and J. Perdew: *Density Functional Methods in Physics* Plenum Publishing Corporation New York (1985).

[22] R.G. Parr and W. Yang: *Density-Functional Theory of Atoms and Molecules* Oxford Science Publishers (1989).

[23] W. Kohn and L.J. Sham: Self-consistent equations including exchange and correlation effects. *Phys. Rev.* **140**, A1133 (1965).

[24] H. Wendel and R. M. Martin: Theory of structural properties of covalent semiconductors. *Phys. Rev. B* **19**, 5251 (1979).

[25] J. Harris: Simplified method for calculating the energy of weakly interacting fragments. *Phys. Rev. B* **31**, 1770 (1985).

[26] W. M. C. Foulkes: . *PhD Thesis University Cambridge* (1987).

[27] W. M. C. Foulkes and R. Haydock: . *Phys. Rev. B* **39**, 12520 (1989).

[28] A. P. Sutton, M. W. Finnis, D. G. Pettifor, and Y. Ohta: The tight-binding bond model. *J. Phys. C: Solid State Phys.* **21**, 35 (1988).

[29] H. M. Polatoglou and M. Methfessel: Cohesive properties of solids calculated with the simplified total-energy functional of Harris. *Phys. Rev. B* **37**, 10403 (1988).

[30] A. J. Read and R. J. Needs: Tests of the Harris energy functional. *J. Phys.: Condens. Matter* **1**, 7565 (1989).

[31] J. Finnis: The Harris functional applied to surface and vacancy formation energies in aluminium. *J. Phys.: Condens. Matter* **2**, 331 (1990).

[32] N.Chetty, K. W. Jacobsen, and J. K. Nørskov: Optimized and transferable densities from first-principles local density calculations. *J. Phys.: Condens. Matter* **3**, 5437 (1991).

[33] J. Hartford, L. B. Hansen, and B. I. Lundqvist: Harris functional densities: from solid to atom. *J. Phys.: Condens. Matter* **8**, 7379 (1996).

[34] F. W. Averill and G. S. Painter: Harris functional and related methods for calculating total energies in density-functional theory. *Phys. Rev. B* **41**, 10344 (1990).

[35] H. Skriver: *The LMTO Method* Series in Solid-State Sciences 41. Springer Verlag (1984).

[36] O.K. Andersen, T. Saha-Dasgupta, S. Ezhov, L.Tsetseris, O. Jepsen, R. W. Tank, C. Arcangeli, and G. Krier: Third-generation MTOs. ψ_k *Newsletter* **45**, 86 (2001).

[37] J. P. Lewis, K. R. Glaesemann, G. A. Voth, J. Fritsch, A. A. Demkov, J. Ortega, and O. F. Sankey: Further developments in the local-orbital density-functional-theory tight-binding method. *Phys. Rev. B* **64**, 195103 (2001).

[38] A. P. Horsfield: Efficient ab initio tight binding. *Phys. Rev. B* **56**, 6594 (1997).

[39] J. M. Soler, E. Artacho, J. D. Gale, A. García, J. Junquera, P. Ordejón, and D. Sánchez-Portal: The SIESTA method for ab initio order-N materials simulation. *J. Phys.: Condens. Matter* **14**, 2781 (2002).

[40] A. P. Horsfield and A. M. Bratkovsky: Ab initio tight binding. *J. Phys.: Condens. Matter* **12**, r1 (2000).

[41] B. Delley: An all-electron numerical method for solving the local density functional for polyatomic molecules. *J. Chem. Phys.* **92**, 508 (1990).

[42] D. R. Bowler, A. S. Torralba, T. Miyazaki, T. Ohno, and M. J. Gillan: Linear-scaling DFT calculations with the CONQUEST code. ψ_k *Newsletter* **81**, 55 (2007).

[43] C. K. Skylaris, P. D. Haynes, A. A. Mostofi, and M. C. Payne: Introducing ONETEP: Linear-scaling density functional simulations on parallel computers. *J. Chem. Phys.* **122**, 084119 (2005).

[44] K. Koepernik and H. Eschrig: Full-potential nonorthogonal local-orbital minimum-basis band-structure scheme. *Phys. Rev. B* **59**, 1743 (1999).

[45] K. Koepernik, H. Eschrig, I. Opahle, U. Nietzsche, I. Chaplygin, and M. Richter: Full-potential local-orbital minimum-basis scheme FPLO. ψ_k *newsletter* **52**, 101 (2002).

[46] R. Car and M. Parrinello: Unified Approach for Molecular Dynamics and Density-Functional Theory. *Phys. Rev. Lett.* **55**, 2471 (1985).

[47] G. Galli and M. Parrinello: Large scale electronic structure calculations. *Phys. Rev. Lett* **69**, 3547 (1992).

[48] F. Mauri, G. Galli, and R. Car: Orbital formulation for electronic-structure calculations with linear system-size scaling. *Phys. Rev. B* **47**, 9973 (1993).

[49] J. Kim, F. Mauri, and G. Galli: Total-energy global optimizations using nonorthogonal localized orbitals. *Phys. Rev. B* **52**, 1640 (1995).

[50] E. Hernández and M. J. Gillan: Self-consistent first-principles technique with linear scaling. *Phys. Rev. B* **51**, 10157 (1995).

[51] L. L. Boyer, H. T. Stokes, M. M. Ossowski, and M. J. Mehl: Self-consistent atomic deformation method for application of density functional theory. *Phys. Rev. B* **78**, 045121 (2008).

[52] R. Z. Khaliullin, E. A. Cobar, R. C. Lochan, A. T. Bell, and M. Head-Gordon: Unravelling the Origin of Intermolecular Interactions Using Absolutely Localized Molecular Orbitals. *J. Phys. Chem.* **111**, 8753 (2007).

[53] R. Z. Khaliullin, M. Head-Gordon, and A. T. Bell: An efficient self-consistent field method for large systems of weakly interacting components. *J. Chem. Phys.* **124**, 204105 (2006).

[54] G. H. Wannier: The Structure of Electronic Excitation Levels in Insulating Crystals. *Phys. Rev.*, 191 (1937).

[55] N. Mazari and D. Vanderbilt: Maximally localized generalized Wannier functions for composite energy bands. *Phys. Rev. B* **56**, 12847 (1997).

[56] J. M. Foster and S. F. Boys: Canonical Configurational Interaction Procedure. *Rev. Mod. Phys.* **32**, 300 (1960).

[57] S. F. Boys: Construction of Some Molecular Orbitals to Be Approximately Invariant for Changes from One Molecule to Another. *Rev. Mod. Phys.* **32**, 296 (1960).

[58] C. Edminston and K.Ruedenberg: Localized atomic and molecular orbitals. *Rev. Mod. Phys.* **35**, 457 (1963).

[59] J. Pipek and P. G. Mezey: A fast intrinsic localization procedure applicable for ab initio and semiempirical linear combination of atomic orbital wave functions. *J. Chem. Phys.* **90**, 4916 (1989).

[60] N. Marzari, I. Souza, and D. Vanderbilt: An Introduction to Maximally-Localized Wannier Functions. ψ_k *Newsletter* **57**, 129 (2003).

[61] P. L. Silvestrelli: Maximally localized Wannier functions for simulations with supercells of general symmetry. *Phys. Rev. B* **59**, 9703 (1999).

[62] G. Berghold, C. J. Mundy, A. H. Romero, J. Hutter, , and M. Parrinello: General and efficient algorithms for obtaining maximally localized Wannier functions. *Phys. Rev. B* **61**, 10040 (2000).

[63] I. Souza, N. Mazari, and D. Vanderbilt: Maximally localized Wannier functions for entangled energy bands. *Phys. Rev. B* **65**, 035109 (2001).

[64] K. S. Thygesen, L. B. Hansen, and K. W. Jacobsen: Partly Occupied Wannier Functions. *Phys. Rev. Lett* **94**, 026405 (2005).

[65] W.C. Lu, C.Z. Wang, T.L. Chan, K. Ruedenberg, and K.M. Ho: Representation of electronic structures in crystals in terms of highly localized quasiatomic minimal basis orbitals. *Phys. Rev. B.* **70**, 41101 (2004) Quambo for crystals.

[66] W. Kohn: Analytic Properties of Bloch Waves and Wannier Functions. *Phys. Rev.* **115**, 809 (1959).

[67] W. Kohn: Construction of Wannier Functions and Applications to Energy Bands. *Phys. Rev. B*, 4388 (1973).

[68] L. He and D. Vanderbilt: Exponential Decay Properties of Wannier Functions and Related Quantities. *Phys. Rev. Lett* **86**, 5341 (2001).

[69] P. W. Anderson: Self-Consistent Pseudopotentials and Ultralocalized Functions for Energy Bands. *Phys. Rev. Lett* **21**, 13 (1968).

[70] E. Hernandez, M. J. Gillian, and C. M. Goringe: Basis functions for linear-scaling first-principles calculations. *Phys. Rev. B* **55**, 13485 (1997).

[71] J. E. Pask, B. M. Klein, C. Y. Fong, and P. A. Sterne: Real-space local polynomial basis for solid-state electronic-structure calculations: A finite-element approach. *Phys. Rev. B* **59**, 12352 (1999).

[72] X. Qian: Electronic structure and transport in molecular and nanoscale electronics. *PhD Thesis, Massachusetts Institute of Technology* (2008).

[73] U. von Barth and C. D. Gelatt: Validity of the frozen-core approximation and pseudopotential theory for cohesive energy calculations. *Phys. Rev. B* **21**, 2222 (1980).

[74] M. Born: *Atomic Physics, 6th ed.* Blackie and Son / Hafner New York (1959).

[75] K. Kitaura and K. Morokuma: . *Int. J. Quantum Chem.* **2**, 325 (1976).

[76] K. Ruedenberg: The physical nature of the chemical bond. *Rev. Mod. Phys.* **34**, 326 (1962).

[77] Peter Blöchl, private communication.

[78] M. Thieme: Deformierte Ionen als Bausteine kondensierter Materie Master's thesis Institute for Theoretical Physics, Clausthal University of Technology (2003).

[79] C. J. Först: *Computational Materials Science: Oxide-Semiconductor Interfaces and Atomic Fragments for the Descrition of Condensed Matter* PhD thesis Institute for Theoretical Physics, Clausthal University of Technology and Institue for Materials Chemistry, Technical University Vienna (2004).

[80] R. S. Mulliken: Electronic Structures of Molecules XI. Electroaffinity, Molecular Orbitals and Dipole Moments. *J. Chem. Phys.* **3**, 573 (1935).

[81] J. P. Perdew and A. Zunger: Self-interaction correction to density-functional approximations for many-electron systems. *Phys. Rev. B* **23**, 5048 (1981).

[82] P. E. Blöchl: Projector augmented-wave method. *Phys. Rev. B* **50**, 17953 (1994).

[83] P. E. Blöchl, C.J. Först, and J. Schimpl: Projector augmented wave method: ab initio molecular dynamics with full wave functions. *Bull. Mater. Sci.* **26**, 33 (2003).

[84] P. E. Blöchl: Electrostatic Decoupling of Periodic Images of Plane-Wave-Expanded densities and Derived Atomic Point Charges. *J. Chem. Phys.* **103**, 7422 (1986).

[85] K. Kobayashi, N. Kurita, H. Kumahora, and K. Tago: Molecular-bond-energy calculations based on the Harris-functional approximation coupled with the generalized-gradient approximation. *Phys. Rev. B* **45**, 11299 (1992).

[86] M. R. Pederson and K. A. Jackson: . *Phys. Rev. B* **41**, 7453 (1990).

[87] A. Poddey: A dimer method for the determination of transition states Master's thesis Institute for Theoretical Physics, Clausthal University of Technology (2004).

[88] A. Poddey and P. E. Blöchl: Dynamical dimer method for the determination of transition states with ab initio molecular dynamics. *J. Chem. Phys.* **128**, 044107 (2008).

[89] N. W. Ashcroft and N. D. Mermin: *Solid State Physics* Thomson Learning Inc. (1976).

[90] R. Catlow, H. Shercliff, and S. Yip, editors *Handbook of Materials Modeling* chapter "Electronic structure methods: Augmented Waves, Pseudopotentials and the Projector Augmented Wave Method" by P. E. Blöchl, J. Kästner and C. J. Först Kluwer Academic Publishers (2004).

[91] T. A. Albright, J. K. Burdett, and M. H. Whangbo: *Orbital Interactions in Chemistry* J. Wiley & Sons New York (1985).

[92] W. Here, L. Radom, P. Schleyer, and J. Pople: *Ab Initio Molecular Orbital Theory* J. Wiley & Sons (1986).

[93] A.R. Williams, J. Kübler, and Jr. C.D. Gelatt: Cohesive properties of metallic compounds: Augmented-spherical-wave calculations. *Phys. Rev. B* **19**, 6094 (1978) Original paper on the ASW approach.

[94] J. D. Talmann: LSFBTR: A subroutine for calculating spherical bessel transforms. *Comp. Phys. Comm.* **30**, 93 (1983).

[95] C. Cohen-Tannoudji, B. Diu, and F. Laloe: *Quantenmechanik II, p. 221* W. de Gruyter Verlag (1999).

[96] E.U. Condon and G.H. Shortley: *The Theory of Atomic Spectra* University Press Cambridge (1935).

[97] A. Lindner: *Drehimpulse in der Quantenmechanik* Teubner Stuttgart (1984).

[98] M. van Gelderen: The Shift Operators and Translations of Spherical Harmonics. *DEOS Progress Letters* **98.1**, 57 (1998).

[99] E. W. Hobson: *The Theory of Spherical and Ellipsoidal Harmonics.* Chelsea New York (1955).

[100] J. Ivanic and K. Ruedenberg: Rotation matrices for real spherical harmonics. Direct determination by recursion. *J. Phys. Chem.* **100**, 6342 (1996).

Index